HIGH-ACCURACY WAVE FUNCTION COMPUTATIONS OF PROTOTYPES FOR ALKYL RADICAL OXIDATION AND THE HO_3 RADICAL

by

Marcus A. Bartlett

(Under the Direction of Wesley D. Allen)

ABSTRACT

The propyl + O_2 reaction is an important model of chain branching reactions in larger combustion systems. Highly-accurate energetics of the *n*- and *i*-propyl + O_2 systems were obtained by focal point analyses (FPA) extrapolating to the *ab initio* limit based on explicit quantum chemical computations with electron correlation treatments through CCSDT(Q) and basis sets up to cc-pV5Z. A mixed Hessian methodology was implemented and benchmarked which makes computations of CCSD(T)/cc-pVTZ vibrational frequencies feasible for large systems and thus provides necessary improvements to the zero-point vibrational energies (ZPVE) for the propyl + O_2 systems. The first systematic conformational search of four QOOH intermediates of the propyl + O_2 systems were also completed, uncovering a total of 35 rotamers lying within 1.6 kcal mol mol^{-1} of their respective lowest-energy minima. The definitive energetics for stationary points on the propyl + O_2 potential energy surfaces provide key benchmarks for future studies of hydrocarbon oxidation. We also present a comprehensive study of the enigmatic hydridotrioxygen (HO_3) radical. This species has been probed in numerous gas-phase spectroscopy experiments, in part because it was thought to have a role in the tropospheric HO_x cycle. Moreover, HO_3 has been the subject of a vast amount of computational research over the past 50 years, which has served to

highlight the difficult and unusual molecular structure and energetics of this molecule. For example, the central O–O bond length in HO_3 has been highly vexing for quantum chemical methods, with reported values ranging all the way from 1.34 to 1.75 Å! We have solved the prominent riddles of HO_3 using convergent coupled-cluster methods extended all the way to CCSDTQ(P).

INDEX WORDS: computational chemistry, basis set extrapolation, focal point analysis, physical organic chemistry, quantum tunneling, combustion chemistry, molecular equilibrium structures, second-order vibrational perturbation theory, fundamental frequencies, Cooley-Numerov

HIGH-ACCURACY WAVE FUNCTION COMPUTATIONS OF PROTOTYPES FOR ALKYL RADICAL OXIDATION AND THE HO_3 RADICAL

by

Marcus A. Bartlett

B.S., Clayton State University, Morrow GA, 2013

A Dissertation Submitted to the Graduate Faculty of The University of Georgia in Partial Fulfillment of the Requirements for the Degree

DOCTOR OF PHILISOPHY

ATHENS, GEORGIA

2019

HIGH-ACCURACY WAVE FUNCTION COMPUTATIONS OF PROTOTYPES FOR ALKYL RADICAL OXIDATION AND THE HO_3 RADICAL

by

Marcus A. Bartlett

Major Professor:	Wesley D. Allen
Committee:	Henry F. Schaefer III Gary E. Douberly

Electronic Version Approved:

Suzanne Barbour
Dean of the Graduate School
The University of Georgia
May 2019

DEDICATION

To my Family

"The true sign of intelligence is not knowledge but imagination."

-Albert Einstein

TABLE OF CONTENTS

CHAPTER 1

INTRODUCTION AND LITERATURE REVIEW

1.1 INTRODUCTION

Quantum chemistry entails the application of quantum mechanics to the understanding of chemical phenomena. In recent decades the application of *ab initio* computational chemistry has gained momentum for both experimentalists and theorists alike. Quantum chemical computations are utilized by both theoretical and experimental chemists in research topics ranging from drug design to the understanding of atmospheric and combustion chemistry. Computational chemistry has become vastly popular as a way to investigate chemical systems that are either difficult to find or are expensive to purchase. Computational chemists are able to obtain meaningful chemical predictions before actual experiments are run, thus creating a better prepared experimental chemistry community. Modern *ab initio* electronic structure theory is able to obtain chemical accuracy for energetics and fundamental vibrational frequencies of 1 kcal mol^{-1} and 10 cm^{-1}, respectively.

1.2 THEORETICAL METHODS

1.2.1 SCHRÖDINGER EQUATION

In 1925 and 1926, two equivalent formulations of quantum mechanics were derived independently by Werner Heisenberg[1] and Erwin Schrödinger[2] utilizing matrix mechanics and partial differential equations, respectively. These two methods were shown to be mathematically

equivalent, thus here we focus on the more popular of the two, the derivation by Erwin Schrödinger. The time-dependent Schrödinger equation (TDSE) (Eq. 1.1) gives the physical foundation of modern quantum chemistry,

$$i\hbar\frac{\partial}{\partial t}\Psi = \hat{H}\Psi \tag{1.1}$$

where Ψ is the wave function, $\hbar$ is the reduced Planck constant, and $\hat{H}$ is the Hamiltonian operator, which contains the kinetic $\hat{T}$ and potential energy $\hat{V}$ terms. All knowable information about the state of a system is contained in the wave function Ψ.

Many applications of quantum mechanics to chemistry do not utilize the TDSE, as most chemical systems involve bound states where the potential energy operator is independent of time. The kinetic energy operator is also independent of time, thus we can invoke a separation of space and time variables to yield the time-independent Schrödinger equation (TISE) (Eq. 1.2):

$$\hat{H}\Psi = E\Psi \tag{1.2}$$

Due to the fact that electrons are much lighter than the nuclei, nuclear velocities are much smaller than the electronic velocities. The electrons are thus able to adjust very quickly to changes in nuclear positioning. This separation is known as the Born-Oppenheimer approximation[3] and provides a basis on which a potential energy surface, upon which nuclei move, is generated. The coupling between the nuclear and electronic velocities can be neglected in the Hamiltonian, providing a model in which the nuclei are perceived to be stationary from the electronic point of view. The molecular wave function is thus separated into electronic and nuclear components ($\Psi_{total} = \Psi_e \cdot \Psi_N$), and the purely electronic Schrödinger equation ($\hat{H}_e\Psi_e = E_e\Psi_e$) can be solved in a similar manner as Eq. 1.2. Note that only the nuclear kinetic

terms may be neglected, and we must not forget to account for internuclear repulsion. The Schrödinger equation for electronic motion is thus given by,

$$\hat{H}_e \Psi_e = U \Psi_e \tag{1.3}$$

where $\hat{H}_e$ is the electronic Hamiltonian, Ψ_e is the electronic wave function, and U is the Born-Oppenheimer potential energy surface.

While the electronic Hamiltonian operator ($\hat{H}_e$) of Eq. 1.3 depends only on the spatial coordinates of the electrons, realistically to completely describe an electron we must specify its spin. If relativistic effects are neglected, electron spin must be introduced as an ad hoc quantum effect. A molecular orbital (MO) gives a description of an electron not only by its three spatial coordinates but also by one spin function (α or β). However, building our many electron Ψ from a product of MOs, known as a Hartree product, does not account for the indistinguishability of electrons. This is a clear violation of the Pauli Principle, which states that all fermions have to be described by a wavefunction that is antisymmetrical with respect to interchange of the space and spin coordinates of any two fermions. However, the antisymmetry nature of the wave function can be achieved by creating it from a Slater determinant (SD) (Eq. 1.4):

$$\Phi_{\mathrm{SD}} = \begin{bmatrix} \phi_1(1) & \phi_2(1) & \cdots & \phi_N(1) \\ \phi_1(2) & \phi_2(2) & \cdots & \phi_N(2) \\ \vdots & \vdots & \ddots & \vdots \\ \phi_1(N) & \phi_2(N) & \cdots & \phi_N(N) \end{bmatrix} \tag{1.4}$$

The columns of the SD are composed of different one-electron molecular orbitals (ϕ_i) and the electron coordinates (i) differ along the rows.

1.2.2 GAUSSIAN BASIS SETS

One of the major techniques in *ab initio* quantum chemistry is the utilization of a basis set to expand Ψ. The MOs can be constructed by a linear combination of atom-centered one-electron atomic orbitals. This expansion of MOs leads to a set of quantum mechanical operator integrals over the atomic orbital basis functions. The ease of integration greatly depends on the type of basis function, i.e. atomic orbital, that is utilized. There are two types of atomic orbital basis functions commonly employed in *ab initio* calculations: Slater type orbitals (STO) (Eq. 1.5) and Gaussian type orbitals (GTO) (Eq. 1.6),

$$\phi^{\mathrm{STO}}_{l_x l_y l_z}(x,y,z) = N x^{l_x} y^{l_y} z^{l_z} e^{-\zeta r} \tag{1.5}$$

$$\phi^{\mathrm{GTO}}_{l_x l_y l_z}(x,y,z) = N x^{l_x} y^{l_y} z^{l_z} e^{-\zeta r^2} \tag{1.6}$$

where N is a normalization constant, the sum of integers (l_x, l_y, l_z) dictates what type of orbital is being represented, ζ specifies the size of the orbital, and r is the distance from the nucleus.

While the exponential dependence of r in the STO exactly mirrors the orbitals for the hydrogen atom, these functions give rise to difficult multi-center electron-repulsion integrals. The utilization of GTOs, which display an r^2 exponential dependence, are much easier to integrate because of the Gaussian product theorem.[4] However, the price of this cost reduction is largely paid for in accuracy, as GTOs have problems representing the proper behavior near the nucleus. To alleviate this pitfall, a linear combination of primitive GTOs is used to form what are called contracted GTOs.

The correlation-consistent basis sets (cc-pV*X*Z, *X* = D, T, Q, 5, 6...) developed by Dunning and co-workers[5-6] are among the most widely employed basis sets in high-accuracy *ab initio* quantum chemistry computations. The cc-pV*X*Z label stands for correlation-consistent

(cc), polarized valence (pV), *X* zeta basis set, where zeta refers to the number of functions in the valence shell. Dunning basis sets are constructed such that systematic increases in the number of basis functions are used as *X* increases, allowing for smooth convergence toward the complete basis seat (CBS) limit.

Certain chemical situations often require modifications to be made to the Dunning basis set. The study of Rydberg states, anions, or long-range electrostatic interactions typically require the addition of diffuse functions. These types of modifications are found in the set of augmented Dunning basis sets, denoted as aug-cc-pV*X*Z,[7] which are built by the addition of a single primitive GTO for each angular momentum shell to the original cc-pV*X*Z basis set. Another example of Dunning basis set modification is when one is interested in retrieving the correlation of core electrons. Adding GTOs with larger orbital exponents to the cc-pV*X*Z basis set produces the correlation-consistent polarized core-valence (pCV) cc-pCV*X*Z basis sets.[8]

1.2.3 GENERAL HARTREE-FOCK APPROXIMATION

While the electronic Schrödinger equation (Eq. 1.3) can easily be solved for one electron systems, such as the H_2^+ molecule, for larger electronic systems we must rely on approximations. The Hartree-Fock (HF) approximation, oft called the HF mean field theory or self-consistent field (SCF) theory, is central to quantum chemistry and builds a picture in which electrons occupy MOs. The HF approximation is an independent-particle model in which MOs are delocalized one-electron functions that describe electron movement in an average field of all other electrons. The major goal of HF theory is to variationally optimize the MOs in such a way that we may obtain the energetically best many-electron function. A major assumption of HF theory is that Ψ can be represented by a single Slater determinant. Thus, electron-electron repulsion is only included as an average effect.

The variational principle can be utilized in order to derive the working HF equations, by minimizing the energy subject to orthonormality constraints on the orbitals. The variational principle states that the expectation value of $\hat{H}_e$ over a normalized well-behaved trial wave function is greater than or equal to the true ground-state energy ε_0, as shown by Eq. 1.5.

$$\langle \Psi_e | \hat{H}_e | \Psi_e \rangle \geq \varepsilon_0 \tag{1.5}$$

The best set of spin orbitals utilized in the construction of Ψ_e are those that minimize the electronic energy. Variations in orbitals must be performed such that they remain both orthogonal and normalized, creating a constrained optimization problem. The Fock operator (Eq. 1.6) is an effective one-electron energy operator and accounts for orbital variations of the electronic energy:

$$\hat{F} = \hat{H}^{core} + \sum_j (\hat{J}_j - \hat{K}_j) \tag{1.6}$$

The $\hat{H}^{core}$ term accounts for the kinetic energy of an electron and the potential energy terms for electron-nuclear attraction, while the $\hat{J}_j$ and $\hat{K}_j$ operators are the Coulomb and exchange operators, respectively, and account for the repulsion between electrons. The $\hat{H}_e$ operator is not simply a sum of Fock operators, however. The canonical MOs (ϕ_j) are eigenfunctions of the Fock operator, and we can obtain the orbital energies ε_j by solving the following set of pseudo-eigenvalue equations:

$$\hat{F}\phi_j = \varepsilon_j \phi_j \tag{1.7}$$

Typically, the unknown MOs are expressed as a basis set expansion in terms of some known functions:

$$\phi_i = \sum_s C_{si}\tilde{\chi}_s \tag{1.8}$$

The basis functions $\tilde{\chi}_s$ are formed by a linear combination of atomic orbitals (Eq. 1.8) and are generally not solutions to the atomic HF problem. The HF equations (Eq. 1.7) can now be written as follows:

$$\sum_s F_{rs}C_{si} = \varepsilon_i \sum_s S_{rs}C_{si} \tag{1.9}$$

where F_{rs} and S_{rs} are the Fock and overlap matrix elements, respectively, C_{si} denotes the molecular orbital coefficients, and the ε_i are the orbital energies. Eq. 1.9 is famously known as the Roothaan equations[9] and must be solved iteratively, as the F_{rs} matrix elements involve integration over the molecular orbitals that are in turn eigenfunctions of $\hat{F}$. This iterative procedure of obtaining the set of molecular orbital coefficients that gives the lowest electronic energy is called the self-consistent-field (SCF) method.

1.2.4 MØLLER–PLESSET SECOND-ORDER PERTURBATION THEORY

As previously stated, the Hartree-Fock method treats electron correlation indirectly by a mean-field approach. The HF wave function is able to account for roughly 99% of the total energy, but the remaining 1% is essential to accurately describe important chemical phenomena. The difference between the HF energy and the exact energy is known as the electron correlation energy. The positions and momenta of electrons are strongly coupled to one another. Dynamic correlation corresponds to the instantaneous correlation of electronic motions and must be accounted for rather than just mean-field interactions. Obtaining this last 1% of the total energy

accounted for by electron correlation, as many say, is the reason that quantum chemists retain employment!

Many post-Hartree-Fock methods are available for obtaining the correlation energy. Since the HF method determines the energetically best one-determinant wave function, these post HF methods usually adopt the HF determinant as the reference wave function. The generic multi-determinant trial wave function $\left|\Psi_e\right\rangle$ and correlation energy (E^{corr}) can be written as,

$$\Psi_e = c_0\Phi_0 + \sum_{i=1} c_i\Phi_i \tag{1.10}$$

$$E^{\text{corr}} = E^{\text{exact}} - E^{\text{HF}} \tag{1.11}$$

where Φ_0 is taken as Φ_{HF}, Φ_i represents excited Slater determinants, c_0 and c_i are the determinant coefficients, and E^{corr} and E^{HF} are the correlation and HF energies, respectively. For single reference chemical systems, c_0 is usually close to one.

Rigorous treatment of electron correlation must be considered for an accurate accounting of the correlation energy. Electron correlation methods differ mainly in how they compute the excited determinant c_i coefficients. One popular post-HF method to compute the correlation energy is perturbation theory. The idea behind perturbative methods is that the problem under consideration only differs slightly from a problem previously solved, in this case the HF problem. The many-body perturbation theory Hamiltonian operator (Eq. 1.12) consists of two parts: a reference ($\hat{H}_0$) and a perturbation ($\hat{H}'$).

$$\hat{H} = \hat{H}_0 + \lambda\hat{H}' \tag{1.12}$$

Under the perturbation the wave function and energy become the following:

$$\Psi = \Psi_0 + \lambda^1\Psi_1 + \lambda^2\Psi_2 + \cdots \tag{1.13}$$

$$E = E_0 + \lambda^1 E_1 + \lambda^2 E_2 + \cdots \tag{1.14}$$

The ordering parameter λ scales the strength of the perturbation and is usually set to unity after the equations have been derived. The reference, or zeroth-order, wave function is signified by Ψ_0 and the first-order correction to this wave function can be expressed as $\Psi_1 = \sum_i c_i \Phi_i$. Plugging the perturbative wave function and energy into $\hat{H}_e \Psi_e = E_e \Psi_e$ and collecting terms of like powers of λ, it can be shown that the first- and second-order perturbative corrections to the electronic energy are $E_1 = \langle \Phi_0 | \hat{H}' | \Phi_0 \rangle$ and $E_2 = \sum_i c_i \langle \Phi_0 | \hat{H}' | \Phi_i \rangle$, respectively.

The most commonly utilized form of perturbation theory is second-order Møller-Plesset perturbation theory (MP2).[10] In MP2 theory, the reference Hamiltonian operator is the sum of a single Fock operator as a function of the various electrons (*N*):

$$\hat{H}_0 = \sum_{i=1}^{N} \hat{F}_i \tag{1.15}$$

The zeroth-order energy E_0 is thus simply the sum of the HF orbital energies. Since the orbital energy is the energy of an electron in the field of nuclei, and electrons, $\hat{H}_0$ double-counts the electron-electron repulsion. The perturbation operator (Eq. 1.16) is the difference between the exact instantaneous electron-electron repulsion and the HF mean field approximation to electron-electron interaction.

$$\hat{H}' = \sum_i^N \sum_{j>i}^N \frac{1}{r_{ij}} - \sum_i^N \sum_j^N (\hat{J}_j - \hat{K}_j) \tag{1.16}$$

The first-order correction is the expectation value of $\hat{H}'$ over the HF reference wave function. Hence, the sum of the zeroth- and first-order correlation energy corrections is simply the HF energy ($E_0 + E_1 = E_{\mathrm{HF}}$). Thus, the electron correlation energy doesn't begin until second-order when utilizing the reference Hamiltonian of Eq. (1.15).

The second-order correction contains only interactions of the reference determinant $|\Phi_0\rangle$ with doubly-excited determinants $|\Phi_{ij}^{ab}\rangle$ due to Brillouin's theorem.[11] Contributions from triple and higher-order excitations do not exist because the perturbation is a two-particle operator. The final MP2 energy is thus given by

$$E_{MP2} = E_{HF} + \sum_{i<j}^{\mathrm{occ}} \sum_{a<b}^{\mathrm{vir}} \frac{\left\langle \Phi_0 \middle| \hat{H}' \middle| \Phi_{ij}^{ab} \right\rangle \left\langle \Phi_{ij}^{ab} \middle| \hat{H}' \middle| \Phi_0 \right\rangle}{E_0 - E_{ij}^{ab}} \quad , \tag{1.17}$$

where *i, j,…* signify the occupied spin molecular orbitals and *a, b,…* denote the virtual spin molecular orbitals. The denominator can be written in terms of the energies of the MOs ($\varepsilon_i + \varepsilon_j - \varepsilon_a - \varepsilon_b$), and the second-order correction can blow up when the denominator is small, *i.e*, when occupied and virtual orbital energies become sufficiently close. The computational cost of MP2 formally scales as N^5, and it is a fairly computationally inexpensive method. MP2 theory provides a decent description of dynamical correlation and is able to account for roughly 80-90% of the correlation energy.

1.2.5 COUPLED CLUSTER THEORY

In modern quantum chemistry, significant advances in recovering the correlation energy were made with the development of coupled cluster (CC) theory.[12-13] When CC theory is expanded to include all possible electron excitations it is able to recover the full configuration interaction (FCI) solution, which is the exact solution to the Schrödinger equation in the space

spanned by a given one-particle (atomic orbital) basis set. CC theory is currently accepted as the most accurate post-HF method in recovering the correlation energy.

The multi-determinant CC electronic wavefunction Ψ_{CC} is formed via an exponential of an excitation operator $\hat{T}$

$$\left|\Psi_{CC}\right\rangle = e^{\hat{T}}\left|\Phi_0\right\rangle \tag{1.18}$$

$$e^{\hat{T}} = 1 + \hat{T} + \frac{1}{2}\hat{T}^2 + \frac{1}{6}\hat{T}^3 + \ldots \tag{1.19}$$

where $\hat{T}$ consists of excitation operators of different orders $\hat{T}_i$. These excitation operators involve cluster amplitudes $t_{ijk\ldots}^{abc\ldots}$ where once again *i, j,…* signify the occupied spin molecular orbitals and *a, b,…* denote the virtual spin molecular orbitals. The result of these excitation operators acting on a reference determinant Φ_0 produces excited determinants according to the order of excitation. The singly and doubly excited determinants produced when $\hat{T}_1$ and $\hat{T}_2$ act on Φ_0 are given by Eq's 1.21 and 1.22, respectively.

$$\hat{T} = \hat{T}_1 + \hat{T}_2 + \ldots. \tag{1.20}$$

$$\hat{T}_1\Phi_0 = \sum_{i}^{\text{occ}}\sum_{a}^{\text{vir}} t_i^a \Phi_i^a \tag{1.21}$$

$$\hat{T}_2\Phi_0 = \sum_{i<j}^{\text{occ}}\sum_{a<b}^{\text{vir}} t_{ij}^{ab} \Phi_{ij}^{ab} \tag{1.22}$$

Due to the complexity of the CC wave function (Eq. 1.18), solving the variational condition of Eq. 1.5 is not generally feasible. Employing a similarity transformation

($\bar{H} \equiv e^{-\hat{T}} \hat{H} e^{\hat{T}}$) allows the energy (Eq. 1.23) and amplitude (Eq. 1.24) equations to be derived by utilizing projection formulas:

$$\left\langle \Phi_0 \left| e^{-\hat{T}} \hat{H} e^{\hat{T}} \right| \Phi_0 \right\rangle = E_{CC} \tag{1.23}$$

$$\left\langle \Phi_{ijk\ldots}^{abc\ldots} \left| e^{-\hat{T}} \hat{H} e^{\hat{T}} \right| \Phi_0 \right\rangle = 0 \tag{1.24}$$

The $\hat{T}$ operator can be expanded to include excitations up to N^{th} order, where N is the number of electrons in the molecular system. However, expanding out this far is generally not feasible as computational expense increases drastically with increases in N. Therefore, the $\hat{T}$ operator is often truncated to include only lower level excitations. Truncated CC methods however still recover the majority of the electron correlation, as higher excited determinants contribute much less to the total electron correlation. This excitation truncation gives different variations in CC theory and is what the CC notation is built upon. Including only double excitations ($\hat{T} = \hat{T}_2$) is denoted CCD, singles and doubles ($\hat{T} = \hat{T}_1 + \hat{T}_2$) is denoted CCSD,[14] and singles, doubles, and triples ($\hat{T} = \hat{T}_1 + \hat{T}_2 + \hat{T}_3$) is CCSDT.[15]

CC theory is quite attractive as it is both size extensive and size consistent. Size extensivity corresponds to the energy scaling linearly with the size of the system. Size consistency means that the method correctly obtains the energy of two non-interacting dissociated systems. Higher-order excitations, such as CCSDT, are often times too expensive to perform for large systems. Thus, higher order excitations are usually approximated with a perturbative treatment. The most popular CC method is performed by incorporating singles, doubles, and a perturbative treatment of triple excitations [CCSD(T)].[16] CCSD(T) is often

considered to be the "golden standard" of quantum chemistry, and due to a cancelation of errors it is often superior to the more expensive CCSDT method.

1.2.6 FOCAL POINT ANALYSIS

The accuracy of *ab initio* quantum chemistry computations largely depends on the extent of electron correlation included in the many-electron wave function and the size of the atomic orbital basis functions. The computational cost of solving the exact Schrödinger equation utilizing FCI with a complete basis set (CBS) is far too computationally demanding. Similarly, to obtain the exact energy using CC methods, we must not only include all excitations in our excitation operator but also utilize the largest basis set possible. Ab initio limits can be approached by composite schemes, such as the focal-point analysis (FPA)[17-20] approach developed by Allen and co-workers.

The success of the FPA method relies on a duel extrapolation to the one- and *N*-particle limits of electronic structure theory. CBS limits are able to be approached when employing the correlation-consistent family of basis sets (cc-pV*X*Z or aug-cc-pV*X*Z, *X* = D, T, Q, 5, 6, ..., ∞), which systematically approach completeness with increases in the cardinality numbers *X*. The three-parameter exponential function (Eq. 1.25) of Feller[21] is utilized to extrapolate the HF energy to the CBS limit (E_{CBS}^{HF}).

$$E_X^{HF} = A + Be^{-CX} \tag{1.25}$$

The post HF dynamical correlation energy employs a two-parameter X^{-3} function[22] (Eq. 1.26) to extrapolate the CBS limit. Note that this expression extrapolates only the correlation energy and not the total energy.

$$E_{\mathrm{CBS}}^{\mathrm{corr}} = A + BX^{-3} \tag{1.26}$$

Many previous studies have shown that the correlation increment resulting from double excitations δ[CCSD] is the most important. Thus, large basis sets must be employed up through this level of theory, and electron correlation convergence is sometimes not even reached with basis sets with cardinalities as large as $X = 6$. However, while triple excitations are generally necessary for chemical accuracy, smaller basis sets with cardinalities of $X = 3$ or 4 are sufficient to reach satisfactory convergence of the δ[CCSD(T)] increment. The contribution of quadruple excitations, while often not necessary, can occasionally be significant, requiring the δ[CCSDT(Q)] increment to be evaluated with smaller basis sets ($X = 2$ and 3). Extrapolation schemes are not feasible at this level of theory due to a large demand in computational expense. Thus, an additivity scheme is employed for higher-order correlation. For example, the composite additivity approach to estimating the CCSDT(Q)/CBS energy is given by Eq. 1.27.

$$E_{\mathrm{CBS}}^{\mathrm{CCSDT(Q)}} \approx E_{\mathrm{CBS}}^{\mathrm{CCSD(T)}} + E_{\mathrm{Y}}^{\mathrm{CCSDT(Q)}} - E_{\mathrm{Y}}^{\mathrm{CCSD(T)}} \text{ (Y = cc-pVDZ or aug-cc-pVDZ)} \tag{1.27}$$

1.3 ANHARMONIC FORCE FIELDS

The potential energy surface (PES) of a chemical system provides the energy landscape upon which chemical reactions occur. Hence, obtaining accurate equilibrium molecular structures of both local minima and transition states (TS) is crucial in gaining chemical insight. PESs describe the changes in total energy of a chemical system as a function of the nuclear

positions. The multi-dimensional PES is very computationally demanding at high levels of accuracy. Thus, one-dimensional (1-D) reaction paths are often employed in quantum chemical studies. Two such 1-D methods entail mapping the intrinsic reaction path (IRP)[23] and the distinguished reaction path (DRP).[24-25] The IRP is a steepest descent reaction path which is obtained by following the energy gradient downhill starting from a TS. DRPs are obtained by performing constrained optimizations along the PES, by fixing one internal coordinate and optimizing all others at each point along the reaction path. Nonetheless, DRPs can be cast into a steepest descent formalism.[25] In many areas of chemistry, such as molecular spectroscopy, the nuclear motion can be characterized locally in the vicinity of a minimum structure.

The most common approach to describing the PES in a localized region near a minimum is to employ an anharmonic force field. An anharmonic force field is defined as the elements of a Taylor-series expansion of the PES in the vicinity around a chosen reference geometry. This expansion about a reference configuration is written as follows:

$$V(\mathbf{Q}) = V_0 + \frac{1}{2}\sum_{ij} H_{ij}Q_iQ_j + \frac{1}{6}\sum_{ijk} H_{ijk}Q_iQ_jQ_k + \frac{1}{24}\sum_{ijkl} H_{ijkl}Q_iQ_jQ_kQ_l + \cdots \qquad (1.28)$$

where **Q** denotes a set of complete and non-redundant nuclear displacement coordinates. Common coordinate choices include Cartesian, internal, and normal coordinates. Computing this potential expansion to infinite order is both impossible and impractical; thus $V(\mathbf{Q})$ is typically truncated to fourth order, which is known as a quartic force field (QFF). The harmonic oscillator vibrational approximation involves retaining only quadratic force constants in $V(\mathbf{Q})$. The gradient term in $V(\mathbf{Q})$ vanishes when the expansion is set about a stationary geometry. The quadratic (H_{ij}), cubic (H_{ijk}), and quartic (H_{ijkl}) force constants are the second-, third-, and fourth-

order energy derivatives with respect to **Q** and are evaluated at the reference point. These force constants are typically computed either by numerical finite-difference differentiation methods or by numerical least-squares fitting. The indices on the force constants correspond to the coordinates in which the derivatives of the PES are taken.

1.3.1 SECOND-ORDER VIBRATIONAL PERTURBATION THEORY

Computational vibrational spectroscopy has been developed extensively over the years and is an indispensable tool in the interpretation and prediction of molecular spectra. Since chemical systems cannot be accurately modeled under the harmonic approximation, anharmonic and mode coupling effects must be considered to gain a precise description of chemical phenomena. Ideally, accurate representations of full-dimensional PESs would be utilized in conjunction with variational methods in obtaining exact rovibrational levels. This however can become quite computationally demanding. Thus, vibrational second-order perturbation theory (VPT2)[26] has been widely used in conjunction with accurate QFF representations of the PES to go beyond the zeroth-order normal-mode approximation.

In VPT2 theory, the vibrational energy levels $G(v)$ of an asymmetric top molecule are given by

$$G(v) = \sum_i \omega_i \left(v_i + \frac{1}{2}\right) + \sum_i \sum_{j \le i} x_{ij} \left(v_i + \frac{1}{2}\right)\left(v_j + \frac{1}{2}\right) + \cdots \tag{1.29}$$

where ω_i is the harmonic vibrational frequency of the kth normal mode, x_{ij} denotes the vibrational anharmonic constants, and v_i signifies the normal-mode quantum numbers. The formulas for x_{ij} are summarized in Eq. 1.30 below. The B_α and ζ_{ij}^{α} are the rotational constants and Coriolis constants, respectively, for inertial axis α.

$$x_{ii} = \frac{1}{16}\left(\phi_{iiii} - \sum_{j=1} \frac{\phi_{iij}^2(8\omega_i^2 - 3\omega_j^2)}{\omega_j^2(4\omega_i^2 - \omega_j^2)}\right) - \frac{5}{48}\frac{\phi_{iii}^2}{\omega_i} \tag{1.30a}$$

$$x_{ij} = \frac{1}{4}\left(\phi_{iijj} - \sum_{k=1} \frac{\phi_{iik}\phi_{jjk}}{\omega_k^2} - 2\sum_{k=1} \frac{\phi_{ijk}^2(\omega_i^2 + \omega_j^2 - \omega_k^2)}{\eta_{ijk}}\right) + \left(\frac{\omega_i}{\omega_j} + \frac{\omega_j}{\omega_i}\right)\sum_{\alpha} B_\alpha(\zeta_{ij}^\alpha)^2 \tag{1.30b}$$

$$\text{where} \quad \eta_{ijk} = \left[(\omega_i + \omega_j)^2 - \omega_k^2\right]\left[(\omega_i + \omega_j)^2 - \omega_k^2\right] \tag{1.30c}$$

The ϕ_{ijk} and ϕ_{ijkl} quantities are the cubic and quartic force constants in the reduced normal coordinate space.[27] The fundamental, combination band, and overtone frequencies of an asymmetric top molecule are summarized in Eqs. 1.31 – 1.33.

$$\nu_i = \omega_i + \Delta_i = \omega_i + 2x_{ii} + \frac{1}{2}\sum_{i \neq j} x_{ij} \tag{1.31}$$

$$\left(\nu_i + \nu_j\right) = \nu_i + \nu_j + 2x_{ij} \tag{1.32}$$

$$(2\nu_i) = 2(\nu_i + x_{ii}) \tag{1.33}$$

Accuracy of within 10 cm^{-1} is expected when VPT2 is utilized on top of a high quality QFF. However, VPT2 should not be treated as a black box method and one must scrutinize each moving piece. One pitfall of VPT2 is the presence of Fermi resonances,[28-29] which arise from Eq. 1.30. When an overtone or combination level is reasonably close to another fundamental frequency ($2\omega_i \approx \omega_j$ or $\omega_i + \omega_j \approx \omega_k$), the denominators of Eqs 1.30a and 1.30c blow up, thus causing a breakdown of the VPT2 equations. In cases of Fermi resonances, one must deperturb the resonance utilizing an effective Hamiltonian.[28-29] VPT2 has also been said to be ineffective

for molecules with floppy low-frequency modes; however, in our own research we find this to not be true for all cases.

1.3.2 EQUILIBRIUM MOLECULAR STRUCTURES

While the Born-Oppenheimer equilibrium structure can be extracted entirely from experimental data, this process is quite difficult. Rotational constants for all vibrationally excited states corresponding to fundamental frequencies must be known. The difficulty of doing this grows with system size, as rotational constants must be known for not only the parent, but also several of its isotopologues. Many research groups now capitalize on advances in theoretical chemistry in order to obtain highly accurate equilibrium structures. One such strategy is to apply computed zero-point vibrational corrections to microwave rotational constants to deduce the equilibrium structure via a least-squares fitting procedure.

The simplest treatment of the rotational energy levels occurs under the rigid rotor model, in which rotational levels are inversely and precisely proportional to the principal moments of inertia. Utilizing vibrational perturbation theory, we can derive the following power series expansion (Eq. 1.34), corresponding to the rotational constants B_v described by the quantum numbers $\{v_1, v_2, v_3, \ldots.\}$.

$$B_v = B_e - \sum_i \alpha_i^B \left(v_i + \frac{1}{2}\right) + \frac{1}{2}\sum_{ij} \gamma_{ij}^B \left(v_i + \frac{1}{2}\right)\left(v_j + \frac{1}{2}\right) + \cdots \tag{1.34}$$

The α_i^B and γ_{ij}^B coefficients are the first and second vibration-rotation interaction constants, respectively.[29-32] If this arbitrary vibrational state, corresponding to given values of v_i is chosen

as the vibrational ground state, then we would obtain the following equilibrium rotational constant B_e:

$$B_e = B_0 + \frac{1}{2}\sum_i \alpha_i^B + \cdots \tag{1.35}$$

Eq. 1.35 shows that the sum of the first-order vibration-rotation interaction constants, also known as alpha constants, is necessary in the computation of B_e, and not the individual constants themselves. This is important because the sum of the first-order vibration-rotation interaction constants is not affected by small denominators, *i.e.,* Coriolis resonances, as are the alpha constants themselves.

There are many types geometric structures that have been considered over the years. Ground-state rotational constants alone, derived from microwave spectra, can be utilized in obtaining a molecular structure. This procedure utilizes a least-squares fitting of ground state rotational constants and produces what is known as the effective structure (r_0). The equilibrium structure derived using rotational constants found by Eq. 1.35 is often called the semiexperimental (r_e^{SE}) equilibrium structure. This name is given due to the fact that the structure is obtain by data from both experiment (rotational constants) and theory (vibrational corrections). Many previous studies[30-34] have showcased the effectiveness of the approach in obtaining highly accurate r_e^{SE} structures from high-level *ab initio* methods.

1.4 OVERVIEW OF CHAPTERS

In Chapter 2 and 3, we explore the *n*- and *i*-propyl + O_2 reactions as important models of hydrocarbon combustion systems. We employ FPA methods to extrapolate energetics to the *ab initio* limit based on explicit quantum mechanical computations with electron correlation

treatments through CCSDT(Q) and basis sets up to cc-pV5Z. All reaction species and transition states were fully optimized at the rigorous CCSD(T)/cc-pVTZ level of theory, revealing some substantial differences in comparison to DFT. In Chapter 3, we report a comprehensive study of the enigmatic hydridotrioxygen (HO_3) radical. The HO_3 species has been subject of a vast amount of computational research over the past 50 years, which has highlighted great difficulties in obtaining reliable molecular structures and energetics of the molecule. For example, the central O – O bond length in HO_3 has been a problematic parameter to nail down, with reported values ranging from 1.34 to 1.75 Å! We employ convergent coupled-cluster methods with electron correlation treatments all the way up to CCSDTQ(P) to solve riddles of the HO_3 species.

1.5 REFERENCES

(1) Heisenberg, W., *Z. Phys.* **1925**, *33*, 879-893.

(2) Schrödinger, E., *Phys. Rev.* **1926**, *28*, 1049-1070.

(3) Born, M.; Oppenheimer, R., *Ann. Phys.* **1927**, *389*, 457-484.

(4) Besalú, E.; Carbó-Dorca, R., *J. Math. Chem.* **2011**, *49*, 1769-1784.

(5) Dunning, T. H., Jr., *J. Chem. Phys.* **1989**, *90*, 1007-1023.

(6) Peterson, K. A.; Woon, D. E.; Dunning, T. H., Jr., *J. Chem. Phys.* **1994**, *100*, 7410-7415.

(7) Kendall, R. A.; Dunning, T. H., Jr.; Harrison, R. J., *J. Chem. Phys.* **1992**, *96*, 6796-6806.

(8) Woon, D. E.; Dunning, T. H., Jr., *J. Chem. Phys.* **1995**, *103*, 4572-4585.

(9) Roothaan, C. C. J., *Rev. Mod. Phys.* **1951**, *23*, 69-89.

(10) Møller, C.; Plesset, M. S., *Phys. Rev.* **1934**, *46*, 618.

(11) Brillouin, L., *J. Phys. Radium* **1932**, *3*, 373-389.

(12) Čížek, J., *J. Chem. Phys.* **1966**, *45*, 4256-4266.

(13) Crawford, T. D.; Schaefer, H. F., An Introduction to Coupled Cluster Theory for Computational Chemists. In *Rev. Comput. Chem*, Lipkowitz, K. B.; Boyd, D. B., Eds. John Wiley & Sons, Inc.: New Jersey, 2000; Vol. 14, pp 33-136.

(14) Purvis, G. D.; Bartlett, R. J., *J. Chem. Phys.* **1982**, *76*, 1910-1918.

(15) Noga, J.; Bartlett, R. J., *J. Chem. Phys.* **1987**, *86*, 7041-7050.

(16) Raghavachari, K.; Trucks, G. W.; Pople, J. A.; Head-Gordon, M., *Chem. Phys. Lett.* **1989**, *157*, 479-483.

(17) East, A. L. L.; Allen, W. D., *J. Chem. Phys.* **1993**, *99*, 4638-4650.

(18) Császár, A. G.; Allen, W. D.; Schaefer III, H. F., *J. Chem. Phys.* **1998**, *108*, 9751-9764.

(19) Császár, A. G.; Tarczay, G.; Leininger, M. L.; Polyansky, O. L.; Tennyson, J.; Allen, W. D., In *Spectroscopy from Space*, J. Demaison, K. S., Ed. Kluwer: Dordrecht: The Netherlands, 2001; pp 317-339.

(20) Gonzales, J. M.; Allen, W. D.; Schaefer III, H. F., *J. Phys. Chem. A* **2005**, *109*, 10613-10628.

(21) Feller, D., *J. Chem. Phys.* **1992**, *96*, 6104-6114.

(22) Helgaker, T.; Klopper, W.; Koch, H.; Noga, J., *J. Chem. Phys.* **1997**, *106*, 9639-9646.

(23) Fukui, K.; Kato, S.; Fujimoto, H., *J. Am. Chem. Soc.* **1975**, *97*, 1-7.

(24) Collins, M. A., *Adv. Chem. Phys.* **1982**, *46*, 481.

(25) Allen, W. D.; Bodi, A.; Szalay, V.; Császár, A. G., *J. Chem. Phys.* **2006**, *124*, 224310.

(26) Nielsen, H. H., *Rev. Mod. Phys.* **1951**, *23*, 90-136.

(27) Clabo, D. A.; Allen, W. D.; Remington, R. B.; Yamaguchi, Y.; Schaefer, H. F., *Chem. Phys.* **1988**, *123*, 187-239.

(28) Allen, W. D.; Yamaguchi, Y.; Császár, A. G.; Clabo, D. A.; Remington, R. B.; Schaefer, H. F., *Chem. Phys.* **1990**, *145*, 427-466.

(29) Clabo, D. A.; Allen, W. D.; Remington, R. B.; Yamaguchi, Y.; Schaefer, H. F., *Chem. Phys.* **1988**, *123*, 187-239.

(30) Vázquez, J.; Stanton, J. F., Semiexperimental Equilibrium Structures: Computational Aspects. In *Equilibrium Molecular Structures: From Spectroscopy to Quantum Chemistry*, Demaison, J.; Boggs, J. E.; Császár, A. G., Eds. CRC Press: Boca Raton, FL, 2011; pp 53-88.

(31) East, A. L. L.; Johnson, C. S.; Allen, W. D., *J. Chem. Phys.* **1993**, *98*, 1299-1328.

(32) East, A. L. L.; Allen, W. D.; Klippenstein, S. J., *J. Chem. Phys.* **1995**, *102*, 8506-8532.

(33) Baraban, J. H.; Changala, P. B.; Stanton, J. F., *J. Mol. Spectrosc.* **2018**, *343*, 92-95.

(34) Jaeger, H. M.; Schaefer, H. F.; Demaison, J.; Császár, A. G.; Allen, W. D., *J. Chem. Theory Comput.* **2010**, *6*, 3066-3078.

CHAPTER 2

THE MULTICHANNEL *n*-PROPYL + O_2 REACTION SURFACE: DEFINITIVE THEORY ON A MODEL HYDROCARBON OXIDATION MECHANISM[†]

[†]Reproduced from Bartlett, M.A.; Liang, T.; Pu, L.; Schaefer, H. F.; Allen, W.D. 2018. *J. Chem. Phys.* 148: 094303, with the permission of AIP Publishing.

2.1 ABSTRACT

The *n*-propyl + O_2 reaction is an important model of chain branching reactions in larger combustion systems. In this work, focal point analyses (FPA) extrapolating to the *ab initio* limit were performed on the *n*-propyl + O_2 system based on explicit quantum chemical computations with electron correlation treatments through CCSDT(Q) and basis sets up to cc-pV5Z. All reaction species and transition states were fully optimized at the rigorous CCSD(T)/cc-pVTZ level of theory, revealing some substantial differences in comparison to the DFT geometries existing in the literature. A mixed Hessian methodology was implemented and benchmarked that essentially makes the computations of CCSD(T)/cc-pVTZ vibrational frequencies feasible and thus provides critical improvements to zero-point vibrational energies (ZPVE) for the *n*-propyl + O_2 system. Two key stationary points, *n*-propylperoxy radical (**MIN1**) and its concerted elimination transition state (**TS1**), were located 32.7 kcal mol^{-1} and 2.4 kcal mol^{-1} below the reactants, respectively. Two competitive β-hydrogen transfer transition states (**TS2** and **TS2′**) were found separated by only 0.16 kcal mol^{-1}, a fact unrecognized in the current combustion literature. Incorporating **TS2′** in master equation (ME) kinetic models might reduce the large discrepancy of 2.5 kcal mol^{-1} between FPA and ME barrier heights for **TS2**. **TS2** exhibits an anomalously large diagonal Born-Oppenheimer correction (Δ_{DBOC} = 1.71 kcal mol^{-1}), which is indicative of a nearby surface crossing and possible nonadiabatic reaction dynamics. The first systematic conformational search of three QOOH intermediates was completed, uncovering a total of 32 rotamers lying within 1.6 kcal mol^{-1} of their respective lowest-energy minima. Our definitive energetics for stationary points on the *n*-propyl + O_2 potential energy surface provide key benchmarks for future studies of hydrocarbon oxidation.

2.2 INTRODUCTION

Reactions of alkyl radicals (R) with O_2 are paramount to low-temperature oxidation mechanisms involved in chemical phenomena such as autoignition and engine knock.[1-2] Comprehensive reviews have been published recently on both experimental and theoretical investigations of elementary reactions in low-temperature autoignition chemistry.[3-5] Hydrocarbon (RH) oxidation processes are initiated through abstraction of an H atom (Eq. 2.1), preferentially from the weakest C–H bond. Initially, O_2 is apt to attack RH; however, as the hydroxyl radical pool builds, OH can become the predominant abstractor:

$$\mathrm{RH + Y \rightarrow R + YH} \qquad \mathrm{Y = O_2, OH, \ldots} \qquad (2.1)$$

Barrierless addition of O_2 to R produces an alkylperoxy radical RO_2 (Eq. 2.2), which in turn drives the sequence of reactions given by Eqs. 2.3 – 2.10:

$$\mathrm{R + O_2 \rightleftharpoons RO_2} \qquad (2.2)$$

$$\mathrm{RO_2 \rightarrow alkene + HO_2} \qquad (2.3)$$

$$\mathrm{RO_2 \rightleftharpoons QOOH} \qquad (2.4)$$

$$\mathrm{QOOH \rightarrow aldehyde + OH} \qquad (2.5)$$

$$\mathrm{QOOH \rightarrow cyclic\ ether + OH} \qquad (2.6)$$

$$\mathrm{QOOH \rightarrow alkene + HO_2} \qquad (2.7)$$

$$\mathrm{QOOH + O_2 \rightleftharpoons OOQOOH} \qquad (2.8)$$

$$\mathrm{OOQOOH \rightarrow OH + ketohydroperoxide} \qquad (2.9)$$

$$\mathrm{ketohydroperoxide \rightarrow OH + alkoxy\ radical} \qquad (2.10)$$

where QOOH is a carbon-centered hydroperoxyalkyl radical, and OOQOOH is an oxygen-centered hydroperoxyalkyl peroxy radical. Figure 2.1 gives a schematic potential energy surface (PES) of the *n*-propyl + O_2 reaction mechanism comprised of Eqs. 2.2 – 2.7.

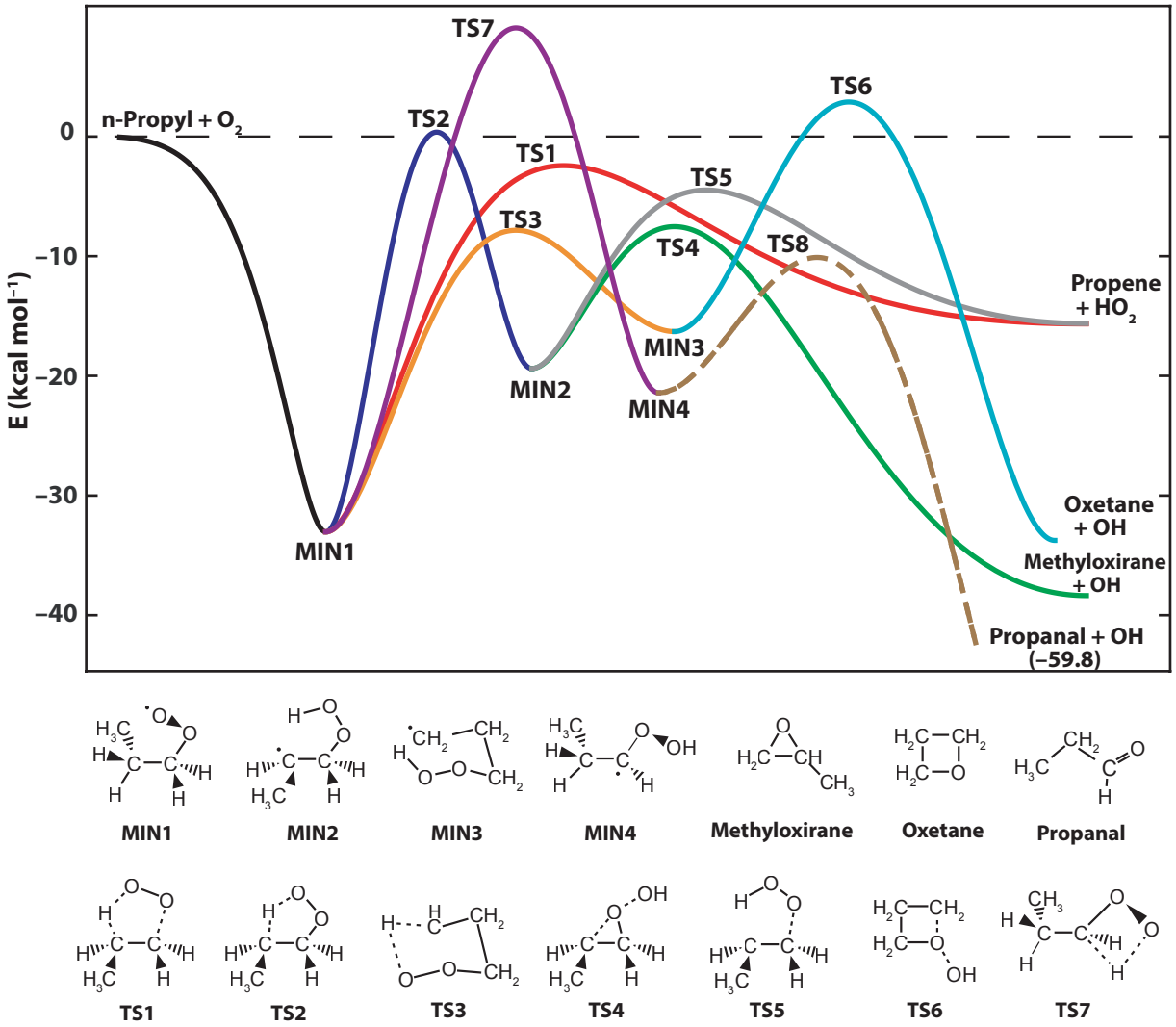

Figure 2.1 Schematic potential energy surface (PES) for *n*-propyl + O_2 reactions.

Multiple unimolecular transformations of stabilized RO_2 radicals are possible, including reverse fragmentation back to R + O_2, concerted elimination to produce an alkene + HO_2 (Eq. 2.3), and isomerization to form QOOH via hydrogen transfer (Eq. 2.4). The equilibrium of Eq. 2.2 lies well to the right in the region of 500-600 K, but at higher temperatures (T > 1000 K), the reaction

shifts back to the separated reactants, removing the RO_2 chain carrier. Moreover, the concerted elimination step is effectively chain terminating at low temperatures, because HO_2 radicals are relatively unreactive. These two effects lead to a negative temperature coefficient (NTC) region, in which hydrocarbon reactivity decreases with increasing temperature. Finally, a complete kinetic model that reproduces all aspects of R + O_2 experiments must include not only reactions (2.1) – (2.10) but also formally direct pathways from the reactants or each intermediate to every other intermediate or bimolecular product.

A high-profile 2015 investigation[6] exploited the resonance-stabilized character of cycloheptadieneyl radicals to achieve the first detection of an elusive QOOH species produced via internal hydrogen transfer of RO_2 (Eq. 2.4). The decomposition of QOOH species formed by 1,*n*-hydrogen transfers is a chain propagating step when the O–O bond is cleaved to give either an aldehyde + OH (n = 3, Eq. 2.5) or a cyclic ether + OH ($n \geq 4$, Eq. 2.6). A QOOH molecule produced via a 1,4-hydrogen transfer can also directly break the C–O bond, yielding an alkene + HO_2 radical (Eq. 2.7). Since QOOH is a carbon-centered radical, it is susceptible to a second O_2 oxidation attack (Eq. 2.8) to give OOQOOH. As with QOOH, the OOQOOH radicals can undergo internal hydrogen abstraction followed by dissociation to produce multiple OH radicals, acting effectively as a chain branching pathway (Eqs. 2.9 – 2.10).

As a model of alkyl radical oxidation, the ethyl + O_2 system has been exhaustively studied by experimental and theoretical investigations,[7-16] and critical details of this system are now well established.[14, 16] The lowest-energy ethyl + O_2 reaction channel involves the concerted elimination of HO_2 from the ethylperoxy intermediate (C_2H_5OO) to form ethylene + HO_2.[11-13] Master equation (ME) kinetic models[14] fit to measured reaction rates agree with rigorous *ab initio* computations

carried out through the CCSDT(Q) level[16] in placing the concerted elimination transition state below the ethyl + O_2 reactants by 3.0 kcal mol^{-1}.

The reactions of R + O_2 rapidly become complicated as the size of the alkyl radical grows, as a result of increased numbers of conformers and isomers. The study of larger alkyl + O_2 reactions is essential for full understanding of practical fuel combustion processes. In the past few years, reactions of propyl,[15, 17-39] butyl,[26, 40-46] neopentyl,[47-49] cyclopentyl,[50] and cyclohexyl[51-52] radicals with O_2 have been examined. Experimental findings show that as the alkyl chains are lengthened, isomerization reactions involving QOOH radicals can more effectively compete with concerted elimination of HO_2.[15] Therefore, the ethyl + O_2 system may be too small to be a true prototype for general alkyl radical oxidation, and propyl + O_2 may be a better candidate. The *n*-propyl + O_2 system is chosen for investigation here because it is the smallest system whose reactions can involve a favorable 6-membered ring transition state (**TS6**).

Early experimental work by Knox[17-19] used gas-chromatography (GC) to show that propene is the major product of the oxidation of propane at 591 K. Similarly, the GC analyses of Baker et al.[20] found that propene is the major stable product formed by adding propane to a slowly reacting mixture of H_2 + O_2 at 753 K. Slagle et al.[21-22] studied the kinetics and mechanism of the *n*-propyl + O_2 reaction from 297 to 635 K using a heated tubular reactor coupled to a photoionization mass spectrometer. Concentrations of *n*-propyl and propene were monitored in real-time experiments initiated by laser photolysis of the $C_6F_5C_4H_9$ radical precursor, and at 635 K the $R + O_2 \rightleftharpoons RO_2$ equilibrium was observed together with a delayed production of propene. Kaiser[23-24] studied propene generation as a function of both temperature (450 – 550 K) and pressure (55 – 550 Torr) upon UV irradiation of mixtures of propane, Cl_2, and O_2. Propane, propyl radicals, and C_3H_7Cl formation was monitored by GC analysis. At 490 K, propene yields are inversely dependent on

total pressure, proving that the mechanism involves rearrangement of an activated propyl peroxy adduct that can be stabilized by collisions. More recently, low-temperature oxidation of propane was studied by Cord et al.[36] in a jet-stirred reactor at atmospheric pressure using both GC and synchrotron vacuum ultraviolet photoionization mass spectrometry (SVUV-PIMS) for detection. Mole fractions of the reactants and products were measured as a function of temperature (530 – 730 K) giving attention to oxygenated products. With the aid of the EXGAS software,[53] a revised model of the propyl + O_2 system was generated that produced good simulations of formation of the main products as well as global reactivity.

Time-resolved formation of OH[15, 32, 38] and HO_2[25-26, 38] in propyl oxidation has been probed via laser-spectroscopic methods. Desain et al.[25] investigated HO_2 production from the C_3H_7 + O_2 reaction as a function of temperature (296 – 683 K) using laser photolysis/CW infrared frequency-modulation spectroscopy. Formation of HO_2 occured on two disparate time scales – a prompt yield, and a delayed production that becomes predominant at higher temperatures. The propene + HO_2 product fraction varies from about 5% near T = 500 K to 100% at T = 683 K. Subsequently, Desain et al.[15] studied hydroxyl radical formation from the ethyl + O_2 and propyl + O_2 reactions via laser-induced fluorescence by probing the OH transition ($A^2\Sigma^+ \leftarrow X^2\Pi$). Pulsed-photolytic Cl-initiated oxidation of propane at temperatures between 296 and 700 K produced more OH than does the corresponding ethane oxidation. Rate constants for the formation of all products in the ethyl + O_2 and propyl + O_2 systems were predicted by temperature-dependent parameterizations produced via the time-dependent ME approach of Klippenstein and Miller.[54] Both the time behavior and quantity of HO_2 formation from both systems are accurately described by the ME model; however, OH production is underpredicted and overpredicted at higher and lower temperatures, respectively.

Estupiñán and co-workers[30] investigated HO_2 formation in the ethyl + O_2 and propyl + O_2 systems using laser photolysis/long-path frequency-modulation spectroscopy with initial alkyl formation by 266 nm photolysis of alkyl iodides. Experimental results were compared to integrated rate equation models based on time-dependent ME results. The reaction of each propyl isomer was probed, permitting isolation and refinement of the *i*-propyl + O_2 reaction model. Previous models by Desain et al.[15] accurately described the time scale and amount of HO_2 formation for the ethyl + O_2 and *n*-propyl + O_2 cases; however, the refined model[30] underestimates both the prompt and slower HO_2 formation for the *i*-propyl + O_2 reaction. Subsequently, Estupiñán et al.[31] investigated HO_2 and DO_2 formation in the nondeuterated and deuterated ethyl + O_2 and propyl + O_2 systems between 623 and 748 K using laser photolysis/long-path infrared frequency-modulation spectroscopy. Experimental measurements showed good agreement with kinetic models based on the time-dependent ME over a wide range of temperatures and pressures, suggesting that the theory of HO_2 formation from ethyl + O_2 and propyl + O_2 is now well established.

The study of Huang et al.[32] reinvestigated the Desain experiments[15] in order to resolve the inconsistencies of the temperature dependence of the OH yield. Secondary reactions that produce OH were averted by utilizing a cleaner source of chlorine radicals [$(COCl)_2$] in which the co-product (CO) is not reactive. Excellent agreement was then observed between experiment and the ME model. Welz et al.[38] studied the low-temperature oxidation of propane at P = 4 Torr and T = 530, 600, and 670 K by time-resolved multiplexed photoionization mass spectrometry (MPIMS). Oxidation was initiated via pulsed laser photolysis of $(COCl)_2$, which generates a 1:1 mixture of *n*-propyl and *i*-propyl. At all three temperatures propene was the major stable product formed via concerted elimination of HO_2 in both the *n*-propyl and *i*-propyl cases. Experimental results were then modeled and interpreted via the multiscale informatics (MSI) methodology of

Burke and co-workers.[39] This model was able to successfully capture the competition between prompt and thermal product formation.

Much attention has also been given to the theoretical study of the propyl + O_2 system. Desain et al.[26] computed the key stationary points of the propyl + O_2 system at the QCISD(T)/6-311G(d,p)//B3LYP/6-31G(d) level of theory, with MP2/6-311++G(3df,2pd) basis set corrections appended for final energetics. Variational transition-state theory was utilized to describe the barrierless entrance channel to the propylperoxy radical adduct based on B3LYP/6-31G* reaction path energies. Time-dependent ME simulations were utilized for the reactions of both *n*-propyl and *i*-propyl + O_2 to produce rate constants that were in good agreement with empirical rate coefficients, branching fractions, and equilibrium constants. Wijaya et al.[27] investigated the rates and thermochemistry for the cyclization of various QOOH species leading to cyclic ether formation by quantum chemical computations utilizing composite complete-basis-set (CBS) methods, such as CBS-QB3, as well as density functional theory (DFT). The B3LYP functional consistently underestimated the barrier heights of cyclic ether formation. Green et al.[28] utilized the CBS-QB3 method to compute rate constants for the intramolecular radical attack within QOOH to form hydroxyalkyoxyl (HOQO) radicals. These channels were consistently found to have higher barrier heights than the competing $\mathrm{QOOH} \rightarrow \mathrm{cyclic\ ether} + \mathrm{OH}$ pathways, and in no case was the HOQO channel predicted to be able to compete with the cyclic ether channel. Thus, existing combustion models are not expected to have large errors by neglecting channels involving HOQO. Merle and co-workers[29] investigated the conformational distribution and decomposition pathways of the *n*-propylperoxy radical utilizing the CBS-QB3, B3LYP/6-31+G**, and mPW1K/6-31+G** levels of theory. Their detailed potential energy

surface at the CBS-QB3 level of theory suggests the importance of bimolecular products generated from 1,4-H transfer reactions at temperatures above 500 K.

Huynh et al.[34] investigated stationary points on the potential energy surfaces for both *n*- and *i*- propyl + O_2 systems utilizing CBS-QB3. High-pressure rate constants were obtained via transition state theory coupled with corrections for both tunneling and hindered rotations. These high-pressure rate constants were then utilized to derive pressure- and temperature-dependent rate constants obtained via Quantum Rice-Ramsperger-Kassel (QRRK) and modified strong collision (MSC) theories. Their model generated results in good agreement with previous experimental HO_2 profiles.[30] Zhang and Dibble[43] studied the kinetics of HO_2 elimination from *n*-propylperoxy radical and 1,4- and 1,5- H-migration using canonical variational transition state theory with multidimensional small curvature tunneling (SCT). A benchmark was performed at the CCSD(T) level of theory in order to gauge the accuracy of a combination of 7 density functionals and basis sets. In a separate study[55] they investigated the effects of olefin group substitution on alkylperoxy radical kinetics; CBS-QB3 calculations were utilized to perform RRKM master equation (RRKM/ME) simulations to determine the pressure dependence of selected rate constants.

Goldsmith et al.[35] theoretically studied the kinetics of QOOH + O_2 reactions involved in the *n*- and *i*-propyl + O_2 systems. Energetics of key stationary points were generated at the QCISD(T)/CBS level of theory and coupled with the RRKM/ME method to obtain pressure and temperature dependence of rate constants.[35] QOOH + O_2 reactions were found responsible for radical pool growth during the first few milliseconds following reaction initiation. Their research confirms that *n*-propyl is the smallest alkyl radical to exhibit low temperature combustion behavior

found in larger systems, but they also mention that *n*-butyl may be a better choice as a combustion archetype.

We aim to firmly establish the essential features of the *n*-propyl + O_2 potential energy surface utilizing highly accurate coupled cluster methods with large basis sets in order to obtain energies with errors of only tenths of a kcal mol^{-1}. The current literature is replete with geometries optimized by DFT, and thus executing full geometry optimizations at the "gold standard" CCSD(T)/cc-pVTZ level of theory is essential. Theoretical barrier heights for the *n*-propyl + O_2 system found in the current literature exhibit major disparities when compared to results obtained by ME models fitted to measured reaction rates. Utilizing focal point analyses (FPA) with correlation treatments up to CCSDT(Q) and basis sets up to cc-pV5Z has previously been shown to match ME results for the ethyl + O_2 system.[16] Employing zero-point vibrational energies (ZPVE) at high levels of theory is critical to the accuracy of our FPA relative energies. We employ a mixed Hessian methodology to compute ZPVE corrections of CCSD(T)/cc-pVTZ level quality, making these daunting computations feasible for larger combustion systems. In this work we perform FPA to the *ab initio* limit based on explicit computations through the CCSDT(Q) level of theory and basis sets up to cc-pV5Z, which is critically needed to establish the *n*-propyl + O_2 system as a benchmark for combustion chemistry.

2.3 THEORETICAL METHODS

2.3.1 GENERAL SCHEME

Electronic wave functions were determined in this study by restricted (RHF),[56] restricted open-shell (ROHF),[57] and unrestricted (UHF)[58] Hartree-Fock methods; second-order Møller-Plesset (MP2)[59] and Z-averaged (ZAPT2)[60] perturbation theory; and coupled cluster (CC)[61-62]

theory incorporating up to single and double excitations (CCSD),[63] perturbative contributions from connected triple excitations [CCSD(T)],[64] full triple excitations (CCSDT),[65] as well as a perturbative treatment of quadruple excitations [CCSDT(Q)].[66] The correlation methods employed a spin orbital formalism into which either ROHF or UHF orbitals were inserted, as signified by an RO or U prefix. This study primarily used the correlation-consistent (cc) families of basis sets cc-pV*X*Z (*X* = D, T, Q, 5),[67-68] cc-pCV*X*Z (*X* = T),[69] and aug-cc-pV*X*Z (*X* = D, T),[70] although CCSDT(Q) computations were performed with the 6-31G* basis set.[71]

The focal point analysis (FPA)[72-75] scheme developed by Allen and co-workers was employed to compute precise relative energies for the lowest conformers of all stationary points by extrapolation to full correlation and complete basis set limits. The quantum chemistry packages Molpro 2010.1,[76] CFOUR 1.0,[77] PSI 3.4,[78] GAMESS version 25 Mar 2010,[79-80] and MPQC 2.3.0,[81] as well as Kállay's MRCC[82] program were employed in this study.

2.3.2 GEOMETRY OPTIMIZATION

For all reactants, products, intermediates, and transition states, geometric structures were initially optimized at the (frozen-core) ROMP2/aug-cc-pVDZ level of theory, and then single-point ROCCSD(T)/cc-pVTZ energies were computed to determine the lowest-energy conformers. A series of dihedral angles was chosen to uniquely identify each conformer: $\tau(C_1C_2C_3O_4)$, $\tau(C_2C_3O_4O_5)$, and $\tau(C_3O_4O_5H_9)$. The following Klyne-Prelog[83-86] labels were utilized for each dihedral angle: G^+ (gauche, $+30^\circ < \tau < +90^\circ$), G^- (gauche, $-90^\circ < \tau < -30^\circ$), A^+ (anticlinal, $+90^\circ < \tau < +150^\circ$), A^- (anticlinal, $-150^\circ < \tau < -90^\circ$), and T (trans, $|\tau| > 150^\circ$). For the lowest-energy conformer of each species, ROCCSD(T)/cc-pVDZ

optimizations were then executed. Finally, these structures were used as starting points for subsequent full geometry optimizations at the ROCCSD(T)/cc-pVTZ level.

The final ROCCSD(T)/cc-pVTZ geometry optimizations were executed with the OPTKING module in the PSI 3.4 package using 3-point numerical gradients evaluated from single-point energies computed with the Molpro 2010.1 package. Fixed ROCCSD(T)/cc-pVDZ Hessians from the CFOUR 1.0 program were used to speed up convergence. Optimized geometries in Cartesian coordinates as well as depictions of the structures and internal coordinates of all stationary points are provided in Table S4 of the Supporting Information.

2.3.2 FOCAL POINT ANALYSIS

In our FPA computations, E, ΔE, and δ refer to the absolute energies, relative energies between species, and relative energy increments with respect to preceding levels of electron correlation. The Hartree-Fock[87] (E_{HF}) and correlation energies[88] (ε) were extrapolated with the following equations:

$$E_{\mathrm{HF}}(X) = E_{\mathrm{HF}}^{\infty} + A \exp(-bX) \tag{2.11}$$

$$\varepsilon(X) = \varepsilon^{\infty} + \frac{B}{X^3} \tag{2.12}$$

where X is the cardinal number of a correlation consistent cc-pVXZ basis. The extrapolations in the Hartree-Fock case employed X = {3, 4, 5}, while those for ROCCSD, ROCCSD(T), and ZAPT2 correlation energies used X = {3, 4}.

To test eqs. 2.11 and 2.12, we also investigated 10 alternative extrapolation schemes that coupled four Hartree-Fock formulas (exp,[87] expgauss,[68] exp-2,[89] Schwenke[90]) with four correlation energy formulas (X^{-3},[88] Schwartz4,[91] Schwartz6,[91] Schwenke[90]). These extrapolation schemes are detailed in Table S11. For 16 reactions starting with *n*-propyl + O_2 and going to various

intermediates and products, reaction energies (ΔE_e) from eqs. 2.11 and 2.12 were compared with results generated by a weighted average of 7 viable methods. This ΔE_e comparison gave an overall mean average deviation (MAD) of 0.05 kcal mol^{-1} and a standard deviation of 0.03 kcal mol^{-1}. Moreover, for the four product channels shown in Fig. 2.1, the (exp, X^{-3}) extrapolation formulas gave δ[ROCCSD/cc-pV5Z] reaction energy increments accurate to within 0.12 kcal mol^{-1} when compared to explicit ROCCSD/cc-pV5Z results. We have also compared δ[ZAPT2/cc-pV5Z] relative energy increments produced by the X^{-3}, Schwartz4, and Schwartz6 correlation extrapolation formulas with explicit ZAPT2/cc-pV5Z results for all 16 reactions investigated in the *n*-propyl + O_2 system. The X^{-3} and Schwartz6 extrapolation formulas provide good agreement with the explicit ΔE_e values, exhibiting a MAD of 0.15 and 0.13 kcal mol^{-1}, respectively. However, the Schwartz4 formula proved to be an outlier and was thus excluded from further consideration. All in all, we conclude that the (1σ) uncertainty in our chosen (exp, X^{-3}) extrapolation scheme is ca. 0.1 kcal mol^{-1}.

Single-point energies computed by the ROCCSDT and UCCSDT(Q) levels of theory were used as additive corrections:

$$\delta[\text{ROCCSDT}] = \Delta E(\text{ROCCSDT/cc-pVDZ}) - \Delta E(\text{ROCCSD(T)/cc-pVDZ}) \quad (2.13)$$

$$\delta[\text{CCSDT(Q)}] = \Delta E(\text{UCCSDT(Q)/6-31G}^*) - \Delta E(\text{ROCCSDT/6-31G}^*) \quad (2.14)$$

These computationally demanding ROCCSDT and UCCSDT(Q) correlation increments were computed with modest basis sets (cc-pVDZ, 6-31G*) using CFOUR 1.0 and Kállay's MRCC program coupled with CFOUR 1.0, respectively.

Core electron correlation effects were accounted for by subtracting all-electron (AE) and frozen-core (FC) ROCCSD(T) energies computed with the cc-pCVTZ basis set:

$$\Delta(\text{core}) = \Delta E_e(\text{AE-ROCCSD(T)/cc-pCVTZ}) - \Delta E_e(\text{FC-ROCCSD(T)/cc-pCVTZ}) \quad (2.15)$$

A first-order relativistic correction,[92] Δ(rel), was computed from the one-electron mass-velocity and Darwin terms at the ROCCSD(T)/cc-pVTZ level. The diagonal correction to the Born-Oppenheimer approximation (DBOC),[93] which corrects for relaxation of the clamped nucleus assumption, was computed at the ROHF HF/aug-cc-pVTZ level. However, DBOC values were not included in the final FPA energetics because some transition states are sufficiently close to a conical intersection that the DBOC term becomes anomalously large. This illuminating phenomenon is discussed in detail below. The adiabatic DBOC is evaluated as

$$E_{\mathrm{DBOC}} = \left\langle \Psi_e(\mathbf{r};\mathbf{R}) \middle| \hat{T}_n \middle| \Psi_e(\mathbf{r};\mathbf{R}) \right\rangle \tag{2.16}$$

where $\Psi_e(\mathbf{r};\mathbf{R})$ is the electronic wave function, $\mathbf{r}$ is the set of electronic coordinates, $\mathbf{R}$ is the set of nuclear coordinates, and $\hat{T}_n$ is the nuclear kinetic energy operator.

Harmonic vibrational frequencies and zero-point vibrational energy (ZPVE) corrections, $\Delta\mathrm{ZPVE(harm)}$, were computed initially at the ROCCSD(T)/cc-pVDZ level of theory. Important refinements were then made by means of a mixed Hessian (mixed-H) scheme designed to closely approximate the vibrational frequencies that would be obtained at the ROCCSD(T)/cc-pVTZ level, except at much reduced computational cost. In the mixed-H approach, the ROCCSD(T)/cc-pVTZ normal modes for a given species in the internal coordinate representation were assumed to be equivalent to their ROCCSD(T)/cc-pVDZ counterparts. The diagonal quadratic force constants for these normal modes were then evaluated by finite-differences of ROCCSD(T)/cc-pVTZ energies. Back-transformation[77] of the resulting diagonal, normal-coordinate force constant matrix into the internal coordinate space provided a complete force constant matrix from which harmonic frequencies and total energy distributions (TEDs)[94-96] could be computed. Our mixed-H scheme was benchmarked by comparison with explicit ROCCSD(T)/cc-pVTZ computations, as detailed in Table S7. Remarkably, the mean absolute deviation between explicit and mixed-H

ROCCSD(T)/cc-pVTZ harmonic vibrational frequencies is only 0.68 cm^{-1} for **MIN1**, and the corresponding ZPVE(harm) values differ by only 0.002 kcal mol^{-1}. Likewise, for *n*-propyl, propene, methyloxirane, oxetane, and propanal, the overall mean absolute errors in the harmonic vibrational frequencies and ZPVEs are 0.56 cm^{-1} and 0.009 kcal mol^{-1}, respectively, bolstering confidence in our mixed-H scheme. The final ZPVE values adopted in this study were explicit ROCCSD(T)/cc-pVTZ values for the reactant and product species and mixed-H approximations to ROCCSD(T)/cc-pVTZ for all intermediates and transition states.

The final focal point energy estimating ROCCSDT(Q) relative energies at the CBS limit was found by summing up extrapolation results, additive corrections, and auxiliary terms to give:

$$\Delta E_{\mathrm{FP}} = E_{\mathrm{HF}}^{\infty} + \delta^{\infty}[\mathrm{ROCCSD(T)}] + \delta[\mathrm{ROCCSDT}] + \delta[\mathrm{CCSDT(Q)}] + \Delta(\mathrm{core}) + \Delta(\mathrm{rel}) + \Delta\mathrm{ZPVE(harm)} \quad (2.17)$$

ZPVE, relativistic, and DBOC computations were performed with the CFOUR 1.0 package, while core correlation corrections were computed with the Molpro 2010.1 package. From both the basis set and electron correlation convergence properties of our focal point tables, we estimate a 1σ uncertainty of 0.2 kcal mol^{-1} for final energetic predictions (Table 2.1). This uncertainty is consistent with the 2σ uncertainties proposed for a similar high-level thermochemical scheme (ANL0) when applied to combustion reactions.[4]

2.4 DISCUSSION AND ANALYSIS OF THE R + O_2 REACTION

The essential features of the *n*-propyl + O_2 potential energy surface investigated in this research are depicted in Figure 2.1. The stationary points chosen are the same as those used by Klippenstein and co-workers[26] in their ME modeling, as well as those of the pathway for

1,3-hydrogen transfer from *n*-propylperoxy (**MIN1**) to propanal + OH. The direct H-abstraction pathway from *n*-propyl + O_2 to propene + HO_2 was excluded from further study after finding that the corresponding transition state lies 15.3 kcal mol^{-1} above the reactants, as computed at the ROCCSD(T)/cc-pVTZ//B3LYP/6-311+(d,p) level of theory with B3LYP/6-311+(d,p) ZPVE corrections. Table 2.1 compares our relative enthalpies at 0 K ($\Delta_{rxn} H_0^\circ$) for all stationary points of the *n*-propyl + O_2 system to those of previous studies. A detailed discussion of these results follows.

TABLE 2.1. Relative enthalpies at 0 K ($\Delta_{rxn} H_0^\circ$, kcal mol^{-1}) for stationary points of the *n*-propyl + O_2 system.

	$\Delta_{rxn} H_0^\circ$ (kcal mol^{-1})									
Ref.	26 QCISD(T) (2002)	15 ME[a] (2003)	32 ME[a] (2011)	27 CBS-Q[b] (2003)	29 CBS-Q[b] (2005)	34 CBS-Q[b] (2010)	55 CBS-Q[b] (2011)	43 CCSD(T) (2011)	35 QCISD(T)[c] (2012)	This Work
n-propyl+O_2	0.0	0.0	0.0	0.0	0.0	0.0	0.0	0.0	0.0	0.00
MIN1	–34.9	–33.9	—	—	–34.8	–34.8	—	—	–33.3	–32.71
MIN2	–21.6	—	—	—	–21.4	—	–19.4	—	–20.4	–19.19
MIN3	–19.8	—	—	–17.4	–18.9	—	–17.2	—	–18.1	–17.44
MIN4	—	—	—	—	—	—	—	—	—	–21.20
TS1	–5.2	–3.8	–3.8	—	–3.9	–2.4	–2.4	–3.2	–2.7	–2.41
TS2	–2.6	–2.1	–2.1	—	–2.7	–1.2	—	–0.1	—	+0.37
TS2′	—	—	—	—	—	—	—	—	–0.2	+0.53
TS3	–11.2	—	—	—	–10.9	–9.5	–9.5	–8.6	–8.5	–7.75
TS4	–6.5	—	—	—	–9.3	—	—	—	–8.1	–7.45
TS5	–3.4	—	—	—	–6.1	—	—	—	–3.2	–4.42
TS6	+3.6	—	—	+3.4	+0.8	—	—	—	+2.9	+2.87
TS7	—	—	—	—	+6.1	—	—	—	(+8.1)[d]	+9.04
propene+HO_2	—	—	—	–15.1	–16.6	—	–16.5	—	–16.5	–15.47
methyloxirane +OH	—	—	—	—	–38.8	—	—	—	–38.6	–37.99
oxetane+OH	—	—	—	—	–34.9	–34.5	—	—	–35.1	–33.42
propanal+OH	—	—	—	—	–60.0	—	—	—	–61.5	–59.82

[a] Fitted by master equation analysis to experimental kinetic data.

[b] Literature CBS-QB3 energies values.

[c] Restricted QCISD(T)/CBS energies including B3LYP/6-311++G(d,p) ZPVE corrections.

[d] Direct transition state from **MIN1** to propanal + OH.

Cyclic transition states (**TS2**–**TS3**, **TS7**) leading to QOOH species undergo distortion from ring planarity, raising the specter of multireference electronic character. The open-shell T_1 diagnostic of Jayatilaka and Lee[97] measures the magnitude of orbital relaxation in the coupled cluster wavefunction and is utilized as a diagnostic for the presence of multireference character. While for closed-shell species, $T_1 > 0.02$ is often taken as an indicator of multireference character,[98] open-shell species tend to have larger T_1 values[98] and a less defined threshold. To add further certainty in our assessment of multireference character, we also report the largest doubles amplitudes ($T_{2,\max}$) in the CCSD(T)/cc-pVTZ wave function.

In Table 2.2, the T_1 diagnostic and $T_{2,\max}$ amplitudes are given for the minima and transition states on the *n*-propyl + O_2 potential energy surface, as well as the HO_2 and OH fragments, all computed with the Molpro 2010.1 package. The CN radical is also included as a benchmark, because it is reasonably well described at the single reference CCSD(T) level of theory even though this species exhibits large spin contamination when using unrestricted methods.[99-101] All minima and TSs, as well as HO_2 and OH, have smaller T_1 and $T_{2,\max}$ values than CN and show no signs of significant multireference character. The lone exception is **TS4**, which exhibits a slightly larger $T_{2,\max}$ value, which is nonetheless smaller than 0.1. Thus, the *n*-propyl + O_2 system can be safely studied with single-reference coupled cluster methods.

TABLE 2.2 T_1 diagnostic values and $T_{2,max}$ amplitudes at the CCSD(T)/cc-pVTZ level of theory

	T_1	$T_{2,max}$		T_1	$T_{2,max}$
MIN1	0.029	<0.05	**TS1**	0.032	0.083
MIN2	0.012	<0.05	**TS2**	0.024	<0.05
MIN3	0.012	<0.05	**TS2′**	0.024	<0.05
MIN4	0.016	<0.05	**TS3**	0.024	<0.05
n-propyl	0.009	<0.05	**TS4**	0.042	0.095
HO_2 ($^2A''$)	0.037	0.056	**TS5**	0.039	0.073
OH ($^2\Pi$)	0.006	<0.05	**TS6**	0.026	0.065
CN ($^2\Sigma^+$)	0.053	0.093	**TS7**	0.019	<0.05

2.4.1 REACTANTS AND PRODUCTS

Experimentally determined geometries are available for OH,[102] O_2,[102] HO_2,[103] propene,[104] oxetane,[105] and methyloxirane.[106] Our ROCCSD(T)/cc-pVTZ geometries are in excellent agreement with experiment with MADs of 0.003 Å for bond lengths and 0.5° for bond angles. However, a notable difference of 1.24° is seen for $\alpha(H_7–C_1–C_2)$ of propene. The geometric parameters of *n*-propyl (Figure 2.2) are in excellent agreement with previous[107] CCSD(T)/cc-pVTZ results, the MAD being only 0.0002 Å for bond lengths and 0.002° for bond angles. When comparing the B3LYP/6-311++G(d,p) *n*-propyl structure of Goldsmith et al.[35] to our result, the MAD is 0.002 Å for bond lengths and 0.55° for bond angles; however, notable differences of 1.09° and 2.15° are present for $\alpha(C_1–C_2–C_3)$ and $\tau(C_1–C_2–C_3–H_9)$, respectively.

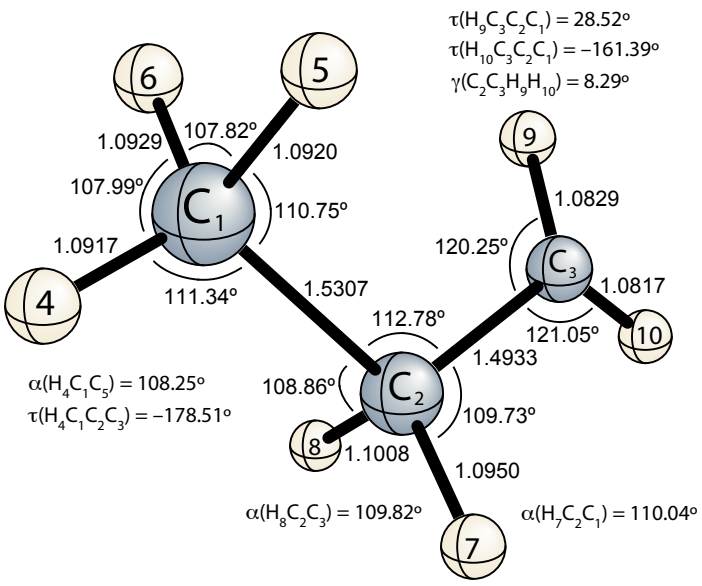

Figure 2.2 Optimum geometry of *n*-propyl radical at ROCCSD(T)/cc-pVTZ level of theory. Bond lengths are in Å.

2.4.2 RO_2 FORMATION

Each reaction path of the *n*-propyl + O_2 reaction shown in Figure 2.1 relies on the initial formation of the *n*-propylperoxy (**MIN1**) radical. The *n*-propyl + O_2 reaction undergoes a barrierless combination leading to the highly exothermic **MIN1** (–32.71 kcal mol^{-1}) reaction intermediate. The **MIN1** species has 5 energetically distinct rotamers resulting from rotations about both the C_2–C_3 and C_3–O_4 bonds: G^+G^+ (0.00 kcal mol^{-1}), G^+A^- (0.56 kcal mol^{-1}), TG^- (0.19 kcal mol^{-1}), G^+T (0.48 kcal mol^{-1}), and TT (0.62 kcal mol^{-1}); the relative energies of these rotamers, given in parentheses, were determined here at the CCSD(T)/cc-pVTZ//MP2/aug-cc-pVDZ level of theory. All but the TT rotamer have energetically equivalent enantiomers whose labels are found by inverting the signs of the G and A designations. Previous CBS-QB3//B3LYP/6-31+G**[29] and more recently CCSDT(Q)/CBS//CCSD(T)/ANO0[108] computations have also given G^+G^+ as the lowest energy RO_2 conformer, in agreement with our work. Tarczay

et al.[109] exhaustively searched the rotamers of **MIN1** utilizing B3LYP and EOMIP-CCSD levels of theory coupled with the 6-31+G*, DZP, and TZP basis sets and found the same 5 rotamers presented in our work; B3LYP gave a different ordering of relative energies of the rotamers of **MIN1** when compared to EOMIP-CCSD. Table S1 shows the correspondence between our nomenclature for **MIN1** rotamers and previous designations.[29, 108-109] Our relative energies display a MAD of only 0.06 kcal mol^{-1} compared to the very high-level results of Hoobler et al.,[108] thus giving high confidence in our theoretical method.

The geometric parameters of **MIN1** (Figure 2.3) found in the aforementioned CCSD(T)/ANO0[108] study are in good agreement with our higher-level geometry. The MAD in bond lengths is 0.007 Å; however, there is a rather large difference of 0.02 Å in $r(O_4–O_5)$. The MAD for bond and dihedral angles is 0.4°, with notable differences for $\tau(C_2–C_3–O_4–O_5)$, which is widened by 0.9°, and $\alpha(C_3–O_4–O_5)$, which is narrowed by 0.7° compared to our results. These differences can be attributed to use of the lower quality ANO0 basis set, which is similarly sized as cc-pVDZ. The agreement for bond lengths with the B3LYP/6-31+G** results of Merle et al.[29] happens to be excellent, with a MAD of 0.002 Å, but this DFT method overestimates angles. The most notable discrepancies are seen for $\alpha(C_1–C_2–C_3)$, $\alpha(C_3–O_4–O_5)$, and $\tau(C_1–C_2–C_3–O_4)$, with values greater than our results by 1.01°, 1.40°, and 1.35°, respectively. The more recent B3LYP/6-311++G(d,p) results of Goldsmith et al.[35] cannot be compared to our lowest energy **MIN1** structure, because they determined that the lowest energy rotamer of **MIN1** was TG$^-$ in their conformational search. In contrast, we find that TG$^-$ is 0.18 kcal mol^{-1} higher in energy than G$^+$G$^+$. This discrepancy shows the necessity of utilizing high-level coupled cluster energetics for these rotamers, as they are very close in energy and sensitive to level of theory.

When comparing **MIN1** with a previous CCSD(T)/cc-pVQZ structure[16] for the ethylperoxy radical, we find close similarities among internal coordinates of the same type. The most notable differences occur for the associated angles $\alpha(C_2–C_3–O_4)$ and $\tau(C_2–C_3–O_4–O_5)$, which show discrepancies of 0.42° and 0.92°, respectively. All other bond lengths and bond angles agree to within 0.01 Å and 0.1°, respectively. Wilke et al[16] found that CCSD(T) bond lengths change by less than 0.003 Å when going from cc-pVTZ to the cc-pVQZ basis set; bond angles were changed by less than 0.3°. Thus, only small variations are expected if optimizations were performed on **MIN1** with the larger cc-pVQZ basis set.

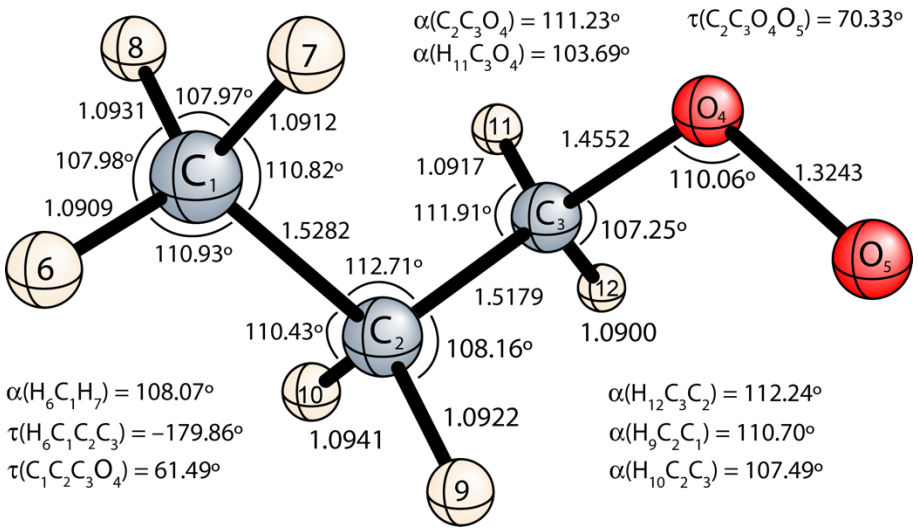

Figure 2.3 Optimum geometry of *n*-propylperoxy radical (**MIN1**) at ROCCSD(T)/cc-pVTZ level of theory. Bond lengths are in Å.

TABLE 2.3 Focal point analysis[a] (in kcal mol^{-1}) for **MIN1** relative to *n*-propyl + O_2

	ΔE_e(ROHF)	+δ [ZAPT2]	+δ [ROCCSD]	+δ [ROCCSD(T)]	+δ [ROCCSDT]	+δ [UCCSDT(Q)]	NET
6-31G*	–31.70	+9.23	–12.92	–0.66	–0.23	+0.38	–35.92
cc-pVDZ	–29.84	+10.35	–12.43	–0.64	–0.22	[+0.38]	[–32.41]
cc-pVTZ	–30.23	+7.13	–12.73	–0.99	[–0.22]	[+0.38]	[–36.67]
cc-pVQZ	–29.89	+6.01	–12.87	–1.12	[–0.22]	[+0.38]	[–37.72]
cc-pV5Z	–29.83	[+5.62]	[–12.93]	[–1.17]	[–0.22]	[+0.38]	[–38.16]
CBS	[–29.82]	[+5.20]	[–12.98]	[–1.22]	[–0.22]	[+0.38]	[–38.67]

FC-ROCCSD(T)/cc-pVTZ reference geometries

$\Delta E_{final} = \Delta E_e$(FPA) + ΔZPVE(harm) + Δ(rel) + Δ(core) = –38.67 + 5.90 + 0.13 – 0.07 = **–32.71 kcal mol^{-1}**

[a]The symbol δ denotes the increment in the relative energy (ΔE) with respect to the preceding level of theory in the hierarchy HF→ZAPT2→ROCCSD→ROCCSD(T)→ROCCSDT→UCCSDT(Q). Square brackets signify results obtained from basis set extrapolations or additivity assumptions.

We find that the relative energy $\Delta_{rxn} H_0^\circ$ of **MIN1** is –32.7 kcal mol^{-1} (Table 2.1) with respect to the separated reactants. For the R–O_2 binding energy of **MIN1**, the Hartree-Fock limit gives a value 8.9 kcal mol^{-1} smaller than ROCCSDT(Q)/CBS and larger by 5.2 kcal mol^{-1} than ZAPT2/CBS, observations that are consistent with previous CBS work[16] performed on the ethylperoxy radical. Simply optimizing the structure at the ROCCSD(T)/cc-pVTZ level of theory yields a well depth (D_e) of 36.82 kcal mol^{-1}; this result is 1.85 kcal mol^{-1} smaller than the targeted ROCCSDT(Q)/CBS value. The majority of the correlation effect is accounted for once δ[ROCCSD(T)] = –1.22 kcal mol^{-1} is included, as the subsequent higher-order contributions of δ[ROCCSDT] = –0.22 kcal mol^{-1} and δ[ROCCSDT(Q)] = +0.38 kcal mol^{-1} largely cancel. The FPA data suggest that the contribution from δ[ROCCSDTQ] would be smaller than 0.3 kcal mol^{-1} and the difference between cc-pV5Z and cc-pVQZ for δ[ROCCSD(T)] would be smaller than 0.1 kcal mol^{-1}. Finally, we note the importance of utilizing larger basis sets (mixed-H(TZ,DZ) vs. cc-pVDZ) for ΔZPVE(harm) corrections, which decreases $\Delta_{rxn} H_0^\circ$ on average by 0.73 kcal mol^{-1} for the species of the *n*-propyl + O_2 reaction. In particular, the binding energy for **MIN1** changes by a very substational +0.6 kcal mol^{-1} when utilizing the mixed-H(TZ,DZ) basis set instead of cc-pVDZ for CCSD(T) ΔZPVE(harm) corrections.

The most recent binding energy of Goldsmith et al.[35] (33.3 kcal mol^{-1}) is 0.6 kcal mol^{-1} higher than our value for **MIN1** (G^+G^+). However, their computations found that the TG^- rotamer was lowest in energy. Our binding energy is smaller than both the original results of Desain et al.[26] and subsequent modifications,[15,32] by 2.2 kcal mol^{-1} and 1.2 kcal mol^{-1}, respectively. The various CBS-QB3 computations produce binding energies higher than our result by 2.1 kcal mol^{-1},[29,34] showing that CBS-QB3 is not well suited for high accuracy computations on these combustion species.

2.4.3 PATHWAYS LEADING FROM RO_2

The concerted elimination reaction occurs through a 5-membered ring transition state (**TS1**, Figure 2.4), wherein the hydrogen on C_2 migrates over to O_5. **TS1** is best viewed as a proton transfer with the unpaired electron in an orbital perpendicular to the ring, as shown in Figure 2.5. The singly occupied molecular orbital (SOMO) is localized on the O_2 moiety and is perpendicular to the in-plane orientation expected for hydrogen transfer. Natural bond orbital (NBO) analysis finds that 74% of the spin density in **TS1** is centered on O_4. In contrast, 87% of the spin density occurs at O_5 in the **MIN1** molecule. The **TS1** spin distribution resembles that of the free HO_2 radical, in which the terminal O atom contains 90% of the spin density. The C_2–H_9 bond extends from 1.092 Å in **MIN1** to 1.341 Å in **TS1**. The relatively short H_9–O_5 distance of 1.269 Å in **TS1** indicates the incipient formation of an O–H bond. During proton transfer, the C_3–O_4 distance drastically increases from 1.455 Å in **MIN1** to 2.142 Å in **TS1**, while the C_2–C_3 distance decreases from 1.518 Å to 1.393 Å, towards the length of a typical C–C double bond. There is a decrease in $\alpha(C_3–O_4–O_5)$ of 10.95° compared to **MIN1**. The ring structure of **TS1** is almost planar with dihedral angles $\tau(C_2–C_3–O_4–O_5)$ = 2.99° and $\tau(C_3–O_4–O_5–H_9)$ = 0.01°. There are no substantial

differences in our **TS1** and the analogous concerted elimination transition state of previous[16] ethyl + O_2 work, which was optimized at the CCSD(T)/cc-pVQZ level of theory.

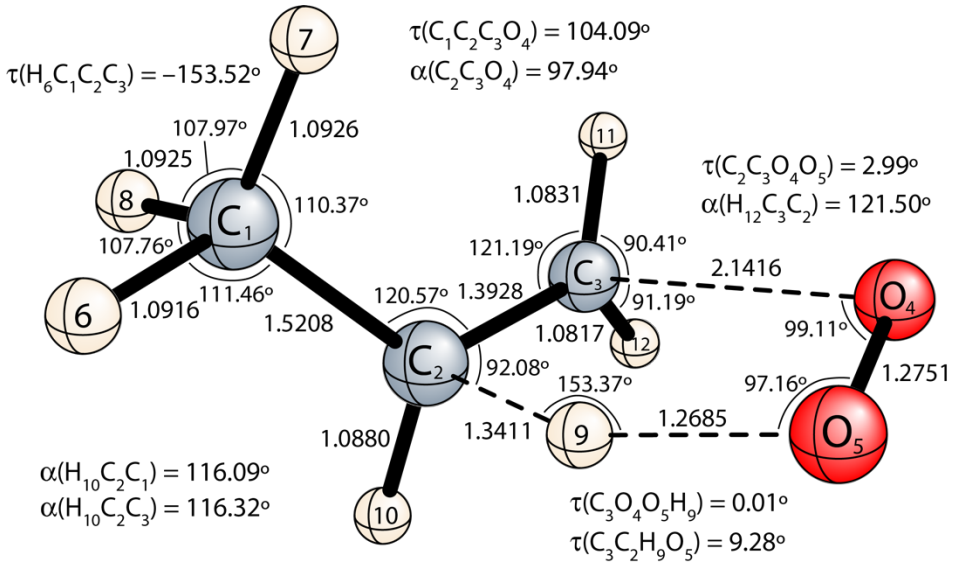

Figure 2.4 Optimum geometry of **TS1** at ROCCSD(T)/cc-pVTZ level of theory. Bond lengths are in Å.

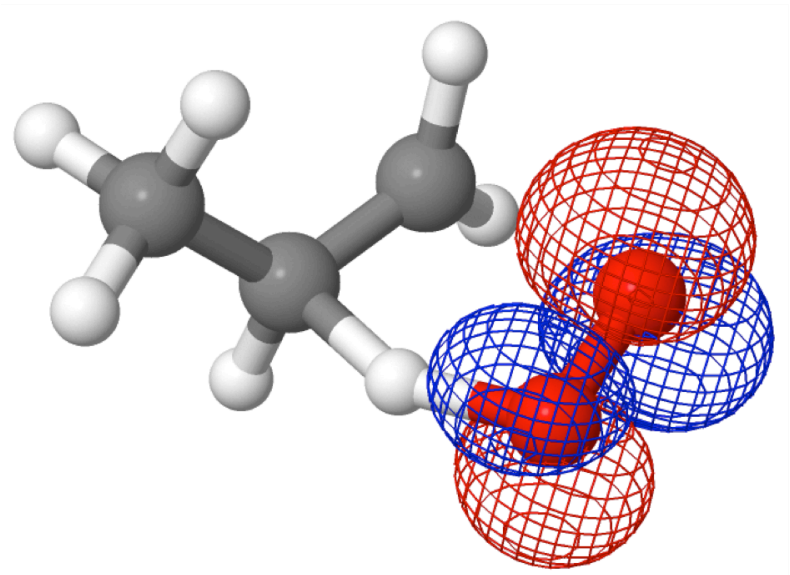

Figure 2.5 Depiction of singly occupied molecular orbital (SOMO) of **TS1**.

The available geometric structures reported in the literature for **TS1** consist entirely of DFT structures. One of the goals of our work is to gauge the impact on geometrical parameters when utilizing highly accurate coupled cluster theory, compared to density functional methods. There is a less than desirable agreement with the B3LYP/6-311++G(d,p) results of Goldsmith et al.,[35] with a MAD of 0.027 Å for bond lengths. The most drastic differences are found for $r(C_3–O_4)$ and $r(O_5–H_9)$, which differ from our results by 0.09 Å and 0.04 Å, respectively. Bond and dihedral angles have a MAD of 0.70° when comparing the two structures. The B3LYP $\alpha(C_2–C_3–O_4)$ and $\alpha(C_3–O_4–O_5)$ values are underestimated by 1.39° and 1.15°, respectively. A similar comparative trend is observed with the B3LYP/6-31+G** **TS1** geometry of Merle et al.[29] The $r(C_3–O_4)$ and $r(O_5–H_9)$ bond lengths are problematic here as well, differing from our values by 0.07 Å and 0.03 Å, respectively. This is slightly better than the aforementioned[35] B3LYP/6-311++G(d,p) structure. There is a similar trend in MADs with a value of 0.02 Å for bond lengths and 0.6° for angles. The angles $\alpha(C_2–C_3–O_4)$, $\alpha(C_3–O_4–O_5)$, and $\alpha(O_4–O_5–H_9)$ differ from ours by 1.3°, 0.9°, and 0.8°, respectively. The M05-2X/6-311+G(2df,fp) **TS1** structure of Zhang and Dibble[43] almost exactly replicates the B3LYP/6-31+G** structure of Merle et al.[29] In each of these comparisons the density functional is unable to accurately predict the $r(C_3–O_4)$ and $r(O_5–H_9)$ distances, which reflect the key bonding changes involved in this transition state. The density functionals are also unable to produce highly accurate bond angles associated with the ring of the **TS1** structure.

The direct elimination of HO_2 was found to be the dominant fate of the RO_2 radical in previous ethyl + O_2 work.[16] Our concerted HO_2 elimination barrier (**TS1**) for *n*-propyl + O_2 is 2.4 kcal mol^{-1} below the reactants by FPA targeting the CCSDT(Q)/CBS level of theory, as compared to 3.0 kcal mol^{-1} in the ethyl + O_2 system. Thus, increasing the system size to larger alkyl radicals

appears to slightly disfavor concerted elimination through **TS1** relative to other pathways. Simply optimizing **TS1** at the ROCCSD(T)/cc-pVTZ level of theory places the barrier 0.12 kcal mol^{-1} above the reactants after correcting for zero-point energy. Extrapolating to the ROCCSD(T) basis set limit lowers this value by 2.0 kcal mol^{-1}. Both high-order correlation and basis set augmentation provide a continuing negative correction for **TS1**, which earlier work[16] identified as the reason for systematic overestimation of the concerted elimination barrier in the ethyl + O_2 system. Our $\Delta_{rxn}\ H_0^\circ$ is higher in energy than that of Desain et al.[26] and subsequent modifications[15,32] by 2.79 kcal mol^{-1} and 1.39 kcal mol^{-1}, respectively. The work of Goldsmith et al.[35] places **TS1** 2.7 kcal mol^{-1} below the reactants, which is 0.3 kcal mol^{-1} lower in energy than our result. The CBS-QB3 method has produced $\Delta_{rxn}\ H_0^\circ$ values for **TS1** in the range of –2.4 kcal mol^{-1} to –3.9 kcal mol^{-1}.[27,29,55] The CCSD(T)/aug-cc-pVTZ result of Zhang and Dibble[43] places **TS1** 0.79 kcal mol^{-1} below our converged FPA value.

TABLE 2.4 Focal point analysis[a] (in kcal mol^{-1}) for the concerted elimination barrier (**TS1**) relative to *n*-propyl + O_2

	ΔE_e(ROHF)	+δ [ZAPT2]	+δ [ROCCSD]	+δ [ROCCSD(T)]	+δ [ROCCSDT]	+δ [UCCSDT(Q)]	NET
6-31G*	+34.72	–22.22	–2.99	–5.15	–0.22	–0.51	+3.64
cc-pVDZ	+32.57	–21.17	–3.04	–5.80	–0.07	[–0.51]	[+1.99
cc-pVTZ	+33.19	–26.28	–1.18	–7.00	[–0.07]	[–0.51]	[–1.85]
cc-pVQZ	+33.34	–27.72	–0.75	–7.26	[–0.07]	[–0.51]	[–2.98]
cc-pV5Z	+33.37	[–28.24]	[–0.60]	[–7.35]	[–0.07]	[–0.51]	[–3.39]
CBS LIMIT	[+33.38]	[–28.78]	[–0.43]	[–7.45]	[–0.07]	[–0.51]	[–3.86]

FC-ROCCSD(T)/cc-pVTZ reference geometries

$\Delta E_{final} = \Delta E_e$(FPA) + ΔZPVE (harm) + Δ(rel) + Δ(core) = –3.86 + 1.39 + 0.07 – 0.01 = **–2.41 kcal mol^{-1}**

[a] See footnote for Table 2.3.

The energy correction that accounts for electron correlation beyond ROCCSD(T) (δ[ROCCSDT] + δ[UCCSDT(Q)]) for **TS1** is –0.58 kcal mol^{-1}, which is 0.3 kcal mol^{-1} smaller in magnitude than the corresponding correction for **TS1** in the ethyl + O_2 reaction.[16] For the

associated concerted elimination reaction of the *t*-butyl + O_2 system, this correlation energy correction is –0.40 kcal mol^{-1},[110] a value that is 0.18 kcal mol^{-1} smaller in magnitude than our value for **TS1**. It would be ideal to obtain universal *ad-hoc* corrections for both the value of δ[ROCCSDT] + δ[UCCSDT(Q)] and basis set corrections past cc-pV5Z due to the expense of these computations for larger systems such as *n*-butyl and *n*-pentyl + O_2. However, our hard comparisons of this value for the ethyl, propyl, and *t*-butyl + O_2 systems suggest that such a correction may be elusive.

TS1 exhibits a reaction mode frequency of 1302*i* cm^{-1} at the FC-ROCCSD(T)/Mixed-H(TZ,DZ) level of theory, in good agreement with the FC-CCSD(T)/cc-pVTZ result (1340*i* cm^{-1}) for the ethyl + O_2 system.[16] Moore et al.[110] report a comparable frequency (1312*i* cm^{-1}) at the FC-CCSD(T)/ANO0 level of theory for the HO_2 elimination pathway of *t*-butyl + O_2, whose reaction mode is very similar to that of **TS1**. The only previous report of the reaction mode frequency of **TS1** was a B3LYP/6-31+G** value of 1031*i* cm^{-1},[29] in poor agreement with our CCSD(T) result. The CCSD(T) ΔZPVE(harm) correction to the **TS1** barrier changes by 0.66 kcal mol^{-1} when improving the basis set from cc-pVDZ to mixed-H(TZ,DZ), showing that large errors can accrue if the ZPVE is not evaluated at high levels of theory.

The next possible fate of **MIN1** is to traverse the β-hydrogen transfer transition state (**TS2**, Figure 2.6) leading to **MIN2**. This motion is similar to **TS1**; however, **TS2** involves hydrogen rather than proton transfer and occurs through a non-planar 5-membered ring. The distortion from ring planarity occurs because the SOMO (Figure 2.7) must be directed into the C_2–H_9–O_5 plane in order to effect the hydrogen transfer. **TS2** exhibits an unphysically large Δ_{DBOC} correction (1.71 kcal mol^{-1}), which is an indication of a nearby surface crossing on the Born-Oppenheimer potential energy surface. Goldsmith et al.[35] mentions that **TS2** lies near a conical intersection, pointing out

that their barrier differs by more than 2 kcal mol^{-1} from previous work. Figure 2.8 is a qualitative depiction that gives insight into the non-planarity of **TS2**. Specifically, the reaction path must skirt around the conical intersection into a nonplanar geometry to avoid a high energy barrier.

Rienstra-Kiracofe et al.[13] found that the asymmetrical β-hydrogen transfer transition state of the ethyl + O_2 system is on the ground-state hyperspace due to a conical intersection between the $^2A'$ and $^2A''$ states in the C_s configuration space. At **TS1** the $^2A''$ state lies below $^2A'$ by 44 kcal mol^{-1}. However, at the best planar **TS2** geometry, $^2A'$ has moved below $^2A''$ by about 10 kcal mol^{-1}. By distorting into the C_1 configuration space, the asymmetrical **TS2** structure undergoes significant stabilization due to a second order Jahn-Teller interaction of the ($^2A'$,$^2A''$) states. Moore et al.[110] optimized an $\tilde{A}$ $^2A'$ hydrogen transfer structure for the *t*-butyl + O_2 system but were unsuccessful in obtaining the corresponding planar $\tilde{X}$ $^2A''$ structure. They note that the presence of a nearby surface crossing creates sensitivity to geometrical perturbations on the potential energy surface near their initial structural guess. They computed EOM-EE-CCSD/cc-pVTZ vertical excitation energies for several points on the *t*-butyl + O_2 surface, observing that the HO_2 elimination (**TS1**) and intramolecular β-hydrogen transfer (**TS2**) barriers are inverted on the $\tilde{A}$ surface.

The β-hydrogen transfer transition state of the *t*-butyl + O_2 system also exhibits a large DBOC correction to the relative energy (Δ_{DBOC} = 0.4 kcal mol^{-1}).[110] We propose that Δ_{DBOC} can be utilized as a diagnostic for the presence of nearby conical intersections. While Δ_{DBOC} is usually a small correction ($\pm$0.02 kcal mol^{-1}) to the Born Oppenheimer potential energy surface, this is not the case in the vicinity of a conical intersection. Meek and Levine[111] show that E_{DBOC} is non-integrable over domains including a conical intersection because the second derivative of the $\hat{T}_n$

operator blows up at such points. They recommend that DBOC not be used when employing mixed quantum-classical methods and approximate quantum dynamical methods.[111]

An interesting feature of the β-hydrogen transfer for the *n*-propyl + O_2 system is that it can occur via two distinct conformers of **TS2** that differ by the direction of puckering from ring planarity. The alternative to **TS2** in which O_4 puckers downward is structure **TS2′** (Figure 2.9), lying only 0.16 kcal mol^{-1} higher in energy (Table S14-G). There is a lack of general acknowledgement of the existence of two β-hydrogen transfer transition states in the literature. While the majority of previous work has utilized **TS2**, Goldsmith et al.[35] report only **TS2′**. Merle and co-workers[29] give Cartesian coordinates for both structures in their supplementary material; however, they only report energetics for **TS2** in the body of their paper and do not point out that there are two non-degenerate conformers. **TS2′** (Figure 2.13) also exhibits a large Δ_{DBOC} correction (1.67 kcal mol^{-1}) indicative of a nearby conical intersection.

Similar to **TS1**, the **TS2** structure displays a relatively short H_9–O_5 bond distance of 1.242 Å. The C_2–H_9 bond increases by 0.24 Å when going from **MIN1** to **TS2**. The changes in $r(C_2–C_3)$ and $r(C_3–O_4)$ are less drastic than found in **TS1**, increasing and decreasing by 0.012 Å and 0.027 Å, respectively. There is a decrease in $\alpha(C_3–O_4–O_5)$ of 8.57° compared to **MIN1**, smaller than the corresponding internal coordinate change in **TS1** by 2.38°. The ring structure of **TS2** is highly non-planar with $\tau(C_2–C_3–O_4–O_5) = 47.12°$ and $\tau(C_3–O_4–O_5–H_9) = –34.73°$.

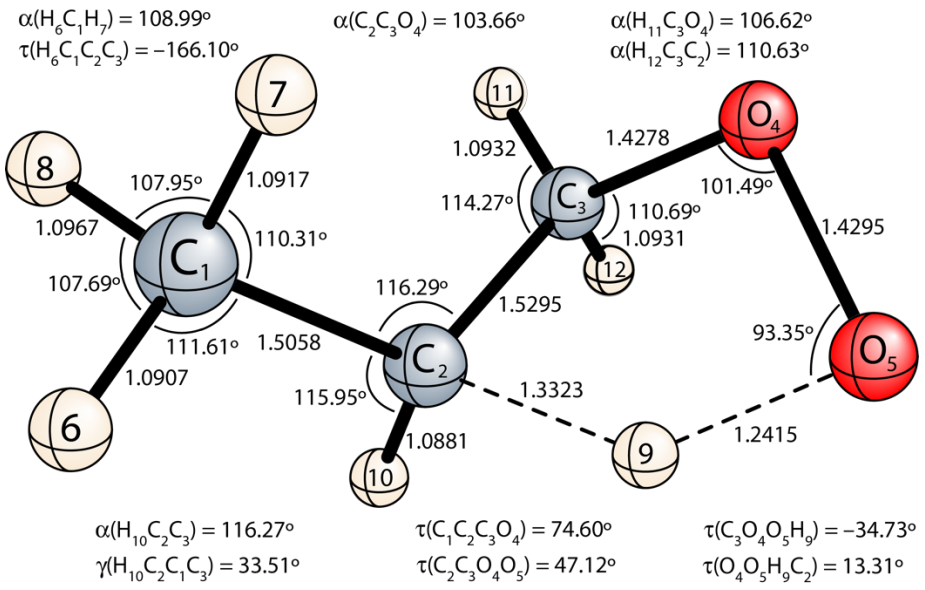

Figure 2.6 Optimum geometry of **TS2** at ROCCSD(T)/cc-pVTZ level of theory. Bond lengths are in Å.

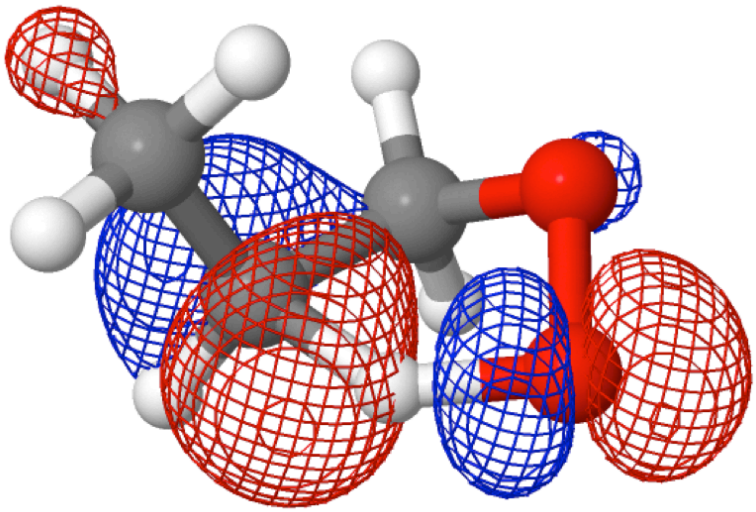

Figure 2.7. Depiction of singly occupied molecular orbital (SOMO) of **TS2**.

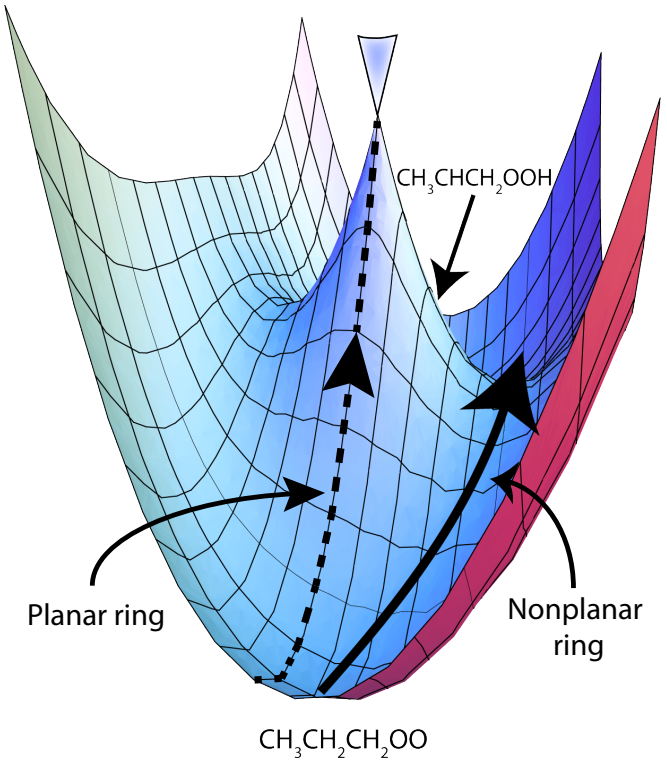

Figure 2.8 Qualitative depiction of conical intersection near **TS2** and **TS2′**.

At the B3LYP/6-31+G** level of theory,[29] there is a MAD of 0.01 Å for bond lengths and 0.8° for angles compared to our **TS2** structure. The largest difference in bond lengths is 0.04 Å for $r(H_9–C_2)$. The angles $\alpha(C_1–C_2–C_3)$, $\alpha(C_3–O_4–O_5)$, $\tau(C_2–C_3–O_4–O_5)$, and $\tau(C_3–O_4–O_5–H_9)$ show differences of 1.15°, 0.97°, 1.35°, and 1.06°, respectively. Similar agreement is found at the M05-2X/6-311+G(2df,2p) level of theory,[43] with a MAD of 0.01 Å for bond lengths and 0.7° for angles. Larger differences of 1.13° and 2.11° are observed for $\alpha(C_3–O_4–O_5)$ and $\alpha(C_2–H_9–O_5)$, respectively.

Our **TS2** structure lies 0.37 kcal mol^{-1} above the separated reactants. The focal point layout of **TS2** (Table 2.5) indicates that the cc-pV5Z basis set yields Hartree-Fock results within 0.02 kcal mol^{-1} of the CBS limit. For the δ[ROCCSD(T)] correction, the difference between cc-pVTZ

and cc-pVDZ basis sets is 1.0 kcal mol^{-1}, compared to a difference of 0.26 kcal mol^{-1} between cc-pVQZ and cc-pVTZ. Much of the electron correlation is accounted for at the ROCCSD(T) level of theory (δ[ROCCSD(T)] = –4.77 kcal mol^{-1}), as the δ[ROCCSDT] + δ[UCCSDT(Q)] correction term for **TS2** is only –0.06 kcal mol^{-1}. This is smaller in magnitude by 0.52 kcal mol^{-1} when compared to the corresponding term for **TS1**. It is expected that the δ[ROCCSDTQ] contribution and the difference between cc-pVQZ and cc-pV5Z for δ[ROCCSD(T)] are both smaller than 0.1 kcal mol^{-1}. Our $\Delta_{rxn} H_0^\circ$ is higher in energy than that of Desain et al.[26] and subsequent modifications[15,32] by 2.97 kcal mol^{-1} and 2.47 kcal mol^{-1}, respectively. Previous CBS-QB3 energies vary from our result by 3.07 kcal mol^{-1} and 1.57 kcal mol^{-1}.[29,34] All of these disparities are substantial, justifying our more rigorous computations. In constrast, the CCSD(T)/aug-cc-pVTZ energy of Zhang and Dibble[43] is only 0.47 kcal mol^{-1} lower in energy than our value. **TS2** exhibits a hydrogen-transfer reaction-mode frequency of 2199i cm^{-1}, which again is in good agreement with the B3LYP/6-31+G** result[29] (2171i cm^{-1}). There is a change of +0.72 kcal mol^{-1} for ΔZPVE (harm) when using our mixed-H(TZ,DZ) basis set over cc-pVDZ.

TABLE 2.5 Focal point analysis[a] (in kcal mol^{-1}) for the β-hydrogen transfer barrier (**TS2**) relative to *n*-propyl + O_2

	ΔE_e(ROHF)	+δ [ZAPT2]	+δ [ROCCSD]	+δ [ROCCSD(T)]	+δ [ROCCSDT]	+δ [UCCSDT(Q)]	NET
6-31G*	+31.92	–20.17	–2.21	–2.92	–0.07	–0.04	+6.50
cc-pVDZ	+31.03	–18.95	–2.14	–3.32	–0.02	[–0.04]	[+6.57]
cc-pVTZ	+30.40	–24.92	–0.41	–4.32	[–0.02]	[–0.04]	[+0.69]
cc-pVQZ	+30.72	–26.75	+0.04	–4.58	[–0.02]	[–0.04]	[–0.63]
cc-pV5Z	+30.75	[–27.40]	[+0.21]	[–4.68]	[–0.02]	[–0.04]	[–1.18]
CBS LIMIT	[+30.73]	[–28.08]	[+0.38]	[–4.77]	[–0.02]	[–0.04]	[–1.81]

FC-ROCCSD(T)/cc-pVTZ reference geometries

$\Delta E_{final} = \Delta E_e$(FPA) + ΔZPVE (harm) + Δ(rel) + Δ(core) = –1.81 + 2.01 + 0.14 + 0.03 = **+0.37 kcal mol^{-1}**

[a] See footnote for Table 2.3.

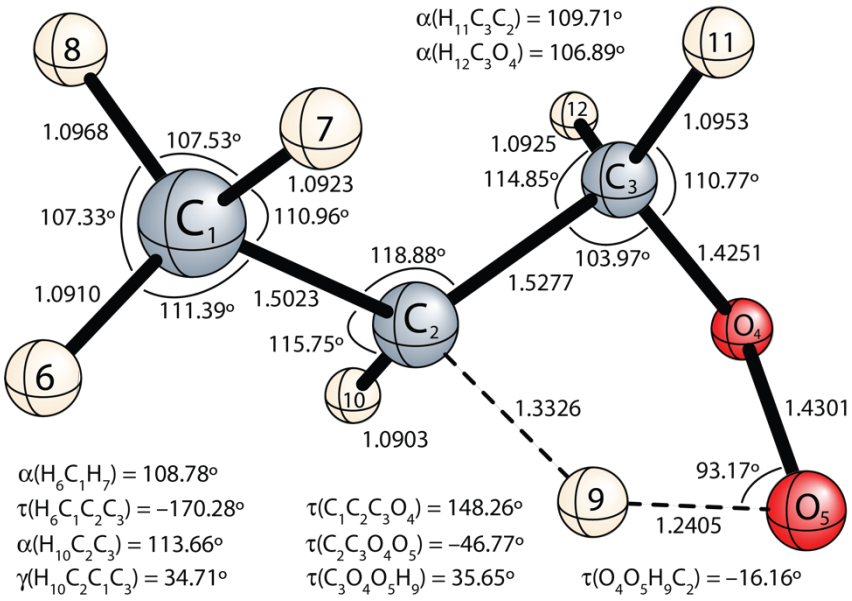

Figure 2.9 Optimum geometry of **TS2′** at ROCCSD(T)/cc-pVTZ level of theory. Bond lengths are in Å.

The γ-hydrogen transfer transition state (**TS3**, Figure 2.10) occurs by H_7 migrating from C_1 to O_5, creating a 6-membered ring structure with a reaction mode frequency of 2007*i* cm^{-1}. The C_1–H_7 bond increases by 0.27 Å when going from **MIN1** to **TS3**. The dihedral angle $\tau(C_2–C_3–O_4–O_5)$ changes from 70.33° to –70.86° when going from **MIN1** (Figure 2.3) to **MIN3** because the O_4–O_5 moiety must rotate over the C_2–C_3–O_4 plane in order to favorably position O_5 for accepting the incoming H_7 atom. **TS3**, a non-planar structure with H_7 displaced slightly downward relative to C_3 in the 6-membered ring, is located 7.75 kcal mol^{-1} *below* the separated reactants. **TS3** exhibits a substantial Δ_{DBOC} correction (0.33 kcal mol^{-1}), which is nonetheless smaller than for **TS2** and **TS2′**, suggesting further displacement from a conical intersection.

Previously reported CBS-QB3 results provide **TS3** energies that are lower than our value by 3.15 kcal mol^{-1} and 1.75 kcal mol^{-1}.[29,34,55] The QCISD(T)/CBS result of Goldsmith et al.[35] for **TS3** is 0.75 kcal mol^{-1} lower than our FPA result. The CCSD(T)/aug-cc-pVTZ result of Zhang and Dibble[43] places **TS3** 8.6 kcal mol^{-1} below the reactants, 0.85 kcal mol^{-1} lower than our converged FPA value. DFT geometries from the literature[29,35,43,55] produce MADs for bond lengths ranging from 0.008 Å to 0.015 Å compared to our result; bond angles and dihedrals exhibit MADs ranging from 0.63° to 1.02°.

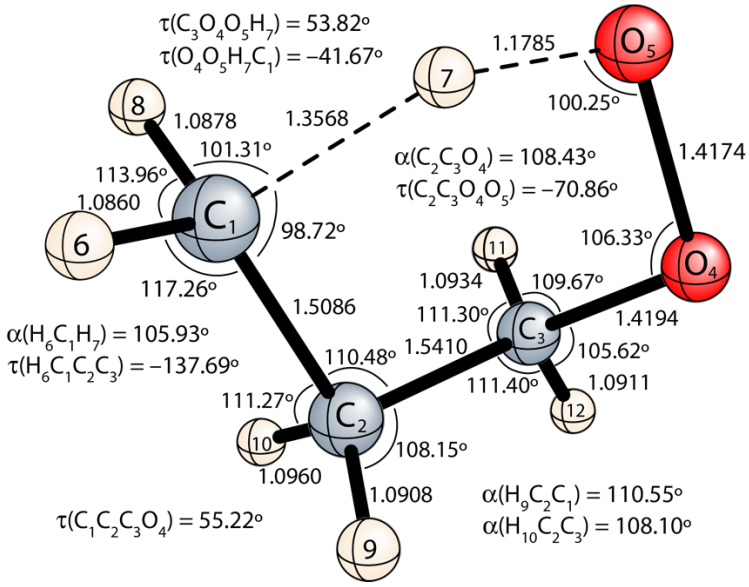

Figure 2.10 Optimum geometry of **TS3** at ROCCSD(T)/cc-pVTZ level of theory. Bond lengths are in Å.

Lastly, **MIN1** can also undergo an α–hydrogen transfer transition state (**TS7**, Figure 2.11) in which H_{12} transfers from C_3 to O_5, creating a 4-membered ring structure with a reaction mode frequency of 1879*i* cm^{-1}. This transition state is highly unfavorable due to ring strain and lies 9.04 kcal mol^{-1} above the separated reactants, yet it is lower than the QCISD(T)/CBS result of Goldsmith et al.[35] by 0.94 kcal mol^{-1}. The high-energy nature of this transition state indicates that

it would be a significant feature of the *n*-propyl + O_2 potential energy surface only at higher temperatures.

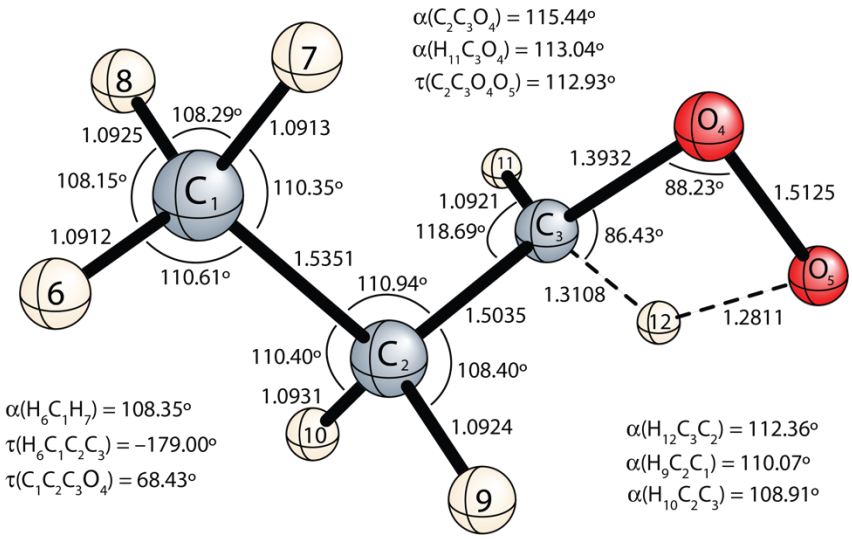

Figure 2.11 Optimum geometry of **TS7** at ROCCSD(T)/cc-pVTZ level of theory. Bond lengths are in Å.

2.4.4 QOOH SPECIES

Each of the transition states leading from **MIN1** produces a QOOH species, except for **TS1**, which leads to the propene + HO_2 products. These QOOH species are distinguished by the location of the carbon radical center. **MIN2** (Figure 2.12), **MIN3** (Figure 2.13), and **MIN4** (Table S3) are the products of β-, γ-, and α-hydrogen transfer reactions, respectively, placing the radical center on C_2, C_1, and C_3, in order. **MIN4** is depicted only in the SI because it is produced by passing through the highly unfavorable **TS7** transition state and is thus less important than the other QOOH species.

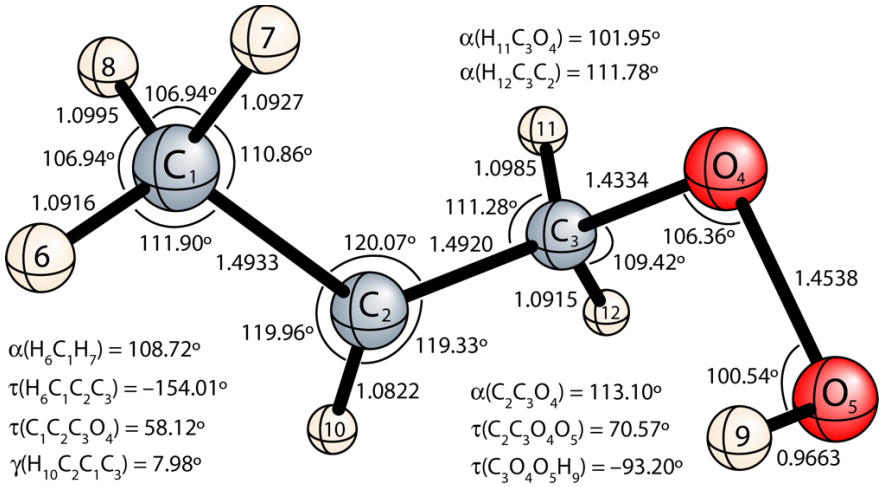

Figure 2.12 Optimum geometry of **MIN2** at ROCCSD(T)/cc-pVTZ level of theory. Bond lengths are in Å.

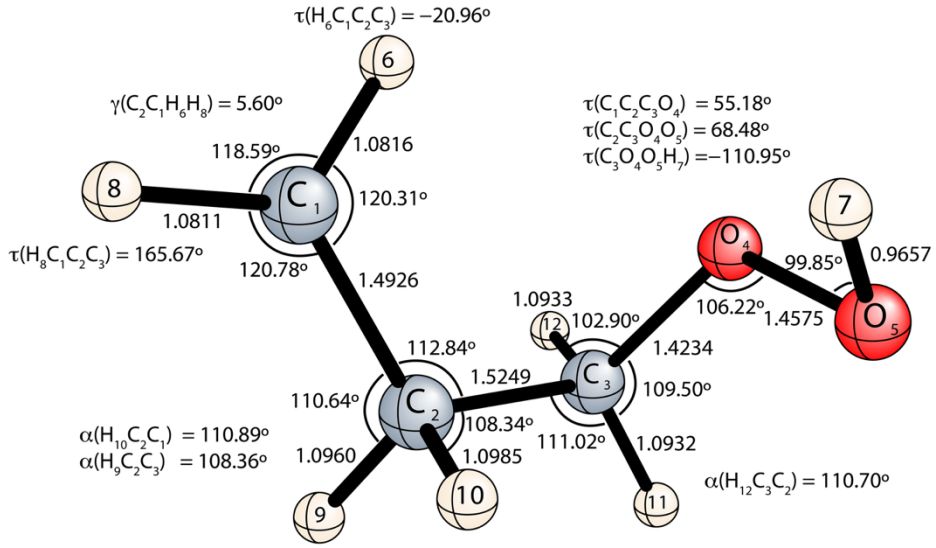

Figure 2.13 Optimum geometry of **MIN3** at ROCCSD(T)/cc-pVTZ level of theory. Bond lengths are in Å.

The complete rotamer space of each QOOH species was systematically investigated by scanning over all three dihedral angles of interest: τ_1(C_1–C_2–C_3–O_4), τ_2(C_2–C_3–O_4–O_5), and τ_3(C_3–O_4–O_5–H). In 30° increments between 0° and 180°, the τ_1(C_1–C_2–C_3–O_4) coordinate was

fixed while full 360° relaxed energy scans were performed for $\tau_2(C_2–C_3–O_4–O_5)$ and $\tau_3(C_3–O_4–O_5–H)$ at the B3LYP/6-31G* level of theory.[71, 112-115] Near each minimum apparent from the scans, MP2/aug-cc-pVDZ optimizations were started and converged to give a final set of structures. The relative energies (Table S1) of the energetically distinct rotamers were then determined by single-point CCSD(T)/cc-pVTZ computations using MP2/aug-cc-pVDZ optimum geometries and ZPVE corrections. As fully documented in SI, we located 9 **MIN2** rotamers with relative energies of 0 – 1.14 kcal mol^{-1}, 12 **MIN3** rotamers in the 0 – 1.60 kcal mol^{-1} range, and 11 **MIN4** rotamers clustered in the 0 – 0.96 kcal mol^{-1} window. The lowest energy rotamers for **MIN2**, **MIN3**, and **MIN4** are $G^+G^+A^-$, $G^+G^+A^-$, and G^+TA^-, respectively. Comparing our geometries to those given in the literature is difficult due to major disparities. No systematic conformational searches for **MIN2** and **MIN3** have been reported previously. For **MIN2**, G^+TA^-,[35] $G^+G^+A^+$,[29] and G^+TA^+ rotamers have been given,[43] while for **MIN3**, TG^-A^-,[35] TTA^+,[55] $G^+G^-A^-$,[43] and $G^+G^+A^+$ have been reported.[29] There is not a single agreement for the lowest energy rotamer of any QOOH species reported in the literature for the *n*-propyl + O_2 system. Similar to **MIN1**, high levels of theory are necessary to determine the lowest energy rotamers of QOOH species. While the differences in relative energies between rotamers may seem quite small, uncertainty in the energy ordering of the rotamers can cause much confusion in these already complex combustion systems.

Our FPA computations (Table 2.1) place the lowest-energy rotamers of **MIN2**, **MIN3**, and **MIN4** below the reactants by 19.19, 17.44, and 21.20 kcal mol^{-1}, respectively, providing considerable improvements to previous thermochemical predictions. The QCISD(T)/CBS work of Goldsmith et al.[35] places **MIN2** and **MIN3** below our converged FPA result by 1.21 kcal mol^{-1} and 0.66 kcal mol^{-1}, respectively. For **MIN2**, earlier CBS-QB3 $\Delta_{rxn} H_0^\circ$ results are lower than ours

by 0.21 kcal mol^{-1} and 2.21 kcal mol^{-1}.[29,53] Similarly for **MIN3**, CBS-QB3 produces $\Delta_{rxn} H_0^\circ$ values both higher and lower in energy than our result ranging from 17.2 kcal mol^{-1} to 18.9 kcal mol^{-1} below the reactants.[25,29,53] Again, there are no $\Delta_{rxn} H_0^\circ$ values in the literature for **MIN4**; however, we can assume similar discrepancies would arise from CBS-QB3 computations.

2.4.5 PATHWAYS LEADING FROM QOOH

Four possible fragmentation pathways (Figure 2.1) were investigated that originate from QOOH species: C_2–O_4 bond formation and OH elimination (**TS4**, Figure 2.14), C_3–O_4 bond cleavage and HO_2 elimination (**TS5**, Figure 2.15), C_1–O_4 bond formation and OH elimination (**TS6**, Figure 2.16), and O_4–O_5 bond cleavage and OH elimination (**TS8**). There is limited previous information on these transition states in the literature with only a few studies supplying energies[26-27,29,35] and geometries.[27,29,35] As with the QOOH species, major discrepancies between our transition state structures (**TS4**–**TS6**) and those found in the literature mainly involve dihedral angles. Once **TS2** is passed, **TS4** and **TS5**, lying well below the reactants, provide no further hindrance to direct product formation from *n*-propyl + O_2. The chain propagating pathway through **TS4** is the most favorable route ($\Delta_{rxn} H_0^\circ$ = –7.45 kcal mol^{-1}) leading out of **MIN2**, lying 3.03 kcal mol^{-1} below the chain terminating pathway through **TS5**. In contrast, once **TS3** is passed to yield **MIN3**, the chain propagating pathway through **TS6** is hindered by a barrier that is 2.87 kcal mol^{-1} above the *n*-propyl + O_2 reactants.

Attempts were made to obtain a transition state **TS8** leading to propanal + OH from **MIN4**. Our initial attempt entailed the same optimization protocol utilized throughout our study. To understand why such a transition state could not be found, an unrelaxed scan of ROCCSD/cc-pVTZ and ROCCSD(T)/cc-pVTZ energies was performed as the $r(O_4$–$O_5)$ coordinate was

stretched in 0.02 Å increments starting from the **MIN4** structure. As shown in Figure 2.17, two distinct solutions for the electronic wave function were found in the region expected for **TS8,** and the corresponding energy curves cross near $r(O_4–O_5)$ = 1.735 Å. Careful control of the starting molecular orbitals was used to ensure continuity of the two solutions for the electronic wave function. Prior to the crossing point, the lowest-energy solution has 88% of the NBO spin density on the C_3 atom, with the radical oriented perpendicular to the $C_2–C_3–O_4$ plane. In contrast, after the crossing point the lowest solution has the spin density predominantly (83%-97%) centered on the O_5 atom, with the radical directed along the $O_4–O_5$ bond. Depictions of the SOMOs of these two solutions for the reference ROHF electronic wavefunction can be found in Figure S1. The results of Figure 2.17 suggest that a conical intersection may be very close to **TS8** and that multireference coupled cluster (or configuration interaction) methods will be necessary to nail down the precise features of the potential energy surface in this region. We performed initial searches using CASSCF with various active spaces, but again optimizations of **TS8** were unsuccessful. Based on our analysis, we estimate the barrier of the transition state from **MIN4** to propanal + OH to be about 10 kcal mol^{-1} below the separated reactants.

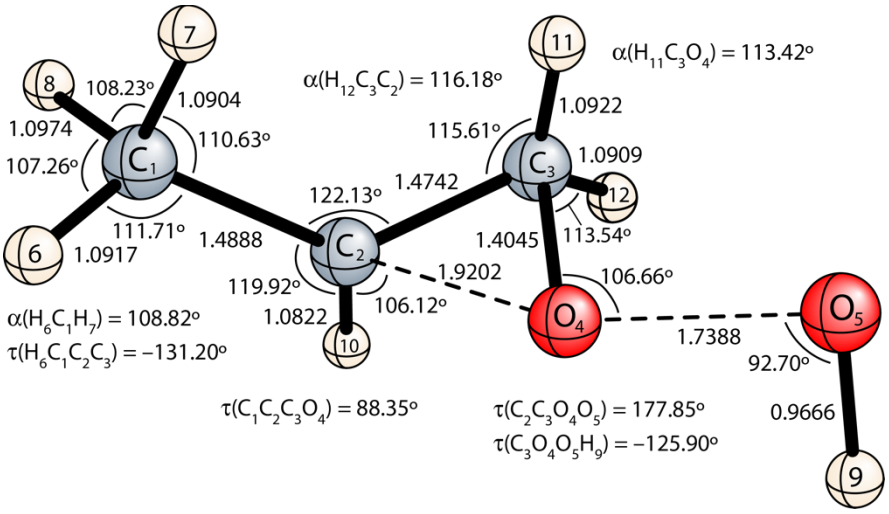

Figure 2.14 Optimum geometry of **TS4** at ROCCSD(T)/cc-pVTZ level of theory. Bond lengths are in Å.

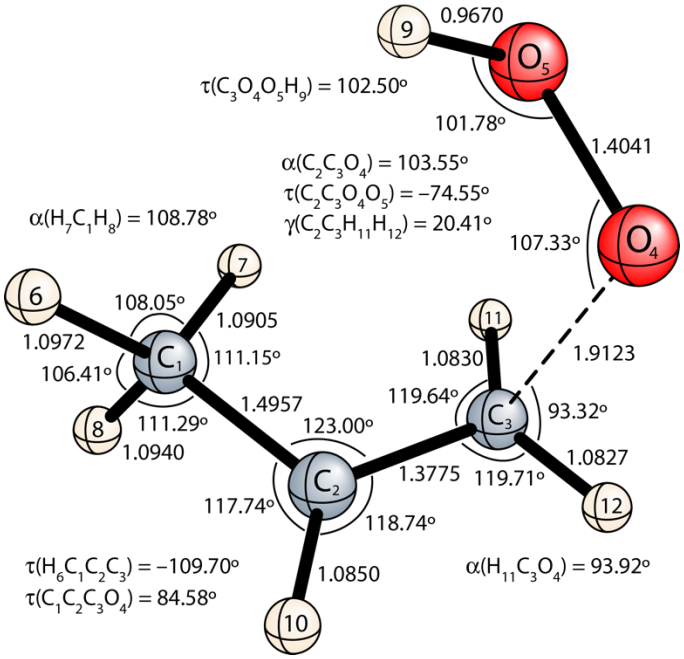

Figure 2.15 Optimum geometry of **TS5** at ROCCSD(T)/cc-pVTZ level of theory. Bond lengths are in Å.

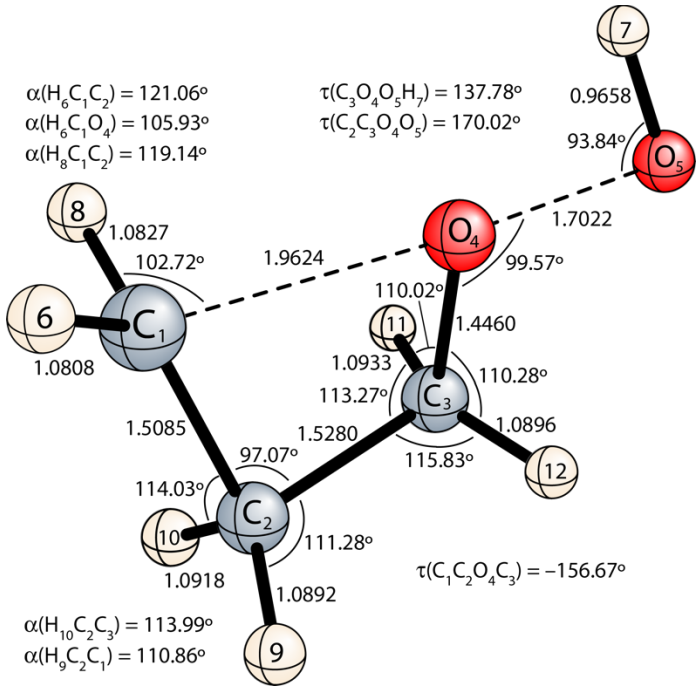

Figure 2.16 Optimum geometry of **TS6** at ROCCSD(T)/cc-pVTZ level of theory. Bond lengths are in Å.

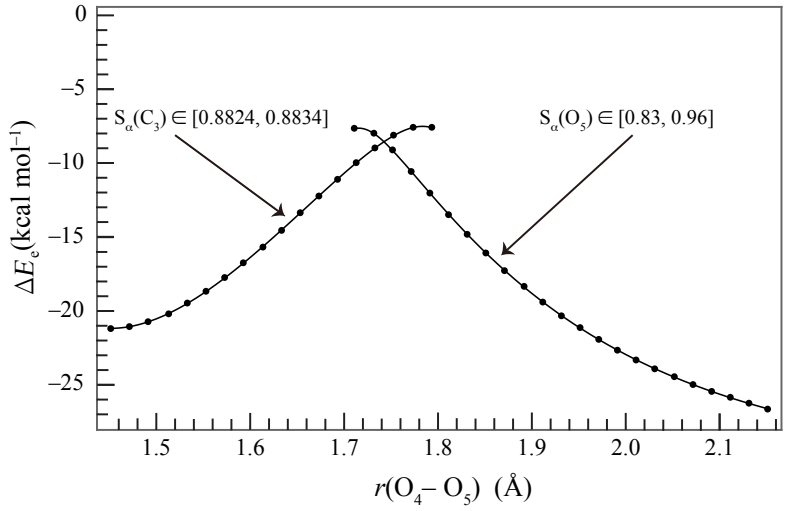

Figure 2.17 Crossing of two electronic states found when the $r(O_4–O_5)$ coordinate of **MIN4** is elongated. ΔE_e(kcal mol^{-1}) was computed at the ROCCSD(T)/cc-pVTZ level of theory. The S_α intervals specify how the spin density on the given atom in the underlying ROHF reference wave function changes over the range of $r(O_4–O_5)$ values shown.

Based on our results, the production of OH at low temperature is mainly a product of **MIN1** → **TS2** (**TS2′**) → **MIN2** → **TS4** → methyloxirane + OH, rather than **MIN1** → **TS3** → **MIN3** → **TS6** → oxetane + OH. While **TS3** is more favorable than **TS2**, the pathway leading to oxetane + OH is greatly hindered by the high barrier of **TS6**. Methyloxirane + OH is lower in energy than oxetane + OH by 4.57 kcal mol^{-1}, making the pathway through **TS4** not only kinetically, but also thermodynamically favorable.

The experimental model of Huang et al.,[32] assuming that methyloxirane + OH was the dominant source of OH, overpredicted the measured methyloxirane yield. At 670 K, Welz and co-workers[38] observed that methyloxirane was the major C_3H_6O isomer product; however, at temperatures ranging between 530 to 600 K propanal was produced in comparable amounts. Their experiment produced a substantially lower yield of methyloxirane than given by the earlier study,[32] and they suggest the existence of another significant OH channel. Welz et al.[38] find that the sum concentration of acetone, propanal, and oxetane is comparable to that of methyloxirane. The large barriers (Table 2.1) that must be surmounted in order to produce these species make this observation problematic.

At 650 K, Cord et al.[36] measured yields of oxetane, relative to methyloxirane, comparable to those of Welz et al.;[38] however, their subsequent kinetic model significantly underpredicted the yield of oxetane. This disparity was rationalized by the reaction flux of the **MIN3** → oxetane + OH reaction being diverted to the **MIN3** + O_2 reaction, as well as uncertainties in the computed **TS6** barrier height due to spin contamination. The competition between these two **MIN3** pathways is an important aspect of autoignition chemistry, with *n*-propyl + O_2 acting as a prototype. Goldsmith et al.[35] showed in their computational study the significance of the favorable six-membered ring intramolecular H-abstraction transition state (**TS3**) in low temperature chain

branching as a gateway to QOOH + O_2 pathways. They found that **MIN3** is responsible for significant chain branching associated with QOOH + O_2 reactions, while **MIN2** accounted for less than 0.01% of such chain branching.

While the acetone found by Welz et al.[38] can be attributed to the *i*-propyl + O_2 reaction, the observed propanal is due to the constitutional isomer *n*-propyl reacting with O_2. A transition state from **MIN1** leading directly to propanal + OH that is 8.1 kcal mol^{-1} above the separated reactants has been reported;[35] however, no molecular geometry was supplied. This process would entail a concerted reaction involving a simultaneous 1,2-H shift and C–O bond cleavage/OH elimination. Such saddle points have been reported,[34] but they were found to be prohibitively high. In an attempt to rationalize their experimental yields of propanal, Welz et al.[38] suggest that the previously reported[35] barrier height of 8.1 kcal mol^{-1} would need to be lowered by 3.0 kcal mol^{-1}. However, as previously stated, our 1,2-H transfer from **MIN1** to **MIN4** is 9.04 kcal mol^{-1} above the separated reactants, well above this suggestion. Another product channel could arise from **MIN3** → **MIN2** → **MIN4** → propanal + OH; however, we find that the transition state from **MIN3** to **MIN2** is 22.2 kcal mol^{-1} above the reactants at the ROCCSD(T)/cc-pVTZ//ROCCSD(T)/cc-pVDZ level of theory. We were unable to locate a direct transition state from **MIN2** to **MIN4**.

2.5 CONCLUSIONS

The essential features of the *n*-propyl + O_2 reaction system were explored utilizing focal point analyses (FPA) to obtain *ab initio* energetics that push the boundaries of accuracy for combustion systems. FPA energetics were obtained with electron correlation treatments through CCSDT(Q) and with basis sets up to cc-pV5Z. The primary minimum (**MIN1**) and the most

favorable pathway transition state (**TS1**) were found to lie 32.7 kcal mol^{-1} and 2.4 kcal mol^{-1}, respectively, below the reactants. The first systematic conformational search of three QOOH intermediates (**MIN2**, **MIN3**, **MIN4**) was performed, uncovering a total of 32 rotamers lying within 1.6 kcal mol^{-1} of their respective lowest-energy minima. Fully optimized CCSD(T)/cc-pVTZ geometries were compared to the large number of DFT structures in the literature for stationary points on the *n*-propyl + O_2 potential energy surface. Substantial mean average deviations were observed for both bond lengths and angles in most cases, demonstrating the necessity of highly correlated methods for geometry optimizations of combustion chemistry species. Accurate ZPVE corrections, which are crucial for definitive energetics, were determined utilizing our newly developed mixed Hessian approach. Remarkably, the mean absolute deviation between explicit and mixed Hessian ROCCSD(T)/cc-pVTZ harmonic frequencies is only 0.68 cm^{-1} in our benchmarks, with the corresponding ZPVE(harm) values differing by only 0.002 kcal mol^{-1}. Two competitive β-hydrogen abstraction transition states (**TS2**, **TS2′**) were located, separated by only 0.16 kcal mol^{-1}, with the lower of the two (**TS2**) lying 0.37 kcal mol^{-1} above the separated reactants. This fact is underappreciated in current combustion literature and could be the root cause for the disagreement between FPA and ME results for the barrier height of **TS2**. Incorporation of **TS2′** into previous ME models[32] is expected to raise the fitted barrier height of **TS2**, bringing about better agreement with our FPA result. Both **TS2** and **TS2′**, along with **TS3**, exhibit anomalously large DBOC corrections, indicative of nearby conical intersections. We propose that the DBOC correction be utilized as a diagnostic for the presence of nearby conical intersections and possible nonadiabatic reaction dynamics on potential energy surfaces such as those of *n*-propyl + O_2.

While the chain-terminating, concerted elimination of HO_2 pathway (**TS1**) from **MIN1** predominates in the *n*-propyl + O_2 system, this pathway is less favorable when compared to ethyl + O_2.[16] The most energetically favorable OH producing pathway begins with a **MIN1** → **MIN2** isomerization over **TS2**/**TS2′** followed by O–O bond scission and ring closure over **TS4** to yield methyloxirane + OH. The **MIN1** → **MIN3** reaction over the 6-membered ring transition state **TS3** is the most preferred isomerization, but subsequent fragmentation to oxetane + OH is blocked by a high barrier (**TS6**). However, under high pressure conditions, **MIN3** might be attacked by another O_2 before the reverse reaction to **MIN1** occurs, likely leading to chain branching. In any event, it is important to extend high-level computational studies to the *n*-butyl + O_2 system to understand the prototypical behavior of autoignition chemistry. We hypothesize that the pathway through the 7-membered ring hydrogen-transfer transition state to the δ-QOOH species followed by a 6-membered ring transition to oxacyclopentane + OH is more favorable in the *n*-butyl + O_2 system than the associated concerted elimination of HO_2.

2.6 SUPPLEMENTARY MATERIAL

See the Supplementary Material for the following: conformational energies, harmonic vibrational frequencies, and Cartesian coordinates for all conformers of **MIN1**, **MIN2**, **MIN3**, and **MIN4** (Table S1–S4); Cartesian coordinates, geometrical depictions, and harmonic vibrational frequencies for all stationary points of the *n*-propyl + O_2 system (Table S5–S7); benchmark of the mixed-Hessian(TZ,DZ) scheme for FC-ROCCSD(T) harmonic vibrational frequencies of **MIN1**, *n*-propyl, propene, propanal, oxetane, and methyloxirane (Table S8); comparison of energetic results from various FPA extrapolation schemes (Table S11); single-point energies at various

levels of theory for all stationary points at FC-ROCCSD(T)/cc-pVTZ structures (Table S14); and focal point analyses of relative energies for all reaction paths considered in Table 2.1 (Table S15).

The Supplementary Material for this chapter is provided at https://aip.scitation.org/doi/suppl/10.1063/1.5017305. From " Bartlett, M.A.; Liang, T.; Pu, L.; Schaefer, H. F.; Allen, W.D. 2018. *J. Chem. Phys.* 148: 094303"

2.7 ACKNOWLEDGEMENTS

This work was supported by The Department of Energy, Office of Basic Sciences, Computational and Theoretical Chemistry Grant DE-SC0015512. The high-level *ab initio* computations utilized resources of the National Energy Research Scientific Computing Center, a DOE office of Science User Facility supported by the Office of Sciences of the U.S. Department of Energy under grant No. DE-AC02-05CH11231. We thank Chia-Hua Wu for advice in the implementation of the mixed Hessian formalism. We also thank Drs. Stephen Klippenstein and Kevin B. Moore III for helpful discussions on combustion chemistry.

2.8 REFERENCES

(1) Westbrook, C. K., *Proc. Combust. Inst.* **2000**, *28*, 1563--1577.

(2) Merchant, S. S.; Goldsmith, C. F.; Vandeputte, A. G.; Burke, M. P.; Klippenstein, S. J.; Green, W. H., *Combust. Flame* **2015**, *162*, 3658-3673.

(3) Taatjes, C. A., *J. Phys. Chem. A* **2006**, *110*, 4299-4312.

(4) Zádor, J.; Taatjes, C. A.; Fernandes, R. X., *Prog. Energy Combust. Sci.* **2011**, *37*, 371-421.

(5) Klippenstein, S. J., *Proc. Combust. Inst.* **2017**, *36*, 77-111.

(6) Savee, J. D.; Papajak, E.; Rotavera, B.; Huang, H.; Eskola, A. J.; Welz, O.; Sheps, L.; Taatjes, C. A.; Zádor, J.; Osborn, D. L., *Science* **2015**, *347*, 643-646.

(7) Baldwin, R. R.; Dean, C. E.; Walker, R. W., *J. Chem. Soc., Faraday Trans. 2* **1986**, *82*, 1445-1455.

(8) Gulati, S. K.; Walker, R. W., *J. Chem. Soc., Faraday Trans. 2* **1988**, *84*, 401-407.

(9) Baldwin, R. R.; Stout, D. R.; Walker, R. W., *J. Chem. Soc., Faraday Trans.* **1991**, *87*, 2147-2150.

(10) Quelch, G. E.; Gallo, M. M.; Schaefer, H. F., *J. Am. Chem. Soc.* **1992**, *114*, 8239-8247.

(11) Quelch, G. E.; Gallo, M. M.; Shen, M.; Xie, Y.; Schaefer, H. F.; Moncrieff, D., *J. Am. Chem. Soc.* **1994**, *116*, 4953-4962.

(12) Ignatyev, I. S.; Xie, Y.; Allen, W. D.; Schaefer, H. F., *J. Chem. Phys.* **1997**, *107*, 141-155.

(13) Rienstra-Kiracofe, J. C.; Allen, W. D.; Schaefer, H. F., *J. Phys. Chem. A* **2000**, *104*, 9823-9840.

(14) Miller, J. A.; Klippenstein, S. J., *Int. J. Chem. Kinet.* **2001**, *33*, 654-668.

(15) DeSain, J. D.; Klippenstein, S. J.; Miller, J. A.; Taatjes, C. A., *J. Phys. Chem. A* **2003**, *107*, 4415-4427.

(16) Wilke, J. J.; Allen, W. D.; Schaefer, H. F., *J. Chem. Phys.* **2008**, *128*, 074308.

(17) Knox, J. H., *Trans. Faraday Soc.* **1959**, *55*, 1362-1374.

(18) Knox, J. H., *Trans. Faraday Soc.* **1960**, *56*, 1225-1234.

(19) Knox, J. H., *Chem. Commun. (London).* **1965**, 108-109.

(20) Baker, R. R.; Baldwin, R. R.; Walker, R. W., *Trans. Faraday Soc.* **1970**, *66*, 3016-3031.

(21) Slagle, I. R.; Park, J.-Y.; Gutman, D., *Proc Combust Inst.* **1985**, *20*, 733-741.

(22) Slagle, I. R.; Ratajczak, E.; Heaven, M. C.; Gutman, D.; Wagner, A. F., *J. Am. Chem. Soc.* **1985**, *107*, 1838-1845.

(23) Kaiser, E. W.; Wallington, T. J., *J. Phys. Chem.* **1996**, *100*, 18770-18774.

(24) Kaiser, E. W., *J. Phys. Chem. A* **1998**, *102*, 5903-5906.

(25) DeSain, J. D.; Clifford, E. P.; Taatjes, C. A., *J. Phys. Chem. A* **2001**, *105*, 3205-3213.

(26) DeSain, J. D.; Taatjes, C. A.; Miller, J. A.; Klippenstein, S. J.; Hahn, D. K., *Faraday Discuss.* **2002**, *119*, 101-120.

(27) Wijaya, C. D.; Sumathi, R.; Green, W. H., *J. Phys. Chem. A* **2003**, *107*, 4908-4920.

(28) Green, W. H.; Wijaya, C. D.; Yelvington, P. E.; Sumathi, R., *Mol. Phys.* **2004**, *102*, 371-380.

(29) Merle, J. K.; Hayes, C. J.; Zalyubovsky, S. J.; Glover, B. G.; Miller, T. A.; Hadad, C. M., *J. Phys. Chem. A* **2005**, *109*, 3637-3646.

(30) Estupiñán, E. G.; Klippenstein, S. J.; Taatjes, C. A., *J. Phys. Chem. B* **2005**, *109*, 8374-8387.

(31) Estupiñán, E. G.; Smith, J. D.; Tezaki, A.; Klippenstein, S. J.; Taatjes, C. A., *J. Phys. Chem. A* **2007**, *111*, 4015-4030.

(32) Huang, H.; Merthe, D. J.; Zádor, J.; Jusinski, L. E.; Taatjes, C. A., *Proc. Combust. Inst.* **2011**, *33*, 293-299.

(33) Miyoshi, A., *J. Phys. Chem. A* **2011**, *115*, 3301-3325.

(34) Huynh, L. K.; Carstensen, H.-H.; Dean, A. M., *J. Phys. Chem. A* **2010**, *114*, 6594-6607.

(35) Goldsmith, C. F.; Green, W. H.; Klippenstein, S. J., *J. Phys. Chem. A* **2012**, *116*, 3325-3346.

(36) Cord, M., et al., *J. Phys. Chem. A* **2012**, *116*, 12214-12228.

(37) Goldsmith, C. F.; Tomlin, A. S.; Klippenstein, S. J., *Proc. Combust. Inst.* **2013**, *34*, 177-185.

(38) Welz, O.; Burke, M. P.; Antonov, I. O.; Goldsmith, C. F.; Savee, J. D.; Osborn, D. L.; Taatjes, C. A.; Klippenstein, S. J.; Sheps, L., *J. Phys. Chem. A* **2015**, *119*, 7116-7129.

(39) Burke, M. P., et al., *J. Phys. Chem. A* **2015**, *119*, 7095-7115.

(40) Wilk, R. D.; Cohen, R. S.; Cernansky, N. P., *Ind. Eng. Chem. Res.* **1995**, *34*, 2285-2297.

(41) Chen, C.-J.; Bozzelli, J. W., *J. Phys. Chem. A* **1999**, *103*, 9731-9769.

(42) Strelkova, M. I.; Safonov, A. A.; Sukhanov, L. P.; Umanskiy, S. Y.; Kirillov, I. A.; Potapkin, B. V.; Pasman, H. J.; Tentner, A. M., *Combust. Flame* **2010**, *157*, 641-652.

(43) Zhang, F.; Dibble, T. S., *Phys. Chem. Chem. Phys.* **2011**, *13*, 17969-17977.

(44) Cord, M.; Sirjean, B.; Fournet, R.; Tomlin, A.; Ruiz-Lopez, M.; Battin-Leclerc, F., *J. Phys. Chem. A* **2012**, *116*, 6142-6158.

(45) Eskola, A. J.; Welz, O.; Savee, J. D.; Osborn, D. L.; Taatjes, C. A., *J. Phys. Chem. A.* **2013**, *117*, 12216-12235.

(46) Prince, J. C.; Treviño, C.; Williams, F. A., *Combust. Flame* **2017**, *175*, 27-33.

(47) Wang, S.; Miller, D. L.; Cernansky, N. P.; Curran, H. J.; Pitz, W. J.; Westbrook, C. K., *Combust. Flame* **1999**, *118*, 415-430.

(48) DeSain, J. D.; Klippenstein, S. J.; Taatjes, C. A., *Phys. Chem. Chem. Phys.* **2003**, *5*, 1584-1592.

(49) Petway, S. V.; Ismail, H.; Green, W. H.; Estupiñán, E. G.; Jusinski, L. E.; Taatjes, C. A., *J. Phys. Chem. A* **2007**, *111*, 3891-3900.

(50) DeSain, J. D.; Taatjes, C. A., *J. Phys. Chem. A* **2001**, *105*, 6646-6654.

(51) Fernandes, R. X.; Zador, J.; Jusinski, L. E.; Miller, J. A.; Taatjes, C. A., *Phys. Chem. Chem. Phys.* **2009**, *11*, 1320-1327.

(52) Knepp, A. M.; Meloni, G.; Jusinski, L. E.; Taatjes, C. A.; Cavallotti, C.; Klippenstein, S. J., *Phys. Chem. Chem. Phys.* **2007**, *9*, 4315-4331.

(53) Buda, F.; Bounaceur, R.; Warth, V.; Glaude, P. A.; Fournet, R.; Battin-Leclerc, F., *Combust. Flame* **2005**, *142*, 170-186.

(54) Klippenstein, S. J.; Miller, J. A., *J. Phys. Chem. A* **2002**, *106*, 9267-9277.

(55) Zhang, F.; Dibble, T. S., *J. Phys. Chem. A* **2011**, *115*, 655-663.

(56) Roothaan, C. C. J., *Rev. Mod. Phys.* **1951**, *23*, 69-89.

(57) Roothaan, C. C. J., *Rev. Mod. Phys.* **1960**, *32*, 179-185.

(58) Pople, J. A.; Nesbet, R. K., *J. Chem. Phys.* **1954**, *22*, 571-572.

(59) Møller, C.; Plesset, M. S., *Phys. Rev.* **1934**, *46*, 618.

(60) Lee, T. J.; Jayatilaka, D., *Chem. Phys. Lett.* **1993**, *201*, 1.

(61) Čížek, J., *J. Chem. Phys.* **1966**, *45*, 4256-4266.

(62) Crawford, T. D.; Schaefer, H. F., An Introduction to Coupled Cluster Theory for Computational Chemists. In *Rev. Comput. Chem*, Lipkowitz, K. B.; Boyd, D. B., Eds. John Wiley & Sons, Inc.: New Jersey, 2000; Vol. 14, pp 33-136.

(63) Purvis, G. D.; Bartlett, R. J., *J. Chem. Phys.* **1982**, *76*, 1910-1918.

(64) Raghavachari, K.; Trucks, G. W.; Pople, J. A.; Head-Gordon, M., *Chem. Phys. Lett.* **1989**, *157*, 479-483.

(65) Noga, J.; Bartlett, R. J., *J. Chem. Phys.* **1987**, *86*, 7041-7050.

(66) Bomble, Y. J.; Stanton, J. F.; Kállay, M.; Gauss, J., *J. Chem. Phys.* **2005**, *123*, 054101.

(67) Dunning, T. H., Jr., *J. Chem. Phys.* **1989**, *90*, 1007-1023.

(68) Peterson, K. A.; Woon, D. E.; Dunning, T. H., Jr., *J. Chem. Phys.* **1994**, *100*, 7410-7415.

(69) Woon, D. E.; Dunning, T. H., *J. Chem. Phys.* **1995**, *103*, 4572-4585.

(70) Kendall, R. A.; Dunning, T. H., Jr.; Harrison, R. J., *J. Chem. Phys.* **1992**, *96*, 6796-6806.

(71) Hariharan, P. C.; Pople, J. A., *Theor. Chim. Acta.* **1973**, *28*, 213-222.

(72) East, A. L. L.; Allen, W. D., *J. Chem. Phys.* **1993**, *99*, 4638-4650.

(73) Császár, A. G.; Allen, W. D.; Schaefer III, H. F., *J. Chem. Phys.* **1998**, *108*, 9751-9764.

(74) Császár, A. G.; Tarczay, G.; Leininger, M. L.; Polyansky, O. L.; Tennyson, J.; Allen, W. D., In *Spectroscopy from Space*, J. Demaison, K. S., Ed. Kluwer: Dordrecht: The Netherlands, 2001; pp 317-339.

(75) Gonzales, J. M.; Allen, W. D.; Schaefer III, H. F., *J. Phys. Chem. A* **2005**, *109*, 10613-10628.

(76) Werner, H.-J., et al. *Molpro, Version 2010.1, a Package of Ab Initio Programs Written By*, 2010.

(77) *CFOUR,* a quantum chemical program package written by J.F. Stanton, J. Gauss, M.E. Harding, P.G. Szalay with contributions from A.A. Auer, R.J. Bartlett, U. Benedikt, C. Berger, D.E. Bernholdt, Y.J. Bomble, L. Cheng, O. Christiansen, M. Heckert, O. Heun, C. Huber, T.-C. Jagau, D. Jonsson, J. Jusélius, K. Klein, W.J. Lauderdale, F. Lipparini, D.A. Matthews, T. Metzroth, L.A. Mück, D.P. O'Neill, D.R. Price, E. Prochnow, C. Puzzarini, K. Ruud, F. Schiffmann, W. Schwalbach, C. Simmons, S. Stopkowicz, A. Tajti, J. Vázquez, F. Wang, J.D. Watts and the integral packages *MOLECULE* (J. Almlöf and P.R. Taylor), *PROPS* (P.R. Taylor), *ABACUS* (T. Helgaker, H.J. Aa. Jensen, P. Jørgensen, and J. Olsen), and *ECP* routines by A. V. Mitin and C. van Wüllen. For the current version, see *http://www.cfour.de*.

(78) Crawford, T. D., et al., *J. Comput. Chem.* **2007**, *28*, 1610-1616.

(79) Schmidt, M. W., et al., *J. Comput. Chem.* **1993**, *14*, 1347-1363.

(80) Gordon, M. S.; Schmidt, M. W., Advances in Electronic Structure Theory: Gamess a Decade Later. In *Theory and Applications of Computational Chemistry: The First Forty Years*, Frenking, G.; Kim, K. S.; Scuseria, G. E., Eds. Elsevier: Amsterdam, 2005; pp 1167-1189.

(81) Janssen, C. L.; Nielsen, I. B.; Leininger, M. L.; Valeev, E. F.; Kenny, J. P.; Seidl, E. T. *The Massively Parallel Quantum Chemistry Program (MPQC) Written By* Version 2.3.1; Sandia National Laboratories: Livermore, CA, 2008.

(82) Kállay, M., et al. *MRCC, a Quantum Chemical Program Suite*, *J. Chem. Phys.* **139**, 094105 (2013).

(83) Eliel, E. L.; Wilen, S. H., *Stereochemistry of Organic Compounds*; John Wiley & Sons: New York, 1993.

(84) Dobrowolski, J. C.; Rode, J. E.; Sadlej, J., *Comput. Theor. Chem* **2007**, *810*, 129-134.

(85) Wilke, J. J.; Lind, M. C.; Schaefer, H. F.; Császár, A. G.; Allen, W. D., *J. Chem. Theory Comput.* **2009**, *5*, 1511-1523.

(86) He, K.; Allen, W. D., *J. Chem. Theory Comput.* **2016**, *12*, 3571-3582.

(87) Feller, D., *J. Chem. Phys.* **1992**, *96*, 6104-6114.

(88) Helgaker, T.; Klopper, W.; Koch, H.; Noga, J., *J. Chem. Phys.* **1997**, *106*, 9639-9646.

(89) Karton, A.; Martin, J. M. L., *Theor. Chem. Acc.* **2006**, *115*, 330-333.

(90) Schwenke, D. W., *J. Chem. Phys.* **2005**, *122*, 014107.

(91) Martin, J. M. L., *Chem. Phys. Lett.* **1996**, *259*, 669.

(92) Ajith Perera, S.; Bartlett, R. J., *Chem. Phys. Lett.* **1993**, *216*, 606-612.

(93) Handy, N. C.; Yamaguchi, Y.; Schaefer III, H. F., *J. Chem. Phys.* **1986**, *84*, 4481-4484.

(94) Pulay, P.; Török, F., *Acta. Chim.* **1965**, *44*, 287.

(95) Keresztury, G.; Jalsovszky, G., *J. Mol. Struct.* **1971**, *10*, 304-305.

(96) Allen, W. D.; Császár, A. G.; Horner, D. A., *J. Am. Chem. Soc.* **1992**, *114*, 6834-6849.

(97) Jayatilaka, D.; Lee, T. J., *J. Chem. Phys.* **1993**, *98*, 9734.

(98) Lee, T. J.; Taylor, P. R., *Int. J. Quantum Chem.* **1989**, *36*, 199-207.

(99) Lauderdale, W. J.; Stanton, J. F.; Gauss, J.; Watts, J. D.; Bartlett, R. J., *Chem. Phys. Lett.* **1991**, *187*, 21-28.

(100) Lauderdale, W. J.; Stanton, J. F.; Gauss, J.; Watts, J. D.; Bartlett, R. J., *J. Chem. Phys.* **1992**, *97*, 6606-6620.

(101) Urban, M.; Watts, J. D.; Bartlett, R. J., *Int. J. Quantum Chem.* **1994**, *52*, 211-225.

(102) Huber, K. P.; Herzberg, G., In *Molecular Spectra and Molecular Structure. Iv. Constants of Diatomic Molecules*, Springer, Ed. Van Noestrand Reinhold: New York, 1979; pp 498-508.

(103) Lubic, K. G.; Amano, T.; Uehara, H.; Kawaguchi, K.; Hirota, E., *J. Chem. Phys.* **1984**, *81*, 4826-4831.

(104) Lide, D. R.; Christensen, D., *J. Chem. Phys.* **1961**, *35*, 1374-1378.

(105) Creswell, R. A., *Mol. Phys.* **1975**, *30*, 217-222.

(106) Creswell, R. A.; Schwendeman, R. H., *J. Mol. Spectrosc.* **1977**, *64*, 295-301.

(107) Li, C.; Agarwal, J.; Wu, C.-H.; Allen, W. D.; Schaefer, H. F., *J. Phys. Chem. B* **2015**, *119*, 728-735.

(108) Hoobler, P. R.; Turney, J. M.; Schaefer, H. F., *J. Chem. Phys.* **2016**, *145*, 174301.

(109) Tarczay, G.; Zalyubovsky, S. J.; Miller, T. A., *Chem. Phys. Lett.* **2005**, *406*, 81-89.

(110) Moore III, K. B.; Turney, J. M.; Schaefer III, H. F., *J. Chem. Phys.* **2017**, *146*, 194304.

(111) Meek, G. A.; Levine, B. G., *J. Chem. Phys.* **2016**, *144*, 184109.

(112) Vosko, S. H.; Wilk, L.; Nusair, M., *Can. J. Phys.* **1980**, *58*, 1200-1211.

(113) Lee, C.; Yang, W.; Parr, R. G., *Phys. Rev. B* **1988**, *37*, 785-789.

(114) Becke, A. D., *J. Chem. Phys.* **1993**, *98*, 5648-5652.

(115) Stephens, P. J.; Devlin, F. J.; Chabalowski, C. F.; Frisch, M. J., *J. Phys. Chem.* **1994**, *98*, 11623-11627.

CHAPTER 3

THE *i*-PROPYL + O_2 REACTION MECHANISM: A MODEL OF SECONDARY ALKYL RADICAL OXIDATION [†]

[†]Bartlett, M.A.; Liang, T.; Pu, L.; Schaefer, H. F.; Allen, W.D. To be submitted for publication.

3.1 ABSTRACT

The *i*-propyl + O_2 reaction is an important model of chain branching reactions in larger combustion systems. In this work, focal point analyses (FPA) extrapolating to the *ab initio* limit were performed on the *i*-propyl + O_2 system based on explicit quantum chemical computations with electron correlation treatments through CCSDT(Q) and basis sets up to cc-pV5Z. All reaction species and transition states were fully optimized at the rigorous CCSD(T)/cc-pVTZ level of theory, revealing some substantial differences in comparison to the DFT geometries existing in the literature. Two key stationary points, *i*-propylperoxy radical (**MIN1**) and its concerted elimination transition state (**TS1**), were located 34.8 kcal mol^{-1} and 4.4 kcal mol^{-1} below the reactants, respectively. The β-hydrogen transfer transition state (**TS2)** exhibits an anomalously large diagonal Born-Oppenheimer correction (Δ_{DBOC} = 1.09 kcal mol^{-1}), which is indicative of a nearby surface crossing and possible nonadiabatic reaction dynamics. Our definitive energetics for stationary points on the *i*-propyl + O_2 potential energy surface provide key benchmarks for future studies of hydrocarbon oxidation.

3.2 INTRODUCTION

Hydrocarbon oxidation reactions are continuing to attract interest from the scientific community despite decades of rigorous scientific investigations on the subject.[1] Hydrocarbon oxidation as a means to power automobiles is not going away any time soon. Hydrocarbons have a rather long shelf-life, and high energy density, and are easily transported. A major issue surrounding hydrocarbon combustion is the generation of NO_x and soot by-products when utilizing current engine technologies and fuel sources. The formation of soot is dominant in diesel engine technologies, which exhibit a large fuel-air (equivalence) ratio. Moreover, the high peak temperatures generated by spark ignition engines result in toxic NO_x formation. New advances in engine technologies that are geared toward higher fuel efficiency and lower emissions are currently being developed.[2-3] Homogeneous charge compression ignition (HCCI) engines utilize high compression ratios and lean fuel mixtures, resulting in very high efficiency and low soot/NO_x formation. These types of engines perform at relatively low temperatures (~500 – 1000 K) and execute rapid combustion, which results in a large portion of unburned hydrocarbons. Central to this process is the reactivity of alkyl radicals, and as a result of the lean fuel mixture, alkyl peroxy radicals. Thus, it is of great importance to achieve a detailed understanding of low temperature combustion of hydrocarbon species.

The reactions of low temperature oxidation of hydrocarbon species can be summarized in Figure 3.1. The reaction scheme is initiated by the association of an alkyl radical (R) with molecular oxygen (O_2). At low temperatures and moderate pressures the R + O_2 reaction proceeds largely to form an alkyl peroxy radical (ROO).[1] These ROO molecules can dissociation back to the R + O_2 reactants, produce the conjugate alkene and HO_2 via a concerted elimination reaction,

or isomerize via H-atom internal abstraction to form a hydroperoxyalkyl radical (QOOH). The latter avenue for the ROO radical to form QOOH is of great interest, because until 2015 the elusive QOOH species had escaped experimental detection.[4] These QOOH species rapidly decompose to form an OH radical and an oxygen heterocycle, or they fragment to HO_2 and an alkene. The formation of the OH radical is important for chain propagation because the OH radical can react with the hydrocarbon fuel source (RH) to create more alkyl radicals (R), thus creating a cycle of fuel consumption.

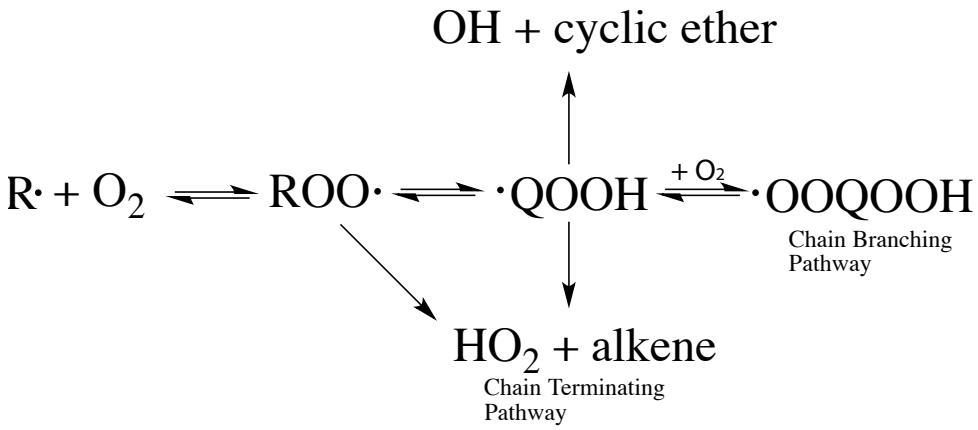

Figure 3.1 General mechanism for alkyl + O_2 reactions.

The ethyl + O_2 model reaction has been studied extensively, both theoretically and experimentally.[5-14] The lowest-energy ethyl + O_2 reaction channel involves the concerted elimination of HO_2 from the ethylperoxy intermediate (C_2H_5OO) to form ethylene + HO_2.[9-11] However, since HO_2 is relatively unreactive, the channel leading to alkene + HO_2 would be chain terminating at low temperatures. Master equation kinetic models[12] fit to measured reaction rates agree with rigorous *ab initio* computations carried out through the CCSDT(Q) level[14] in placing the concerted elimination transition state below the ethyl + O_2 reactants by 3.0 kcal mol^{-1}.

The reactions of R + O_2 become increasingly complicated as the size of the alkyl radical chain grows due to an increase in the numbers of conformers and isomers. Knowledge obtained by studying larger alkyl + O_2 reactions is quite beneficial for understanding fuel combustion processes. A vast amount of research has been conducted on combustion reactions of propyl,[13,15-38] butyl,[24,39-45] neopentyl,[46-48] cyclopentyl,[49] and cyclohexyl[50-51] radicals. Experimental studies have shown that as the length of the alkyl chain grows, intramolecular hydrogen abstraction reactions to produce QOOH radicals are able to better compete with the concerted elimination of HO_2.[13] Therefore propyl + O_2, and even more so butyl + O_2, may be a better paradigm of hydrocarbon combustion due to the ability to isomerize to QOOH species via a 6-membered (*n*-propyl + O_2) or 7-membered (*n*-butyl + O_2) ring transition state. For a more detailed review of previous theoretical and experimental research surrounding the propyl + O_2 system, we direct the reader to our previous paper on the *n*-propyl + O_2 system.[38]

In our previous study[38] on *n*-propyl + O_2 the essential features of the potential energy surface were established utilizing highly accurate coupled cluster methods with large basis sets to obtain energies with errors of only tenths of a kcal mol^{-1}. In this work, we extend this protocol to firmly establish the features of the *i*-propyl + O_2 system. Utilizing focal point analyses (FPA) with correlation treatments up to CCSDT(Q) and basis sets up to cc-pV5Z has previously been shown to match Master Equation (ME) kinetic model results for the ethyl + O_2 system.[14] Employing zero-point vibrational energies (ZPVE) at high levels of theory is critical to the accuracy of our FPA relative energies. We employ a mixed Hessian methodology to compute ZPVE corrections of CCSD(T)/cc-pVTZ level quality, making these daunting computations feasible for larger combustion systems. In this work we perform FPA to the *ab initio* limit based on explicit

computations through the CCSDT(Q) level of theory and basis sets up to cc-pV5Z, which is critically needed to establish the key features of the *i*-propyl + O_2 system.

3.3 THEORETICAL METHODS

3.3.1 GENERAL SCHEME

Electronic wave functions were determined in this study by restricted (RHF),[52] restricted open-shell (ROHF),[53] and unrestricted (UHF)[54] Hartree-Fock methods; second-order Møller-Plesset (MP2)[55] and Z-averaged (ZAPT2)[56] perturbation theory; and coupled cluster (CC)[57-58] theory incorporating up to single and double excitations (CCSD),[59] perturbative contributions from connected triple excitations [CCSD(T)],[60] full triple excitations (CCSDT),[61] as well as a perturbative treatment of quadruple excitations [CCSDT(Q)].[62] The correlation methods employed a spin orbital formalism into which either ROHF or UHF orbitals were inserted, as signified by an RO or U prefix. This study primarily used the correlation-consistent (cc) families of basis sets cc-pV*X*Z *(X* = D, T, Q, 5),[63-64] cc-pCV*X*Z (*X* = T),[65] and aug-cc-pV*X*Z (*X* = D, T),[66] although CCSDT(Q) computations were performed with the 6-31G* basis set.[67]

The focal point analysis (FPA)[68-71] scheme developed by Allen and co-workers was employed to compute precise relative energies for the lowest conformers of all stationary points by extrapolation to full correlation and complete basis set limits. The quantum chemistry packages Molpro 2010.1,[72] CFOUR 1.0,[73] PSI 3.4,[74] GAMESS version 25 Mar 2010,[75-76] and MPQC 2.3.0,[77] as well as Kállay's MRCC[78] program were employed in this study.

3.3.2 GEOMETRY OPTIMIZATION

For all reactants, products, intermediates, and transition states, geometric structures were initially optimized at the (frozen-core) ROMP2/aug-cc-pVDZ level of theory, and then single-point ROCCSD(T)/cc-pVTZ energies were computed to determine the lowest-energy conformers. A series of dihedral angles was chosen to uniquely identify each conformer: $\tau(C_1C_2C_3O_4)$, $\tau(C_2C_3O_4O_5)$, and $\tau(C_3O_4O_5H_9)$. The following Klyne-Prelog[79-82] labels were utilized for each dihedral angle: G^+ (gauche, $+30^\circ < \tau < +90^\circ$), G^- (gauche, $-90^\circ < \tau < -30^\circ$), A^+ (anticlinal, $+90^\circ < \tau < +150^\circ$), A^- (anticlinal, $-150^\circ < \tau < -90^\circ$), and T (trans, $|\tau| > 150^\circ$). For the lowest-energy conformer of each species, ROCCSD(T)/cc-pVDZ optimizations were then executed. Finally, these structures were used as starting points for subsequent full geometry optimizations at the ROCCSD(T)/cc-pVTZ level.

The final ROCCSD(T)/cc-pVTZ geometry optimizations were executed with the OPTKING module in the PSI 3.4 package using 3-point numerical gradients evaluated from single-point energies computed with the Molpro 2010.1 package. Fixed ROCCSD(T)/cc-pVDZ Hessians from the CFOUR 1.0 program were used to speed up convergence. Optimized geometries in Cartesian coordinates as well as depictions of the structures and internal coordinates of all stationary points are provided in Tables A3 and A4 of the Supporting Information.

3.3.2 FOCAL POINT ANALYSES

In our FPA computations, E, ΔE, and δ refer to the absolute energies, relative energies between species, and relative energy increments with respect to preceding levels of electron

correlation. The Hartree-Fock[83] (E_{HF}) and correlation energies[84] (ε) were extrapolated with the following equations:

$$E_{\mathrm{HF}}(X) = E_{\mathrm{HF}}^{\infty} + A\exp(-bX) \tag{3.11}$$

$$\varepsilon(X) = \varepsilon^{\infty} + \frac{B}{X^3} \tag{3.12}$$

where X is the cardinal number of a correlation consistent cc-pVXZ basis. The extrapolations in the Hartree-Fock case employed X = {3, 4, 5}, while those for ROCCSD, ROCCSD(T), and ZAPT2 correlation energies used X = {3, 4}.

Single-point energies computed by the ROCCSDT and UCCSDT(Q) levels of theory were used as additive corrections:

$$\delta[\mathrm{ROCCSDT}] = \Delta E(\mathrm{ROCCSDT/cc\text{-}pVDZ}) - \Delta E(\mathrm{ROCCSD(T)/cc\text{-}pVDZ}) \tag{3.13}$$

$$\delta[\mathrm{CCSDT(Q)}] = \Delta E(\mathrm{UCCSDT(Q)/6\text{-}31G^{*}}) - \Delta E(\mathrm{ROCCSDT/6\text{-}31G^{*}}) \tag{3.14}$$

These computationally demanding ROCCSDT and UCCSDT(Q) correlation increments were computed with modest basis sets (cc-pVDZ, 6-31G*) using CFOUR 1.0 and Kállay's MRCC program coupled with CFOUR 1.0, respectively.

Core electron correlation effects were accounted for by subtracting all-electron (AE) and frozen-core (FC) ROCCSD(T) energies computed with the cc-pCVTZ basis set:

$$\Delta(\mathrm{core}) = \Delta E_{\mathrm{e}}(\mathrm{AE\text{-}ROCCSD(T)/cc\text{-}pCVTZ}) - \Delta E_{\mathrm{e}}(\mathrm{FC\text{-}ROCCSD(T)/cc\text{-}pCVTZ}) \tag{3.15}$$

A first-order relativistic correction,[85] Δ(rel), was computed from the one-electron mass-velocity and Darwin terms at the ROCCSD(T)/cc-pVTZ level. The diagonal correction to the Born-Oppenheimer approximation (DBOC),[86] which corrects for relaxation of the clamped nucleus assumption, was computed at the ROHF HF/aug-cc-pVTZ level. Harmonic vibrational frequencies and zero-point vibrational energy (ZPVE) corrections, $\Delta\mathrm{ZPVE(harm)}$, were computed utilizing the mixed Hessian (mixed-H) scheme, previously designed in our work[38] on the *n*-propyl

+ O_2 system, to closely approximate vibrational frequencies obtained at the ROCCSD(T)/cc-pVTZ level of theory. Final ZPVE values employed in this study were explicit ROCCSD(T)/cc-pVTZ values for both reactant and product species and mixed-H approximations to ROCCSD(T)/cc-pVTZ for all transition states and intermediate species.

The final focal point energy estimating ROCCSDT(Q) relative energies at the CBS limit was found by summing up extrapolation results, additive corrections, and auxiliary terms to give:

$$\Delta E_{\mathrm{FP}} = E_{\mathrm{HF}}^{\infty} + \delta^{\infty}[\mathrm{ROCCSD(T)}] + \delta[\mathrm{ROCCSDT}] + \delta[\mathrm{CCSDT(Q)}] + \Delta(\mathrm{core}) + \Delta(\mathrm{rel}) + \Delta\mathrm{ZPVE(harm)} \quad (3.16)$$

ZPVE, relativistic, and DBOC computations were performed with the CFOUR 1.0 package, while core correlation corrections were computed with the Molpro 2010.1 package.

3.4 DISCUSSION AND ANALYSIS OF THE *i*-PROPYL + O_2 REACTION

The important features of the *i*-propyl + O_2 potential energy surface investigated in this work are depicted in Figure 3.2. In this study we chose to investigate the stationary points previously used by Klippenstein and co-workers[24] in their master equation (ME) modeling. Table 3.1 includes relative enthalpies at 0 K ($\Delta_{\mathrm{rxn}} H_0^{\circ}$) for all stationary points of the *i*-propyl + O_2 system, allowing comparison between our results and those obtained from previous studies.

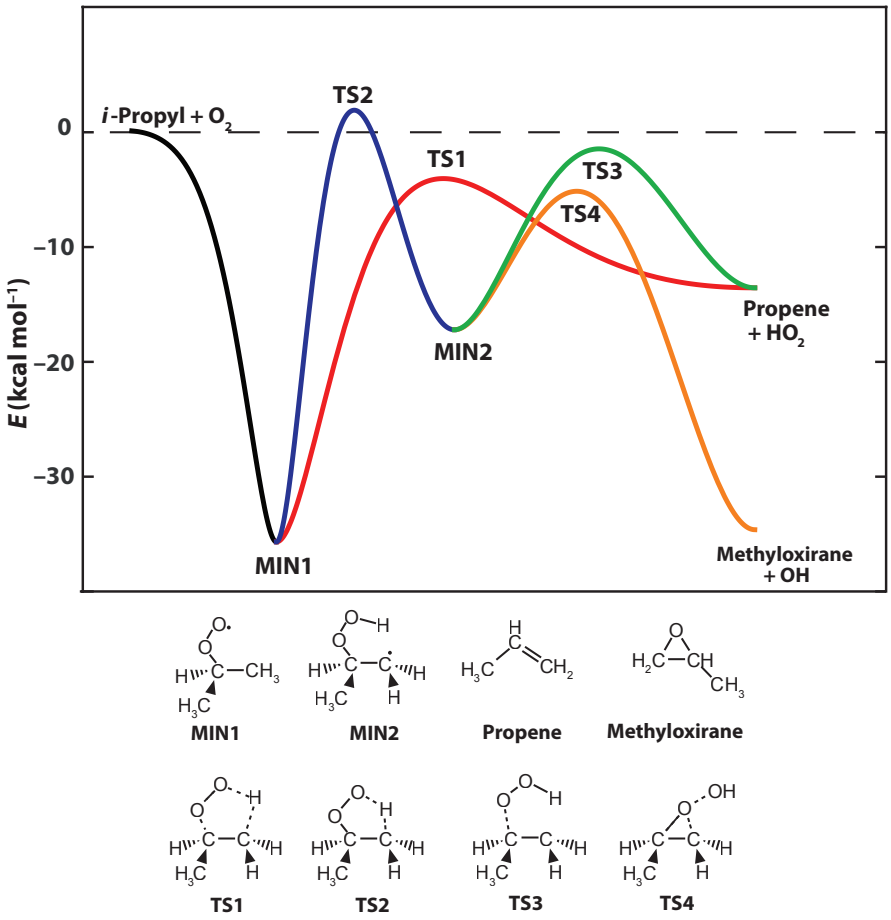

Figure 3.2 Schematic potential energy surface (PES) for *i*-propyl + O_2 reactions.

TABLE 3.1 Relative enthalpies at 0 K ($\Delta_{rxn} H_0^\circ$, kcal mol^{-1}) for stationary points of the *i*-propyl + O_2 system.

	$\Delta_{rxn} H_0^\circ$ (kcal mol^{-1})						
Ref.	24	13	30	30	32	33	This Work
	QCISD(T) (2002)	ME[a] (2003)	ME[a] (2010)	ME[a] (2011)	CBS-Q[b] (2011)	QCISD(T)[c] (2012)	
i-propyl+O_2	0.0	0.0	0.0	0.0	0.0	0.0	0.00
MIN1	–36.8	—	–34.8	–34.8	–36.2	–34.8	–34.8
MIN2	–20.2	—	—	—	—	–18.0	–17.4
TS1	–7.0	–4.7	–5.0	–5.0	–3.6	–4.2	–4.42
TS2	–1.4	–0.2	—	–1.7	+1.6	+1.2	+1.37
TS3	–1.9	—	—	—	—	–1.3	–1.52
TS4	–4.9	—	—	—	—	–5.6	–5.59
TS5	—	—	—	—	—	(+5.5)[d]	—
propene+HO_2	—	—	—	—	—	–13.5	–13.75
methyloxirane+OH	—	—	—	—	—	–35.5	–33.34
acetone + OH	—	—	—	—	—	–65.5	–64.38

[a]Fitted by master equation analysis to experimental kinetic data.

[b]Literature CBS-QB3 energies values.

[c]Restricted QCISD(T)/CBS energies including B3LYP/6-311++G(d,p) ZPVE corrections.

[d]Direct transition state from **MIN1** to acetone + OH.

Since cyclic transition states leading to QOOH species undergo distortion from ring planarity, we must investigate the presence of multireference electronic character. The presence of multireference character can be gauged using the open-shell T_1 diagnostic,[87,88] which measures the extent of orbital relaxation in the coupled cluster wave function. Values of T_1 greater than 0.02 are often taken as an indicator of multireference character[88] in closed-shell species, while open-shell species typically have a less defined threshold and exhibit larger T_1 values.[88] We also provide the largest doubles amplitudes ($T_{2,max}$) in the CCSD(T)/cc-pVTZ wave function to add further certainty in our investigation of multireference character.

The T_1 diagnostic and $T_{2,max}$ amplitudes are listed in Table 3.2 for the minima and transition states on the *i*-propyl + O_2 potential energy surface, as well as O_2 and OH. We include the CN

radical as a benchmark as it is reasonably well described at the single-reference CCSD(T) level of theory.[89-91] All reactions species in this study have T_1 and $T_{2,max}$ values smaller than CN and show no signs of significant multireference character.

TABLE 3.2 T_1 diagnostic values and $T_{2,max}$ amplitudes at the CCSD(T)/cc-pVTZ level of theory

	T_1	$T_{2,max}$		T_1	$T_{2,max}$
MIN1	0.028	<0.05	**TS1**	0.032	0.080
MIN2	0.012	<0.05	**TS2**	0.025	<0.05
i-propyl	0.010	<0.05	**TS3**	0.040	0.095
HO_2 ($^2A''$)	0.037	0.056	**TS4**	0.027	0.053
OH ($^2\Pi$)	0.006	<0.05	CN ($^2\Sigma^+$)	0.053	0.093

3.4.1 REACTANTS AND PRODUCTS

Experimentally determined geometries are available for OH,[92] O_2,[92] HO_2,[93] propene,[94] and methyloxirane.[95] Our ROCCSD(T)/cc-pVTZ geometries are in excellent agreement with experiment with mean absolute deviations (MAD) of 0.004 Å for bond lengths and 0.6° for bond angles. A notable difference of 1.24° is seen for $\alpha(H_7–C_1–C_2)$ of propene. When comparing the B3LYP/6-311++G(d,p) *i*-propyl structure of Goldsmith et al.[33] to our result, we observe MADs of 0.002 Å for bond lengths and 0.73° for bond angles.

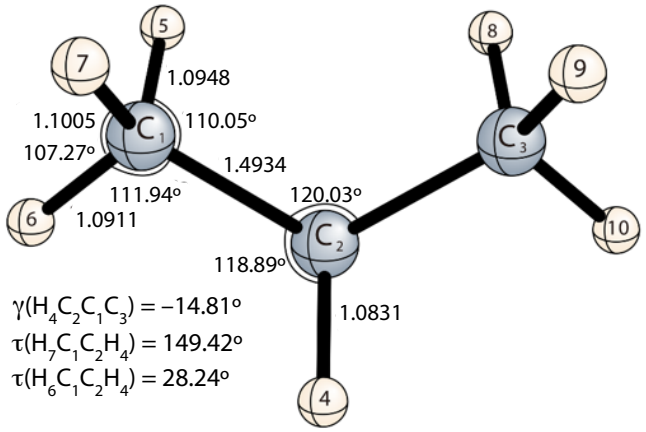

Figure 3.3 Optimum geometry of *i*-propyl radical (C_s) at ROCCSD(T)/cc-pVTZ level of theory. Bond lengths are in Å.

3.4.2 RO_2 FORMATION

Upon the initial abstraction reaction, the *i*-propyl + O_2 system undergoes a highly exothermic (–34.79 kcal mol^{-1}) barrierless combination reaction producing the *i*-propylperoxy (**MIN1**) radical. The **MIN1** species has only 2 energetically distinct rotamers produced by internal rotations about the C_2–O_4 bond: T (0.00 kcal mol^{-1}) and G$^-$ (0.26 kcal mol^{-1}). The relative energies of these species were determined at the CCSD(T)/cc-pVTZ//MP2/aug-cc-pVDZ level of theory. The B3LYP/6-311++G(d,p) **MIN1** structure (T) of Goldsmith et al.[33] displays a MAD of 0.01 Å for bond lengths and 1.49° for bond angles when compared to our structure. Notable differences of 1.73°, 2.84°, and 1.87° are present for α(C_2–O_4–O_5), τ(C_1–C_2–O_4–O_5), and τ(C_3–C_2–O_4–O_5), respectively. We also find that our CCSD(T) bond lengths and angles display MADs of 0.008 Å and 0.4° when comparing cc-pVDZ and cc-pVTZ structures. Wilke et al.[14] observed changes in the ethylperoxy radical of only 0.003 Å and 0.3° for CCSD(T) bond lengths and angles, respectively, when going from cc-pVTZ to the cc-pVQZ basis set. Thus, we can

assume only small changes for internal coordinates of **MIN1** upon optimization with the larger cc-pVQZ basis set.

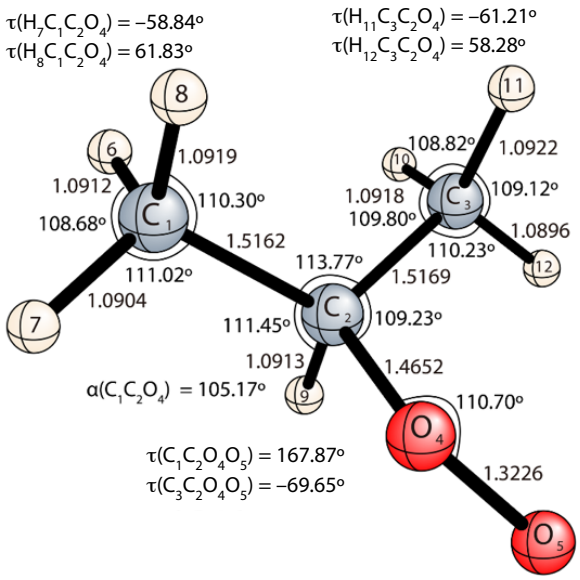

Figure 3.4 Optimum geometry of *i*-propylperoxy radical (**MIN1**) at ROCCSD(T)/cc-pVTZ level of theory. Bond lengths are in Å.

TABLE 3.3 Focal point analysis[a] (in kcal mol^{-1}) for **MIN1** relative to *i*-propyl + O_2.[a]

	ΔE_e(ROHF)	+δ [ZAPT2]	+δ [ROCCSD]	+δ [ROCCSD(T)]	+δ [ROCCSDT]	+δ [UCCSDT(Q)]	NET
6-31G*	–32.11	+8.52	–12.38	–0.75	–0.18	+0.34	–36.55
cc-pVDZ	–30.47	+9.90	–11.89	–0.71	–0.17	[+0.34]	[–33.00]
cc-pVTZ	–31.24	+6.54	–12.12	–1.07	[–0.17]	[+0.34]	[–37.72]
cc-pVQZ	–30.96	+5.38	–12.20	–1.21	[–0.17]	[+0.34]	[–38.82]
cc-pV5Z	–30.90	[+4.96]	[–12.23]	[–1.26]	[–0.17]	[+0.34]	[–39.26]
CBS	[–30.89]	[+4.53]	[–12.26]	[–1.31]	[–0.17]	[+0.34]	[–39.77]
FC-ROCCSD(T)/cc-pVTZ reference geometries							
$\Delta E_{final} = \Delta E_e$(FPA) + ΔZPVE (harm) + Δ(rel) + Δ(core) = –39.77 + 4.91 + 0.13 –0.06 = **–34.79 kcal mol^{-1}**							

[a]The symbol δ denotes the increment in the relative energy (ΔE) with respect to the preceding level of theory in the hierarchy HF→ZAPT2→ROCCSD→ROCCSD(T)→ROCCSDT→UCCSDT(Q). Square brackets signify results obtained from basis set extrapolations or additivity assumptions.

The focal point analysis for **MIN1** relative to the separated *i*-propyl + O_2 reactants is given in Table 3.3. We find that the relative energy $\Delta_{rxn} H_0^\circ$ of **MIN1** is –34.8 kcal mol^{-1} with respect to the separated reactants, which amounts to a larger binging energy by 2.1 kcal mol^{-1} compared to the analogous species in the *n*-propyl + O_2 system.[38] This effect can be rationalized by the stabilizing 1,4-pair correlation effects[96] between C–H bonds in the methyl groups of **MIN1**, which is reduced in the *n*-propylperoxy radical due to the positioning of the O_2 moiety. The Hartree-Fock limit gives a R–O_2 binding energy that is 8.9 kcal mol^{-1} smaller than ROCCSDT(Q)/CBS and larger than ZAPT2/CBS by 4.5 kcal mol^{-1}. These observations are consistent with observations from previous CBS work performed on both the ethylperoxy radical[14] and the *n*-propylperoxy radical.[38] The majority of the electron correlation effect is accounted for once δ[ROCCSD(T)] = –1.31 kcal mol^{-1} is included, as the higher order correlation contributions δ[ROCCSDT] = –0.17 kcal mol^{-1} and δ[ROCCSDT(Q)] = –0.34 kcal mol^{-1} largely cancel. Interestingly, the magnitude of this cancelation differs by only 0.01 kcal mol^{-1} compared to the same correlation increment difference of the *n*-propylperoxy radical.[38] Similar to the *n*-propylperoxy radical,[38] the FPA data suggests that the electron correlation contribution from δ[ROCCSDTQ] would be smaller than 0.3 kcal mol^{-1} and the difference between cc-pV5Z and cc-pVQZ for δ[ROCCSD(T)] would be smaller than 0.1 kcal mol^{-1}.

Our binding energy for **MIN1** is smaller than the original results of Desain et al.[24] by 1.77 kcal mol^{-1} and larger than their subsequent modifications by 0.23 kcal mol^{-1}.[13,30] The CBS/QB3 binding energy of Huynh et al.[32] is higher than our result by 1.2 kcal mol^{-1}, a discrepancy which is 0.9 kcal mol^{-1} smaller than that noted for the *n*-propylperoxy radical. The most recent binding energy (34.8 kcal mol^{-1}) reported by Goldsmith et al.,[33] at the QCISD(T)/CBS level of theory, is within 0.01 kcal mol^{-1} of our value for **MIN1**.

3.4.3 PATHWAYS LEADING FROM RO_2

Similar to the *n*-propyl + O_2 system, the concerted elimination reaction occurs through a 5-membered ring transition state (**TS1**, Figure 3.5) where the H_{12} atom transfers from C_3 to O_5. **TS1** is best viewed as a proton-transfer col with the unpaired electron in a orbital perpendicular to the ring, as shown in Figure 3.6. The singly occupied molecular orbital (SOMO) is localized on the O_2 moiety and is perpendicular to the 5-membered ring. Again similar to the analogous concerted elimination species of the *n*-propyl + O_2 reaction,[38] we observe via natural bond orbital analysis[97] (NBO) that 74% of the sin density of **TS1** is centered on O_4. This distribution of spin resembles that of free HO_2, which has 90% of its spin density on the terminal O atom. As the H_{12} species migrates from C_3 to O_5, the C_3–H_{12} bond distance increases by 0.2776 Å. During this proton transfer, the C_2–O_4 distance drastically increases by 0.6766 Å, while the C_2–C_3 distance decreases by 0.1244 Å. While the $\alpha(C_1–C_2–C_3)$ angle increases by 9.33° when going from **MIN1** to **TS1**, both the $\alpha(C_3–C_2–O_4)$ and $\alpha(C_2–O_4–O_5)$ angles decrease by 12.13° and 10.96°, respectively. The ring structure of **TS1** is nearly planar with $\tau(C_2–C_3–H_{12}–O_5) = 1.11°$ and $\tau(C_3–H_{12}–O_5–O_4) = 0.37°$. The B3LYP/6-311++G(d,p) **TS1** structure of Goldsmith et al.[33] displays a MAD of 0.03 Å for bond lengths and 1.1° for angles when compared to our structure. Notable discrepancies are observed for $r(C_2–O_4)$ and $\alpha(C_2–O_4–O_5)$ of 0.125 Å and 1.7°, respectively.

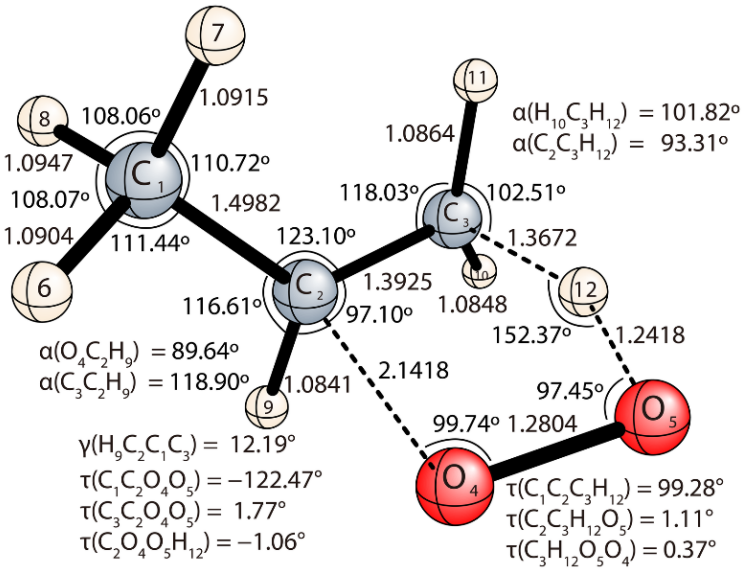

Figure 3.5 Optimum geometry of **TS1** at ROCCSD(T)/cc-pVTZ level of theory. Bond lengths are in Å.

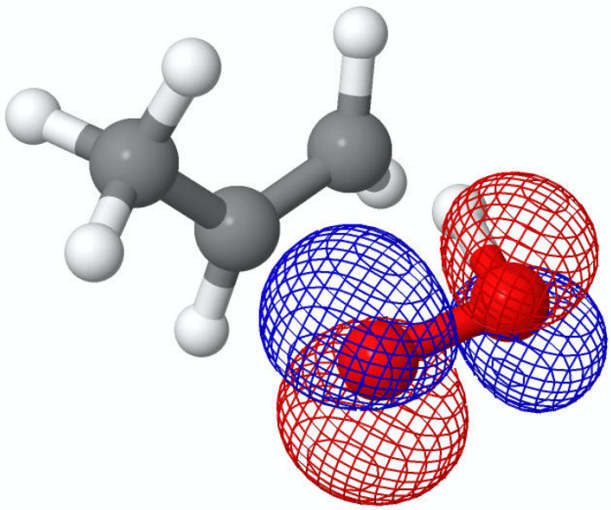

Figure 3.6 Depiction of singly occupied molecular orbital (SOMO) of **TS1**.

The direct elimination of HO_2 via transition state **TS1** was found to be the dominant fate of the RO_2 radical in previous work for both ethyl + O_2 and *n*-propyl + O_2.[14,38] Our concerted HO_2 elimination barrier (**TS1**) for *i*-propyl + O_2 is 4.42 kcal mol^{-1} *below* the reactants by FPA targeting the CCSDT(Q)/CBS level of theory, as compared to 3.0 kcal mol^{-1} in the ethyl + O_2 system[14] and 2.4 kcal mol^{-1} in the *n*-propyl + O_2 system.[38] While increasing the system size to larger alkyl radicals appears to slightly disfavor concerted elimination through **TS1** relative to other pathways, the trend of branched (*i*-propyl) vs. chained alkanes (*n*-propyl) shows that branching stabilizes **TS1**; however, this is more so a consequence of the stabilization of **MIN1** due to stabilizing 1,4-pair correlation effects.[96] Simply optimizing **TS1** at the ROCCSD(T)/cc-pVTZ level of theory places the barrier 1.93 kcal mol^{-1} below the reactants after correcting for zero-point energy. Extrapolating to the ROCCSD(T) basis set limit lowers the barrier of **TS1** by 2.0 kcal mol^{-1}. Both high-order correlation and basis set augmentation provide a continuing negative energy correction for **TS1**, as previously noted for both ethyl + O_2 and *n*-propyl + O_2,[14,38] which has been identified as the reason for systematic overestimation of the concerted elimination barrier. Our **TS1** barrier is higher in energy than that of Desain et al.[24] and subsequent modifications[13,30] by 2.58 kcal mol^{-1} and (0.28, 0.58) kcal mol^{-1}, respectively. The work of Goldsmith et al.[33] places **TS1** 4.2 kcal mol^{-1} below the reactants, which is 0.22 kcal mol^{-1} higher in energy than our result. This discrepancy is 0.08 kcal mol^{-1} smaller than the analogous comparison in the *n*-propyl + O_2 system. The CBS-QB3 method value of Huynh et al.[32] produces a $\Delta_{rxn} H_0^\circ$ value for **TS1** higher in energy than our result by 0.82 kcal mol^{-1}.

TABLE 3.4 Focal point analysis[a] (in kcal mol^{-1}) for the concerted elimination barrier (**TS1**) relative to *i*-propyl + O_2.[a]

	ΔE_e(ROHF)	$+\delta$ [ZAPT2]	$+\delta$ [ROCCSD]	$+\delta$ [ROCCSD(T)]	$+\delta$ [ROCCSDT]	$+\delta$ [UCCSDT(Q)]	NET
6-31G*	30.79	–18.87	–3.83	–4.68	–0.22	–0.43	+2.77
cc-pVDZ	28.14	–17.89	–3.78	–5.32	–0.06	[–0.43]	[+0.66]
cc-pVTZ	28.55	–22.91	–2.17	–6.45	[–0.06]	[–0.43]	[–3.47]
cc-pVQZ	28.69	–24.31	–1.77	–6.69	[–0.06]	[–0.43]	[–4.57]
cc-pV5Z	28.71	[–24.81]	[–1.63]	[–6.78]	[–0.06]	[–0.43]	[–4.99]
CBS	[28.71]	[–25.34]	[–1.48]	[–6.87]	[–0.06]	[–0.43]	[–5.47]
FC-ROCCSD(T)/cc-pVTZ reference geometries							
$\Delta E_{final} = \Delta E_e$(FPA) + ΔZPVE (harm) + Δ(rel) + Δ(core) = –5.47 + 0.98 + 0.07 + 0.00 = **–4.42 kcal mol^{-1}**							

[a] See footnote for Table 3.3.

The energy correction that accounts for electron correlation beyond ROCCSD(T) (δ[ROCCSDT] + δ[UCCSDT(Q)]) for **TS1** is –0.49 kcal mol^{-1}, which is 0.09 kcal mol^{-1} and 0.4 kcal mol^{-1} smaller in magnitude than the corresponding correction for **TS1** in the *n*-propyl + O_2 ethyl + O_2 reactions, respectively.[14,38] We note that both the lengthening of alkyl chains and chain branching serves to diminish this energy increment. The associated increment for the concerted elimination reaction of *t*-butyl + O_2 system is –0.40 kcal mol^{-1}, smaller in magnitude by 0.18 kcal mol^{-1} and only 0.09 kcal mol^{-1} than the corresponding **TS1** values of the *n*-propyl + O_2 and *i*-propyl + O_2 systems, respectively.[38]

TS1 exhibits a reaction mode frequency of 1312*i* cm^{-1} at the FC-ROCCSD(T)/Mixed-H(TZ,DZ) level of theory, in good agreement with the FC-ROCCSD(T)/Mixed-H(TZ,DZ) (1302*i* cm^{-1}) and FC-CCSD(T)/cc-pVTZ (1340*i* cm^{-1}) results for the *n*-propyl + O_2 and ethyl + O_2 systems, respectively.[14,38] Interestingly, our reaction mode frequency for **TS1** happens to be exactly the same as the FC-CCSD(T)/ANO0 result of Moore et al.[98] for the HO_2 elimination pathway of *t*-butyl + O_2. The CCSD(T) ΔZPVE(harm) correction to the **TS1** barrier changes by 0.46 kcal mol^{-1} when improving the basis set from cc-pVDZ to mixed-H(TZ,DZ).

The next possible fate of **MIN1** is to traverse the β-hydrogen transfer transition state (**TS2**, Figure 3.7) leading to **MIN2**. **TS2** involves a hydrogen transfer and occurs through a non-planar 5-membered ring. The distortion from ring planarity occurs because the SOMO (Figure 3.8) must be directed into the C_3–H_{12}–O_5 plane in order to effect the hydrogen transfer. **TS2** exhibits an unphysically large Δ_{DBOC} correction (1.09 kcal mol^{-1}), which is nonetheless 0.62 kcal mol^{-1} smaller than the corresponding value in the *n*-propyl + O_2 system. This large Δ_{DBOC} correction is an indication of a nearby surface crossing on the Born-Oppenheimer potential energy surface. These indications of possible nonadiabatic reaction dynamics have previously been reported for the ethyl + O_2,[14] *n*-propyl + O_2,[38] and *t*-butyl + O_2 systems.[98] The β-hydrogen transfer transition state of *t*-butyl + O_2 system[98] exhibits a Δ_{DBOC} correction of 0.4 kcal mol^{-1}, smaller than our value for **TS2** by 0.69 kcal mol^{-1}. While Δ_{DBOC} is usually a small correction ($\pm$0.02 kcal mol^{-1}) to the Born Oppenheimer potential energy surface, this is not the case in the vicinity of a conical intersection. Meek and Levine[99] show that E_{DBOC} is non-integrable over domains including a conical intersection because the second derivative of the $\hat{T}_n$ operator blows up at such points. They recommend that DBOC not be used when employing mixed quantum-classical methods and approximate quantum dynamical methods.[99]

Similar to **TS1**, the **TS2** structure displays a relatively short H_{12}–O_5 bond distance of 1.221 Å. The C_3–H_{12} bond increases by 0.25 Å when going from **MIN1** to **TS2**. The changes in $r(C_2$–$C_3)$ and $r(C_2$–$O_4)$ are less drastic than observed for **TS1**, increasing and decreasing by 0.01 Å and 0.03 Å, respectively. The $\alpha(C_1$–C_2–$C_3)$, $\alpha(C_3$–C_2–$O_4)$, and $\alpha(C_2$–O_4–$O_5)$ angles change by 1.85°, –6.24°, and –8.58°, respectively, when going from **MIN1** to **TS2**. The ring structure of **TS2** is highly non-planar with $\tau(C_3$–C_4–O_4–$O_5)$ = –45.40° and $\tau(C_2$–O_4–O_5–$H_{12})$ = 34.68°. The B3LYP/6-311++G(d,p) **TS2** structure of Goldsmith et al.[33] displays a MAD of 0.01 Å for bond

lengths and 0.7° for angles when compared to our structure. The *n*-propyl + O_2 system displayed two distinct conformers of the β-hydrogen transfer transition state which differ by the direction of puckering from ring planarity. Upon initial investigation, we were unable to optimize a structure corresponding to inverting the direction of ring puckering observed in **TS2** for the *i*-propyl + O_2 system; however, further investigation is warranted.

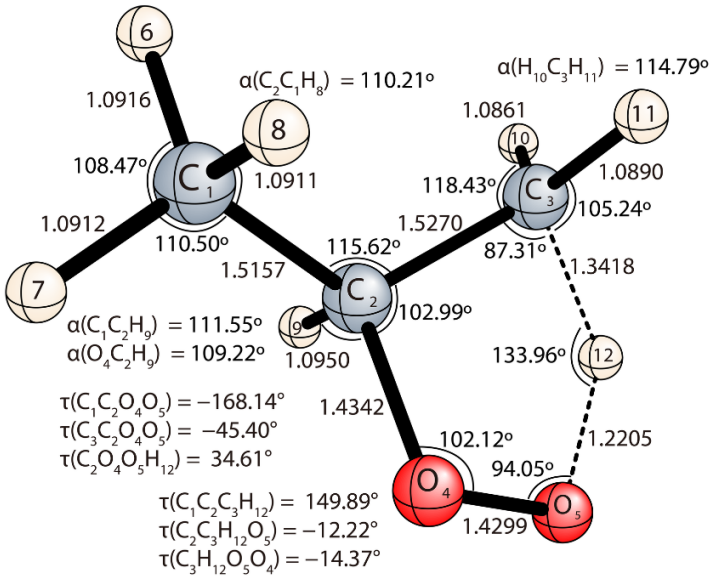

Figure 3.7 Optimum geometry of **TS2** at ROCCSD(T)/cc-pVTZ level of theory. Bond lengths are in Å.

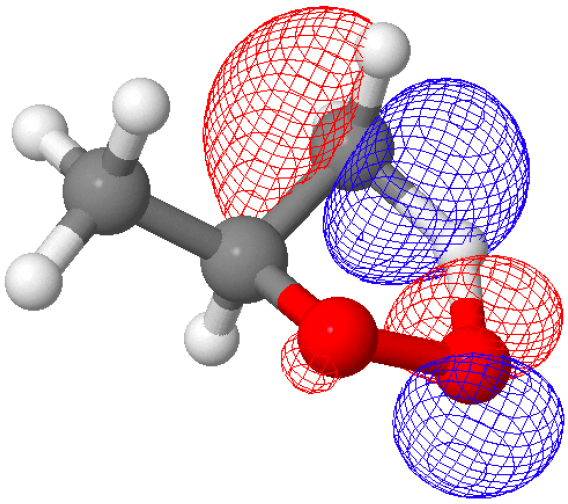

Figure 3.8 Depiction of singly occupied molecular orbital (SOMO) of **TS2**.

Our **TS2** structure lies 1.37 kcal mol^{-1} above the separated reactants. The focal point layout of **TS2** (Table 3.5) indicates that the cc-pV5Z basis set yields Hartree-Fock results within 0.02 kcal mol^{-1} of the CBS limit. For the +δ[ROCCSD(T)] correction, the difference between cc-pVTZ and cc-pVDZ basis sets is 1.0 kcal mol^{-1}, compared to a difference of only 0.25 kcal mol^{-1} between cc-pVQZ and cc-pVTZ. Much of the electron correlation is accounted for at the ROCCSD(T) level of theory (δ[ROCCSD(T)] = –4.59 kcal mol^{-1}), as the net δ[ROCCSDT] + δ[UCCSDT(Q)] correction for **TS2** is only –0.04 kcal mol^{-1}. This shift is smaller in magnitude by 0.45 kcal mol^{-1} when compared to the corresponding term for **TS1**. It is expected that the δ[ROCCSDTQ] contribution and the difference between cc-pVQZ and cc-pV5Z for δ[ROCCSD(T)] are both smaller than 0.1 kcal mol^{-1}. Our **TS2** barrier is higher in energy than that of Desain et al.[24] and subsequent modifications[13,30] by 2.77 kcal mol^{-1} and (1.57, 3.07) kcal mol^{-1}, respectively. The CBS-QB3 level of theory produces a value varying from our result by 0.12 kcal mol^{-1}.[32] The work of Goldsmith et al.[33] places **TS2** 1.2 kcal mol^{-1} above the reactants, which is 0.17 kcal mol^{-1} lower

in energy than our result. **TS2** exhibits a hydrogen-transfer reaction-mode frequency of 2445*i* cm^{-1}, which is larger than the analogous value for the *β*-hydrogen transfer transition state of the *n*-propyl + O_2 system by 246 cm^{-1}. There is a change of +0.19 kcal mol^{-1} for ΔZPVE (harm) when using our mixed-H(TZ,DZ) basis set over cc-pVDZ; this change is smaller by 0.53 kcal mol^{-1} when compared to the same change in the *n*-propyl + O_2 system.

TABLE 3.5 Focal point analysis[a] (in kcal mol^{-1}) for the *β*-hydrogen transfer barrier (**TS2**) relative to *i*-propyl + O_2.[a]

	ΔE_e(ROHF)	+*δ* [ZAPT2]	+*δ* [ROCCSD]	+*δ* [ROCCSD(T)]	+*δ* [ROCCSDT]	+*δ* [UCCSDT(Q)]	NET
6-31G*	33.386	–19.263	–2.228	–2.765	–0.060	–0.032	9.037
cc-pVDZ	32.175	–17.850	–2.371	–3.159	–0.007	[–0.032]	[8.756]
cc-pVTZ	31.049	–23.686	–0.706	–4.157	[–0.007]	[–0.032]	[2.460]
cc-pVQZ	31.325	–25.434	–0.203	–4.406	[–0.007]	[–0.032]	[1.243]
cc-pV5Z	31.347	[–26.057]	[–0.024]	[–4.494]	[–0.007]	[–0.032]	[0.733]
CBS LIMIT	[31.331]	[–26.710]	[0.164]	[–4.587]	[–0.007]	[–0.032]	[0.159]

FC-ROCCSD(T)/cc-pVTZ reference geometries

$\Delta E_{final} = \Delta E_e$(FPA) + ΔZPVE (harm) + Δ(rel) + Δ(core) = 0.16 +1.00 + 0.13 + 0.08 = **1.37 kcal mol^{-1}**

[a] See footnote for Table 3.3.

3.4.4 QOOH SPECIES

Other than the concerted elimination of HO_2 transition state **TS1**, the only other transition state (**TS2**) leading from **MIN1** produces a QOOH species. These QOOH species are distinguished by the location of the carbon radical center. There is only one possible QOOH species (**MIN2**, Figure 3.9) in the *i*-propyl + O_2 system produced via *β*-hydrogen transfer, because abstraction from either methyl group in **MIN1** produces the same product. However, three **MIN2** rotamers were identified at the FC–ROCCSD(T)/cc–pVTZ//MP2/aug-cc-pVDZ level of theory, all lying within the (0, 0.91) kcal mol^{-1} window. These rotamers are TA^+ (0.00 kcal mol^{-1}),

TA^- (0.58 kcal mol^{-1}), and G^-A^+ (0.91 kcal mol^{-1}). The **MIN2** structure of Goldsmith et al.[33] is the only other available geometry in the literature and exhibits a rotamer label of TA^+. Our FPA computations (Table 3.1) place the lowest-energy rotamer of **MIN2** below the reactants by 17.44 kcal mol^{-1}. The QCISD(T)/CBS work of Goldsmith et al.[33] places **MIN2** below our converged FPA result by 0.56 kcal mol^{-1}.

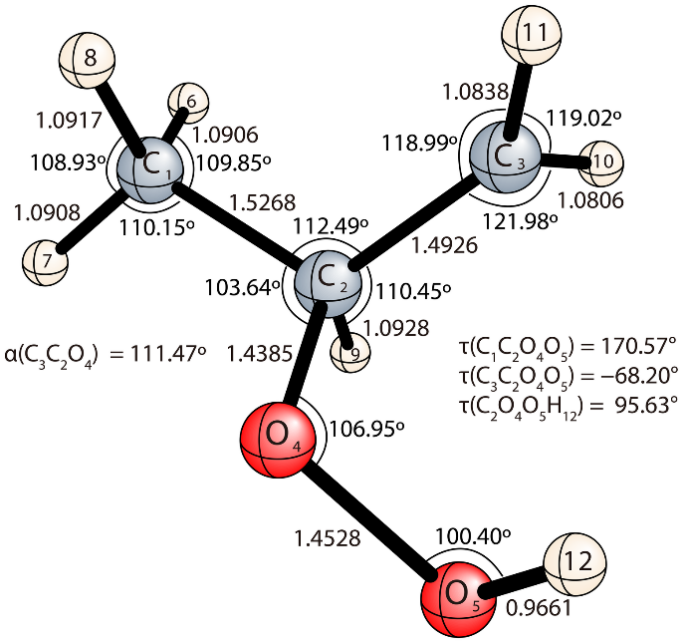

Figure 3.9 Optimum geometry of **MIN2** (TA^+) at ROCCSD(T)/cc-pVTZ level of theory. Bond lengths are in Å.

3.4.5 PATHWAYS LEADING FROM QOOH

Two possible fragmentation pathways (Figure 3.2) were investigated that originate from **MIN2**: C_2–O_4 bond cleavage and HO_2 elimination (**TS3**, Figure 3.10) and C_3 – O_4 bond formation and OH elimination (**TS4**, Figure 3.11). There is a limited amount of previous information on these two transition states in the literature with only two studies[24,33] supplying energies and one study supplying geometries.[33] Similar to the *n*-propyl + O_2 system,[38] major discrepancies are

observed, mainly involving dihedral angles, between our fragmentation structures (**TS3–TS4**) and those found in the literature. While the B3LYP/6-311++G(d,p) **TS3** structure of Goldsmith et al.[33] displays a MAD of only 0.005 Å for bond lengths, it exhibits large MADs of 1.6° and 66.5° for bond and torsion angles, respectively, when compared to our structure. The largest discrepancy of 189.3° is observed for $\tau(C_2–O_4–O_5–H_{12})$ because the H_{12} atom is pointed in an opposite direction. Similarly, the **TS4** structure of Goldsmith et al.[33] displays a MAD of 0.009 Å for bond lengths and (1.8°, 9.1°) for (bond, torsion) angles. Again, the largest discrepancy (21.3°) is noted for $\tau(C_2–O_4–O_5–H_{12})$. Once **TS2** is passed, both **TS3** and **TS4**, lying well below the reactants, provide no further hindrance to direct product formation from *i*-propyl + O_2. As shown in Figure 3.2, the chain propagating pathway through **TS4** is the most favorable ($\Delta_{rxn} H_0^\circ$ = –5.59 kcal mol^{-1}) leading out of **MIN2**, lying 4.07 kcal mol^{-1} below the chain terminating pathway through **TS3**.

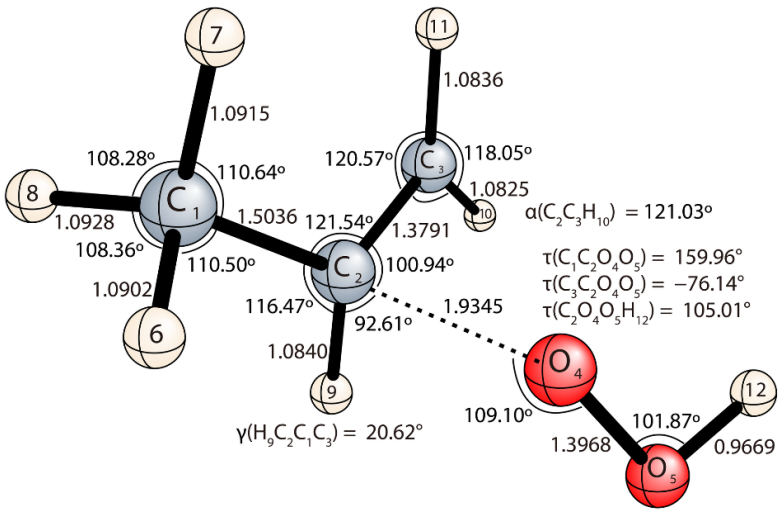

Figure 3.10 Optimum geometry of **TS3** at ROCCSD(T)/cc-pVTZ level of theory. Bond lengths are in Å.

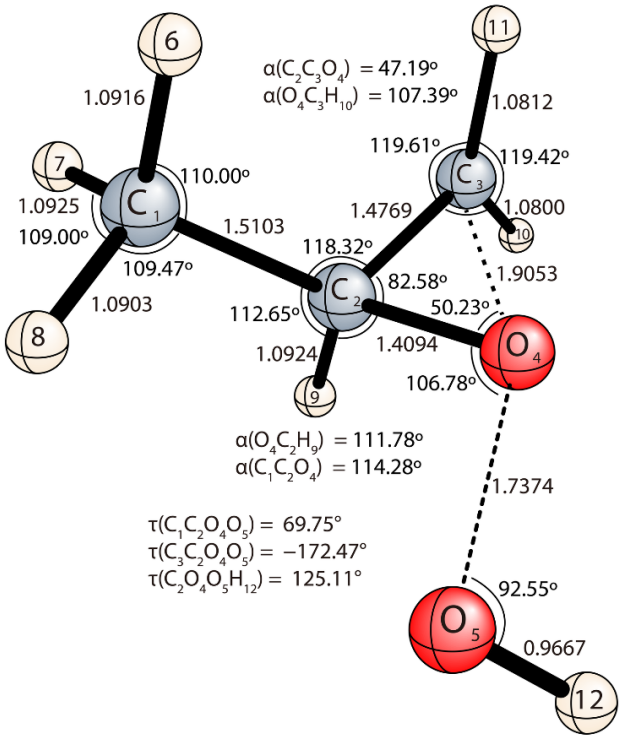

Figure 3.11 Optimum geometry of **TS4** at ROCCSD(T)/cc-pVTZ level of theory. Bond lengths are in Å.

One must also consider the pathway leading to acetone + OH from a QOOH (**MIN3**) species produced via internal α-hydrogen transfer within **MIN1**. While our study currently lacks structures and energetics of both a transition state leading to **MIN3** from **MIN1**, as well as **MIN3** itself, the analogous transition state observed in the *n*-propyl + O_2 system[38] was calculated to be 9.04 kcal mol^{-1} above the separated reactants. Attempts were also made to obtain a transition state leading to propanal + OH from **MIN4** of the *n*-propyl + O_2 system without success.[38] Two distinct solutions for the electronic wave function were found in the region of this transition state, suggesting that a conical intersection may be very nearby. The barrier from **MIN4** to propanal + OH was estimated to be about 10 kcal mol^{-1} below the separated reactants. We can speculate that the analogous transition state in the *i*-propyl + O_2 system would exhibit similar troubles; however,

further investigation is warranted. Nonetheless, the conlusion should remain that the production of OH at low temperatures is largely a product of **MIN1** → **TS2** → **MIN2** → **TS4** → methyloxirane + OH.

The experimental model of Huang et al.,[30] assuming that methyloxirane + OH was the dominant source of OH, overpredicted the measured methyloxirane yield. At 670 K, Welz and co-workers[36] observed that methyloxirane was the major C_3H_6O isomer product; however, at temperatures ranging between 530 to 600 K propanal was produced in comparable amounts. Their experiment produced a substantially lower yield of methyloxirane than given by the earlier study,[30] and they suggest the existence of another significant OH channel. Welz et al.[36] find that the sum concentration of acetone, propanal, and oxetane is comparable to that of methyloxirane. However, as previously stated, large barriers must be surmounted in order to produce these species.[38]

While the propanal found by Welz et al.[36] can be attributed to the *n*-propyl + O_2 reaction, the observed acetone is due to the constitutional isomer *i*-propyl reacting with O_2. A transition state from **MIN1** leading directly to acetone + OH that is 5.5 kcal mol^{-1} above the separated reactants has been reported;[33] however, no molecular geometry was supplied. This process would entail a concerted reaction involving a simultaneous 1,2-H shift and C–O bond cleavage/OH elimination. Such saddle points have been reported,[32] but they were found to be prohibitively high. In an attempt to rationalize their experimental yields of acetone, Welz et al.[36] suggest that the previously reported[33] barrier height of 5.5 kcal mol^{-1} would need to be lowered by 3.8 kcal mol^{-1}.

3.5 CONCLUSIONS

The essential features of the *i*-propyl + O_2 reaction system were explored utilizing focal point analyses (FPA) to obtain *ab initio* energetics that push the boundaries of accuracy for combustion systems. FPA energetics were obtained with electron correlation treatments through CCSDT(Q) and with basis sets up to cc-pV5Z. The primary minimum (**MIN1**) and the most favorable pathway transition state (**TS1**) were found to lie 34.8 kcal mol^{-1} and 4.4 kcal mol^{-1}, respectively, below the reactants. Fully optimized CCSD(T)/cc-pVTZ geometries were compared to the large number of DFT structures in the literature for stationary points on the *i*-propyl + O_2 potential energy surface. Substantial mean absolute deviations were observed for both bond lengths and angles in some cases, demonstrating the necessity of highly correlated methods for geometry optimizations of combustion chemistry species. Accurate ZPVE corrections, which are crucial for definitive energetics, were determined utilizing our newly developed mixed Hessian approach. The effect of TZ quality basis sets for ZPVE corrections is nonetheless smaller for the *i*-propyl + O_2 system than was observed for *n*-propyl + O_2, with cc-pVDZ ΔZPVE(harm) values displaying a MAD of only 0.31 kcal mol^{-1} when compared to utilizing cc-pVTZ mixed Hessian values. **TS2** exhibits an anomalously large DBOC correction, which is indicative of a nearby conical intersection. This is further demonstration that the DBOC correction can be utilized as a diagnostic for the presence of nearby conical intersections and possible nonadiabatic reaction dynamics on potential energy surfaces.

While the chain-terminating, concerted elimination of HO_2 pathway predominates in the *n*-propyl + O_2 system with **TS1** lying at –2.4 kcal mol^{-1}, this pathway is less favorable when compared to ethyl + O_2, whose corresponding barrier is 0.6 kcal mol^{-1} lower.[14] However, chain

branching stabilizes **TS1** in the *i*-propyl + O_2 system, thus making it more favorable compared to ethyl + O_2.[14] The most energetically favorable OH producing pathway begins with a **MIN1** → **MIN2** isomerization over **TS2** followed by O–O bond scission and ring closure over **TS4** to yield methyloxirane + OH. It is important to extend high-level computational studies to the *n*-butyl + O_2 system to understand the prototypical behavior of autoignition chemistry. We hypothesize that the pathway through the 7-membered ring hydrogen-transfer transition state to the δ-QOOH species followed by a 6-membered ring transition to oxacyclopentane + OH is more favorable in the *n*-butyl + O_2 system than the associated concerted elimination of HO_2.

3.6 SUPPLEMENTARY MATERIAL

The Supplementary Material for this chapter is provided in Appendix A.

3.7 ACKNOWLEDGEMENTS

This work was supported by The Department of Energy, Office of Basic Sciences, Computational and Theoretical Chemistry Grant DE-SC0015512. The high-level *ab initio* computations utilized resources of the National Energy Research Scientific Computing Center, a DOE office of Science User Facility supported by the Office of Sciences of the U.S. Department of Energy under grant No. DE-AC02-05CH11231.

3.8 REFERENCES

(1) Zádor, J.; Taatjes, C. A.; Fernandes, R. X., *Prog. Energy Combust. Sci.* **2011**, *37*, 371-421.

(2) Dec, J. E., *Proc. Combust. Inst.* **2009**, *32*, 2727-2742.

(3) Taatjes, C. A., *J. Phys. Chem. A* **2006**, *110*, 4299-4312.

(4) Savee, J. D.; Papajak, E.; Rotavera, B.; Huang, H.; Eskola, A. J.; Welz, O.; Sheps, L.; Taatjes, C. A.; Zádor, J.; Osborn, D. L., *Science* **2015**, *347*, 643-646.

(5) Baldwin, R. R.; Dean, C. E.; Walker, R. W., *J. Chem. Soc., Faraday Trans. 2.* **1986**, *82*, 1445-1455.

(6) Gulati, S. K.; Walker, R. W., *J. Chem. Soc., Faraday Trans. 2.* **1988**, *84*, 401-407.

(7) Baldwin, R. R.; Stout, D. R.; Walker, R. W., *J. Chem. Soc., Faraday Trans.* **1991**, *87*, 2147-2150.

(8) Quelch, G. E.; Gallo, M. M.; Schaefer, H. F., *J. Am. Chem. Soc* **1992**, *114*, 8239-8247.

(9) Quelch, G. E.; Gallo, M. M.; Shen, M.; Xie, Y.; Schaefer, H. F.; Moncrieff, D., *J. Am. Chem. Soc* **1994**, *116*, 4953-4962.

(10) Ignatyev, I. S.; Xie, Y.; Allen, W. D.; Schaefer, H. F., *J. Chem. Phys.* **1997**, *107*, 141-155.

(11) Rienstra-Kiracofe, J. C.; Allen, W. D.; Schaefer, H. F., *J. Phys. Chem. A* **2000**, *104*, 9823-9840.

(12) Miller, J. A.; Klippenstein, S. J., *Int. J. Chem. Kinet.* **2001**, *33*, 654-668.

(13) DeSain, J. D.; Klippenstein, S. J.; Miller, J. A.; Taatjes, C. A., *J. Phys. Chem. A* **2003**, *107*, 4415-4427.

(14) Wilke, J. J.; Allen, W. D.; Schaefer, H. F., *J. Chem. Phys.* **2008**, *128*, 074308.

(15) Knox, J. H., *Trans. Faraday Soc.* **1959**, *55*, 1362-1374.

(16) Knox, J. H., *Trans. Faraday Soc.* **1960**, *56*, 1225-1234.

(17) Knox, J. H., *Chem. Commun. (London).* **1965**, 108-109.

(18) Baker, R. R.; Baldwin, R. R.; Walker, R. W., *Trans. Faraday Soc.* **1970**, *66*, 3016-3031.

(19) Slagle, I. R.; Park, J.-Y.; Gutman, D., *Proc Combust Inst.* **1985**, *20*, 733-741.

(20) Slagle, I. R.; Ratajczak, E.; Heaven, M. C.; Gutman, D.; Wagner, A. F., *J. Am. Chem. Soc* **1985**, *107*, 1838-1845.

(21) Kaiser, E. W.; Wallington, T. J., *J. Phys. Chem.* **1996**, *100*, 18770-18774.

(22) Kaiser, E. W., *J. Phys. Chem. A* **1998**, *102*, 5903-5906.

(23) DeSain, J. D.; Clifford, E. P.; Taatjes, C. A., *J. Phys. Chem. A* **2001**, *105*, 3205-3213.

(24) DeSain, J. D.; Taatjes, C. A.; Miller, J. A.; Klippenstein, S. J.; Hahn, D. K., *Faraday Discuss.* **2002**, *119*, 101-120.

(25) Wijaya, C. D.; Sumathi, R.; Green, W. H., *J. Phys. Chem. A* **2003**, *107*, 4908-4920.

(26) Green, W. H.; Wijaya, C. D.; Yelvington, P. E.; Sumathi, R., *Mol. Phys.* **2004**, *102*, 371-380.

(27) Merle, J. K.; Hayes, C. J.; Zalyubovsky, S. J.; Glover, B. G.; Miller, T. A.; Hadad, C. M., *J. Phys. Chem. A* **2005**, *109*, 3637-3646.

(28) Estupiñán, E. G.; Klippenstein, S. J.; Taatjes, C. A., *J. Phys. Chem. B* **2005**, *109*, 8374-8387.

(29) Estupiñán, E. G.; Smith, J. D.; Tezaki, A.; Klippenstein, S. J.; Taatjes, C. A., *J. Phys. Chem. A* **2007**, *111*, 4015-4030.

(30) Huang, H.; Merthe, D. J.; Zádor, J.; Jusinski, L. E.; Taatjes, C. A., *Proc. Combust. Inst.* **2011**, *33*, 293-299.

(31) Miyoshi, A., *J. Phys. Chem. A* **2011**, *115*, 3301-3325.

(32) Huynh, L. K.; Carstensen, H.-H.; Dean, A. M., *J. Phys. Chem. A* **2010**, *114*, 6594-6607.

(33) Goldsmith, C. F.; Green, W. H.; Klippenstein, S. J., *J. Phys. Chem. A* **2012**, *116*, 3325-3346.

(34) Cord, M., et al., *J. Phys. Chem. A* **2012**, *116*, 12214-12228.

(35) Goldsmith, C. F.; Tomlin, A. S.; Klippenstein, S. J., *Proc. Combust. Inst.* **2013**, *34*, 177-185.

(36) Welz, O.; Burke, M. P.; Antonov, I. O.; Goldsmith, C. F.; Savee, J. D.; Osborn, D. L.; Taatjes, C. A.; Klippenstein, S. J.; Sheps, L., *J. Phys. Chem. A* **2015**, *119*, 7116-7129.

(37) Burke, M. P., et al., *J. Phys. Chem. A* **2015**, *119*, 7095-7115.

(38) Bartlett, M. A.; Liang, T.; Pu, L.; Schaefer, H. F.; Allen, W. D., *J. Chem. Phys.* **2018**, *148*, 094303.

(39) Wilk, R. D.; Cohen, R. S.; Cernansky, N. P., *Ind. Eng. Chem. Res.* **1995**, *34*, 2285-2297.

(40) Chen, C.-J.; Bozzelli, J. W., *J. Phys. Chem. A* **1999**, *103*, 9731-9769.

(41) Strelkova, M. I.; Safonov, A. A.; Sukhanov, L. P.; Umanskiy, S. Y.; Kirillov, I. A.; Potapkin, B. V.; Pasman, H. J.; Tentner, A. M., *Combust. Flame* **2010**, *157*, 641-652.

(42) Zhang, F.; Dibble, T. S., *Phys. Chem. Chem. Phys* **2011**, *13*, 17969-17977.

(43) Cord, M.; Sirjean, B.; Fournet, R.; Tomlin, A.; Ruiz-Lopez, M.; Battin-Leclerc, F., *J. Phys. Chem. A* **2012**, *116*, 6142-6158.

(44) Eskola, A. J.; Welz, O.; Savee, J. D.; Osborn, D. L.; Taatjes, C. A., *J. Phys. Chem. A* **2013**, *117*, 12216-12235.

(45) Prince, J. C.; Treviño, C.; Williams, F. A., *Combust. Flame* **2017**, *175*, 27-33.

(46) Wang, S.; Miller, D. L.; Cernansky, N. P.; Curran, H. J.; Pitz, W. J.; Westbrook, C. K., *Combust. Flame* **1999**, *118*, 415-430.

(47) DeSain, J. D.; Klippenstein, S. J.; Taatjes, C. A., *Phys. Chem. Chem. Phys* **2003**, *5*, 1584-1592.

(48) Petway, S. V.; Ismail, H.; Green, W. H.; Estupiñán, E. G.; Jusinski, L. E.; Taatjes, C. A., *J. Phys. Chem. A* **2007**, *111*, 3891-3900.

(49) DeSain, J. D.; Taatjes, C. A., *J. Phys. Chem. A* **2001**, *105*, 6646-6654.

(50) Fernandes, R. X.; Zador, J.; Jusinski, L. E.; Miller, J. A.; Taatjes, C. A., *Phys. Chem. Chem. Phys* **2009**, *11*, 1320-1327.

(51) Knepp, A. M.; Meloni, G.; Jusinski, L. E.; Taatjes, C. A.; Cavallotti, C.; Klippenstein, S. J., *Phys. Chem. Chem. Phys* **2007**, *9*, 4315-4331.

(52) Roothaan, C. C. J., *Rev. Mod. Phys.* **1951**, *23*, 69-89.

(53) Roothaan, C. C. J., *Rev. Mod. Phys.* **1960**, *32*, 179-185.

(54) Pople, J. A.; Nesbet, R. K., *J. Chem. Phys.* **1954**, *22*, 571-572.

(55) Møller, C.; Plesset, M. S., *Phys. Rev.* **1934**, *46*, 618.

(56) Lee, T. J.; Jayatilaka, D., *Chem. Phys. Lett.* **1993**, *201*, 1.

(57) Čížek, J., *J. Chem. Phys.* **1966**, *45*, 4256-4266.

(58) Crawford, T. D.; Schaefer, H. F., An Introduction to Coupled Cluster Theory for Computational Chemists. In *Rev. Comput. Chem*, Lipkowitz, K. B.; Boyd, D. B., Eds. John Wiley & Sons, Inc.: New Jersey, 2000; Vol. 14, pp 33-136.

(59) Purvis, G. D.; Bartlett, R. J., *J. Chem. Phys.* **1982**, *76*, 1910-1918.

(60) Raghavachari, K.; Trucks, G. W.; Pople, J. A.; Head-Gordon, M., *Chem. Phys. Lett.* **1989**, *157*, 479-483.

(61) Noga, J.; Bartlett, R. J., *J. Chem. Phys.* **1987**, *86*, 7041-7050.

(62) Bomble, Y. J.; Stanton, J. F.; Kállay, M.; Gauss, J., *J. Chem. Phys.* **2005**, *123*, 054101.

(63) Dunning, T. H., Jr., *J. Chem. Phys.* **1989**, *90*, 1007-1023.

(64) Peterson, K. A.; Woon, D. E.; Dunning, T. H., Jr., *J. Chem. Phys.* **1994**, *100*, 7410-7415.

(65) Woon, D. E.; Dunning, T. H., *J. Chem. Phys.* **1995**, *103*, 4572-4585.

(66) Kendall, R. A.; Dunning, T. H., Jr.; Harrison, R. J., *J. Chem. Phys.* **1992**, *96*, 6796-6806.

(67) Hariharan, P. C.; Pople, J. A., *Theor Chim Acta* **1973**, *28*, 213-222.

(68) East, A. L. L.; Allen, W. D., *J. Chem. Phys.* **1993**, *99*, 4638-4650.

(69) Császár, A. G.; Allen, W. D.; Schaefer III, H. F., *J. Chem. Phys.* **1998**, *108*, 9751-9764.

(70) Császár, A. G.; Tarczay, G.; Leininger, M. L.; Polyansky, O. L.; Tennyson, J.; Allen, W. D., In *Spectroscopy from Space*, J. Demaison, K. S., Ed. Kluwer: Dordrecht: The Netherlands, 2001; pp 317-339.

(71) Gonzales, J. M.; Allen, W. D.; Schaefer III, H. F., *J. Phys. Chem. A* **2005**, *109*, 10613-10628.

(72) Werner, H.-J., et al. *Molpro, Version 2010.1, a Package of Ab Initio Programs Written By*, 2010.

(73) *CFOUR,* a quantum chemical program package written by J.F. Stanton, J. Gauss, M.E. Harding, P.G. Szalay with contributions from A.A. Auer, R.J. Bartlett, U. Benedikt, C. Berger, D.E. Bernholdt, Y.J. Bomble, L. Cheng, O. Christiansen, M. Heckert, O. Heun, C. Huber, T.-C. Jagau, D. Jonsson, J. Jusélius, K. Klein, W.J. Lauderdale, F. Lipparini, D.A. Matthews, T. Metzroth, L.A. Mück, D.P. O'Neill, D.R. Price, E. Prochnow, C. Puzzarini, K. Ruud, F. Schiffmann, W. Schwalbach, C. Simmons, S. Stopkowicz, A. Tajti, J. Vázquez, F. Wang, J.D. Watts and the integral packages *MOLECULE* (J. Almlöf and P.R. Taylor), *PROPS* (P.R. Taylor), *ABACUS* (T. Helgaker, H.J. Aa. Jensen, P. Jørgensen, and J. Olsen), and *ECP* routines by A. V. Mitin and C. van Wüllen. For the current version, see *http://www.cfour.de*.

(74) Crawford, T. D., et al., *J. Comput. Chem.* **2007**, *28*, 1610-1616.

(75) Schmidt, M. W., et al., *J. Comput. Chem.* **1993**, *14*, 1347-1363.

(76) Gordon, M. S.; Schmidt, M. W., Advances in Electronic Structure Theory: Gamess a Decade Later. In *Theory and Applications of Computational Chemistry: The First Forty Years*, Frenking, G.; Kim, K. S.; Scuseria, G. E., Eds. Elsevier: Amsterdam, 2005; pp 1167-1189.

(77) Janssen, C. L.; Nielsen, I. B.; Leininger, M. L.; Valeev, E. F.; Kenny, J. P.; Seidl, E. T. *The Massively Parallel Quantum Chemistry Program (MPQC) Written By* Version 2.3.1; Sandia National Laboratories: Livermore, CA, 2008.

(78) Kállay, M., et al. *MRCC, a Quantum Chemical Program Suite*, *J. Chem. Phys.* **139**, 094105 (2013).

(79) Eliel, E. L.; Wilen, S. H., *Stereochemistry of Organic Compounds*; John Wiley & Sons: New York, 1993.

(80) Dobrowolski, J. C.; Rode, J. E.; Sadlej, J., *Comput. Theor. Chem* **2007**, *810*, 129-134.

(81) Wilke, J. J.; Lind, M. C.; Schaefer, H. F.; Császár, A. G.; Allen, W. D., *J. Chem. Theory Comput.* **2009**, *5*, 1511-1523.

(82) He, K.; Allen, W. D., *J. Chem. Theory Comput.* **2016**, *12*, 3571-3582.

(83) Feller, D., *J. Chem. Phys.* **1992**, *96*, 6104-6114.

(84) Helgaker, T.; Klopper, W.; Koch, H.; Noga, J., *J. Chem. Phys.* **1997**, *106*, 9639-9646.

(85) Perera, A. S.; Bartlett, R. J., *Chem. Phys. Lett.* **1993**, *216*, 606-612.

(86) Handy, N. C.; Yamaguchi, Y.; Schaefer III, H. F., *J. Chem. Phys.* **1986**, *84*, 4481-4484.

(87) Jayatilaka, D.; Lee, T. J., *J. Chem. Phys.* **1993**, *98*, 9734.

(88) Lee, T. J.; Taylor, P. R., *Int. J. Quantum Chem.* **1989**, *36*, 199-207.

(89) Lauderdale, W. J.; Stanton, J. F.; Gauss, J.; Watts, J. D.; Bartlett, R. J., *Chem. Phys. Lett.* **1991**, *187*, 21-28.

(90) Lauderdale, W. J.; Stanton, J. F.; Gauss, J.; Watts, J. D.; Bartlett, R. J., *J. Chem. Phys.* **1992**, *97*, 6606-6620.

(91) Urban, M.; Watts, J. D.; Bartlett, R. J., *Int. J. Quantum Chem.* **1994**, *52*, 211-225.

(92) Huber, K. P.; Herzberg, G., In *Molecular Spectra and Molecular Structure. IV. Constants of Diatomic Molecules*, Springer, Ed. Van Noestrand Reinhold: New York, 1979; pp 498-508.

(93) Lubic, K. G.; Amano, T.; Uehara, H.; Kawaguchi, K.; Hirota, E., *J. Chem. Phys.* **1984**, *81*, 4826-4831.

(94) Lide, D. R.; Christensen, D., *J. Chem. Phys.* **1961**, *35*, 1374-1378.

(95) Creswell, R. A.; Schwendeman, R. H., *J. Mol. Spectrosc.* **1977**, *64*, 295-301.

(96) McKee, W. C.; Schleyer, P. v. R., *J. Am. Chem. Soc* **2013**, *135*, 13008-13014.

(97) Weinhold, F., *J. Comput. Chem.* **2012**, *33*, 2363-2379.

(98) Moore III, K. B.; Turney, J. M.; Schaefer III, H. F., *J. Chem. Phys.* **2017**, *146*, 194304.

(99) Meek, G. A.; Levine, B. G., *J. Chem. Phys.* **2016**, *144*, 184109.

CHAPTER 4

RIDDLES OF THE STRUCTURE AND VIBRATIONAL DYNAMICS OF HO_3 RESOLVED NEAR THE AB INITIO LIMIT[†]

[†]Bartlett, M.A.; Kazez, A.H.; Agarwal, J.; Schaefer, H. F.; Allen, W.D. To be submitted for publication

4.1 ABSTRACT

The hydridotrioxygen (HO_3) radical has been probed in numerous gas-phase spectroscopy experiments, in part because it was thought to have a role in the tropospheric HO_x cycle. Moreover, HO_3 has been the subject of a vast amount of computational research over the past 50 years, which has served to highlight the difficult and unusual molecular structure and energetics of this molecule. For example, the central O–O bond length in HO_3 has been a highly vexing parameter for quantum mechanical methods, with reported values ranging all the way from 1.34 to 1.75 Å! We have solved the riddles of HO_3 using convergent coupled-cluster methods extended all the way to CCSDTQ(P) and with basis sets up to cc-pV6Z. The dissociation energy (D_0) of *trans*-HO_3 into O_2 and OH was found to be 2.71 kcal mol^{-1}, smaller by experiment by only 0.23 kcal mol^{-1}. Likewise, the *cis*-*trans* energy separation (ΔE_0^{tc}) and barrier height (ΔE_0^{b}) of isomerization were found to be 0.52 kcal mol^{-1} and 0.27 kcal mol^{-1}, respectively, giving the most accurate results to date. We report a new semiexperimental equilibrium structure of *trans*-HO_3 utilizing FPA-Q2 vibration-rotation interaction constants in conjunction with existing microwave rotational constants. A systematic analysis of fitting procedures was performed in which 96 possibilities were scrutinized. We find that the molecular structure is most sensitive to ZPV effects from the HOO bending mode, and not the torsional mode as previously proposed. Our FPA-Q2 quartic force field (QFF) produces combination bands in excellent agreement with experiment. VPT2 has been shown to be well behaved for this system for both vibrational frequencies and molecular structure, which is counter to previous understandings. Lastly, our results give conclusive evidence that the reason that *cis*-HO_3 has been missed by all previous experimental studies is because it converts to *trans*-HO_3 within a few picoseconds by quantum mechanical tunneling, even under cryogenic conditions.

4.2 INTRODUCTION

The hydridotrioxygen (HO_3) radical has been studied extensively[1-8] because of its possible relevance as an intermediate in the tropospheric HO_x cycle and as a potential sink of OH radicals. Evidence for the existence of a loosely bound HO_3 species comes from studies of atmospheric reactions R1–R3.

$$O + HO_2 \rightarrow OH + O_2 \quad \text{(R1)}$$

$$O_3 + H \rightarrow OH\ (v \leq 9) + O_2 \quad \text{(R2)}$$

$$O_2 + OH(v) \rightarrow OH(v-1) + O_2 \quad \text{(R3)}$$

$$O_2 + OH \rightleftharpoons HO_3 \quad \text{(R4)}$$

When ^{18}O isotopical labelling is utilized in R1, the products are $H^{16}O + {}^{18}O^{16}O$, proving that the reaction occurs via a transitory $H^{16}O^{16}O^{18}O$ species rather than by direct hydrogen abstraction.[1] The O_3 + H reaction (R2) is highly exothermic ($\Delta_{rxn} H^{\circ}_{298}$ = –323.5 kcal mol^{-1}) and produces vibrationally excited OH radicals, which are the source of the observed Meinel bands in the upper atmosphere.[2-3] Much of the OH excitation is distributed in the highest accessible vibrational levels v = 7 – 9. Klenerman and Smith[3] note that the potential energy surface of R2 would be highly attractive if HO_3 were weakly bound relative to the OH + O_2 asymptote. The rate constant for (R3) is larger than expected if normal repulsive forces were the cause of vibrational relaxation, and McCabe et al.[4] speculated that a weak O_2–OH bond was responsible for this phenomenon. However, these studies regarding R1 – R3 do not provide direct structural or energetic evidence for the existence of HO_3.

Whether or not HO_3 acts as a sink of OH radicals greatly depends on the dissociation energy (D_0) of HO_3 with respect to OH + O_2. The first experimental estimate of the enthalpy of formation of HO_3 came from an FT-ICR study by Speranza[5] in 1996 that measured the efficiency of electron

transfer to HO_3^+ from various electron donors. The resulting $\Delta_f H^\circ$ value gave an estimate of 10 ± 5 kcal mol^{-1} for the dissociation energy D_0. In 2007 Lester and co-workers[6] ascertained an improved upper limit for the dissociation energy ($D_0 \leq 5.31$ kcal mol^{-1}) by using infrared (IR) action spectroscopy to determine the OH product distribution following dissociation of vibrationally excited HO_3 radicals. If D_0 were equal to this limiting value, calculations[7] of the equilibrium constant of R4 show that up to 25% of atmospheric OH radicals would be bound as HO_3 radicals. However, a significantly smaller $D_0 = 2.94 \pm 0.1$ kcal mol^{-1} was measured in 2010 by observing laser-induced fluorescence of OH radicals in the presence of O_2 at temperatures between 55.7 and 110.8 K.[8] With this revised dissociation energy, the calculated fraction of atmospheric OH bound to O_2 is less than 0.1%, showing that HO_3 does not act as a sink for OH radicals.[8] Nonetheless, the first direct experimental detection of HO_3 in 1999, based on neutralization-reionization mass spectrometric techniques applied to an HO_3^+ precursor, revealed that the lifetime of HO_3 exceeds microseconds at ambient temperatures.[9] Low-temperature kinetic experiments in 2010 found that the dissociation rate for (R4) starts to exceed the association rate above 90 K.[10]

In 2000, the generation of HO_3 in Ar matrices by several different reactions was reported,[11] and the first vibrational assignments were proposed for this molecule: ν_1(OH stretch) = 3361 cm^{-1}, ν_3(HOO bend) = 1223 cm^{-1}, and ν_4(OOO bend) = 566 cm^{-1}. A few years later, $\nu_3 = 1259$ cm^{-1} was assigned from experiments that irradiated $H_2O + O_2$ ice mixtures with either 0.8 MeV protons[12] or 5 keV electrons.[13] The series of papers in 2007 and 2008 by Lester and co-workers[6-7,14-16] probed the dissociation dynamics of both HO_3 and DO_3 by IR action spectroscopy in the gas phase and assigned the ν_1(OH/OD) stretching fundamentals as well as several combination and overtone bands. They deduced $\nu_3 = 998$ cm^{-1}, $\nu_4 = 482$ cm^{-1},

ν_5(central OO stretch) = 244 cm^{-1}, and ν_6(HO_3 torsion) = 129 cm^{-1} from their combination bands and observed ν_1 = 3569.3 cm^{-1} directly, all of which brought into question and showed large discrepancies with the previously reported condensed-phase frequencies.[11-13] They also attributed broad, rotationally unstructured peaks observed in their IR spectra to *cis*-HO_3.[15] Douberly and co-workers[17-19] performed several He nanodroplet experiments on HO_3 and recorded IR spectra in the 3500 – 3700 cm^{-1} region; they assigned ν_1 = 3569.46 cm^{-1} and $\nu_1 + \nu_6$ = 3699.10 cm^{-1},[18] in full accord with the gas-phase results of Lester and co-workers.[15] No evidence was found for *cis*-HO_3 in the He nanodroplets, but IR signatures were observed for HO_3–$(O_2)_n$ clusters as large as n = 4.[17] Stark spectra of *trans*-HO_3 solvated in superfluid He yielded the inertial dipole moment components of the molecule, which are sensitive measures of its structure.[19]

A series of microwave spectroscopy experiments[20-23] extending from 2005 to 2017 measured rotational constants for the HO_3, $H^{18}OOO$, $HO^{18}OO$, $HOO^{18}O$, $HO^{18}O^{18}O$, $H^{18}O^{18}O^{18}O$, DO_3, $D^{18}OOO$, $DO^{18}O^{18}O$, and $D^{18}O^{18}O^{18}O$ isotopologues. All of the observed pure rotational lines were attributed to *trans*-HO_3, and no evidence of *cis*-HO_3 was found in the microwave spectra, despite extensive searching. Extracting an r_0 structure proved problematic, as unphysical O–H [$r_0(H_1–O_2)$] and terminal O–O [$r_0(O_3–O_4)$] bond lengths result from unconstrained fits. The microwave r_0 structure of Suma et al.,[20] displaying a long central O–O bond length [$r_0(O_2–O_3)$] of 1.688 Å, was ascertained by fixing the O–H and terminal O–O bond lengths to multireference configuration interaction (MRCI+Q) *ab-initio* values. Subsequent unconstrained r_0 structures of McCarthy and co-workers[21,23] consistently exhibited central O–O distances near 1.68 Å, but with concomitant unphysical O–H distances in the vicinity of 0.90–0.91 Å. The anomalous $r_0(H_1–O_2)$ bond length has been attributed to the floppy torsional mode of HO_3, which produces large deviations from planarity. The average torsional deviation from planarity has been estimated as

22°,[23] and the vibrationally averaged projection of the O–H distance onto the O–O–O plane has been computed to be 0.90 Å.[19]

The semiexperimental r_e structure of McCarthy et al.,[21] produced by applying CCSD(T)/aug-cc-pVQZ vibrational corrections to microwave rotational constants, exhibits $r_e(O_2–O_3)$ = 1.660 Å and a dubious $r_e(H_1–O_2)$ of 0.944 Å. In 2013 Suma et al.[24] revisited the r_e structure utilizing vibrational corrections at the MRCI+Q/AVQZ level of theory paired with rotational constants from previous experiments. They ascertained $r_e(O_2–O_3)$ = 1.665 Å and $r_e(O_2–H_1)$ = 0.961 Å, in much better agreement with the distance in free OH. The large differences between r_e and r_0 for the central $O_2–O_3$ distance were attributed to strong coupling between this mode and the H–O–O bending and terminal O–O stretching modes. Nonetheless, the most recent microwave studies[23] on HO_3 isotopologues show that the structural puzzles regarding the O–H and central O–O bonds are still unresolved.

While both the *cis* and *trans* conformers of HO_3 are accessible potential energy minima, the *cis* conformer has been apparently absent in most experiments and only possibly present with poorly defined features in others. The absence of *cis*-HO_3 signatures in both FTMW gas-phase spectroscopy[20-21] and IR spectroscopy in helium nanodroplets[17] would not be in contradiction with the unstructured peaks attributed to *cis*-HO_3 in IR action spectroscopy[15] if the lifetime of this conformer is shorter than the timescale of the former experiments but longer than the timescale of the latter. Alternatively, the IR action spectroscopy bands assigned to *cis*-HO_3 may correspond to different species altogether, such as $HO_3–(O_2)_n$ clusters.[18] One possible reason for the fleeting existence of *cis*-HO_3 is rapid hydrogen tunneling to the lower-energy *trans* conformer.[16-17] A definitive *ab initio* computation of a very short hydrogen tunneling half-life would help resolve the enigma of the *cis* conformer.

Table 4.1. Previous theoretical results for problematic relative energies (kcal mol^{-1}) and the central O–O distance (Å) of HO_3.

Level of Theory	Ref.	Year	$r_e(O_2–O_3)$	D_e (D_0)[a]	$\Delta E_e^{tc}(\Delta E_0^{tc})$[a]	$\Delta E_e^{b}(\Delta E_0^{b})$[a]
RHF/4-31G	25	1973	1.44	—	—	—
CASSCF/[5s4p1d/3s1p]	26	1984	1.40	—	−0.6	—
MCSCF/DZP	27	1985	1.472	+13.8	—	—
QCISD(T)/6-31G**	28	1995	1.506	—	+0.6	—
G2M(RCC) //B3LYP/6-311+G(3df,2p)	29	1996	1.543	+1.3	−0.7	(+0.7)[b]
UCISD/6-311G++(d,p)	30	1997	1.429	−5.6	+0.1	−1.0
CCSD(T)/6-311+G(3df,3pd) //B3LYP/6-311+G(3df,3pd)	31	1999	1.543	—	−0.7	—
MRMP2/cc-pVTZ //CASSCF/cc-pVTZ	32	2000	1.75	+3.9(+2.7)	+0.8(+0.9)	—
QCISD(T)/CBS(2,3)	33	2001	1.495	+5.3	−1.2	—
CCSD(T)/CBS(3,4)	34	2002	1.477	—	—	—
CCSD(T)/6-311++(2df,2p) //B3LYP/6-311++(2df,2p)	35	2006	1.544	—	+0.3	+0.3
MRCI+Q/6-311++(2df,2p) //MRCI/6-311+G(d,p)	36	2007	1.647	+5.4(+1.4)	—	—
CASSCF(7,7)/6-311+G(2df,2p)	36	2007	1.459	—	—	—
CASSCF(19,15)/6-311+G(2df,2p)	36	2007	1.758	—	—	—
CCSD(T)/CBS(3,4)	37	2008	1.582	—	—	—
HCTH/aug-cc-pVTZ	38	2008	1.610	+9.9(+6.2)	+1.1	+2.4
CCSD(T)/CBS(4,5) //CCSD(T)/cc-pVQZ	39	2009	1.584	+3.5(+0.7)	+0.2(−0.1)	—
CCSDT(Q)/CBS(4,5) //CCSD(T)/cc-pVQZ	39	2009	1.584	+5.2(+2.5)	—	—

CASPT2(19,15)/aug-cc-pVTZ	40	2010	1.682	+5.8(+3.0)	—	—
MRCI+Q/CBS(5,6)	41	2011	1.668	+4.6(+2.3)	—	—
EOMIP-CCSD*/ANO1	42	2011	1.62	—	+0.1	+0.7
MRCI+Q/CBS(5,6) //MRCI/cc-pVTZ	43	2011	1.695	—	+0.1(+0.5)	+1.0[c]
MRCI+Q/CBS(5,6) //CAS(19,13)/aug-cc-pVQZ	44	2012	1.648	+4.7(+2.7)	+0.1	—
MRCI-F12/cc-pVQZ-F12 //MRCI+Q/aug-cc-pV6Z	45	2013	1.668	+4.7	—	—
2RDM(M)/aug-cc-pVQZ //2RDM(M)/aug-cc-pVTZ	46	2013	1.619	—	+0.4(+1.8)	+1.6(+0.2)
MRCI+Q/CBS(5,6) //MRCI+Q/aug-cc-pV5Z	24	2013	1.655	+4.5(+1.8)	—	—
CCSDT(Q)/CBS(4,5) //CCSDT(Q)/CBS(4,5)	19	2013	1.649	+5.8(+2.8)	—	—
FPA-P//FPA-Q3	This work[d]	2019	1.670	+5.5(+2.7)	+0.4 (+0.5)	+0.8(+0.3)

[a] D_e is the energy for dissociation of *trans*-HO_3 to OH + O_2; ΔE_e^{tc} is the *trans* → *cis* isomerization energy; and ΔE_e^{b} is the energy difference between the torsional transition state and *cis* minimum. ZPVE-corrected values for these quantities are given in parentheses. [b] B3LYP/6-311+G(3df,2p) energetics [c] MRCI+Q/cc-pVTZ energetics. [d] See Tables 4.5, 4.6, 4.7, and 4.8.

For 45 years HO_3 has been the subject of a vast amount of computational research, as summarized in Table 4.1.[19,21,24-46] The molecular structure and energetics are highly sensitive to both basis set and electron correlation treatment. Multireference correlated wave functions have often been deemed necessary for reliable predictions. Early quantum chemical studies reported disparate lowest energy conformers (*gauche*,[27] *cis*,[29] and *trans*[32]). After much work the general conclusion is now that the HO_3 potential energy surface exhibits both *cis* and *trans* conformers, with *trans* being very slightly lower than *cis*.[47] Based on MRCI+Q/CBS(5,6)//MRCI+Q/cc-pVTZ single points, the $\Delta E_e^{tc}(\Delta E_0^{tc})$ *cis–trans* energy difference has been predicted to be 0.12 ± 0.05

(0.51 ± 0.08) kcal mol^{-1}.[41,43,47] In contrast, the CCSD(T)/aug-cc-pVQZ level of theory places the *cis* conformer lower in energy (ΔE_e^{tc} = −0.12 kcal mol^{-1}).[43]

The central O–O bond length [r_e(O_2–O_3)] in HO_3 has been a highly vexing parameter for *ab initio* methods, with reported values ranging all the way from 1.34 to 1.75 Å (Table 4.1)! Single-reference correlated methods and density functional theory consistently give r_e values that are much too small. Notably, CCSD(T)/CBS computations[37] yield r_e = 1.582 Å, which is shorter than the experimental r_0 value by 0.1 Å.[23] CASSCF methods are not immune to such difficulties, as r_e is very sensitive to choice of active space and limited wave functions can even give a nonplanar equilibrium structure.[27,32] For example, CASSCF(7,7)/6-311+G(2df,2p) predicts[36] r_e = 1.459 Å and an H_1–O_2–O_3–O_4 dihedral angle [τ_e($H_1O_2O_3O_4$)] of 91.0°, while CASSCF(19,15) with the same basis set produces[36] r_e = 1.758 Å and a *trans* equilibrium structure. The incorporation of dynamical electron correlation via multireference CASPT2 and MRCI methodologies greatly improves predicted r_e(O_2–O_3) values.[24,40] Suma and co-workers[24] found r_e(O_2–O_3) = 1.655 Å at the MRCI+Q/aug-cc-pV5Z level of theory, within 0.01 Å of the semiexperimental r_e distance they extracted from microwave rotational constants. Nonetheless, multireference wave functions are not necessary to accurately predict the structural parameters of HO_3 *if* coupled cluster theory is employed through quadruple excitations. In particular, a CCSDT(Q)/CBS study has given r_e(O_2–O_3) = 1.649 Å, a value supported by Stark effect measurements of the dipole moment of *trans*-HO_3.[19]

The energy profiles for the dissociation and isomerization of HO_3 have also been staunch challenges for electronic structure theory. Predicted D_e(HO–O_2) values in the literature range from −5.4 kcal mol^{-1} to +13.8 kcal mol^{-1}. A barrier on the dissociation path is present at the CASSCF,[26,40] EOMIP-CCSD*,[39] QCISD(T)/CBS(2,3),[33] and CCSD(T)-CBS (W1U) [48] levels of

theory but is absent at CASPT2,[40] MRCI/CBS(Q,5),[44] MRCI/CBS(5,6),[41] and MRCI+Q.[45] The most recent theoretical values of D_0 tend to fall within the 1–3 kcal mol^{-1} window,[40] with the exception of the HCTH result[38] of D_0 = 6.2 kcal mol^{-1}. Dissociation energies[19,39] of D_0 = 2.5 and 2.84 kcal mol^{-1} have been found at the CCSDT(Q)/CBS//CCSD(T)/cc-pVQZ and CCSDT(Q)/CBS(4,5)//CCSDT(Q)/CBS(4,5) levels of theory, the latter[19] being within 0.1 kcal mol^{-1} of experiment.[8] A key observation in these studies was that CCSDT(Q) corrections for quadruple excitations were more than half as large as D_0 itself. The *cis–trans* isomerization barrier is also a sensitive parameter to level of theory, with vibrationless values ranging from –0.8 to +2.4 kcal mol^{-1}. The bare isomerization barrier is placed at 1.0 kcal mol^{-1} above *cis*-HO_3 at the MRCI/CBS(5,6) level of theory, the most accurate computation to date.[43]

The theoretical prediction of the vibrational spectrum of HO_3 is complicated by the presence of multiple low-frequency, large amplitude modes. Prior to 2006 only harmonic vibrational frequencies were reported in the literature, and these were computed merely at the B3LYP level with various basis sets.[29,31,48-49] Harmonic frequencies have since been computed utilizing CCSD,[46] CCSD(T),[43,46] RCCSD(T)-F12,[45] 2-RDM(M),[46] CR-CC(T),[46] RS2,[45] MRCI,[43-45] MRCI+Q,[45] and MR-AQCC.[45] Anharmonic vibrational frequencies at the B3LYP/cc-pVTZ level of theory, reported without giving computational details,[15,48] display errors as large as 210 cm^{-1} in comparison to the experimental fundamental frequencies deduced by Lester and co-workers.[15] In 2013 an MRCI+Q/aug-cc-pVQZ fitted quartic force field was computed[24] and used with second-order vibrational perturbation theory (VPT2) to obtain fundamental frequencies with errors less than 19 cm^{-1} compared to experiment. In addition, an anharmonic ZPVE correction to the dissociation energy has been computed by applying VPT2 to a

CCSD(T)/ANO1 force field.[39] Nonetheless, concerns have been raised over the appropriateness of employing VPT2 for such a floppy molecule as HO_3.[39]

The possibility of *cis–trans* isomerization of HO_3 via hydrogen tunneling has been considered in a few theoretical studies.[24,38,42] Suma et al.[24] dismissed the possibility of rapid conformational tunneling based on the lack of splitting of vibrational levels computed on a one-dimensional MRCI+Q/aug-cc-pVQZ torsional potential. In contrast, Braams and Yu[38] estimated a conformational tunneling half-life on the order of nanoseconds based on their multidimensional potential energy surface constructed from HCTH/aug-cc-pVTZ energy points. A key to resolving this issue is to obtain a converged *ab initio* barrier and torsional energy profile for HO_3.

We aim to establish the problematic parameters of HO_3 utilizing high level single-reference coupled cluster theory. Both the relative energetics and the $r_e(O_2–O_3)$ value are highly sensitive to level of theory, requiring the inclusion of pentuple and quadruple excitations, respectively. Fundamental, overtone, and combination bands for both *cis*- and *trans*-HO_3 were computed utilizing VPT2 theory in conjunction with a high-level single-reference coupled cluster QFF. We also obtain exact torsional energy levels and wave functions using the Cooley-Numerov method[50-51] on a highly-accurate one-dimensional torsional potential. Lastly, in order to shed light on the mystery surrounding the existence of *cis*-HO_3, we perform a tunneling analysis utilizing both an exact scattering methodology, as well as WKB theory. Previous work by Allen and co-workers[52-56] has very successfully used a similar approach to analyze the rates of chemical reactions exhibiting tunneling behavior in numerous experiments.

4.3 THEORETICAL METHODS

4.3.1 GENERAL SCHEME

A panoply of methods was utilized to obtain electronic wave functions in this study: restricted open-shell (ROHF)[57] and unrestricted (UHF)[58] Hartree-Fock theory; second-order Møller-Plesset (MP2)[59] perturbation theory; and coupled cluster (CC)[60-61] theory incorporating single and double excitations (CCSD),[62] perturbative connected triple excitations [CCSD(T)],[63] full triple excitations (CCSDT),[64] perturbative quadruple excitations [CCSDT(Q)],[65] full quadruple excitations (CCSDTQ),[66] and perturbative pentuple excitations [CCSDTQ(P)].[67,68] These methods were applied with the correlation-consistent (cc) basis sets cc-pV*X*Z (X = D, T, Q, 5, 6)[69-70] and cc-pCVQZ.[71] Definitive relative energies were computed by extrapolation to full correlation and complete basis set (CBS) limits utilizing the focal-point analysis (FPA) pioneered by Allen and co-workers.[72-74] The correlation methods employed a spin orbital formalism into which either ROHF or UHF orbitals were employed, as signified by an RO or U prefix.

4.3.2 GEOMETRY OPTIMIZATION

Extrapolations of the Hartree-Fock[75] (E_{HF}) and ROMP2, ROCCSD, and ROCCSD(T) correlation energies[76] (ε) employed the equations:

$$E_{\mathrm{HF}}(X) = E_{\mathrm{HF}}^{\infty} + A\exp(-bX) \tag{4.1}$$

$$\varepsilon(X) = \varepsilon^{\infty} + \frac{B}{X^3} \tag{4.2}$$

where X is the cardinal number of the adopted correlation consistent cc-pV*X*Z basis set family. Three FPA methods denoted as FPA-Q2, FPA-Q3, and FPA-P were employed. For FPA-Q2 the Hartree-Fock extrapolations used X = {3, 4, 5}, while those for ROMP2, ROCCSD, and

ROCCSD(T) correlation energies used X = {4, 5}. FPA-Q3 and FPA-P both extrapolate Hartree-Fock utilizing X = {4, 5, 6} and ROMP2, ROCCSD, and ROCCSD(T) with X = {5, 6}. The FPA schemes invoked the following additive basis-set corrections for higher-order correlation:

$$\delta[\text{UCCSDT}] = \Delta E(\text{UCCSDT/cc-pV}X\text{Z}) - \Delta E(\text{ROCCSD(T)/cc-pV}X\text{Z}) \quad (4.3)$$

$$\delta[\text{UCCSDT(Q)}] = \Delta E(\text{UCCSDT(Q)/cc-pV}X\text{Z}) - \Delta E(\text{UCCSDT/cc-pV}X\text{Z}) \quad (4.4)$$

where X = D and T in the FPA-Q2 and FPA-Q3 cases, respectively, ΔE and δ refer to the relative energies and relative energy increments with respect to antecedent levels of electron correlation, respectively. The FPA-P scheme is an extension of FPA-Q3 with the inclusion of full quadruple excitations and a perturbative treatment of pentuple excitations:

$$\delta[\text{UCCSDTQ}] = \Delta E(\text{UCCSDTQ/cc-pVDZ}) - \Delta E(\text{UCCSDT(Q)/cc-pVDZ}) \quad (4.5)$$

$$\delta[\text{UCCSDTQ(P)}] = \Delta E(\text{UCCSDTQ(P)/cc-pVDZ}) - \Delta E(\text{UCCSDTQ/cc-pVDZ}) \quad (4.6)$$

The UCCSDT, UCCSDT(Q), UCCSDTQ, and UCCSDTQ(P) correlation energies were computed using Kállay's MRCC program,[77] while all other results were obtained with MOLPRO 2012.1.[78]

Core electron correlation effects were accounted for by subtracting all-electron (AE) and frozen-core (FC) ROCCSD(T) energies computed with the cc-pCVQZ basis set:

$$\Delta(\text{core}) = \Delta E_{\text{e}}(\text{AE-ROCCSD(T)/cc-pCVQZ}) - \Delta E_{\text{e}}(\text{FC-ROCCSD(T)/cc-pCVQZ}) \quad (4.7)$$

For stationary points a first-order relativistic term,[79] Δ(rel), and the diagonal Born-Oppenheimer correction, Δ(DBOC),[80] were computed at the ROCCSD(T)/cc-pVTZ and ROHF/aug-cc-pVTZ levels of theory, respectively. The core correlation corrections were computed with the MOLPRO 2012.1 package, while the relativistic and DBOC computations were performed with the CFOUR package.[81] The final vibrationless focal point energy estimating UCCSDTQ(P) relative energies at

the CBS limit was found by summing up extrapolation results, additive corrections, and auxiliary corrections to give:

$$\Delta E_{\mathrm{FP}} = E_{\mathrm{HF}}^{\infty} + \delta^{\infty}[\mathrm{ROCCSD(T)}] + \delta[\mathrm{UCCSDT}] + \delta[\mathrm{UCCSDT(Q)}] + \delta[\mathrm{UCCSDTQ}] + \delta[\mathrm{UCCSDTQ(P)}] + \Delta(\mathrm{core}) + \Delta(\mathrm{rel}) + \Delta(\mathrm{DBOC}) \quad (4.8)$$

4.3.3 GEOMETRY OPTIMIZATION AND VIBRATIONAL FREQUENCY COMPUTATIONS

A distinguished reaction path (DRP)[82-83] was generated for the *cis*-HO_3 → *trans*-HO_3 isomerization reaction by a series of constrained optimizations at the FPA-Q2 level of theory in which the torsional angle $\tau(H_1O_2O_3O_4)$ was fixed in increments of 10° between 0° and 180°. For this purpose numerical gradients were computed in internal coordinates by utilizing a 3-point finite difference formula. For each displacement FPA-Q2 energies were computed. All geometry optimizations were carried out until the RMS force was converged to 10^{-7} E_h/a_0. To test the accuracy of the 3-point numerical gradient, we also performed geometry optimizations for the $\tau(H_1O_2O_3O_4)$ = 30°, 50°, and 130° structures utilizing a 5-point gradient. No significant differences in optimum geometries were observed, with bond lengths and angles in agreement to 0.0001 Å and 0.001°, respectively. The *cis*-HO_3, *trans*-HO_3, and **TSct** stationary points were further optimized at the FPA-Q3 level of theory, with relative energies computed at the FPA-P level of theory. Optimized geometries in Cartesian coordinates, along with internal coordinate depictions of structures, and single-point energies along the DRP can be found in supplementary Table B.1 and B.2, respectively.

Harmonic vibrational frequencies and zero-point vibrational energy corrections, $\Delta\mathrm{ZPVE(harm)}$, of all points along the torsional potential energy curve were computed at the FPA-Q2 level utilizing a 3-point finite difference formula and displacing along the internal coordinates. Each frequency computation required 43 FPA-Q2 displacements. A DRP projected frequency analysis[83] was utilized to evaluate the harmonic vibrational frequencies and $\Delta\mathrm{ZPVE(harm)}$ for each value of $\tau(H_1O_2O_3O_4)$. The energy points and kinetic energy matrix elements along the DRP were fit to a Fourier series in terms of the torsional reaction coordinate. Subsequently, the Cooley-Numerov method[50-51] was utilized to obtain the exact vibrational energies and wave functions of this torsional potential.

Full internal coordinate quartic force fields (QFF) for *cis*-HO_3 and *trans*-HO_3 were computed by accurate finite difference methods via FPA-Q2 energy computations on a grid of 263 points. The displacements from the reference structure involved step sizes of 0.01 Å for bond stretches, 0.02 rad for bond angles, and 0.04 rad for the torsional coordinate.[84] A nonlinear coordinate transformation of the force constants from internal coordinates to normal coordinates was performed using the INTDER program,[85-88] after which second-order vibrational perturbation theory (VPT2)[89,90] was utilized in the computation of spectroscopic constants and fundamental vibrational frequencies.

Semiexperimental ground-state rotational constants (A_e^{semi}, B_e^{semi}, C_e^{semi}), were obtained by correcting experimental rotational constants (A_0^{exp} , B_0^{exp}, C_0^{exp}) with the first-order vibration-rotation interaction constants (α_i).[91] The α_i interaction constants require the quadratic force constants in normal coordinates, derivatives of the inertia tensor with respect to the normal coordinates, the Coriolis matrices for the three principal axes, and the diagonal (ϕ_{iii}) and semidiagonal (ϕ_{ijj}) cubic force constants. Semiexperimental equilibrium structures (r_e) of *trans*-

HO_3 were then found by a least-squares fitting of the inertial moments of up to 10 isotopologues (HO_3, $H^{18}OOO$, $HO^{18}OO$, $HOO^{18}O$, $HO^{18}O^{18}O$, $H^{18}O^{18}O^{18}O$, DO_3, $D^{18}OOO$, $DO^{18}O^{18}O$, $D^{18}O^{18}O^{18}O$). Systematic variations in the details of the least-squares fit were investigated: different combinations of rotational constants and isotopologues; fitting directly to rotational constants (RC) vs. inertial moments (IM); and alteration of the weights in the least-squares sum as powers ($n = 0$, 1, or 2) of the corresponding reciprocal experimental uncertainties. The substitution structure (r_s) of *trans*-HO_3 was also determined via the Kraitchman equations.[92-93] The r_0, r_e, and r_s structures were all obtained with the MolStruct molecular structure refinement program.[77]

4.3.4 QUANTUM MECHANICAL TUNNELING

Quantum mechanical tunneling computations for *cis-trans* isomerization were undertaken on the generated DRP in terms of the arc length in mass-weighted Cartesian coordinates. The tunneling probability (κ) for a collision of the reactant with the barrier was computed by an exact scattering method[54] involving numerical integration of the Schrödinger equation and confirmed within the WKB semiclassical formalism.[94] Tunneling rate constants were found by multiplying the tunneling probabilities with the barrier collision frequency (ω_6) of the torsional reaction-mode and including a degeneracy factor of 2 for clockwise and counterclockwise torsional vibrations. The energy (ε) of the barrier collisions was equated to the reaction-mode ZPVE ($\omega_6/2$). This approach has proved very effective for computing tunneling rates in numerous recent studies[52-56] and apparently balances out higher-level reaction path curvature (corner cutting) and multidimensional mode coupling effects.

4.4 RESULTS AND DISCUSSION

4.4.1 MULTIREFERENCE CHARACTER

The long central O_2–O_3 bond raises the question of multireference electronic character in HO_3. Large UHF spin contamination and a T_1 diagnostic (mistakenly) deemed to be very high have been noted by Denis et al.[34,95] The multireference question in HO_3 was also addressed by Varner et al.[39] via comparisons with the isoelectronic FO_2 radical, whose dissociation energy is recovered well by CCSDT(Q)/CBS computations.[96] Their diagnostics indicate that *trans*-HO_3 has less multireference character than FO_2, and they concluded that higher-order single-reference coupled cluster theory provides a sufficient treatment of electron correlation in HO_3.

In Table 4.2, the T_1 diagnostic[97,98] and $T_{2,\max}$ amplitudes are given for the minima and transition state (**TSct**) on the *cis*-HO_3 → *trans*-HO_3 isomerization pathway, as well as OH and O_2. Closed-shell species exhibiting substantial multireference character usually have $T_1 > 0.02$, while open-shell species have a less defined threshold.[98] The CN radical is included here as a benchmark because it is well described at the CCSD(T) level of theory despite exhibiting large UHF spin contamination.[99-101] All HO_3 structures exhibit T_1 diagnostics near 0.04, smaller than CN and within the range of values for transition states of the *n*-propyl + O_2 reaction network described well by high-order single-reference coupled cluster methods.[102] The $T_{2,\max}$ of *cis*-HO_3 (0.10) is comparable to that of O_2 (0.10) and CN (0.09), while the corresponding values for *trans*-HO_3 (0.16) and **TS** (0.15) are noticeably larger. Nonetheless, these larger $T_{2,\max}$ values do not indicate excessive multireference character.

To further analyze the electronic structure of HO_3, we computed a full valence CASSCF(19,13)/cc-pVTZ wave function at the FPA-Q3 geometry. The resulting configuration

interaction (CI) coefficients based on CASSCF natural orbitals show that *cis*-HO_3, *trans*-HO_3, and **TSct** are all dominated by a single Slater determinant. The second largest CI coefficients (C_2) in the CASSCF expansions for the HO_3 species range in magnitude from 0.22 to 0.28 (Table 4.2), and no other CI coefficients exceed 0.1. By comparison, ozone has $C_2 \approx -0.34$ and hence significantly larger multireference character.[103] The electronic configuration corresponding to C_2 involves the expected $\sigma^2 \rightarrow (\sigma^*)^2$ double excitation within the O_2–O_3 bond necessary to properly dissociate HO_3. Figure 4.1 depicts the doubly occupied $\sigma(10a')$ and $\sigma^*(11a')$ molecular orbitals associated with this transition, along with the singly occupied molecular orbital (SOMO) $\pi(3a'')$. All of this evidence leads us to safely state that any multiconfigurational nature of HO_3 can be handled if single-reference coupled cluster methods are utilized with high levels of electron correlation.

TABLE 4.2. T_1 diagnostics (CCSD(T)/cc-pVTZ), $T_{2,\max}$ amplitudes (CCSD(T)/cc-pVTZ), and first, second, and third largest CI coefficients (C_1, C_2, and C_3) (CASSCF(19,13)/cc-pVTZ).

	T_1	$T_{2,\max}$	C_1	C_2	$\lvert C_3 \rvert$
cis-HO_3 ($^2A''$)	0.042	0.101	0.93	−0.22	0.09
trans-HO_3 ($^2A''$)	0.043	0.156	0.91	−0.28	0.09
TSct HO_3	0.041	0.154	0.92	−0.28	0.08
O_2 ($^3\Sigma_g^-$)	0.006	0.101	0.97	−0.16	0.08
OH ($^2\Pi$)	0.006	<0.05	0.99	−0.10	<0.05
CN ($^2\Sigma^+$)	0.053	0.093	0.97	−0.10	0.10

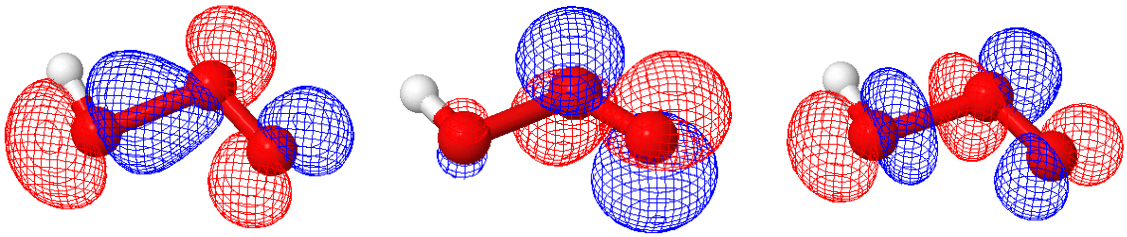

Figure 4.1. Frontier natural orbitals involved in the two important electronic configurations of the *trans*-HO_3 wave function: $\Psi = C_1|\ldots(10a')^2(3a'')^1| + C_2|\ldots(3a'')^1(11a')^2|$.

4.4.2 EQUILIBRIUM GEOMETRIES AND ROTATIONAL CONSTANTS

The stationary points on the HO_3 isomerization potential energy surface are depicted in Figure 4.2. Experimentally determined structures are available for OH,[104] O_2,[104] and *trans*-HO_3.[20,21,23] Our FPA-Q3 equilibrium structure for OH($^2\Pi$) is r_e = 0.9696 Å, in excellent agreement with experiment,[104] differing by only 0.0001 Å; this agreement becomes exact at the FPA-P level of theory. For $O_2(^3\Sigma^-)$ the FPA-Q3 and FPA-P methods yield r_e = 1.2069 Å and r_e = 1.2070 Å, respectively, as compared to the spectroscopic value of 1.2075 Å for this diatomic molecule.[104] The inclusion of relativistic effects, via the Δ(rel) term described above, in the FPA-P geometry optimization for $O_2(^3\Sigma^-)$ reduces the difference between theory and experiment to −0.0002 Å.

Our FPA-Q3 structure for *trans*-HO_3 has terminal O–H and O–O bond distances only 0.0010 Å shorter and 0.0088 Å longer, respectively, than the corresponding values for the free diatomics. Because the accuracy of FPA-Q3 for the diatomic bond distances is so high, we deem these shifts upon HO_3 formation to be very reliable. The CCSDT(Q)/CBS *trans*-HO_3 structure of Liang et al.[19] is in good agreement with our improved FPA-Q3 structure, exhibiting mean absolute

deviations (MAD) of 0.008 Å for bond lengths and 0.29° for bond angles. These small differences are due to the use of an FPA-Q2 CBS extrapolation scheme in their geometry optimization. As expected from previous work,[31,34-35,37,39] CCSD(T) theory, even with CBS(3,4) basis set extrapolation, underpredicts $r_e(O_2–O_3)$ by a stunning 0.17 Å when compared to our FPA-Q3 structure. MRCI+Q/CBS(5,6) displays much better agreement with FPA-Q3, with a difference in $r_e(O_2–O_3)$ of 0.002 Å.[43] Structural information for *cis*-HO_3 is much more limited.[30,32-34] The QCISD(T)/CBS(2,3) and CCSD(T)/CBS(3,4) *cis*-HO_3 structures[33-34] display differences of −0.11 Å and −0.10 Å for $r_e(O_2–O_3)$, respectively, when compared to our FPA-Q3 structure. Similar to *trans*-HO_3, single-reference coupled cluster methods without quadruple or higher excitations considerably underestimate the central bond length. The FC-CCSD(T)/AVQZ structure of Varandas exhibits an $r_e(O_2–O_3)$ value differing by 0.04 Å compared to our FPA-Q3 structure; this discrepancy is decreased to 0.008 Å at the FC-MRCI/VTZ level of theory.[44] FC-MRCI/VTZ also produces a **TSct** structure with a MAD of 0.02 Å for bond lengths and 1.07° for bond angles when compared to our FPA-Q3 structure.[44]

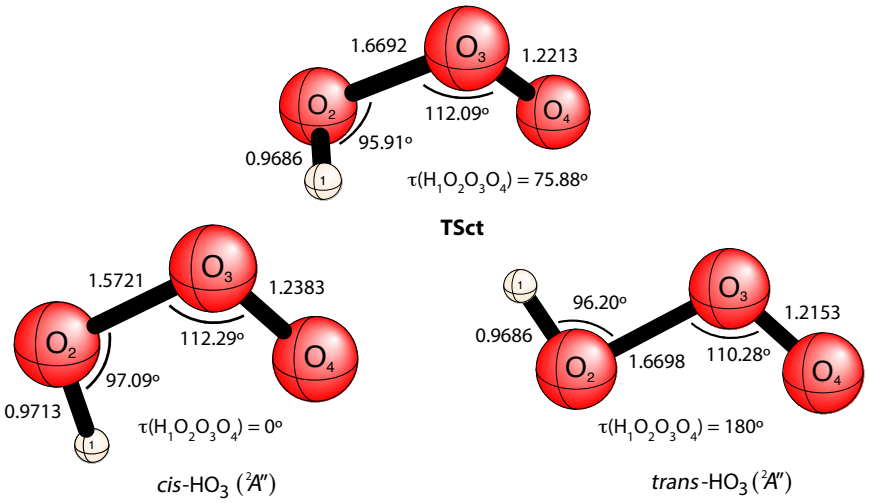

Figure 4.2. Optimum structures of *cis*-HO_3, **TSct**, and *trans*-HO_3 at the FPA-Q3 level of theory. Bond lengths are in Å.

The unusually long central O–O bond of *trans*-HO_3 (1.6698 Å) has an equilibrium distance 0.22 Å greater than that in hydrogen peroxide,[105] evidencing a peculiar, intricate interaction between unpaired electrons on OH and O_2.[36] The image of the highest doubly occupied orbital of HO_3 [$\sigma(10a')$, Figure 4.1] gives insight into this issue. This orbital is clearly derived from the in-plane π^* antibonding orbital of O_2 by distortion toward the hydroxyl group to form a σ(O–O) bonding interaction. However, this σ bonding is quite weak, and the terminal $r_e(H_1–O_2)$ and $r_e(O_3–O_4)$ distances of *trans*-HO_3 do not change significantly from the analogous diatomic values. The predominant Lewis structure of HO_3 shows that the formation of a normal central O–O covalent bond in this species would involve the enthalpy change $\Delta H_0 = BE[\pi(O–O)] – BE[\sigma(O–O)]$, where BE denotes a prototypical bond energy. In terms of the dissociation energies (D_0) of hydrogen peroxide and molecular oxygen, ΔH_0 can thus be quantified as $\Delta H_0 = D_0(O_2) – 2D_0(HO–OH)$. Using current enthalpies of formation at 0 K from the Active Thermochemical Tables,[106] we find $\Delta H_0 = 118.0 – 2(49.0) = +20.0$ kcal mol^{-1}. This analysis reveals that the formation of a normal central covalent bond in HO_3 would be very unfavorable on energetic grounds, owing to the relative weakness of prototypical σ(O–O) bonds. We conclude that HO_3 only has weak central O–O bonding possibilities.

Mansergas et al.[36] analyzed the bonding features of *trans*-HO_3 utilizing the atoms in molecule (AIM) theory of Bader.[107] Their analysis was carried out using the first-order density matrix obtained at both the QCISD and MRCI levels of theory with a 6-311+G(2df,2p) basis set. While the central O–O bond does display a bond critical point (bcp) with an energy density characteristic of a stabilizing effect, the Laplacian of the electron density at the bcp of *trans*-HO_3 is positive, showing that the interaction is not a true covalent bond. The predominant Lewis

structure of a hypothetical HO_3 species with a normal covalent O–O bond indicates that the terminal O_4 atom would have the highest spin density. However, natural bond orbital[108] (NBO) analysis of *trans*-HO_3 at the RO-CCSD(T)/cc-pVTZ//FPA-Q3 level of theory finds that the O_2 and O_3 atoms have spin densities of +0.72 and +0.34, respectively, while only –0.05 resides on O_4. This data supports the conclusion that *trans*-HO_3 is bound by only limited O_2–O_3 covalent bonding. As *trans*-HO_3 converts to *cis*-HO_3, the spin density does migrate somewhat toward the terminal O_4 atom; in particular, the natural spin densities on O_2, O_3, and O_4 become +0.70, +0.41, and –0.09, respectively. This migration is associated with a modest increase in covalent bond character, and accordingly the $r_e(O_2O_3)$ distance of *cis*-HO_3 is 0.098 Å shorter than that of *trans*-HO_3. SAPT0 theory[109] is unable to give reliable insight into the bonding of *cis*-HO_3 versus *trans*-HO_3 because this method places *cis*-HO_3 much too low in relative energy.

A new semiexperimental equilibrium structure of *trans*-HO_3 can be extracted from existing microwave rotational constants by means of the FPA-Q2 vibration-rotation interaction constants (α_i) listed in Table 4.3. The FPA-Q2 α_i constants for all HO_3 isotopologues utilized in this study are listed in supplementary Table B3. The α_i values can be decomposed[90-91,110-111] into inertial-derivative (id), Coriolis (Cor), and anharmonicity (anh) components, all of which are listed in Table 4.3. While the anh component of α_i is largest in most cases, it is generally not dramatically bigger than the id and Cor components, and in some cases it is actually smaller. For example, α_4^A(id) is only 4% smaller in magnitude than α_4^A(anh); α_5^B(Cor) is 3.3 times larger than α_5^B(anh); and all three terms for α_5^A are comparable. The essential observation is that there is no anharmonic blowup in the VPT2 treatment and all the α_i constants are modest in size. Remarkably, the contribution ($\alpha_i/2$) of each vibration-rotation interaction constant to the zero-point vibrational (ZPV) effect on the corresponding rotational constant never exceeds 1.5% and is smallest in the

case of A_e. By comparison, for the H_2O molecule, the ZPV effect is largest on A_e and amounts to as much as 5% for the bending vibration.[90] These data give surprising support for the application of VPT2 theory to *trans*-HO_3, because this methodology is commonly applied to prototypical molecules such as H_2O.

The MRCI+Q/AVQZ α_i constants of Suma et al.[24] exhibit mixed agreement with our FPA-Q2 values. Sizable differences are found for the α_i^A constants, with the largest disparity of 181.8 MHz occurring for α_6^A. The α_i^B and α_i^C constants for i = 1–5 show much better agreement with differences less than 10 MHz. For the (α_6^B, α_6^C) constants involving the torsional vibration, the MRCI values (9.3, –48.7) MHz are substantially different on both an absolute and percentage basis from the FPA-Q2 results of (71.6, –1.1) MHz. Some of the differences between the MRCI and FPA-Q2 α_i constants are likely due to the manner in which the underlying force fields were obtained. Suma et al.[24] obtained an effective anharmonic force field by computing 437 energy points in the vicinity of *trans*-HO_3, covering the following geometry ranges: -0.19 Å $< \Delta r_e(H_1O_2) < +0.26$ Å, -0.18 Å $< \Delta r_e(O_2O_3) < +0.23$ Å, -0.12 Å $< \Delta r_e(O_3O_4) < +0.11$ Å, $-8.0° < \Delta\theta_e(O_2O_3O_4) < +8.0°$, $-23° < \Delta\theta_e(H_1O_2O_3) < +23°$, and $0° < \Delta\tau_e(H_1O_2O_3O_4) < +149°$.[24] The MRCI energies were then fit to a 93-term polynomial up to fourth degree for $\Delta r_e(O_3O_4)$, $\Delta\theta_e(O_2O_3O_4)$, $\Delta\theta_e(H_1O_2O_3)$, and $\cos[\tau(H_1O_2O_3O_4)]$; fifth degree for $\Delta r_e(H_1O_2)$; and sixth degree for $\Delta r_e(O_2O_3)$.[24] Presumably, the customary VPT2 equations subsequently were applied to the quadratic and cubic terms in this polynomial to find α_i^A values. In contrast, our α_i constants were obtained by a direct application of VPT2 to an anharmonic force field that represents the true potential energy surface derivatives at the *trans*-HO_3 minimum.

TABLE 4.3. Vibration-rotation interaction constants (α_i, in MHz) for *trans*-HO_3.[a]

	FPA-Q2				ZPV effect (%)[b]	MRCI+Q/AVQZ[c]
α_1^A	237.4	(−17.8,	−176.3,	431.5)	0.17	265.3
α_2^A	200.8	(−378.5,	−17.1,	596.4)	0.14	224.4
α_3^A	511.7	(−78.2,	−207.1,	797.1)	0.36	563.7
α_4^A	−219.7	(−842.7,	−251.6,	875.0)	−0.16	−161.0
α_5^A	−78.7	(−90.0,	−72.0,	83.6)	−0.06	−9.8
α_6^A	968.9	(0,	2233.4,	−1264.5)	0.69	1150.7
α_1^B	3.7	(−0.2,	−1.5,	5.4)	0.02	2.1
α_2^B	−166.6	(−5.4,	−1.4,	−159.8)	−0.84	−177.3
α_3^B	296.5	(−4.4,	−9.1,	310.1)	1.49	304.8
α_4^B	148.4	(−11.8,	−7.7,	167.8)	0.75	157.1
α_5^B	162.8	(−72.4,	−0.7,	235.9)	0.82	173.8
α_6^B	71.6	(0,	47.2,	24.4)	0.36	9.3
α_1^C	6.0	(−0.1,	−4.8,	10.9)	0.04	5.2
α_2^C	−126.4	(−3.0,	−10.4,	−113.0)	−0.72	−134.2
α_3^C	255.1	(−0.6,	5.9,	249.8)	1.46	262.0
α_4^C	143.6	(−0.1,	1.5,	142.1)	0.82	151.0
α_5^C	155.9	(−39.5,	13.5,	181.9)	0.89	165.8
α_6^C	−1.1	(0,	0,	−1.1)	−0.01	−48.7

[a]In parentheses the α_i constants are decomposed into inertial-derivative, Coriolis, and anharmonicity components, in order. [b]Corresponding contribution (α_i /2) to the zero-point vibrational effect as a percentage of the equilibrium rotational constant. [c]Ref. 24

The experimental ground-state rotational constants (A_0^{exp}, B_0^{exp}, C_0^{exp}) of the 10 *trans*-HO_3 isotopologues deviate significantly from our FPA-Q3 equilibrium values ($A_{\mathrm{e}}^{\mathrm{FPA}}$, $B_{\mathrm{e}}^{\mathrm{FPA}}$, $C_{\mathrm{e}}^{\mathrm{FPA}}$) due to vibrational averaging effects, *inter alia*. In this data set, a MAD of 401.9 MHz is observed with differences as large as 1000.8 MHz. Correcting the experimental rotational constants for ZPV effects greatly improves the agreement with theory, as the MAD and maximum deviation are reduced to 74.3 MHz and 169.7 MHz, respectively. Table 4.4 reports the ^{18}O isotopic shifts among

the experimental, semiexperimental (A_e^{semi}, B_e^{semi}, C_e^{semi}), and theoretical rotational constants. These data are best analyzed in four groups: HO_3(*A*), HO_3(*BC*), DO_3(*A*), and DO_3(*BC*) pertaining to shifts in the *A* and (*B*,*C*) rotational constants within the HO_3 and DO_3 series of isotoplogues. The ZPV correction strikingly reduces the MAD between the experimental and theoretical ^{18}O shifts from 87.6 to 18.3 MHz for HO_3(*A*), from 14.6 to 1.5 for HO_3(*BC*), from 104.1 to 17.7 MHz for DO_3(*A*), and from 13.3 to 0.8 MHz for DO_3(*BC*). The performance of VPT2 with our FPA-Q2 force field is outstanding for the *B* and *C* vibrational corrections, whereas the treatment is still quite good for the *A* constants, which are most affected by large-amplitude motion.

TABLE 4.4. Experimental (A_0^{exp}, B_0^{exp}, C_0^{exp}), semiexperimental (A_e^{semi}, B_e^{semi}, C_e^{semi}), and theoretical FPA-Q3 (A_e^{FPA}, B_e^{FPA}, C_e^{FPA}) ^{18}O isotopic shifts (MHz) of *trans*-HO_3 rotational constants.

	(A_0^{exp}, A_e^{semi}, A_e^{FPA})	(B_0^{exp}, B_e^{semi}, B_e^{FPA})	(C_0^{exp}, C_e^{semi}, C_e^{FPA})
Reference values for parent HOOO			
HOOO	(70778.2, 71588.5, 71758.2)	(9987.0, 10244.7, 10201.4)	(8750.2, 8967.2, 8931.7)
^{18}O Isotopic shifts			
$HO^{18}OO$	(−937.8, −995.4, −1009.7)	(−571.9, −585.4, −588.2)	(−455.0, −465.7, −468.4)
$HOO^{18}O$	(−4724,7, −4815.0, −4830.3)	(−21.7, −20.5, −22.7)	(−94.1, −95.8, −96.6)
$HOOO^{18}$	(−1807.2, −1779.4, −1786.5)	(−466.7, −484.2, −482.0)	(−386.8, −399.4, −397.6)
$HOO^{18}O^{18}$	(−6571.1, −6633.6, −6656.36)	(−478.4, −494.8, −494.6)	(−471.1, −485.3, −484.3)
$HO^{18}O^{18}O^{18}$	(−7492.7, −7615.4, −7647.3)	(−1038.8, −1069.7, −1070.34)	(−913.4, −939.2, −939.0)
Reference values for parent DOOO			
DOOO	(67857.4, 68645.7, 68778.6)	(9448.5, 9639.3, 9592.3)	(8299.5, 8458.4, 8418.3)
^{18}O Isotopic Shifts			
$DO^{18}OO$	(−1184.9, −1251.0, −1262.0)	(−478.7, −489.5, −490.1)	(−388.1, −396.9, −397.4)
$DOO^{18}O^{18}$	(−5834.8, −5899.5, −5915.9)	(−461.7, −473.8, −473.1)	(−446.0, −455.9, −454.3)
$DO^{18}O^{18}O^{18}$	(−6973.8, −7102.1, −7127.9)	(−932.4, −954.5, −954.4)	(−824.7, −842.9, −841.9)

The inertial defects[112-115] (Δ) exhibited by both the experimental and semiexperimental rotational constants of the *trans*-HO_3 isotopologues are listed in supplementary Table B4. For the experimental ($A_0^{\exp}$, $B_0^{\exp}$, $C_0^{\exp}$) rotational constants, Δ_0 lies in the [+0.011, +0.024] u$Å^2$ and [−0.033, −0.042] u$Å^2$ intervals for the HO_3 and DO_3 isotopologues, respectively. In comparison, Δ_0 is (+0.049, +0.075, +0.121) u$Å^2$ for (H_2O, H_2CCO, HNCO) and (+0.068, +0.110, +0.152) u$Å^2$ for (D_2O, D_2CCO, DNCO).[105-107] Therefore, the HO_3 Δ_0 values are less positive than expected compared to germane reference molecules, and the DO_3 counterparts are similarly small but of the opposite sign. In general, in small semi-rigid planar molecules, ZPV effects cause Δ to deviate from zero by about +0.1 u$Å^2$,[116] substantially more than observed for the HO_3 isotopologues. Oka and Morino[114-115] have discussed the decomposition of the inertial defect into vibrational, electronic, and centrifugal terms. Interestingly, in VPT2 theory the anharmonic vibrational contribution to Δ_0 vanishes for a semi-rigid planar molecule, and only the harmonic components contribute to the ZPV effect. In such cases the out-of-plane vibrations typically have a negative effect on Δ_0, whereas the in-plane vibrational effects are positive and usually larger.[116] Remarkably, we observe opposite trends for *trans*-HO_3, counter to previous claims.[24] The collective contributions to Δ_0 of the in-plane ν_3(HOO bend), ν_4(OOO bend), and ν_5(central OO stretch) vibrations are −0.266 u$Å^2$ for HO_3 and −0.296 u$Å^2$ for DO_3; the other in-plane vibrations ν_1(OH stretch) and ν_2(terminal OO stretch) do not affect Δ_0 substantially. In contrast, the out-of-plane torsion ν_6 adds +0.219 u$Å^2$ and +0.291 u$Å^2$ to Δ_0 for HO_3 and DO_3, respectively. Clearly, the overall Δ_0 values involve an intricate cancellation of in-plane and out-of-plane ZPV effects.

The residual inertial defects in the semiexperimental rotational constants for HO_3 isotopologues range from −0.020 to −0.023 u$Å^2$. Although small and comparable in magnitude to semiexperimental Δ_e values for HNCO species,[110] the HO_3 residual Δ_e defects are actually farther

from zero than their Δ_0 counterparts. For DO_3 isotopologues the ZPV corrections reduce the inertial defects only slightly from the corresponding Δ_0 values. In ideal cases,[111,117] the semiexperimental inertial defects are substantially less than 0.01 uÅ^2, but neither our FPA-Q2 nor the MRCI+Q/AVQZ α_i^{A} constants are able to reach this benchmark for HO_3 species.

The geometric structures resulting from least-squares fitting of the experimental (A_0^{exp}, B_0^{exp}, C_0^{exp}) and semiexperimental ($A_{\mathrm{e}}^{\mathrm{semi}}, B_{\mathrm{e}}^{\mathrm{semi}}, C_{\mathrm{e}}^{\mathrm{semi}}$) rotational constants are summarized in Table 4.5. Because the inertial defects are non-vanishing, different structural parameters arise from fitting all rotational constants (*ABC*) versus (*BC*), (*AC*), and (*AB*) pairs of them. Allowing the molecule to be non-planar (NP) also yields variations in the fit. All structural parameters obtained from systematic variations (vide supra) in the details of the least-squares fit are provided in supplementary Table B5. A fractional mean absolute residual (fMAR) statistic is used here as a measure of goodness of fit unbiased toward any particular choice of the fitting function. As in earlier refinements for the r_0 structure,[23] Scheme 1 utilizes all 10 experimentally available *trans*-HO_3 isotopologues (HO_3, $H^{18}OOO$, $HO^{18}OO$, $HOO^{18}O$, $HO^{18}O^{18}O$, $H^{18}O^{18}O^{18}O$, DO_3, $D^{18}OOO$, $DO^{18}O^{18}O$, $D^{18}O^{18}O^{18}O$), while Scheme 2 considers all singly-substituted isotopologues (HO_3, $H^{18}OOO$, $HO^{18}OO$, $HOO^{18}O$, DO_3), Scheme 3 employs only the parent and all deuterated isotopologues (HO_3, DO_3, $D^{18}OOO$, $DO^{18}O^{18}O$, $D^{18}O^{18}O^{18}O$), and Scheme 4 utilizes (HO_3, $H^{18}OOO$, $HO^{18}O^{18}O$, $H^{18}O^{18}O^{18}O$, DO_3). Among the myriad choices for combination of rotational constants, target of the fit (IM vs. RC), and power for the weights (n = 0, 1, or 2), Schemes 2, 3, and 4 produce r_{e} internal coordinates that vary from the corresponding Scheme 1 values by a mean, standard deviation, and maximum magnitude of 0.013, 0.67, and 2.3 times the standard errors, respectively. Only 12% of the Scheme 2, 3, and 4 values lie outside one standard error of the corresponding Scheme 1 result, and there are no significant differences in fMAR values

from analogous fits across the 4 schemes. Therefore, our ZPV corrections are successful in removing any systematic structural differences[23] given by the four schemes. Accordingly, the results of Table 4.5 arise from Scheme 1, which is given preference here because it includes the most structural data while still providing very good fits.

Utilizing unity weights (n = 0) when fitting to the inertial moments is not advisable, because structural inconsistencies result when compared to the other approaches. Internal coordinates produced by Scheme 1 (n = 0) vary from n = 2 values by a mean, standard deviation, and maximum magnitude of −0.11, 1.22, and 3.8 times the n = 2 standard error. When utilizing (*ABC*), n = 0, and IM fitting, the fMARs are more than doubled relative to the other (*ABC*) fits. In contrast, Scheme 1 (n = 1) values compared to n = 2 vary by a mean, standard deviation, and maximum magnitude of only −0.01, 0.29, and 0.6 times the standard error, respectively. Interestingly, utilizing n = 2 and fitting to either IM or RC produces geometric parameters which are the same to the number of digits reported in Table B5, albeit not exactly mathematically equivalent. This property, together with the similarity to n = 1 (IM, RC) results, leads us to report the final structural parameters in Table 4.5 from n = 2 (IM) fits.

The *A* rotational constants were found to be a leverage point for internal coordinates involving hydrogen, as found earlier.[23] Excluding *A* from the fit (*BC*, n = 2) underestimates $r_e(H_1O_2)$ and overestimates $\theta_e(H_1O_2O_3)$ by 0.0085 Å and 0.43°, respectively, when compared to (*ABC*, n = 2). The uncertainties and fMARs for (*BC*) fits are on average 1.8 and 5.4 times larger, respectively, than analogous values from the (*ABC*), (*AC*), and (*AB*) fits. The fMAR statistic suggests that the (*AC*) fit is slightly better than (*AB*); however, the corresponding $r_e(H_1O_2)$ and $\theta_e(H_1O_2O_3)$ coordinates deviate a little more from the (*ABC*) values. In summary, we adopt the (*ABC*) fit for the most reliable r_e results because it incorporates the most data and there is no

evident merit in limiting the fit to only pairs of rotational constants. Indeed, the dramatic variations observed in Table 4.4 among the r_0 coordinates obtained by various choices of fitting data are no longer present in the semiexperimental r_e structures.

TABLE 4.5. Structural Parameters of *trans*-HO_3[a]

	$r(H_1O_2)$	$r(O_2O_3)$	$r(O_3O_4)$	$\theta(H_1O_2O_3)$	$\theta(O_2O_3O_4)$	$\tau(H_1O_2O_3O_4)$	fMAR(ppt)[b]
r_e(FPA-Q3)	0.9686	1.6698	1.2153	96.20	110.28	180	—
$r_e(ABC, \lambda_3 = 1.2)$	0.9690(21)	1.6632(26)	1.2148(25)	96.05(17)	110.08(7)	180	0.32
$r_e(ABC)$	0.9606(17)	1.6658(20)	1.2168(19)	95.58(13)	110.15(6)	180	0.29
$r_e(BC)$	0.9521(36)	1.6645(36)	1.2171(34)	96.01(20)	110.26(10)	180	1.74
$r_e(AC)$	0.9594(12)	1.6657(12)	1.2169(12)	95.46(10)	110.16(3)	180	0.26
$r_e(AB)$	0.9609(14)	1.6661(12)	1.2168(12)	95.61(12)	110.16(4)	180	0.42
r_e(Kr)[c]	0.9625	1.6592	1.2183	95.83	110.16	180	—
$r_0(ABC)$	0.9130(28)	1.6942(36)	1.2271(35)	90.96(27)	110.58(10)	180	0.71
$r_0(BC)$	0.8696(125)	1.6938(115)	1.2316(109)	93.24(68)	110.30(33)	180	1.67
$r_0(AC)$	0.9096(38)	1.6941(42)	1.2277(41)	90.55(40)	110.61(12)	180	0.70
$r_0(AB)$	0.9177(45)	1.6943(42)	1.2260(41)	91.50(48)	110.54(12)	180	0.71
r_s(Kr)[c]	0.9205	1.6745	1.2258	92.22	110.47	180	—
r_0(NP)	0.9124(29)	1.6935(38)	1.2277(37)	91.03(29)	110.60(11)	175.88(294)	0.72

[a]Bond distances in Å; bond angles in degrees. All semiexperimental r_e and effective r_0 structures are derived from Scheme 1 data. [b]Fractional mean absolute residual in parts per thousand (ppt). [c]Obtained by applying the Kraitchman equations to Scheme 2 data.

Our semiexperimental $r_e(ABC)$ structure displays a MAD of 0.0045 Å for bond lengths and 0.38° for bond angles when compared to the theoretical FPA-Q3 optimum geometry. The most notable differences are 0.008 Å, 0.004 Å, and 0.62° for $r(H_1O_2)$, $r(O_2O_3)$, and $\theta(H_1O_2O_3)$, respectively. The $r(H_1O_2)$ distance of $r_e(ABC)$ is only 0.009 Å smaller than the experimental bond length of diatomic OH($^2\Pi$).[104] The semiexperimental r_e structure of McCarthy et al.[21] has $r_e(H_1O_2)$ = 0.944 Å and $r_e(O_2O_3)$ = 1.660 Å, both of which are substantially smaller than our $r_e(ABC)$ values.

The more recent semiexperimental r_e of Suma et al.[24] exhibits much better accord with our $r_e(ABC)$ structure, as the MADs for bond distances and angles are only 0.0008 Å and 0.32°, respectively. However, their structure is evidently based on a Scheme 4, $n = 0$ (IM) fit, which was seen to be nonoptimal above. We are able to reproduce their results by employing their α_i constants and setting $n = 0$ in our MolStruct program, but the preferred approach of employing $n = 2$ weights changes their $r_e(H_1O_2)$ and $r_e(O_2O_3)$ values by –0.003 Å and +0.002 Å, respectively.

Our analyses confirm the anomalous $r_0(H_1O_2)$ and $\theta_0(H_1O_2O_3)$ coordinates that result from fits to the experimental rotational constants (A_0, B_0, C_0) if ZPV corrections are not included. Implementing $n = 0$ (IM) fits, our MolStruct program reproduces all of the r_0 data in Table 4 of McCarthy et al.[23] However, the exhaustive investigation of fitting procedures discussed above leads us to recommend $n = 2$ (IM or RC) fits, and the resulting r_0 parameters are listed in Table 4.5. For comparison, this table also gives the r_s and r_e structures given by applying the Kraitchman equations to the Scheme 2 data and invoking the customary first-moment constraints for the position of the central O atom.

The enormous disparities between the r_0 and r_e parameters of *trans*-HO_3 highlight the remarkable sensitivity of the structure to ZPV effects. Suma et al.[24] attribute the major $r_e - r_0$ differences to a large coupling between the in-plane O_2O_3 stretch and $H_1O_2O_3$ bend vibrations. As the length of the weak central O_2O_3 bond increases, the $H_1O_2O_3$ angle contracts in order to adopt the OH···OO structure of a van der Waals complex.[24,44] A more prevalent topic of discussion has been the consequences of the low-frequency out-of-plane torsional vibration on the effective structure of *trans*-HO_3. To address such issues, we have performed a sensitivity analysis of the r_e and r_0 coordinates of *trans*-HO_3 with respect to the ZPV contributions from the normal modes. The ZPV sensitivity of the fitted internal coordinates (R_j, j = 1-5, Table 4.5) of *trans*-HO_3 to scaling factors

(λ_i, i = 1-6) for ZPV contributions from the vibrational normal modes (ν_i) was quantified by numerically evaluating the relative derivative quantities $R_{\lambda,ij} = \frac{100}{R_j}\frac{\partial R_j}{\partial \lambda_i}$. The $R_{\lambda,ij}$ data are given in supplementary Table B6. We find that the molecular structure is indeed most sensitive to ZPV effects from the $H_1O_2O_3$ bending mode (ν_3), not the torsional vibration (ν_6). The two largest magnitudes for r_e fits in Table B6 are $R_{\lambda,31} = 8.7\%$ and $R_{\lambda,34} = 5.0\%$, which involve the dependence of $r_e(H_1O_2)$ and $\theta_e(H_1O_2O_3)$, respectively, on the α_3 constant that accounts for ν_3 zero-point vibrations. In comparison, the corresponding mean absolute $R_{\lambda,ij}$ value is only 0.43%, and the third largest magnitude is $R_{\lambda,64} = 3.1\%$. Similar sensitivities were observed for r_0 fits, in particular, the predominant values are $R_{\lambda,31} = 8.6\%$ and $R_{\lambda,34} = 6.5\%$.

The importance of the ν_3 mode is seen dramatically by re-fitting the geometric structure to experimental *ABC* rotational constants corrected only by α_3 terms. This test produces $r(H_1O_2)$ = 0.9544 Å, as compared to $r_0(H_1O_2)$ = 0.9130 Å and $r_e(H_1O_2)$ = 0.9606 Å in Table 4.5, demonstrating that the unphysical $r_0(H_1O_2)$ values of concern in previous studies can be remedied by α_3 corrections alone. These solitary corrections also reduce the $\theta_e(H_1O_2O_3) - \theta_0(H_1O_2O_3)$ disparity from 4.62° to 1.77°. When our test is executed with ZPV effects only from the ν_6 torsional mode, $r(H_1O_2)$ = 0.9053 Å results, revealing that out-of-plane vibrations are not the principal cause of anomalous $r_0(H_1O_2)$ coordinates.

Releasing planarity constraints in the least-squares refinements also provides compelling indication that torsional vibrations do not have a severe effect on the fitted molecular structure. The nonplanar (NP) r_0 structure (Table 4.5) has $\tau_0(H_1O_2O_3O_4) = 176° \pm 3°$, nowhere near the vibrationally averaged torsional value of 158° estimated earlier.[23] Moreover, the bond lengths and angles of the r_0(NP) and r_0(*ABC*) rows in Table 4.5 display no significant differences. The balance

of effects discussed above that leads to small inertial defects appears to also make the release of planarity constraints inconsequential. For each isotopologue, the expression

$$C(\lambda) = \frac{A_0 B_0 C_0}{A_0 B_0 + \lambda(A_0 C_0 + B_0 C_0 - A_0 B_0)} \tag{4.9}$$

yields C rotational constants that vary from the observed values (C_0) at $\lambda = 0$ to ones with no inertial defect at $\lambda = 1$. Placing the $C(\lambda)$ constants into the r_0(NP) fits produces smooth return to planarity as $\lambda \rightarrow 1$.

We find that scaling $H_1O_2O_3$ bend contributions to α_i constants by 1.2 produces an HO_3 molecular structure (ABC, $\lambda_3 = 1.2$) that exhibits a $r(H_1O_2)$ value of 0.9690, much more in alignment with both FPA-Q3 and free OH. This scaling also corrects for the major discrepancy for $\theta(H_1O_2O_3)$, producing a value which is 0.15° smaller than FPA-Q3, compared to 0.62° for $r_e(ABC)$. While semiexperimental $r(H_1O_2)$, $r(O_3O_4)$, and $\theta(H_1O_2O_3)$ values are brought into better agreement with FPA after scaling ($\lambda_3 = 1.2$), the $r(O_2O_3)$ and $\theta(O_2O_3O_4)$ values are pushed further away from FPA-Q3.

4.4.3 RELATIVE ENERGIES

The focal-point layout for the dissociation energy of *trans*-HO_3 appears in Table 4.6. At the (fixed) FPA-Q3 geometry adopted for the table, the Hartree-Fock CBS limit places *trans*-HO_3 *higher* than O_2 + OH by 45.8 kcal mol^{-1}. The first four correlation increments (δ[ROMP2], δ[ROCCSD], δ[ROCCSD(T)], δ[UCCSDT(Q)]) all lower HO_3 relative to the O_2 + OH fragments, and it is not until the ROCCSD(T) level of theory is reached that the molecule becomes thermodynamically bound. The δ[UCCSDT(Q)] increment of +2.52 kcal mol^{-1} is very substantial, amounting to 44% of the final D_e value. This quadruples correction is 0.79 kcal mol^{-1} larger than a corresponding result reported by Varner et al.,[39] presumably because the latter was computed at

a UCCSD(T)/cc-pVQZ optimum geometry whose O_2–O_3 bond distance (1.58 Å) is too small. Our δ[ROCCSDTQ(P)] increment of only –0.34 kcal mol^{-1} extends the correlation treatment beyond all previous studies and indicates that the FPA-P dissociation energy (D_e = 5.73 kcal mol^{-1}) of HO_3 is now finally converged to the vicinity of 0.1 kcal mol^{-1}.

In accord with previous work,[102] we have tested various CBS extrapolation schemes to confirm that the primary method used here has a 1σ uncertainty of about $\pm$0.15 kcal mol^{-1}. The ROCCSD(T) net D_e values obtained with the cc-pV(D,T,Q)Z basis sets are smaller than the corresponding CBS limit by 5.93, 2.37, and 1.19 kcal mol^{-1}, respectively. However, the ROCCSD(T)/cc-pV6Z result is only 0.37 kcal mol^{-1} short of the limit, with the majority of this basis set incompleteness error being contained in the underlying MP2 component. If the aug-cc-pV*X*Z (*X* = 2 - 6) series of basis sets is employed at the FPA-Q3 geometry, the resulting ROCCSD(T)/CBS D_e value is 0.13 kcal mol^{-1} smaller than its non-augmented counterpart. Remarkably, while the net values for UCCSDT(Q) obtained with the cc-pV(D,T)Z basis sets are different, their δ[UCCSDT(Q)] increments are exactly the same (+2.52 kcal mol^{-1}).

The anharmonic FPA-Q2 zero-point vibrational energy (ZPVE) correction to D_e was computed here via VPT2 with incorporation of the G_0 term for all species,[118] which is equivalent to the Dunham Y_{00} coefficient for diatomics.[119] We obtained ΔZPVE(anharm) = –2.62 kcal mol^{-1}, as compared to –2.78 kcal mol^{-1} if only harmonic components are included. Varner et al.[39] determined ΔZPVE(anharm) = –2.74 kcal mol^{-1} utilizing VPT2 on top of a CCSD(T)/ANO1 quartic force field, but they estimated that this correction could be in error by as much as 0.5 kcal mol^{-1}. Alternative ZPVE corrections[41,44] of –2.33 and –1.98 kcal mol^{-1} to the dissociation energy have been utilized that employ fundamental frequencies derived from the experimental combination bands[15] in the harmonic ZPVE formula. However, the practice of inserting

fundamental frequencies into the harmonic formula is known to give inaccurate ZPVE values,[120] and cross anharmonicity terms would need to be included to extract the experimental fundamental frequencies in the first place. The inherent ZPVE error of the first of these flaws is about 0.3 kcal mol^{-1} for HO_3, but this deficiency is largely cancelled when the corresponding ZPVEs of O_2 and OH are subtracted. Suma et al.[24] used their MRCI+Q force field to correct these flaws and arrived at ΔZPVE(anharm) = –2.71 kcal mol^{-1}, which is based on a ZPVE(HO_3) value within 0.04 kcal mol^{-1} of our FPA-Q2 VPT2 result. The accuracy of our VPT2 treatment for the vibrational frequencies of HO_3 (vide infra) substantiates our ΔZPVE(anharm) = –2.62 kcal mol^{-1} and leads us to estimate a 1σ uncertainty of 0.10 kcal mol^{-1} for it.

In accord with previous protocols,[121] we included a Δ(SOC) term for the dissociation energy by applying a spin-orbit energy correction to the reaction species (OH) having a degenerate electronic ground state. Thus, one half of the experimental[122] ground-state spin-orbit splitting (0.20 kcal mol^{-1}) of the OH radical was subtracted from the FPA-P dissociation energy. Among the auxiliary corrections to D_0 listed in Table 4.6, Δ(core) and Δ(SOC) are significant and amount to a collective –0.40 kcal mol^{-1} shift. Our final dissociation energy (D_0) of *trans*-HO_3 into OH + O_2 is 2.71 ± 0.25 kcal mol^{-1} by FPA targeting the UCCSDTQ(P)/CBS level of theory, with the (1σ) uncertainty arising collectively from errors in CBS extrapolations, electron correlation convergence, and accounting of ZPVE. Our FPA-P D_0 value is in nice agreement with the currently accepted experimental value[8] of 2.94 ± 0.1 kcal mol^{-1} considering the overlap of the error bars.

TABLE 4.6. Focal point analysis[a] (in kcal mol^{-1}) for the dissociation energy of *trans*-HO_3 into OH + O_2.

	ΔE_e(ROHF)	+ δ [ROMP2]	+ δ [ROCCSD]	+δ [ROCCSD(T)]	+δ [UCCSDT(Q)]	+δ [UCCSDTQ(P)]	NET
cc-pVDZ	–46.45	+24.60	+12.12	+7.33	+2.52	–0.34	[–0.21]
cc-pVTZ	–45.56	+28.47	+9.43	+8.82	+2.52	[–0.34]	[+3.35]
cc-pVQZ	–45.69	+29.88	+8.89	+9.26	[+2.52]	[–0.34]	[+4.53]
cc-pV5Z	–45.76	+30.60	+8.67	+9.44	[+2.52]	[–0.34]	[+5.14]
cc-pV6Z	–45.81	+30.91	+8.56	+9.50	[+2.52]	[–0.34]	[+5.37]
CBS LIMIT	[–45.82]	[+31.35]	[+8.41]	[+9.59]	[+2.52]	[–0.34]	[+5.73]

FPA-Q3 reference geometries

$D_0 = D_e$(FPA) + ΔZPVE(anharm) + Δ(core) + Δ(rel) + Δ(DBOC) + Δ(SOC)

D_0 = +5.73 – 2.62 – 0.20 – 0.03 + 0.03 – 0.20 = **+2.71 kcal mol^{-1}**

[a] The symbol δ denotes the increment in the relative energy (D_e) with respect to the preceding level of theory in the hierarchy HF → ROMP2 → ROCCSD → ROCCSD(T) → UCCSDT(Q) → UCCSDTQ(P). Square brackets signify results obtained from basis set extrapolations or additivity assumptions.

A comparison with previous theoretical dissociation energies is best made with D_e values, because only two previous studies[24,39] include anharmonicity in their ΔZPVE corrections. The vexing, wide variations in D_e given by earlier theoretical studies (Table 4.1) was discussed above, so we focus here only on the best and most recent results. If D_e values without Δ(SOC) corrections are compared for uniformity, the CASPT2(19,15)/aug-cc-pVTZ,[40] CCSDT(Q)/CBS(4,5),[39] MRCI+Q/CBS(5,6),[24] and MRCI+Q/CBS(5,6)[44] results published over the last decade deviate from our corresponding FPA-P value (5.5 kcal mol^{-1}) by +0.3, –0.1, –1.0, and –1.0 kcal mol^{-1}, respectively, the last two of which are substantial disagreements. The earlier CCSDT(Q)/CBS(4,5) D_e value from our laboratory[19] is 0.3 kcal mol^{-1} larger than its FPA-P counterpart, which can be attributed almost exclusively to the δ[UCCSDTQ(P)] electron correlation increment included here.

The focal point analysis of the *trans* → *cis* isomerization energy of HO_3 (ΔE_e^{tc}) is found in Table 4.7. At the Hartree-Fock CBS limit, *cis*-HO_3 is 7.99 kcal mol^{-1} more energetically favorable than *trans*-HO_3. All electron correlation methods up through ROCCSD(T) place *cis*-HO_3 below *trans*-HO_3, with *cis*-HO_3 lower by 0.4 kcal mol^{-1} even at the ROCCSD(T)/CBS limit. The sizable δ[UCCSDT(Q)] increment of 0.85 kcal mol^{-1} amounts to over twice the final ΔE_e^{tc} and places *trans*-HO_3 below *cis*-HO_3 by 0.45 kcal mol^{-1}. The minuscule increment δ[UCCSDTQ(P)] = –0.08

kcal mol^{-1} indicates that electron correlation convergence has been reached in our final ΔE_e^{tc} value. Basis set convergence is much faster for ΔE_e^{tc} compared to D_e, with the net ROCCSD(T)/cc-pV6Z result approaching the CBS value within 0.01 kcal mol^{-1}. Utilizing augmented basis sets produces an ROCCSD(T)/CBS value which is merely 0.02 kcal mol^{-1} lower than its non-augmented counterpart. Exploring various CBS extrapolation schemes, as previously mentioned, indicates that our FPA-P ΔE_e^{tc} value of +0.37 kcal mol^{-1} has a basis set incompleteness error less than 0.05 kcal mol^{-1}. A ΔZPVE(anharm) contribution to ΔE_e^{tc} of –0.16 kcal mol^{-1} was obtained via VPT2, compared to its harmonic counterpart of –0.18 kcal mol^{-1}. The other auxiliary corrections [Δ(rel), Δ(core), Δ(DBOC)] to ΔE_e^{tc} are only 0.01 kcal mol^{-1} in magnitude, with Δ(rel) and Δ(DBOC) effectively cancelling one another. Inclusion of auxiliary corrections produces a final prediction of ΔE_0^{tc} = +0.52±0.08 kcal mol^{-1}, with the stated (1σ) uncertainty estimate including all sources of error contained in the FPA-P computation.

While there are many ΔE_e^{tc} values in the literature,[26,28-33,35,38,42-44,46] previous results for ΔE_0^{tc} are quite limited.[32,43,46] Also, all previous ΔE_0^{tc} values were obtained with only harmonic ZPVE corrections. While the MRCI+Q/CBS(5,6) ΔE_0^{tc} result[43] is almost the same as our value, this level of theory underestimates ΔE_e^{tc} by 0.3 kcal mol^{-1} when compared to FPA-P. Hoy et al.[46] find that the parametric 2-RDM(M) method predicts *trans*-HO_3 to be lower in energy compared to *cis*-HO_3 before and after ΔZPVE(harm) is included, whereas CCSD(T) only places *trans*-HO_3 lower after the aug-cc-pVQZ basis set is utilized and ΔZPVE(harm) is included. While the 2-RDM(M)/aug-cc-pVQZ level of theory reproduces our FPA-P ΔE_e^{tc} value, it grossly overestimates ΔE_0^{tc} by 1.3 kcal mol^{-1} due to a dubiously large 2-RDM(M)/cc-pVDZ ΔZPVE(harm) value (1.4 kcal mol^{-1}).

TABLE 4.7. Focal point analysis[a] (in kcal mol^{-1}) for the *trans* → *cis* isomerization energy of HO_3.

	ΔE_e(ROHF)	+ δ [ROMP2]	+ δ [ROCCSD]	+δ [ROCCSD(T)]	+δ [UCCSDT(Q)]	+δ [UCCSDTQ(P)]	NET
cc-pVDZ	–7.59	+5.86	–0.22	+1.95	+0.81	–0.08	[+0.73]
cc-pVTZ	–8.26	+6.44	–1.06	+2.11	+0.85	[–0.08]	[–0.01]
cc-pVQZ	–8.08	+6.70	–1.34	+2.19	[+0.85]	[–0.08]	[+0.24]
cc-pV5Z	–8.02	+6.81	–1.47	+2.32	[+0.85]	[–0.08]	[+0.32]
cc-pV6Z	–7.99	+6.83	–1.50	+2.25	[+0.85]	[–0.08]	[+0.35]
CBS LIMIT	[–7.99]	[+6.87]	[–1.55]	[+2.27]	[+0.85]	[–0.08]	[+0.37]

FPA-Q3 reference geometries

$\Delta E_0^{tc} = \Delta E_e^{tc}$(FPA) + ΔZPVE(anharm) + Δ(core) + Δ(rel) + Δ(DBOC)

ΔE_0^{tc} = +0.37 + 0.16 – 0.01 + 0.01 – 0.01 = **+0.52 kcal mol^{-1}**

[a] For notation see footnote *a* of Table 4.6.

While we have firmly established that *trans*-HO_3 is lower in energy than *cis*-HO_3 with the highest level of theory to date, one may still ponder why this is so. The much shorter $r(O_2O_3)$ distance found in *cis*-HO_3 would imply enhanced stability over the weakly bound *trans*-HO_3, and the orientation of H_1 in *cis*-HO_3 would also give the possibility of favorable H-bonding with the terminal O_4 atom. However, Beames et al.[42] state that there is negligible hydrogen bonding in *cis*-HO_3, unlike that observed in HOONO,[123-124] based on variations in HOOO bond angles as a function of the torsional coordinate. Tightening of bond angles along the isomerization path would be observed in the presence of H-bonding, whereas an increase in the $O_2O_3O_4$ angle is observed, presumably due to steric repulsion between terminal atoms.[42] A very small ν_1 frequency shift between *cis*-HO_3 and *trans*-HO_3 was also found,[42] consistent with a lack of intramolecular H-bonding in *cis*-HO_3. The key fact is that all the qualitative bonding concepts that might typically be explored to explain ΔE_0^{tc} are incorporated into the CCSD(T)/CBS level of theory, which incorrectly predicts the energy ordering. From this perspective, we are simply left to conclude that the final preference for *trans*-HO_3 is an intricate high-order electron correlation effect without a simple description.

The focal point analysis for the *cis* → *trans* barrier to isomerization (ΔE_e^b) is found in Table 4.8. The Hartree-Fock/CBS limit places **TSct** 8.26 kcal mol^{-1} above *cis*-HO_3, a grossly overestimated barrier which is 7.45 kcal mol^{-1} larger than the UCCSDTQ(P)/CBS value. Rapid basis set convergence is observed for all levels of theory; for example, ROCCSD(T)/cc-pV*X*Z for *X* = Q, 5, and 6 produces ΔE_e^b values within 0.032, 0.007, and 0.010 kcal mol^{-1}, respectively, of the corresponding CBS limit. While the electron correlation increment due to quadruple excitations is substantial (δ[UCCSDT(Q)/cc-pVTZ] = –0.42 kcal mol^{-1}), excellent convergence is observed upon inclusion of pentuple excitations (δ[UCCSDTQ(P)/cc-pVDZ] = +0.002 kcal mol^{-1}). The final valence FPA-P ΔE_e^b value of 0.81 kcal mol^{-1} is negligibly affected by Δ(core), Δ(rel), and Δ(DBOC), but the ZPVE correction lowers the barrier to ΔE_0^b = 0.27 kcal mol^{-1} relative to the ground vibrational state of *cis*-HO_3. The minuscule barrier demonstrates that HO_3 can undergo isomerization at energies significantly below the dissociation threshold. Of the several previous barrier predictions in Table 4.1, only two include ZPVE corrections; in particular, ΔE_0^b is given as 0.7 kcal mol^{-1} at B3LYP/6-311+G(3df,2p)[29] and 0.2 kcal mol^{-1} at 2RDM(M)/aug-cc-pVTZ.[46] While the 2RDM(M) method yields a ΔE_0^b result within 0.1 kcal mol^{-1} of our FPA-P value, this level of agreement is a consequence of error cancellation, as the 2RDM(M) bare barrier of ΔE_e^b = 1.6 kcal mol^{-1} is substantially too high. The bare (non-ZPVE corrected) one-dimensional torsional potential energy functions utilized to obtain variational energy levels of HO_3 at the scaled EOMIP-CCSD*/ANO1 and MRCI+Q/AVQZ levels of theory exhibit barrier heights, with respect to *trans*-HO_3, smaller than our analogous FPA-P value by 0.23 and 0.15 kcal mol^{-1}, respectively.[24,42]

TABLE 4.8. Focal point analysis[a] (in kcal mol^{-1}) for the *cis* → *trans* barrier to isomerization (**TSct**).

	ΔE_e(ROHF)	+ δ [ROMP2]	+ δ [ROCCSD]	+δ [ROCCSD(T)]	+δ [UCCSDT(Q)]	+δ [UCCSDTQ(P)]	NET
cc-pVDZ	+7.98	–6.19	+0.73	–1.81	–0.38	+0.002	[+0.34]
cc-pVTZ	+8.45	–6.58	+1.46	–1.94	–0.42	[+0.002]	[+0.98]
cc-pVQZ	+8.32	–6.76	+1.70	–2.01	[–0.42]	[+0.002]	[+0.84]
cc-pV5Z	+8.28	–6.82	+1.80	–2.04	[–0.42]	[+0.002]	[+0.80]
cc-pV6Z	+8.27	–6.83	+1.83	–2.05	[–0.42]	[+0.002]	[+0.80]
CBS	[+8.26]	[–6.85]	[+1.87]	[–2.06]	[–0.42]	[+0.002]	[+0.81]

FPA-Q3 reference geometries

$\Delta E_0^b = \Delta E_e^b$(FPA) + ΔZPVE(harm) + Δ(core) + Δ(rel) + Δ(DBOC)

ΔE_0^b = +0.81 – 0.55 + 0.03 – 0.03 + 0.01= **+0.27 kcal mol^{-1}**

[a] For notation see footnote *a* of Table 4.6.

Because the binding energy of HO_3 is so small and the OH product exhibits a doubly degenerate electronic ground state, consideration must be given to the location of the excited $^2A'$ electronic state of HO_3. A previous QCISD(T)/6-311++G(2d,p) study[28] reported an adiabatic excitation energy of 39 kcal mol^{-1}, but the underlying geometric structures are inaccurate. For HO_2 and CH_3O_2 the adiabatic excitation energies are 20.10 and 21.11 kcal mol^{-1},[125-126] respectively, and the corresponding vertical excitation energies are not very different.[25,28,127-128] The focal point analysis for the vertical excitation energy $T_v(^2A''\rightarrow{}^2A')$ of *trans*-HO_3 is given in supplementary Table B7. ROCCSD(T)/CBS yields $T_v(^2A')$ = 55.14 kcal mol^{-1}, a very large value in comparison to HO_2 and CH_3O_2.[127-128] The key conclusion is that the $^2A'$ state of HO_3 lies much too high in energy to have any bearing on the vibrational dynamics in the shallow well of either the *trans* or *cis* $^2A''$ ground state of HO_3.

4.4.4 VPT2 VIBRATIONAL ANALYSIS

The FPA-Q2 full quartic force fields (QFFs) in internal coordinates for *trans*-HO_3 and *cis*-HO_3 are given in Tables B8-B12, along with the associated harmonic vibrational frequencies.

These force fields were computed at the corresponding FPA-Q2 equilibrium geometries. For comparison, the CCSD(T)/cc-pVQZ//FPA-Q2 QFF for *trans*-HO_3 is provided in Tables B8, B9, and B10. The internal coordinates S_i corresponding to the force constants (F_{ij}, F_{ijk}, F_{ijkl}) are defined in Table B8. In Table B13 vibrational anharmonic constants (x_{ij}) derived from the final FPA-Q2 QFF are listed for *trans*-HO_3, *trans*-DO_3, *cis*-HO_3, and *cis*-DO_3. In Tables B9 and B11, the F_{ijk} and F_{ijkl} values in parentheses correspond to those which negligibly affect the VPT2 anharmonic vibrational analysis. Utilizing the criterion that F_{ijk} or F_{ijkl} must *individually* alter no anharmonic constant by more than 0.25 cm^{-1}, we identify a set of insubstantial force constants that *collectively* alters no x_{ij} value by more than 0.8 cm^{-1} and no fundamental frequency by more than 0.4 cm^{-1}. In brief, it appears that 7 of 40 cubic and 40 of 86 quartic constants can be eliminated from future vibrational studies of *trans*-HO_3 with minimal consequences.

Previous research has demonstrated that high-quality force fields can be determined at lower levels of theory by adopting a highly accurate (nonstationary) reference geometry.[86] Accordingly, the CCSD(T)/cc-pVQZ//FPA-Q2 diagonal quadratic force constants F_{ii} of *trans*-HO_3 associated with stretching modes display excellent agreement with the corresponding FPA-Q2 constants. For example, the CCSD(T)/cc-pVQZ//FPA-Q2 values of F_{11}, F_{22}, and F_{33} are only 0.4%, 0.7%, and 1.0% smaller, respectively, than their FPA-Q2 counterparts. The FPA-Q2 values of F_{11} and F_{33} for *trans*-HO_3 are 0.4% larger and 20% smaller, respectively, than the analogous FPA-Q2 f_{rr} values for the OH and O_2 species. Slightly less agreement is observed for the bending modes, with the CCSD(T)/cc-pVQZ//FPA-Q2 values for F_{44} and F_{55} being 2.7% and 2.0% smaller than the corresponding FPA-Q2 values, respectively. Not surprisingly, the torsional mode is much more sensitive to level of theory, and the CCSD(T)/cc-pVQZ F_{66} value is 47% smaller than its FPA-Q2 counterpart.

The CCSD(T)/cc-pVQZ//FPA-Q2 off-diagonal quadratic force constants show less favorable agreement; notable examples are F_{21} and F_{52}, which are 38% and 52% smaller and larger, respectively, than their analogous FPA-Q2 values. A similar comparison of force constants for *cis*-HO_3 reveals that F_{66} for this isomer is much less sensitive to level of theory, with CCSD(T)/cc-pVQZ//FPA-Q2 producing a value only 11% smaller than FPA-Q2. These trends are manifested in the harmonic vibrational frequencies. The CCSD(T)/cc-pVQZ//FPA-Q2 level of theory produces harmonic frequencies which are on average 6% and 3% too small for *trans*-HO_3 and *cis*-HO_3, respectively, when compared to the FPA-Q2 values. While the CCSD(T)/cc-pVQZ//FPA-Q2 torsional harmonic frequency ω_6 is 27% smaller than FPA-Q2 for *trans*-HO_3, it is only 6% smaller in *cis*-HO_3.

Reasonable agreement between the CCSD(T)/cc-pVQZ//FPA-Q2 and FPA-Q2 levels of theory is observed for most diagonal anharmonic force constants of *trans*-HO_3. The F_{111}, F_{333}, F_{444}, F_{555}, F_{1111}, F_{3333}, and F_{5555} constants display percent deviations of 0.3%, 3.3%, 3.1%, 0.7%, 1.7%, 5.7%, and 11.1%, respectively. On the other hand, F_{222}, F_{2222}, F_{4444}, and F_{6666}, which involve the sensitive central O_2–O_3 stretch, H_1–O_2–O_3 bend, and torsional modes, show disparities of 20.7%, 18.6%, 64.7%, and 56.2%, respectively. The FPA-Q2 values of F_{111} and F_{333} are 0.6% larger and 14% smaller in magnitude, respectively, than the analogous FPA-Q2 f_{rrr} values for the OH and O_2 species. After excluding the set of insubstantial force constants, the MAD between CCSD(T)/cc-pVQZ//FPA-Q2 and FPA-Q2 cubic force constants is 14%. The choice of torsional displacement size (τ_{disp}) in the finite-difference computations is key when constructing the QFF representation of the PES. A τ_{disp} value of 0.06 rad produces F_{6666} = –0.048 aJ·rad^{-4}, smaller in magnitude by 0.011 aJ·rad^{-4} than the corresponding F_{6666} value obtained with τ_{disp} = 0.04 rad. This unusual numerical sensitivity in F_{6666} amounts to a total change in the torsional fundamental

frequency ν_6 of ~7 cm^{-1}, which is about an order of magnitude greater than typically found in anharmonic force field computations but within the accuracy that can be expected from VPT2 theory for a molecule like HO_3.

The literature is replete with harmonic frequencies from various levels of theory,[29,31,43-46,48-49] many of which vary greatly from our FPA-Q2 values. Previous B3LYP harmonic frequencies for *trans*-HO_3 exhibit a collective MAD of 72 cm^{-1} when compared to our FPA-Q2 results, with ω_3, ω_4, and ω_5 being overestimated in particular. The 2-RDM(M) results[46] vary wildly, producing MADs for *trans*-HO_3 and *cis*-HO_3 of 77 cm^{-1} and 109 cm^{-1}, respectively, when compared to our FPA-Q2 harmonic frequencies. Some CCSD(T) harmonic frequencies[41,46] also vary substantially from our FPA-Q2 values; for example, the CCSD(T)/cc-pV5Z frequencies[41] display a MAD of 63 cm^{-1} and 39 cm^{-1} with respect to the corresponding *trans*-HO_3 and *cis*-HO_3 FPA-Q2 values, respectively. Better agreement with FPA-Q2 is observed at the MRCI/cc-pVTZ level of theory,[41] with MADs of only 24 cm^{-1} and 14 cm^{-1} for *trans*-HO_3 and *cis*-HO_3, respectively.

A summary of the final vibrational analysis of *trans*-HO_3 and *trans*-DO_3 is presented in Table 4.9, which includes mode assignments, total energy distributions (TEDs),[88,129-130] harmonic frequencies, anharmonicity components, and fundamental frequencies. The FPA-Q2 combination bands of *trans*-HO_3 and *trans*-DO_3 obtained in this study are presented in Table 4.10. Analogous summaries for *cis*-HO_3 and *cis*-DO_3 appear in Tables B14 and B15. The total anharmonicity contribution ($\Delta_i \equiv \nu_i + \omega_i$) of each fundamental frequency in Table 4.9 is partitioned into the principal anharmonic term (Δ_{anh}), any resonance splitting (Δ_{res}) requiring a first- rather than second-order perturbation treatment, and the Coriolis contribution (Δ_{Cor}). The only resonance that required isolation from the VPT2 procedure was ($\nu_2, \nu_3 + \nu_4$) for *trans*-HO_3, which affects the

terminal O_3–O_4 stretch by 3.4 cm^{-1}. In both *trans*- and *cis*-HO_3 a large Coriolis coupling (Δ_{Cor} = 17-21 cm^{-1}) is observed between the H_1–O_2 stretching and H_1–O_2–O_3–O_4 torsional modes. The TEDs show that all normal modes of the four HO_3 species studied here are dominated by a single internal coordinate except in the (ν_2, ν_3) cases of *cis*-HO_3. The nearly equal mixtures of the terminal O_3–O_4 stretch and H_1–O_2–O_3 bend in these cases have dramatic effects on the anharmonicity constants, as discussed below. Early vibrational assignments[11-13] for HO_3 are vitiated by prodigious discrepancies exceeding 100 cm^{-1} with respect to the FPA-Q2 fundamental frequencies.

The FPA-Q2 combination band differences ($\nu_1 + \nu_k$) $-\nu_1$ (Table 4.10) are in excellent agreement with the experiment results from the Lester[15] and Douberly groups,[18] displaying MADs of only 4.0 cm^{-1} and 2.0 cm^{-1} for *trans*-HO_3 and *trans*-DO_3, respectively, for k = 3-6. The ($\nu_1 + \nu_k$) $-\nu_1$ differences for $k \neq 3$ lie within 2.8 cm^{-1} of the ν_k fundamentals (Table 4.9). However, FPA-Q2 yields ($\nu_1 + \nu_3$) $-\nu_1$ = 1001 cm^{-1} and 786 cm^{-1} for *trans*-HO_3 and *trans*-DO_3, respectively, whereas the corresponding explicit fundamentals are 1026 cm^{-1} and 797 cm^{-1}, in order. Thus, the H_1–O_2–O_3 bending mode demonstrates that the effective experimental fundamentals[15] should not be precisely equated with the (unmeasured) explicit values.

The FPA-Q2 O_2–H_1 stretching fundamental (ν_1) is curiously smaller than the experimental results[15,18] by 11 cm^{-1}. As depicted in Figure 4.3, insight into this problem is gained by comparison with the diatomic OH radical. An analogous diagram for the O–D stretching frequency appears in Figure B1. The FPA-Q2 harmonic frequency $\omega_1(HO_3)$ = 3749.2 cm^{-1} is 9.0 cm^{-1} larger than the corresponding value for free OH, in accord with the 0.001 Å reduction in $r_e(H_1O_2)$ and 0.04 aJ· $Å^{-2}$ increase in the quadratic stretching force constant upon formation of *trans*-HO_3. Inclusion of the diagonal anharmonicity [Δ_{anh}(diag)] terms lowers the frequency difference to +5.7 cm^{-1}.

From this point, coupling with the other vibrational modes engenders a delicate balance between substantial Coriolis effects (Δ_{Cor} = +18.5 cm^{-1}) and off-diagonal anharmonicity [Δ_{anh}(off-diag) = –36.3 cm^{-1}], resulting in a final predicted $\Delta\nu$ = –12.1 cm^{-1}. In comparison, $\Delta\nu$ = +1.3 cm^{-1} from experiment. This analysis leads to two notable conclusions: (1) the very close agreement between the O–H stretching fundamentals of *trans*-HO_3 and diatomic OH does not mean that coupling with other vibrational modes in HO_3 is small; and (2) VPT2 is apparently somewhat deficient in quantifying the contest between Δ_{Cor} and Δ_{anh}(off-diag), causing an error in ν_1 that is unexpectedly larger than observed for the other vibrations. The same competition is present in *trans*-DO_3, although the mass increase diminishes Δ_{Cor} (+15.6 cm^{-1}) and Δ_{anh}(off-diag) (–9.8 cm^{-1}). In this case the final FPA-Q2 $\Delta\nu$ = +11.9 cm^{-1} is too positive rather than too negative vis-à-vis $\Delta\nu$(expt.) = +3.0 cm^{-1}; nonetheless, the FPA-Q2 disparity with experiment for ν_1(O–D str.) is now only 8.2 cm^{-1}. A nice piece of purely experimental evidence for an intricate interplay between Δ_{Cor} and Δ_{anh}(off-diag) is that the observed shift $\Delta\nu$(O–D str.) = +3.0 cm^{-1} is noticeably *larger* than $\Delta\nu$(O–H str.) = +1.3 cm^{-1} for the parent (*trans*-HO_3, diatomic OH) molecules.

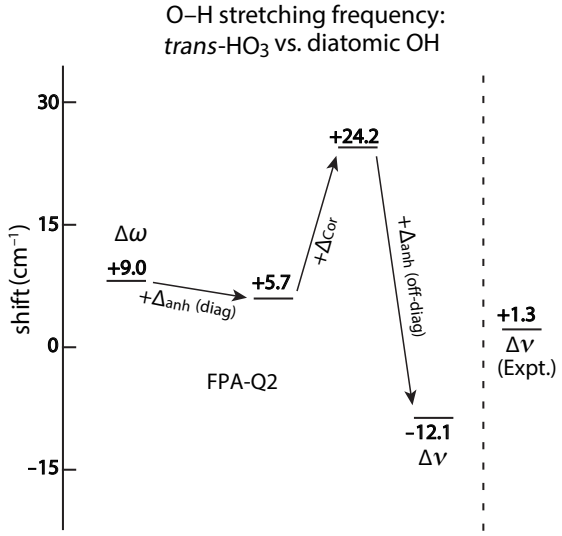

Figure 4.3. Components of the O–H frequency shift in going from diatomic OH to *trans*-HO_3.

TABLE 4.9. Summary of final vibrational analysis for *trans*-HO_3 and *trans*-DO_3.[a]

	Description	TED[b]	ω	Δ_{anh}	Δ_{res}	Δ_{Cor}	ν	MRCI+Q[c]
trans-HO_3								
ν_1	O–H str.	$S_1(100)$	3749.2	–209.4	0	18.5	3558.2	3570.6
ν_2	term. O–O str.	$S_3(96)$–$S_4(3)$–$S_5(1)$	1423.9	–9.1	3.4	0.7	1418.9	1409.9
ν_3	H–O–O bend	$S_4(92)$+$S_5(5)$+$S_3(5)$–$S_2(-2)$	1114.4	–91.5	0	2.8	1025.7	1036.8
ν_4	O–O–O bend	$S_5(79)$–$S_2(14)$–$S_4(6)$+$S_3(2)$	526.6	–36.3	0	1.0	491.3	486.9
ν_5	central O–O str.	$S_2(88)$+$S_5(15)$–$S_3(-2)$	280.0	–38.2	0	0.2	242.0	251.1
ν_6	H–O–O–O tors.	$S_6(100)$	170.3	–60.9	0	21.1	130.5[c]	129.5
trans-DO_3								
ν_1	O–D str.	$S_1(100)$	2730.8	–117.2	0	15.6	2629.1	2637.3
ν_2	term. O–O str.	$S_3(98)$–$S_4(1)$–$S_5(1)$	1421.2	–28.4	0	1.3	1394.1	1384.5
ν_3	D–O–O bend	$S_4(82)$+$S_5(16)$	854.2	–58.8	0	1.7	797.2	804.7
ν_4	O–O–O bend	$S_5(68)$–$S_2(14)$–$S_4(17)$+$S_3(1)$	499.0	–29.3	0	1.8	471.5	468.4
ν_5	central O–O str.	$S_2(88)$+$S_5(15)$–$S_3(-2)$+ $S_4(-1)$	279.0	–31.5	0	0.2	247.7	254.2
ν_6	D–O–O–O tors.	$S_6(100)$	128.2	–43.0	0	18.6	103.7	101.9

Internal coordinates: $S_1 = r(H_1O_2)$, $S_2 = r(O_2O_3)$, $S_3 = r(O_3O_4)$, $S_4 = \theta(H_1O_2O_3)$, $S_5 = \theta(O_2O_3O_4)$, $S_6 = \tau(H_1O_2O_3O_4)$

[a]All values in cm^{-1}. [b]The $S_i(k)$ entries specify the percentage proportions k of the total energy distribution (TED) of each normal vibration among the internal coordinates S_i. The phase of S_i in the normal-mode eigenvector precedes each $S_i(k)$ value. Contributions rounding to less than 1% in magnitude are not listed. [c]Values obtained at MRCI/AVQZ level of theory.[20] [d]A ν_6 value of 135.1 cm^{-1} is obtained if τdisp = 0.06 rad.

TABLE 4.10. Selected combination band differences of *trans*-HO_3 and *trans*-DO_3.

	FPA-Q2	Expt.[a]	MRCI+Q/AVQZ[b]
trans-HO_3			
ν_1	3558.2	3569.3	3570.6
$(\nu_1 + \nu_2) - \nu_1$	1416.1	—	1408.4
$(\nu_1 + \nu_3) - \nu_1$	1001.4	997.9	1015.2
$(\nu_1 + \nu_4) - \nu_1$	488.8	481.9	485.7
$(\nu_1 + \nu_5) - \nu_1$	238.4	243.7	251.5
$(\nu_1 + 2\nu_6) - \nu_1$	232.6	228.7	231.9
$(\nu_1 + \nu_6) - \nu_1$	128.3	128.7	124.7
trans-DO_3			
ν_1	2629.1	2635.1	2637.3
$(\nu_1 + \nu_2) - \nu_1$	1393.3	—	—
$(\nu_1 + \nu_3) - \nu_1$	786.3	783.9	794.7
$(\nu_1 + \nu_4) - \nu_1$	468.3	463.0	466.3
$(\nu_1 + \nu_5) - \nu_1$	245.4	245.3	254.6
$(\nu_1 + 2\nu_6) - \nu_1$	190.7	—	188.4
$(\nu_1 + \nu_6) - \nu_1$	102.5	102.2	99.6

[a]Reference 15. [b]Reference 20.

The MRCI+Q/AVQZ fundamental frequencies of Suma et al.[24] for *trans*-HO_3 and *trans*-DO_3 exhibit MADs of 7.8 cm^{-1} and 6.3 cm^{-1}, respectively, when compared to our corresponding FPA-Q2 values. Interestingly, the MRCI+Q/AVQZ ν_1 values are removed from experiment by only 1-2 cm^{-1}, but this high level of agreement is somewhat fortuitous because the analysis is also based on VPT2 rather than a variational treatment on a full PES that would be necessary to precisely account for the Δ_{Cor} and Δ_{anh}(off-diag) competition. As shown in Table 4.10, the MRCI+Q/AVQZ combination band differences on average deviate from experiment by about

twice as much as FPA-Q2. In particular, the MRCI+Q/AVQZ error for $(\nu_1 + \nu_3) - \nu_1$ is 17.3 cm^{-1}.[15,24]

A key point of interest is whether the unstructured spectral features observed by Lester and co-workers[15] are attributable to *cis*-HO_3 or a different species entirely. The assigned[15] combination band frequencies for *trans*-HO_3 and *cis*-HO_3 were not significantly different from each other, exhibiting a MAD of only 7 cm^{-1} between conformers, with the largest difference being 16.5 cm^{-1} for $(\nu_1 + \nu_6)$. In stark contrast, the FPA-Q2 combination bands for *trans*-HO_3 and *cis*-HO_3 display a MAD of 56.3 cm^{-1} and large differences of 145 cm^{-1} and 150 cm^{-1} are noted for $(\nu_1 + \nu_2)$ and $(\nu_1 + \nu_3)$, respectively. Our FPA-Q2 combination band differences $(\nu_1 + \nu_k) - \nu_1$ for *cis*-HO_3 exhibit a MAD of 68.5 cm^{-1} when compared to experiment,[15] as opposed to only 4.0 cm^{-1} for the analogous *trans*-HO_3 comparison. Our FPA-Q2 ν_1 value for *cis*-HO_3 is smaller than the assigned[15] value by 41.7 cm^{-1}. Liang et al.[18] found that the O–H stretching frequency of the HO_3–$(O_2)_2$ cluster observed in superfluid helium droplets is 3563 cm^{-1}, within 2.4 cm^{-1} of the corresponding unstructured peak assigned to *cis*-HO_3.[15] In summary, the FPA-Q2 results give strong evidence that the previously observed unstructured peaks[15] are not due to the uncomplexed *cis*-HO_3 isomer.

All characteristics of the DRP for *cis-trans* isomerization are provided in Appendix B, including the variation of the optimized internal coordinates (Table B18, Figures B3 – B7, Table B22), and the torsional dependence of the projected harmonic vibrational frequencies of HO_3 and DO_3 (Tables B19 and B20, Figures B8–B12, Table B23 – B24), as well as the Fourier coefficients for the potential function (Table B25), the ZPVE curves (Table B23 – B24), and the kinetic energy matrix elements (Table B26). The DRP characteristics generally bode well for an adiabatic approximation to treat the large-amplitude torsional motion. Specifically, the internal coordinates

and vibrational frequencies vary smoothly and by modest amounts as the torsion angle changes from 0° to 180°, and the ω_1–ω_4 vibrations maintain a large separation in time scales from the torsional motion. However, as discussed above, the central O–O bond does change considerably in the *cis–trans* isomerization, and the corresponding ω_5 frequency dips from 290 cm^{-1} at $\tau = 0°$ to 237 cm^{-1} at $\tau = 80°$, before increasing again to 278 cm^{-1} at $\tau = 180°$. The validity of the torsion angle as a reaction coordinate is demonstrated by comparing the projected (P) and non-projected (NP) frequencies of HO_3 and DO_3 at the isomerization transition state (Table B21). For ω_1–ω_4 the P and NP frequencies all match within 0.1 cm^{-1}, whereas for ω_5 the mean deviation is only 1.6 cm^{-1}.

The Schrödinger equation for torsional vibrations of HO_3 and DO_3 along the DRP can be cast into the form

$$-\tfrac{1}{2}G(\tau)\psi''(\tau) - \tfrac{1}{2}G'(\tau)\psi'(\tau) + V(\tau)\psi(\tau) = E_\tau\psi(\tau) \ , \tag{4.10}$$

where the potential $[V(\tau)]$ and kinetic $[G(\tau)]$ energy functions are specified in Tables B25 and B26, respectively. The details underpinning such a wave equation are often glossed over but warrant careful consideration. The relevant terms in the exact full-dimensional kinetic energy operator for a non-rotating molecule can be expressed in internal coordinates (S_k) as

$$\hat{T} = -\frac{1}{2}\hbar^2 \sum_{kl}^{3N-6} G^{kl} \frac{\partial^2}{\partial S_k \partial S_l} - \frac{1}{2}\hbar^2 \sum_{kl}^{3N-6} H^k \frac{\partial}{\partial S_k} \ . \tag{4.11}$$

The matrix elements

$$G^{kl} = \sum_{n}^{3N} \frac{B_n^k B_n^l}{m_n} \qquad\qquad H^k = \sum_{n}^{3N} \frac{B_{nn}^k}{m_n} \tag{4.12}$$

depend on the nuclear masses m_n as well as elements of the first- and second-order **B** tensors,

$$B_n^k = \frac{\partial S_k}{\partial x_n} \qquad\qquad B_{nn}^k = \frac{\partial^2 S_k}{\partial x_n^2} \tag{4.13}$$

which involve derivatives of the internal coordinates with respect to the Cartesian coordinates x_n.

To apply the full kinetic energy operator $\hat{T}$ to restricted motion along a reaction path, the dependence of the reaction coordinate s on the internal coordinates is required. For this purpose, consider the complete coordinate set $\mathbf{R} = \{Q_1, Q_2, ..., Q_{3N-7}, s\}$ along the reaction path, where the Q_k variables are normal coordinates for displacements from the reaction path at a particular point s. To first order, the internal displacement coordinates are given by $\mathbf{S} = \mathbf{LR}$, where the $\mathbf{L}$ tensor is comprised of eigenvectors of the $\mathbf{GF}_p$ matrix within the formalism of Allen.[83] The eigenvector of $\mathbf{GF}_p$ with zero eigenvalue that is placed in the last column of $\mathbf{L}$ corresponds to the instantaneous direction vector ($\mathbf{v}$, 1) for the DRP, where $\mathbf{v}$ is given by Eq. (15) of Ref. [83]. Because $\mathbf{R} = \mathbf{L}^{-1}\mathbf{S}$, we have $\partial s / \partial S_k = L_{sk}^{-1}(s)$, and thus DRP motion produces

$$\frac{\partial^2}{\partial S_k \partial S_l} = \frac{\partial s}{\partial S_k}\left[\frac{\partial}{\partial s}\left(\frac{\partial s}{\partial S_l}\frac{\partial}{\partial s}\right)\right] = L_{sk}^{-1}(s)L_{sl}^{-1}(s)\frac{\partial^2}{\partial s^2} + L_{sk}^{-1}(s)\frac{\partial L_{sl}^{-1}(s)}{\partial s}\frac{\partial}{\partial s} \tag{4.14}$$

When s is a torsional coordinate τ, the DRP kinetic energy operator becomes

$$\hat{T}_{\mathrm{DRP}} = -\frac{1}{2}G(\tau)\frac{\partial^2}{\partial \tau^2} - \frac{1}{2}H(\tau)\frac{\partial}{\partial \tau} \quad , \tag{4.15}$$

in which

$$G(\tau) = \hbar^2[\mathbf{L}^{-1}\mathbf{G}(\mathbf{L}^{-1})^{\mathrm{T}}]_{\tau\tau} \quad , \tag{4.16}$$

and

$$H(\tau) = \hbar^2\left[\sum_k^{3N-6} H^k L_{\tau k}^{-1} + \sum_{kl}^{3N-6} G^{kl} L_{\tau k}^{-1}\left(\frac{\partial L_{\tau l}^{-1}}{\partial \tau}\right)\right] \quad . \tag{4.17}$$

Because the $\mathbf{G}$ and $\mathbf{L}$ matrices are blocked by symmetry for the *cis* and *trans* conformations and $L_{\tau\tau} = 1$, the $G(\tau)$ function reduces to $\hbar^2$ times the bare $G_{\tau\tau}$ matrix element at these points. For HO_3 torsional vibrations, we find that the $H(\tau)$ function does not have a significant effect on the energy levels.

A more important consideration is that deviations of $H(\tau)$ from the derivative $G'(\tau)$ require a non-unit volume integration function $J(\tau)$ in order for the wave functions to be exactly orthogonal to one another. Our computations revealed that using the explicit $H(\tau)$ from Eq. (4.17) rather than $G'(\tau)$ in the kinetic energy operator changed the lowest 8 torsional excitation energies of HO_3 by a mean absolute value of only 0.89 cm^{-1}. Nonetheless, the mathematical derivations provided in Supplementary Material show that the problem of the volume integration function can be solved merely by employing Eq. (4.10) but with addition of the small term

$$U(\tau) = \frac{1}{4}[H'(\tau) - G''(\tau)] + \frac{1}{8}G(\tau)^{-1}[H(\tau) - G'(\tau)]^2 \qquad (4.18)$$

to the potential energy function. For HO_3 the rms value of $U(\tau)$ over the full range of torsional angles is only 2.8 cm^{-1}. The resulting eigenvalues are identical to those given by use of an explicit $H(\tau)$ in the wave equation, but the eigenfunctions are now rigorously orthogonal with a unit volume integration factor. This approach is equivalent to the more laborious procedure of explicitly determining the correct $J(\tau)$ and using it for integrations.

The eigenstates for HO_3 and DO_3 resulting from both the bare $[V_e(\tau)]$ and ZPVE-corrected $[V_0(\tau)]$ potentials exhibit the energy levels listed in Table 4.11 and the wave functions plotted in Figure 4.4. Two aspects of the potential energy functions are noteworthy. First, as shown in the left panel of Figure 4.4, $V_e(\tau)$ is closely reproduced by the quartic force fields of the *trans*- and *cis*-HO_3 minima for torsional displacements as large as 45° from equilibrium, a surprising finding that lends further support to the validity of the VPT2 results given above. Second, accounting for the ZPVE of the complementary vibrations has a considerable effect on the torsional energy profile, a phenomenon not considered in previous calculations of HO_3 torsional wave functions.[24,42] In particular, the *cis* → *trans* barrier is reduced from 324 to 238 cm^{-1} when ZPVE

effects are included. As a consequence, the first excited state in the *trans* well (n = 1) moves from 22 cm^{-1} above to 33 cm^{-1} below the lowest state in the *cis* well. For the final $V_0(\tau)$ potential, there are three states (n = 0, 1, 3) strongly localized in the *trans* well but only one (n = 2) localized in the *cis* well.

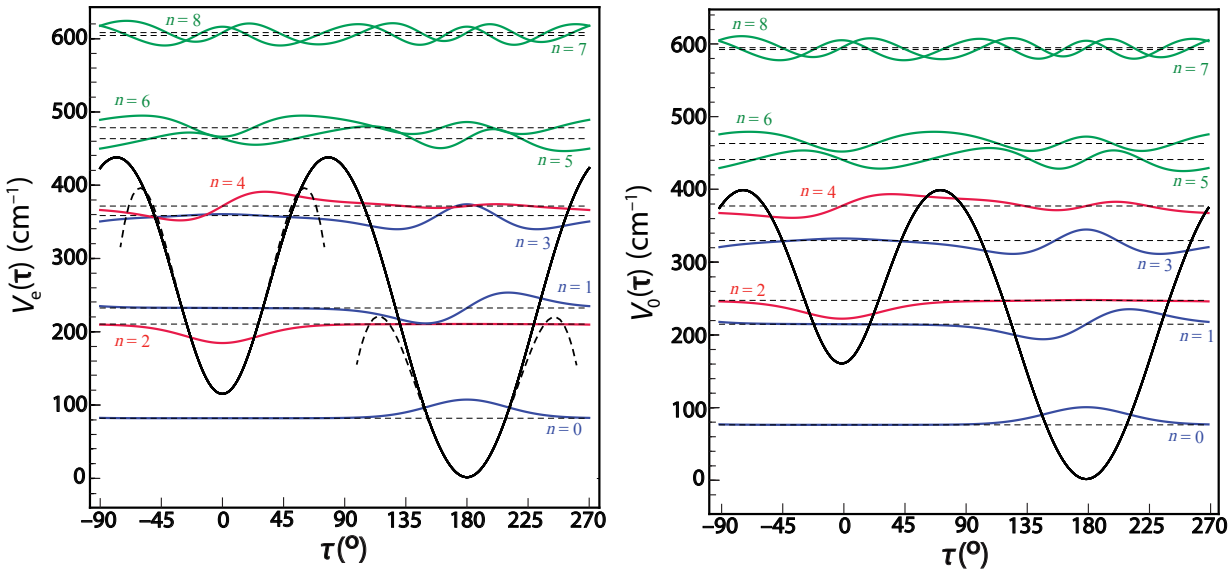

Figure 4.4 Wave functions for the torsional vibrations of the HO_3 radical, superimposed on the FPA-Q2 potential energy curve along the distinguished reaction coordinate τ. The left and right panels correspond to the bare (V_e) and ZPVE-corrected (V_0) potential energy functions, respectively. Blue, red, and green wave function curves correspond to predominantly *trans*-HO_3, *cis*-HO_3, and delocalized states, in order. The quartic force field representations of the potential energy surface in the vicinity of the *trans*-HO_3 and *cis*-HO_3 wells are depicted by dashed curves in the left panel.

The torsional fundamental frequencies of *trans*-HO_3 given by the V_e and V_0 potentials are 151 and 138 cm^{-1}, respectively. The corresponding FPA-Q2 harmonic frequency is ω_6 = 170 cm^{-1}, which is reproduced exactly by a quadratic expansion of $V_e(\tau)$. Thus, the anharmonicity of

the *trans*-HO_3 torsion fundamental produced by the best one-dimensional (1-D) potential (V_0) is –32 cm^{-1}. In comparison, the diagonal and off-diagonal anharmonicities predicted by VPT2 are –24 and –16 cm^{-1}, respectively. Because the 1-D variational results are expected to contain all of the former and some of the latter VPT2 anharmonicity, the agreement between the two methods is quite satisfactory. A similar conclusion arises for *trans*-DO_3, for which VPT2 yields diagonal and off-diagonal torsional anharmonicity components of –14 and –10 cm^{-1}, respectively, whereas the 1-D variational computation gives $\nu_6 - \omega_6 = -20$ cm^{-1}. Overall the consonance of vibrational methods validates the application of VPT2 for *trans*-HO_3 and substantiates the high level of agreement between the VPT2 and experimental $(\nu_1 - \nu_6) - \nu_1$ values (Table 4.10).

The *cis*-HO_3 conformer presents much greater difficulties for an accurate vibrational treatment than its *trans* counterpart. The torsional fundamentals of *cis*-HO_3 supported by the V_e and V_0 potentials are 157 and 127 cm^{-1}, evidencing a large coupling effect with other modes. The torsional anharmonicity arising from the V_0 potential is –83 cm^{-1}, as compared to diagonal and off-diagonal anharmonicities of –22 cm^{-1} and –30 cm^{-1}, respectively, from VPT2. Figure 4.4 reveals that the upper state (n = 4) connected with the *cis*-HO_3 torsional fundamental is not strongly localized in the *cis* well. The mode coupling and delocalization problems observed for *cis*-HO_3 are largely present for *cis*-DO_3 as well.

TABLE 4.11 Torsional energy levels (cm^{-1})[a,b] of HO_3 and DO_3 from the bare (V_e) and ZPVE-corrected (V_0) DRP potential functions.

			HO_3					DO_3	
n	parity	well	$E_n(V_e)$	$E_n(V_0)$	n	parity	well	$E_n(V_e)$	$E_n(V_0)$
0	+	*trans*	81.2	74.7	0	+	*trans*	62.0	57.7
1	–	*trans*	232.1	212.3	1	–	*trans*	179.7	166.1
2	+	*cis*	210.2	245.4	2	+	*cis*	190.8	215.0
3	+	*trans*	358.7	326.9	3	+	*trans*	285.5	262.3
4	–	*cis*	367.6	372.1	4	–	*cis*	324.8	330.5
5	–	mix	461.9	434.5	5	–	mix	376.0	346.4
6	+	mix	473.4	455.6	6	+	mix	416.6	392.0
7	+	mix	596.6	579.4	7	+	mix	461.0	440.3
8	–	mix	599.6	581.9	8	–	mix	480.5	452.3

[a]Referenced to the *trans* potential energy minimum. [b]The eigenstates for levels higher than listed here largely exhibit free-rotor characteristics, asymptotically approaching a doubly-degenerate energy dependence that is quadratic in an effective vibrational angular momentum quantum number.[131]

4.4.5 QUANTUM TUNNELING ANALYSIS

The isotopic shifts cause the barrier for the HO_3 path to be 6% lower than for DO_3 and narrower by 33% at the zero-point energy of the reaction mode. Our exact scattering calculation on the one-dimensional DRP gives a tunneling probability $P_H = 3.95\times10^{-3}$ for the H isomerization reaction, which is 47 times larger than that for D isomerization ($P_D = 8.37\times10^{-5}$). The tunneling half-lives, derived from our exact scattering tunneling probabilities, for H and D tunneling are 1.39×10^{-11} s and 8.55×10^{-10} s, respectively. The key parameters and results of our WKB analysis of the *cis*-HO_3 – *trans*-HO_3 isomerization reaction are summarized in Table B28. The tunneling

half-lives produced via exact scattering are smaller by 22% for H tunneling and 25% for D tunneling, when compared to results obtained via the WKB approximation.

4.5 CONCLUSION

Difficult riddles surrounding the HO_3 species have been explored utilizing focal point analyses (FPA) to obtain *ab initio* energetics that push the boundaries of accuracy of single-reference coupled-cluster methods. FPA energetics were obtained with electron correlation treatments through CCSDTQ(P) and with basis sets up to cc-pV6Z. The dissociation energy (D_0) of *trans*-HO_3 into O_2 and OH was found to be 2.71 kcal mol^{-1}, smaller than experiment by only 0.23 kcal mol^{-1}. Likewise, the *cis*-*trans* energy separation (ΔE_0^{tc}) and barrier height (ΔE_0^{b}) of isomerization were found to be 0.52 kcal mol^{-1} and 0.27 kcal mol^{-1}, respectively, giving the most accurate results to date.

We report a new semiexperimental equilibrium structure of *trans*-HO_3 utilizing FPA-Q2 vibration-rotation interaction constants in conjunction with existing microwave rotational constants. A systematic analysis of fitting procedures was performed in which 96 possibilities were scrutinized. We find that the molecular structure is most sensitive to ZPV effects from the HOO bending mode, and not the torsional mode as previously stated. Large improvements to the previously reported anomalous $r(H_1O_2)$ values were made by correcting with α_3 terms alone. Scaling the HOO bend contributions constituting α_3 produces a *trans*-HO_3 structure that exhibits a $r(H_1O_2)$ value of 0.9690 Å, in much better agreement with both FPA-Q3 and free OH. We also conclude that HO_3 only has weak central O–O bonding possibilities, as the formation of a normal central covalent bond in HO_3 would be very unfavorable on energetics grounds.

Our FPA-Q2 quartic force field (QFF) produces combination bands in excellent agreement with experiment. However, the FPA-Q2 O–H stretching fundamental frequency is smaller than experiment by 11 cm^{-1}. Our analysis of this mode finds that there is a contest between Coriolis and off-diagonal anharmonicity contributions for which VPT2 has apparent difficulties. Otherwise VPT2 has been shown to perform well for this system for both vibrational frequencies and molecular structure, which is counter to previous statements. Lastly, our results give conclusive evidence that the reason that *cis*-HO_3 has been missed by all previous experimental studies is because it converts to *trans*-HO_3 within a few picoseconds by quantum mechanical tunneling, even under cryogenic conditions.

4.6 SUPPLEMENTARY MATERIAL

The Supplementary Material for this chapter is provided in Appendix B.

4.7 ACKNOWLEDGEMENTS

This work was supported by The Department of Energy, Office of Basic Sciences, Computational and Theoretical Chemistry Grant DE-SC0015512. The high-level *ab initio* computations utilized resources of the National Energy Research Scientific Computing Center, a DOE office of Science User Facility supported by the Office of Sciences of the U.S. Department of Energy under grant No. DE-AC02-05CH11231.

4.8 REFERENCES

(1) Sridharan, U. C.; Klein, F. S.; Kaufman, F., *J. Chem. Phys.* **1985**, *82*, 592-593.

(2) Polanyi, J. C.; Sloan, J. J., *Int. J. Chem. Kinet.* **1975**, *1*, 51.

(3) Klenerman, D.; Smith, I. W. M., *J. Chem. Soc., Faraday Trans. 2.* **1987**, *83*, 229-241.

(4) McCabe, D. C.; Smith, I. W. M.; Rajakumar, B.; Ravishankara, A. R., *Chem. Phys. Lett.* **2006**, *421*, 111-117.

(5) Speranza, M., *Inorg. Chem.* **1996**, *35*, 6140-6151.

(6) Murray, C.; Derro, E. L.; Sechler, T. D.; Lester, M. I., *J. Phys. Chem. A* **2007**, *111*, 4727-4730.

(7) Murray, C.; Derro, E. L.; Sechler, T. D.; Lester, M. I., *Acc. Chem. Res.* **2008**, *42*, 419-427.

(8) Le Picard, S. D.; Tizniti, M.; Canosa, A.; Sims, I. R.; Smith, I. W. M., *Science* **2010**, *328*, 1258-1262.

(9) Cacace, F.; de Petris, G.; Pepi, F.; Troiani, A., *Science* **1999**, *285*, 81-82.

(10) Tizniti, M.; Le Picard, S. D.; Canosa, A.; Sims, I. R.; Smith, I. W. M., *Phys. Chem. Chem. Phys* **2010**, *12*, 12702-12710.

(11) Nelander, B.; Engdahl, A.; Svensson, T., *Chem. Phys. Lett.* **2000**, *332*, 403-408.

(12) Cooper, P. D.; Moore, M. H.; Hudson, R. L., *J. Phys. Chem. A* **2006**, *110*, 7985-7988.

(13) Zheng, W.; Jewitt, D.; Kaiser, R. I., *Phys. Chem. Chem. Phys* **2007**, *9*, 2556-2563.

(14) Derro, E. L.; Murray, C.; Sechler, T. D.; Lester, M. I., *J. Phys. Chem. A* **2007**, *111*, 11592-11601.

(15) Derro, E. L.; Sechler, T. D.; Murray, C.; Lester, M. I., *J. Chem. Phys.* **2008**, *128*, 244313.

(16) Derro, E. L.; Sechler, T. D.; Murray, C.; Lester, M. I., *J. Phys. Chem. A* **2008**, *112*, 9269-9276.

(17) Raston, P. L.; Liang, T.; Douberly, G. E., *J. Chem. Phys.* **2012**, *137*, 184302.

(18) Liang, T.; Raston, P. L.; Douberly, G. E., *ChemPhysChem* **2013**, *14*, 764-770.

(19) Liang, T.; Magers, D. B.; Raston, P. L.; Allen, W. D.; Douberly, G. E., *J. Phys. Chem. Lett.* **2013**, *4*, 3584-3589.

(20) Suma, K.; Sumiyoshi, Y.; Endo, Y., *Science* **2005**, *308*, 1885-1886.

(21) McCarthy, M. C.; Lattanzi, V.; Kokkin, D.; Martinez Jr, O.; Stanton, J. F., *J. Chem. Phys.* **2012**, *136*, 034303.

(22) Zou, L.; Hays, B. M.; Weaver, S. L. W., *J. Phys. Chem. A* **2015**, *120*, 657-667.

(23) Barreau, L.; Martinez, O.; Crabtree, K. N.; Womack, C. C.; Stanton, J. F.; McCarthy, M. C., *J. Phys. Chem. A* **2017**, *121*, 6296-6303.

(24) Suma, K.; Sumiyoshi, Y.; Endo, Y., *J. Chem. Phys.* **2013**, *139*, 094301.

(25) Blint, R. J.; Newton, M. D., *J. Chem. Phys.* **1973**, *59*, 6220-6228.

(26) Mathisen, K. B.; Siegbahn, P. E. M., *Chem. Phys.* **1984**, *90*, 225-230.

(27) Dupuis, M.; Fitzgerald, G.; Hammond, B.; Jr., W. A. L.; III, H. F. S., *J. Chem. Phys.* **1986**, *84*, 2691-2697.

(28) Vincent, M. A.; Hillier, I. H., *J. Phys. Chem.* **1995**, *99*, 3109-3113.

(29) Jungkamp, T. P. W.; Seinfeld, J. H., *Chem. Phys. Lett.* **1996**, *257*, 15-22.

(30) Varandas, A. J. C.; Yu, H. G., *Mol. Phys.* **1997**, *91*, 301-318.

(31) Aloisio, S.; Francisco, J. S., *J. Am. Chem. Soc* **1999**, *121*, 8592-8596.

(32) Setokuchi, O.; Sato, M.; Matuzawa, S., *J. Phys. Chem. A* **2000**, *104*, 3204-3210.

(33) Yu, H. G.; Varandas, A. J. C., *Chem. Phys. Lett.* **2001**, *334*, 173-178.

(34) Denis, P. A.; Kieninger, M.; Ventura, O. N.; Cachau, R. E.; Diercksen, G. H. F., *Chem. Phys. Lett.* **2002**, *365*, 440-449.

(35) Chalmet, S.; Ruiz-López, M. F., *ChemPhysChem* **2006**, *7*, 463-467.

(36) Mansergas, A.; Anglada, J. M.; Olivella, S.; Ruiz-Lopez, M. F.; Martins-Costa, M., *Phys. Chem. Chem. Phys* **2007**, *9*, 5865-5873.

(37) Varner, M. E.; Harding, M. E.; Gauss, J.; Stanton, J. F., *Chem. Phys.* **2008**, *346*, 53-55.

(38) Braams, B. J.; Yu, H.-G., *Phys. Chem. Chem. Phys* **2008**, *10*, 3150-3155.

(39) Varner, M. E.; Harding, M. E.; Vázquez, J.; Gauss, J.; Stanton, J. F., *J. Phys. Chem. A* **2009**, *113*, 11238-11241.

(40) Anglada, J. M.; Olivella, S.; Solé, A., *J.Chem. Theory Comput.* **2010**, *6*, 2743-2750.

(41) Varandas, A. J. C., *Phys. Chem. Chem. Phys* **2011**, *13*, 15619-15623.

(42) Beames, J. M.; Lester, M. I.; Murray, C.; Varner, M. E.; Stanton, J. F., *J. Chem. Phys.* **2011**, *134*, 044304.

(43) Varandas, A., *Phys. Chem. Chem. Phys* **2011**, *13*, 9796-9811.

(44) Varandas, A., *J. Chem. Theory Comput.* **2012**, *8*, 428-441.

(45) Zhou, Y.; Hu, H.; Li, L.; Hou, H.; Wang, B., *Comput. Theor. Chem.* **2013**, *1026*, 24-30.

(46) Hoy, E. P.; Schwerdtfeger, C. A.; Mazziotti, D. A., *J. Phys. Chem. A* **2013**, *117*, 1817-1825.

(47) Varandas, A. J., *Int. J. Quantum Chem.* **2014**, *114*, 1327-1349.

(48) Fabian, W. M. F.; Kalcher, J.; Janoschek, R., *Theor. Chem. Acc.* **2005**, *114*, 182-188.

(49) Cerkovnik, J.; Eržen, E.; Koller, J.; Plesničar, B., *J. Am. Chem. Soc* **2002**, *124*, 404-409.

(50) Numerov, B., *Astron. Nachr.* **1927**, *230*, 359-364.

(51) Cooley, J. W., *Math. Comput.* **1961**, *15*, 363-374.

(52) Schreiner, P. R.; Reisenauer, H. P.; Pickard Iv, F. C.; Simmonett, A. C.; Allen, W. D.; Mátyus, E.; Császár, A. G., *Nature* **2008**, *453*, 906.

(53) Schreiner, P. R.; Reisenauer, H. P.; Ley, D.; Gerbig, D.; Wu, C.-H.; Allen, W. D., *Science* **2011**, *332*, 1300-1303.

(54) Schreiner, P. R.; Wagner, J. P.; Reisenauer, H. P.; Gerbig, D.; Ley, D.; Sarka, J.; Császár, A. G.; Vaughn, A.; Allen, W. D., *J. Am. Chem. Soc.* **2015**, *137*, 7828-7834.

(55) Wagner, J. P.; Bartlett, M. A.; Allen, W. D.; Duncan, M. A., *ACS Earth Space Chem.* **2017**, *1*, 361-367.

(56) Linden, M. M.; Wagner, J. P.; Bernhardt, B.; Bartlett, M. A.; Allen, W. D.; Schreiner, P. R., *J. Phys. Chem. Lett.* **2018**, *9*, 1663-1667.

(57) Roothaan, C. C. J., *Rev. Mod. Phys.* **1960**, *32*, 179-185.

(58) Pople, J. A.; Nesbet, R. K., *J. Chem. Phys.* **1954**, *22*, 571-572.

(59) Møller, C.; Plesset, M. S., *Phys. Rev.* **1934**, *46*, 618.

(60) Čížek, J., *J. Chem. Phys.* **1966**, *45*, 4256-4266.

(61) Crawford, T. D.; Schaefer, H. F., An Introduction to Coupled Cluster Theory for Computational Chemists. In *Rev. Comput. Chem*, John Wiley & Sons, Inc.: 2007; pp 33-136.

(62) Purvis, G. D.; Bartlett, R. J., *J. Chem. Phys.* **1982**, *76*, 1910.

(63) Raghavachari, K.; Trucks, G. W.; Pople, J. A.; Head-Gordon, M., *Chem. Phys. Lett.* **1989**, *157*, 479-483.

(64) Noga, J.; Bartlett, R. J., *J. Chem. Phys.* **1987**, *86*, 7041-7050.

(65) Bomble, Y. J.; Stanton, J. F.; Kállay, M.; Gauss, J., *J. Chem. Phys.* **2005**, *123*, 054101.

(66) Kucharksi, S. A.; Bartlett, R. J., *J. Chem. Phys.* **1992**, *97*, 4282-4288.

(67) Kállay, M.; Gauss, J., *J. Chem. Phys.* **2005**, *123*, 214105.

(68) Kállay, M.; Gauss, J., *J. Chem. Phys.* **2008**, *129*, 144101.

(69) Dunning, T. H., Jr., *J. Chem. Phys.* **1989**, *90*, 1007-1023.

(70) Peterson, K. A.; Woon, D. E.; Dunning, T. H., Jr., *J. Chem. Phys.* **1994**, *100*, 7410-7415.

(71) Woon, D. E.; Dunning, T. H., Jr., *J. Chem. Phys.* **1995**, *103*, 4572-4585.

(72) East, A. L. L.; Allen, W. D., *J. Chem. Phys.* **1993**, *99*, 4638-4650.

(73) Császár, A. G.; Allen, W. D.; Schaefer III, H. F., *J. Chem. Phys.* **1998**, *108*, 9751-9764.

(74) Császár, A. G.; Tarczay, G.; Leininger, M. L.; Polyansky, O. L.; Tennyson, J.; Allen, W. D., In *Spectroscopy from Space*, J. Demaison, K. S., Ed. Kluwer: Dordrecht: The Netherlands, 2001; pp 317-339.

(75) Feller, D., *J. Chem. Phys.* **1992**, *96*, 6104-6114.

(76) Helgaker, T.; Klopper, W.; Koch, H.; Noga, J., *J. Chem. Phys.* **1997**, *106*, 9639-9646.

(77) MolStruct is an abstract program developed by Wesley D. Allen for use within Mathematica (Wolfram Research Inc., Champaign, IL) to perform diverse fits of molecular structures to sets of isotopologic rotational constants.

(78) *MOLPRO, version 2012.1, a package of ab initio programs, H.-J. Werner, P. J. Knowles, G. Knizia, F. R. Manby, M. Schütz, and others , see http://www.molpro.net.*

(79) Ajith Perera, S.; Bartlett, R. J., *Chem. Phys. Lett.* **1993**, *216*, 606-612.

(80) Handy, N. C.; Yamaguchi, Y.; Schaefer III, H. F., *J. Chem. Phys.* **1986**, *84*, 4481-4484.

(81) *CFOUR,* a quantum chemical program package written by J.F. Stanton, J. Gauss, M.E. Harding, P.G. Szalay with contributions from A.A. Auer, R.J. Bartlett, U. Benedikt, C. Berger, D.E. Bernholdt, Y.J. Bomble, L. Cheng, O. Christiansen, M. Heckert, O. Heun, C. Huber, T.-C. Jagau, D. Jonsson, J. Jusélius, K. Klein, W.J. Lauderdale, F. Lipparini, D.A. Matthews, T. Metzroth, L.A. Mück, D.P. O'Neill, D.R. Price, E. Prochnow, C. Puzzarini, K. Ruud, F.

Schiffmann, W. Schwalbach, C. Simmons, S. Stopkowicz, A. Tajti, J. Vázquez, F. Wang, J.D. Watts and the integral packages *MOLECULE* (J. Almlöf and P.R. Taylor), *PROPS* (P.R. Taylor), *ABACUS* (T. Helgaker, H.J. Aa. Jensen, P. Jørgensen, and J. Olsen), and *ECP* routines by A. V. Mitin and C. van Wüllen. For the current version, see *http://www.cfour.de*.

(82) Collins, M. A., *Adv. Chem. Phys.* **1982**, *46*, 481.

(83) Allen, W. D.; Bodi, A.; Szalay, V.; Császár, A. G., *J. Chem. Phys.* **2006**, *124*, 224310.

(84) The unusually flat torsional potential of *trans*-HO_3 demands extreme care in executing anharmonic force field computations. We found that a torsional displacement step size of 0.02 rad produces severe numerical errors in the quartic force constants involving this coordinate. Further tests demonstrated that setting this step size to either 0.04 or 0.06 rad gives much more reliable and consistent results.

(85) *INTDER2005,* is a general program developed by Wesley D. Allen and co-workers which performs various vibrational vibrational analyses and higher-order nonlinear transformations among force field representations.

(86) Allen, W. D.; Császár, A. G., *J. Chem. Phys.* **1993**, *98*, 2983-3015.

(87) Allen, W. D.; Császár, A. G.; Szalay, V.; Mills, I. M., *Mol. Phys.* **1996**, *89*, 1213-1221.

(88) Allen, W. D.; Császár, A. G.; Horner, D. A., *J. Am. Chem. Soc* **1992**, *114*, 6834-6849.

(89) Nielsen, H. H., *Rev. Mod. Phys.* **1951**, *23*, 90-136.

(90) Clabo, D. A.; Allen, W. D.; Remington, R. B.; Yamaguchi, Y.; Schaefer, H. F., *Chem. Phys.* **1988**, *123*, 187-239.

(91) Vázquez, J.; Stanton, J. F., Semiexperimental Equilibrium Structures: Computational Aspects. In *Equilibrium Molecular Structures: From Spectroscopy to Quantum Chemistry*, Demaison, J.; Boggs, J. E.; Császár, A. G., Eds. CRC Press: Boca Raton, FL, 2011; pp 53-88.

(92) Kraitchman, J., *Am. J. Phys.* **1953**, *21*, 17-24.

(93) Costain, C. C., *J. Chem. Phys.* **1958**, *29*, 864-874.

(94) Mohsen, R., *Quantum Theory of Tunneling*; World Scientific: Singapore, 2003.

(95) Denis, P. A.; Ornellas, F. R., *J. Phys. Chem. A* **2009**, *113*, 499-506.

(96) Campuzano-Jost, P.; Croce, A. E.; Hippler, H.; Siefke, M.; Troe, J., *J. Chem. Phys.* **1995**, *102*, 5317-5326.

(97) Lee, T. J.; Taylor, P. R., *Int. J. Quantum Chem.* **1989**, *36*, 199-207.

(98) Lee, T. J.; Jayatilaka, D., *Chem. Phys. Lett.* **1993**, *201*, 1.

(99) Lauderdale, W. J.; Stanton, J. F.; Gauss, J.; Watts, J. D.; Bartlett, R. J., *Chem. Phys. Lett.* **1991**, *187*, 21-28.

(100) Lauderdale, W. J.; Stanton, J. F.; Gauss, J.; Watts, J. D.; Bartlett, R. J., *J. Chem. Phys.* **1992**, *97*, 6606-6620.

(101) Urban, M.; Watts, J. D.; Bartlett, R. J., *Int. J. Quantum Chem.* **1994**, *52*, 211-225.

(102) Bartlett, M. A.; Liang, T.; Pu, L.; Schaefer, H. F.; Allen, W. D., *J. Chem. Phys.* **2018**, *148*, 094303.

(103) Lee, T. J.; Allen, W. D.; Schaefer III, H. F., *J. Chem. Phys.* **1987**, *87*, 7062-7075.

(104) Huber, K. P.; Herzberg, G., In *Molecular Spectra and Molecular Structure. IV. Constants of Diatomic Molecules*, Springer, Ed. Van Noestrand Reinhold: New York, 1979; pp 498-508.

(105) Baraban, J. H.; Changala, P. B.; Stanton, J. F., *J. Mol. Spectrosc.* **2018**, *343*, 92-95.

(106) Ruscic, B.; Pinzon, R. E.; Laszewski, G. v.; Kodeboyina, D.; Burcat, A.; Leahy, D.; Montoy, D.; Wagner, A. F., *J. Phys. Conf. Ser.* **2005**, *16*, 561-570.

(107) Bader, R.F.W., *Atoms in Molecules: A Quantum Theory*; Clarendon Press, 1994.

(108) Weinhold, F., *J. Comput. Chem.* **2012**, *33*, 2363-2379.

(109) Jeziorski, B.; Moszynski, R.; Szalewicz, K., *Chem. Rev.* **1994**, *94*, 1887-1930.

(110) East, A. L. L.; Johnson, C. S.; Allen, W. D., *J. Chem. Phys.* **1993**, *98*, 1299-1328.

(111) East, A. L. L.; Allen, W. D.; Klippenstein, S. J., *J. Chem. Phys.* **1995**, *102*, 8506-8532.

(112) Mecke, R., *Z. Phys.* **1933**, *81*, 313-331.

(113) Darling, B. T.; Dennison, D. M., *Phys. Rev.* **1940**, *57*, 128-139.

(114) Oka, T.; Morino, Y., *J. Mol. Spectrosc.* **1961**, *6*, 472-482.

(115) Oka, T.; Morino, Y., *J. Mol. Spectrosc.* **1962**, *8*, 9-21.

(116) Legon, A. C.; Demaison, J., Other Spectroscopic Sources of Molecular Properties: Intermolecular Complexes as Examples. In *Equilibrium Molecular Structures: From Spectroscopy to Quantum Chemistry*, Demaison, J.; Boggs, J. E.; Császár, A. G., Eds. CRC Press: Boca Raton, FL, 2011; pp 205-231.

(117) Puzzarini, C.; Heckert, M.; Gauss, J., *J. Chem. Phys.* **2008**, *128*, 194108.

(118) Schuurman, M. S.; Allen, W. D.; Schaefer, H. F., *J. Comput. Chem.* **2005**, *26*, 1106-1112.

(119) Irikura, K. K., *J. Phys. Chem. Ref. Data* **2007**, *36*, 389-397.

(120) Grev, R. S.; Janssen, C. L.; Schaefer, H. F., III, *J. Chem. Phys.* **1991**, *95*, 5128-5132.

(121) Flowers, B. A.; Szalay, P. G.; Stanton, J. F.; Kállay, M.; Gauss, J.; Császár, A. G., *J. Phys. Chem. A* **2004**, *108*, 3195-3199.

(122) Brown, J. M.; Kerr, C. M. L.; Wayne, F. D.; Evenson, K. M.; Radford, H. E., *J. Mol. Spectrosc.* **1981**, *86*, 544-554.

(123) Konen, I. M.; Pollack, I. B.; Li, E. X. J.; Lester, M. I.; Varner, M. E.; Stanton, J. F., *J. Chem. Phys.* **2005**, *122*, 094320.

(124) Zhang, X.; Nimlos, M. R.; Ellison, G. B.; Varner, M. E.; Stanton, J. F., *J. Chem. Phys.* **2006**, *124*, 084305.

(125) Fink, E. H.; Ramsay, D. A., *J. Mol. Spectrosc.* **1997**, *185*, 304-324.

(126) Pushkarsky, M. B.; Zalyubovsky, S. J.; Miller, T. A., *J. Chem. Phys.* **2000**, *112*, 10695-10698.

(127) Dibble, T. S., *J. Comput. Chem.* **2005**, *26*, 836-845.

(128) Copan, A. V.; Schaefer, H. F.; Agarwal, J., *Mol. Phys.* **2015**, *113*, 2992-2998.

(129) Pulay, P.; Török, F., *Acta. Chim.* **1965**, *44*, 287.

(130) Keresztury, G.; Jalsovszky, G., *THEOCHEM* **1971**, *10*, 304-305.

(131) Crawford, T. D.; Allen, W. D., *Mol. Phys.* **2009**, *107*, 1041-1057.

APPENDIX A

SUPPORTING INFORMATION FOR CHAPTER 3

Table A1. Conformational energies for **MIN1** and **MIN2** at FC-ROCCSD(T)/cc-pVTZ//ROMP2/aug-cc-pVDZ level of theory. The labels identify each conformer as gauche (G), trans (T), or anticlinal (A) with respect to the dihedral angles $\tau_1(C_1C_2O_4O_5)$ and $\tau_2(C_2O_4O_5H_{12})$.[a]

MIN1		
τ_1	ΔEe (kcal mol^{-1})	ΔE_0 (kcal mol^{-1})
T	0.00	0.00
G$^-$	0.26	0.36

MIN2		
$\tau_1\tau_2$	ΔEe(kcal mol^{-1})	ΔE_0(kcal mol^{-1})
TA$^+$	0.00	0.00
TA$^-$	0.65	0.58
G$^-$A$^+$	0.95	0.91

[a]ΔE_0 derived with ROMP2/cc-pVDZ ZPVEs.

Table A2. FC-MP2/aug-cc-pVDZ harmonic vibrational frequencies (cm^{-1}) for rotamers of **MIN1** and **MIN2**.

MIN1		**MIN2**		
T	G^-	G^-A^+	TA^+	TA^-
105	116	68	67	46
203	212	143	147	143
249	250	225	222	205
306	304	247	247	220
344	377	277	278	276
449	393	376	340	344
531	609	422	453	442
805	780	508	483	486
919	928	644	591	611
928	931	802	822	818
947	944	860	889	884
1122	1111	914	918	916
1176	1170	960	940	936
1197	1190	1042	1065	1065
1218	1206	1163	1176	1176
1338	1353	1182	1178	1187
1356	1373	1315	1312	1318
1395	1395	1337	1346	1335
1404	1397	1345	1369	1370
1471	1469	1390	1386	1394
1477	1478	1467	1467	1469
1483	1485	1483	1478	1479
1502	1503	1496	1489	1491
3068	3073	3039	3071	3072
3072	3074	3071	3095	3078
3121	3122	3164	3171	3171
3162	3168	3177	3177	3175
3170	3170	3201	3189	3195
3176	3182	3327	3318	3323
3185	3185	3753	3740	3750

Table A3. Cartesian coordinates (Å) and depictions of FC-MP2/aug-cc-pVDZ optimized structures for the conformers of **MIN1** and **MIN2**.

MIN1, T, C_1

	X	*Y*	*Z*
C_1	−1.621579	0.876102	−0.012791
C_2	−0.463063	−0.037254	0.350466
C_3	−0.627283	−1.470247	−0.128767
O_4	0.717915	0.562612	−0.316775
O_5	1.821277	0.048458	0.135846
H_6	−2.540499	0.510963	0.470639
H_7	−1.778953	0.880763	−1.102529
H_8	−1.432930	1.905722	0.324279
H_9	−0.235913	0.000558	1.426815
H_{10}	−1.486045	−1.933737	0.382065
H_{11}	0.274980	−2.054649	0.097549
H_{12}	−0.809021	−1.489781	−1.214793

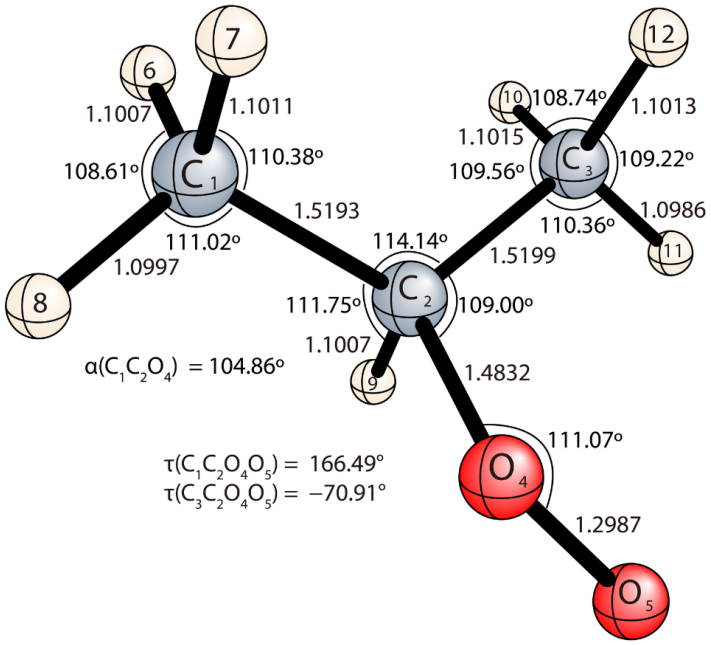

ROMP2/aug-cc–pVDZ

MIN1, G^{-} , C_1

	X	*Y*	*Z*
C_1	1.004013	−1.276030	−0.245664
C_2	0.570514	−0.000001	0.458935
C_3	1.004033	1.276018	−0.245672
O_4	−0.907464	0.000012	0.619873
O_5	−1.506295	0.000000	−0.531624
H_6	2.104004	−1.323284	−0.270221
H_7	0.626464	−2.162606	0.284543
H_8	0.625012	−1.284938	−1.277427
H_9	0.894608	0.000000	1.511456
H_{10}	2.104024	1.323260	−0.270221
H_{11}	0.625039	1.284921	−1.277438
H_{12}	0.626488	2.162602	0.284524

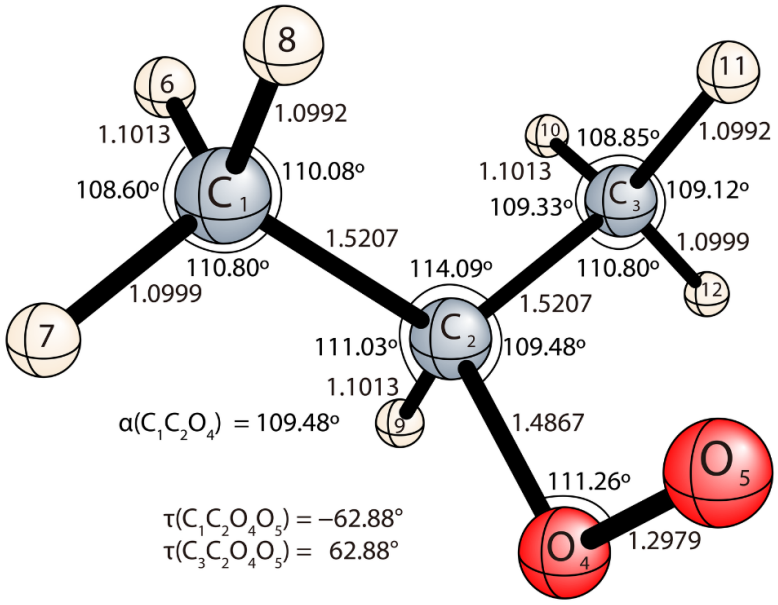

ROMP2/aug-cc–pVDZ

MIN2, $G^{-}A^{+}$, C_1

	X	*Y*	*Z*
C_1	1.059368	−1.169179	−0.222325
C_2	0.547208	0.094373	0.463649
C_3	0.871433	1.349035	−0.282161
O_4	−0.868767	0.015148	0.772754
O_5	−1.573414	0.001514	−0.524135
H_6	2.158368	−1.135848	−0.287800
H_7	0.770588	−2.061220	0.353252
H_8	0.652815	−1.245204	−1.241207
H_9	0.949792	0.148474	1.494847
H_{10}	0.469152	2.300627	0.065565
H_{11}	1.457150	1.324147	−1.201196
H_{12}	−1.960901	−0.888975	−0.471540

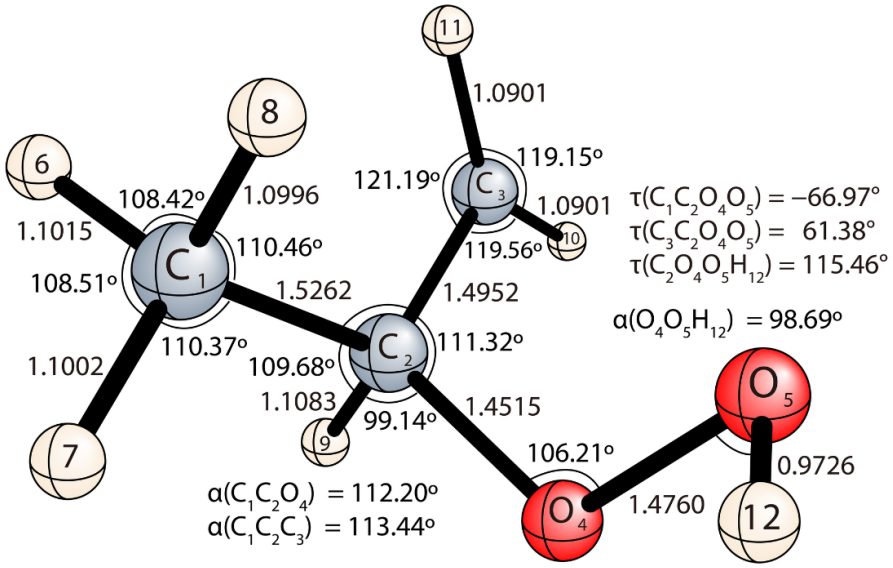

ROMP2/aug-cc–pVDZ

MIN2, TA^+, C_1

	X	*Y*	*Z*
C_1	1.697716	−0.682198	−0.003410
C_2	0.401646	0.052074	0.346491
C_3	0.402183	1.477853	−0.110546
O_4	−0.616699	−0.723624	−0.337086
O_5	−1.909528	−0.209721	0.134404
H_6	2.543037	−0.202411	0.511947
H_7	1.635696	−1.734643	0.310205
H_8	1.877361	−0.640338	−1.088790
H_9	0.198089	−0.010396	1.428386
H_{10}	0.190647	2.301641	0.570536
H_{11}	0.612701	1.700568	−1.159195
H_{12}	−2.128072	0.388243	−0.601754

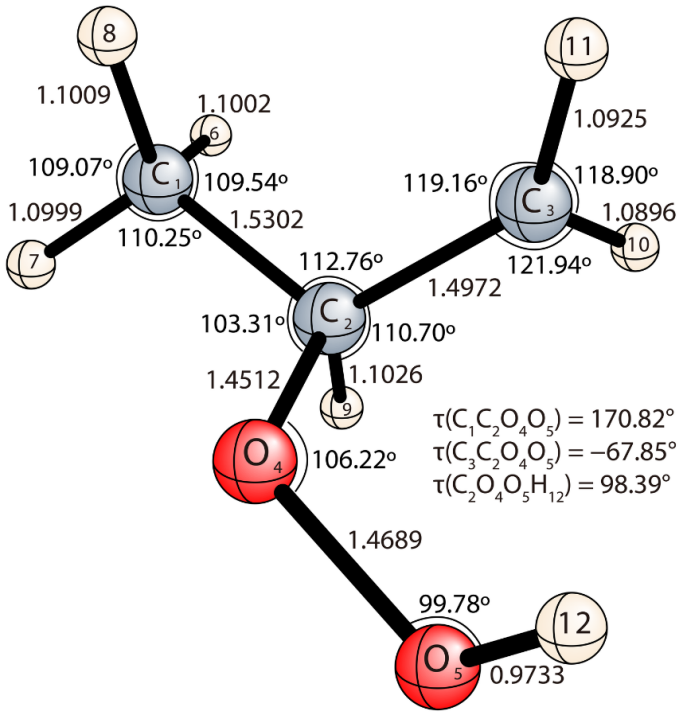

ROMP2/aug-cc–pVDZ

MIN2, TA^{-}, C_1

	X	*Y*	*Z*
C_1	1.684766	−0.720802	0.004158
C_2	0.414016	0.057568	0.342534
C_3	0.471874	1.485927	−0.097376
O_4	−0.622553	−0.673690	−0.368470
O_5	−1.894294	−0.026529	0.004578
H_6	2.537817	−0.279359	0.540736
H_7	1.583547	−1.775516	0.299649
H_8	1.883440	−0.669020	−1.077363
H_9	0.190517	−0.007339	1.421598
H_{10}	−0.000475	2.277249	0.483186
H_{11}	0.850971	1.719796	−1.094036
H_{12}	−2.308614	−0.776830	0.464827

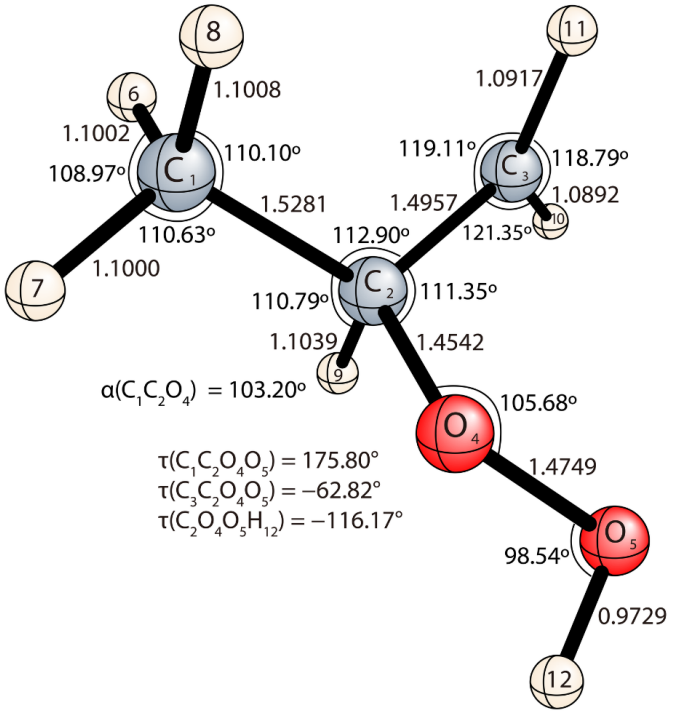

ROMP2/aug-cc–pVDZ

Table A4. Cartesian coordinates (Å) of FC-ROCCSD(T)/cc-pVTZ optimized structures; depictions of FC-ROCCSD(T)/cc-pVTZ and FC-ROCCSD(T)/cc-pVDZ structures.

i–propyl (C_s)

	X	*Y*	*Z*		*X*	*Y*	*Z*
C_1	0.220626	0.005464	–1.293549	H_6	–0.422952	–0.229585	–2.142668
C_2	–0.524540	–0.037390	0.000000	H_7	0.655319	0.999437	–1.478286
C_3	0.220626	0.005464	1.293549	H_8	1.056397	–0.701751	1.289578
H_4	–1.585835	0.178882	0.000000	H_9	0.655319	0.999437	1.478286
H_5	1.056397	–0.701751	–1.289578	H_{10}	–0.422952	–0.229585	2.142668

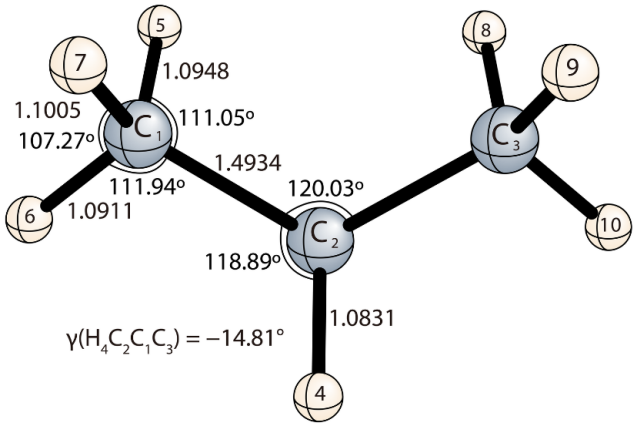

ROCCSD(T)/cc–pVTZ

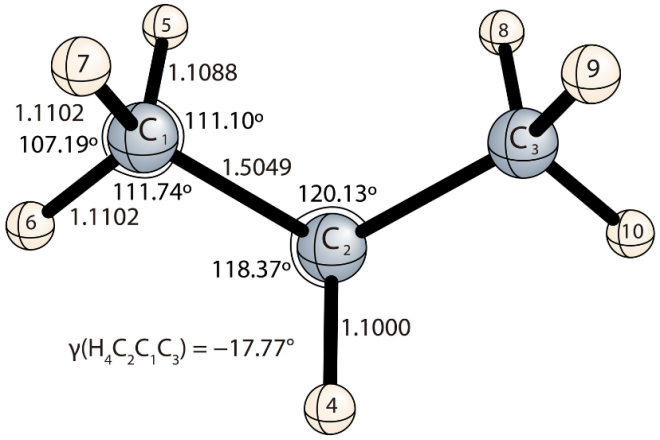

ROCCSD(T)/cc–pVDZ

Propene(C_s)

	X	*Y*	*Z*		*X*	*Y*	*Z*
C_1	–0.019741	0.000000	–0.037365	H_6	2.143654	0.000000	1.686999
C_2	0.041601	0.000000	1.463537	H_7	0.982615	0.000000	–0.469158
C_3	1.174888	0.000000	2.174874	H_8	–0.554177	–0.879197	–0.407071
H_4	–0.908870	0.000000	1.990254	H_9	–0.554177	0.879197	–0.407071
H_5	1.162638	0.000000	3.257503				

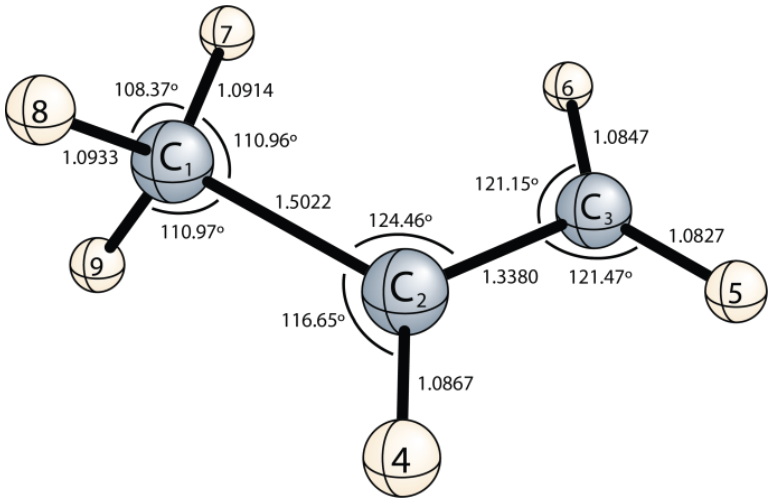

ROCCSD(T)/cc–pVTZ

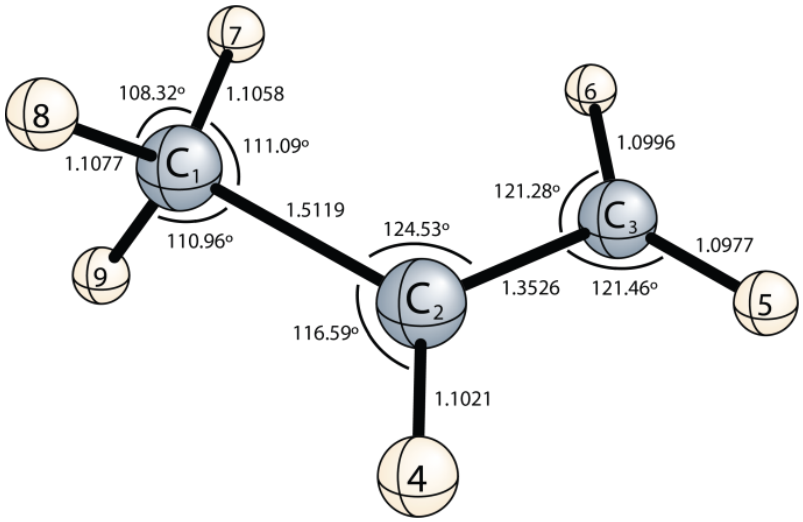

ROCCSD(T)/cc–pVDZ

Methyloxirane(C_1)

	X	*Y*	*Z*		*X*	*Y*	*Z*
C_1	0.048692	–0.182208	–1.553870	H_6	0.148668	–1.261647	–1.429990
C_2	0.043187	0.492212	–0.210037	H_7	0.880054	0.182634	–2.161890
C_3	0.692676	–0.115630	0.957650	H_8	–0.055606	1.574810	–0.218135
O_4	–0.736196	–0.142822	0.812899	H_9	1.183296	–1.077086	0.841776
H_5	–0.881422	0.019699	–2.088909	H_{10}	1.061862	0.512420	1.761361

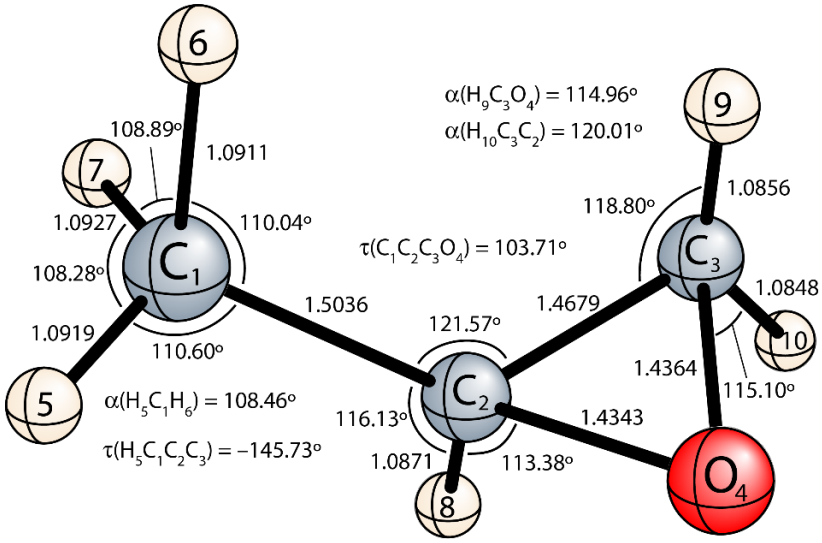

ROCCSD(T)/cc–pVTZ

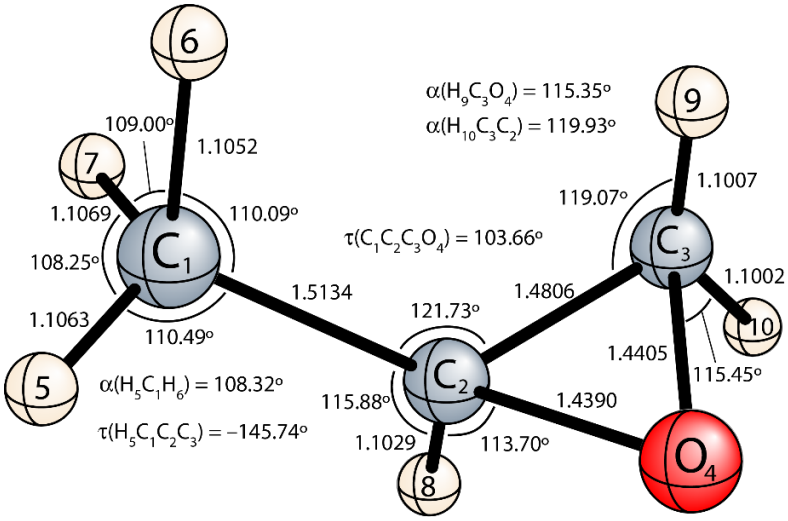

ROCCSD(T)/cc–pVDZ

Acetone(C_{2v})

	X	*Y*	*Z*		*X*	*Y*	*Z*
C_1	–1.286653	–0.703601	0.000066	H_6	–1.323270	–1.351705	–0.879302
C_2	–0.000001	0.097651	–0.000178	H_7	–2.141574	–0.030945	–0.000045
C_3	1.286687	–0.703543	0.000069	H_8	1.323253	–1.351808	–0.879182
O_4	–0.000028	1.313398	–0.000550	H_9	2.141578	–0.030848	–0.000234
H_5	–1.323190	–1.351328	0.879715	H_{10}	1.323335	–1.351105	0.879835

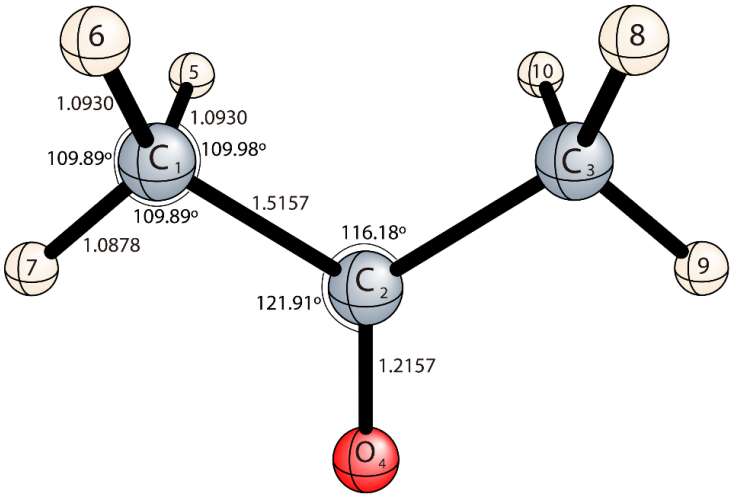

ROCCSD(T)/cc–pVTZ

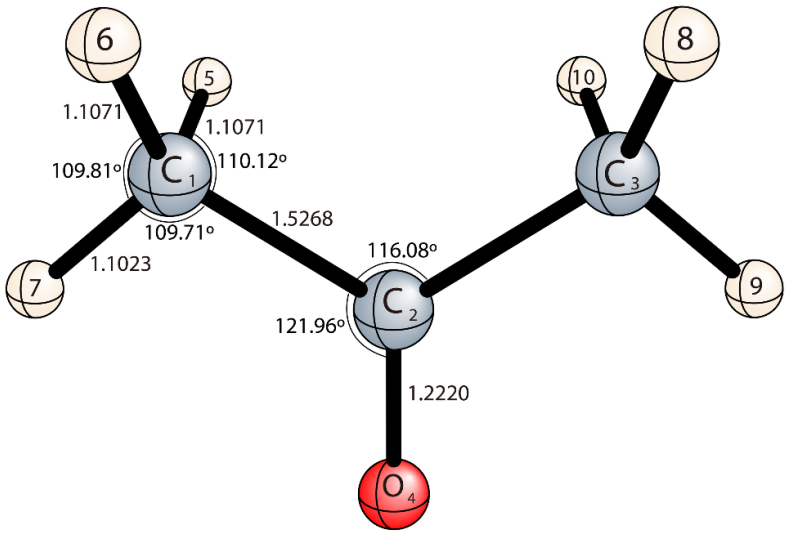

ROCCSD(T)/cc–pVDZ

MIN1(C_1)

	X	*Y*	*Z*		*X*	*Y*	*Z*
C_1	1.636656	0.848262	0.010853	H_7	1.474832	1.872583	−0.326189
C_2	0.457320	−0.034783	−0.347412	H_8	1.791180	0.853941	1.091710
C_3	0.599641	−1.467950	0.128743	H_9	0.242943	0.000309	−1.416875
O_4	−0.697055	0.580665	0.312459	H_{10}	1.437896	−1.945926	−0.382084
O_5	−1.825652	0.053775	−0.132575	H_{11}	0.787235	−1.491167	1.204454
H_6	2.540001	0.462515	−0.464367	H_{12}	−0.309337	−2.028621	−0.087115

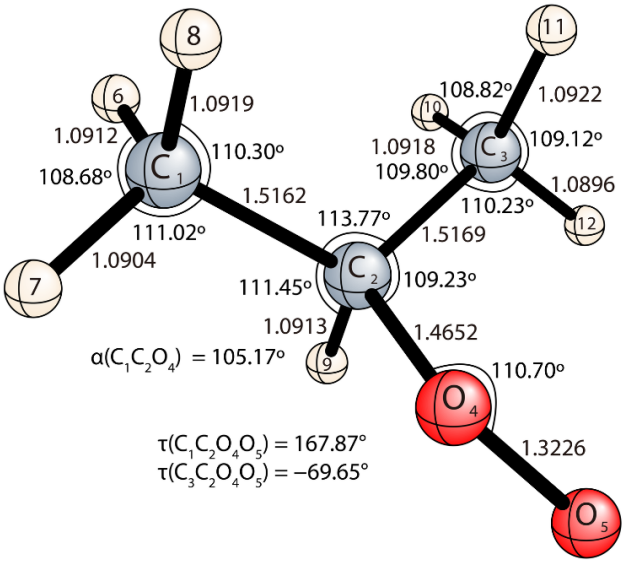

ROCCSD(T)/cc–pVTZ

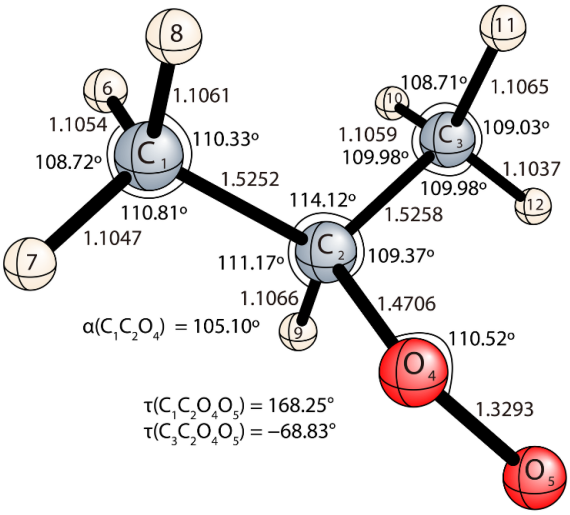

ROCCSD(T)/cc–pVDZ

MIN2(C_1)

	X	*Y*	*Z*		*X*	*Y*	*Z*
C_1	1.730325	0.724215	0.002944	H_7	1.621291	1.758369	−0.326439
C_2	0.475681	−0.073559	−0.344352	H_8	1.896264	0.711732	1.081872
C_3	0.545548	−1.485221	0.135537	H_9	0.292007	−0.045093	−1.421199
O_4	−0.580024	0.653090	0.309004	H_{10}	0.494801	−2.323836	−0.544082
O_5	−1.834577	0.088401	−0.157714	H_{11}	0.674914	−1.674065	1.194837
H_6	2.598052	0.281802	−0.487652	H_{12}	−2.018147	−0.539886	0.552842

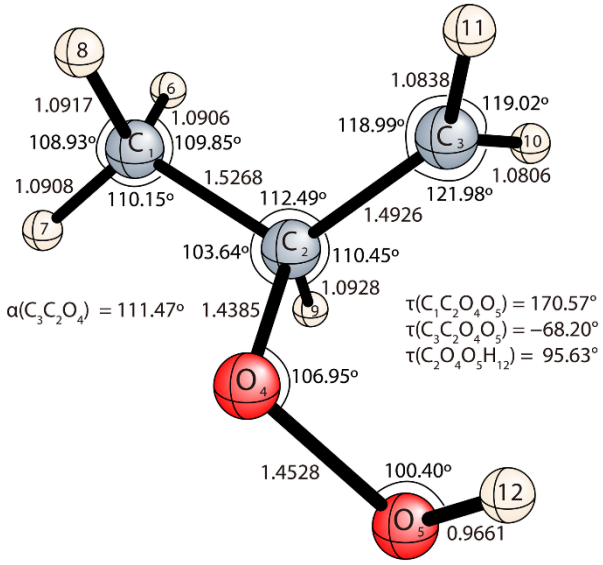

ROCCSD(T)/cc–pVTZ

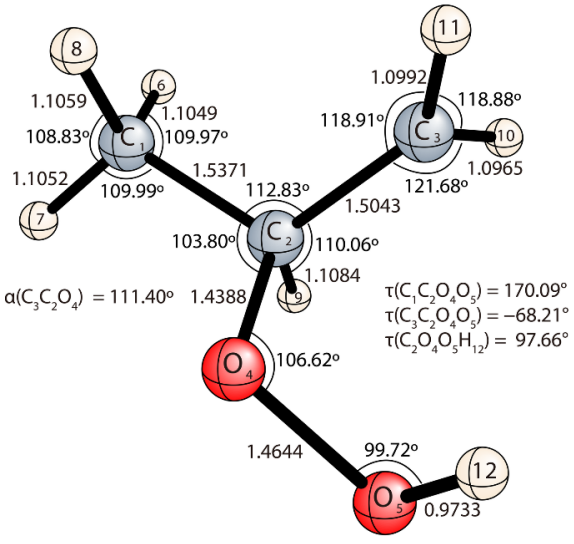

ROCCSD(T)/cc–pVDZ

TS1(C_1)

	X	*Y*	*Z*		*X*	*Y*	*Z*
C_1	1.656211	−0.810509	−0.325336	H_7	1.464578	−0.691329	−1.393231
C_2	0.879994	0.195773	0.468072	H_8	2.727637	−0.665023	−0.154461
C_3	0.468319	1.420326	−0.051698	H_9	0.838502	0.041243	1.540261
O_4	−0.993155	−0.822258	0.262469	H_{10}	0.286082	2.241257	0.633659
O_5	−1.685511	0.106193	−0.283510	H_{11}	0.819438	1.698945	−1.041298
H_6	1.402511	−1.829996	−0.033263	H_{12}	−0.800726	0.977367	−0.301698

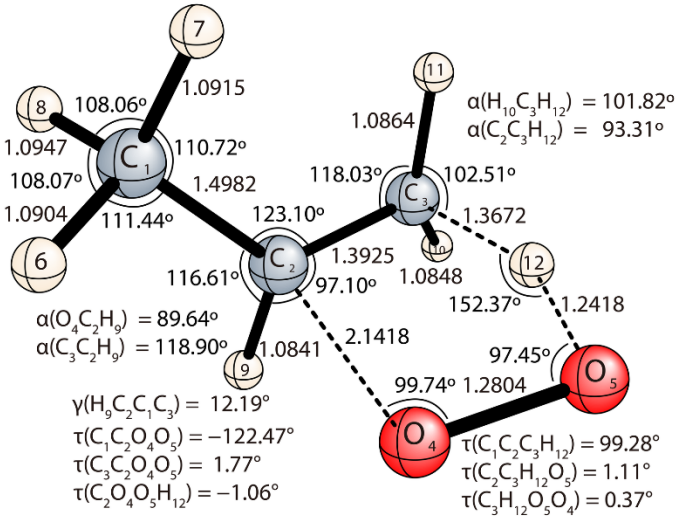

ROCCSD(T)/cc–pVTZ

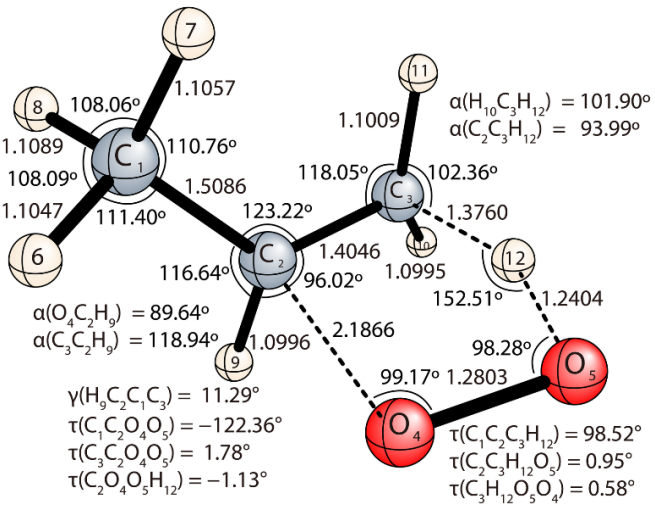

ROCCSD(T)/cc–pVDZ

TS2(C_1)

	X	*Y*	*Z*		*X*	*Y*	*Z*
C_1	−1.867291	−0.383898	0.074087	H_7	−2.084462	−1.391739	−0.283464
C_2	−0.487996	0.053736	−0.377034	H_8	−1.928423	−0.373989	1.163408
C_3	−0.025095	1.414169	0.139441	H_9	−0.396870	0.035107	−1.468036
O_4	0.469260	−0.849902	0.192183	H_{10}	−0.146099	2.280270	−0.504625
O_5	1.705063	−0.176493	−0.060771	H_{11}	−0.216365	1.600068	1.195262
H_6	−2.621070	0.295620	−0.328030	H_{12}	1.228005	0.937221	0.086724

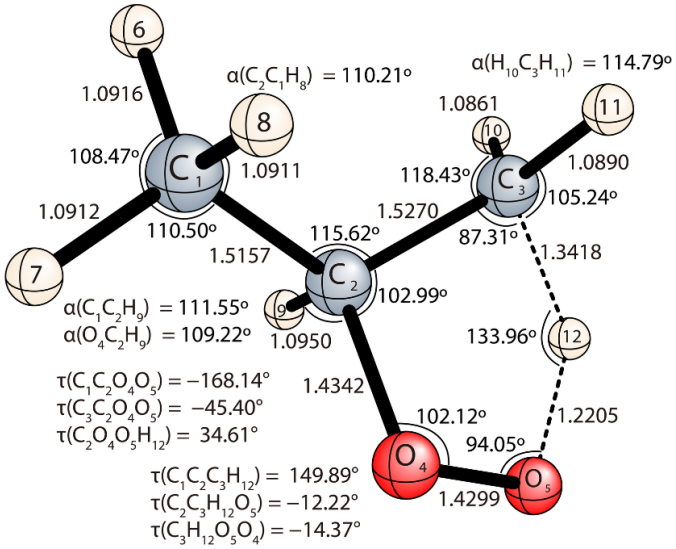

ROCCSD(T)/cc–pVTZ

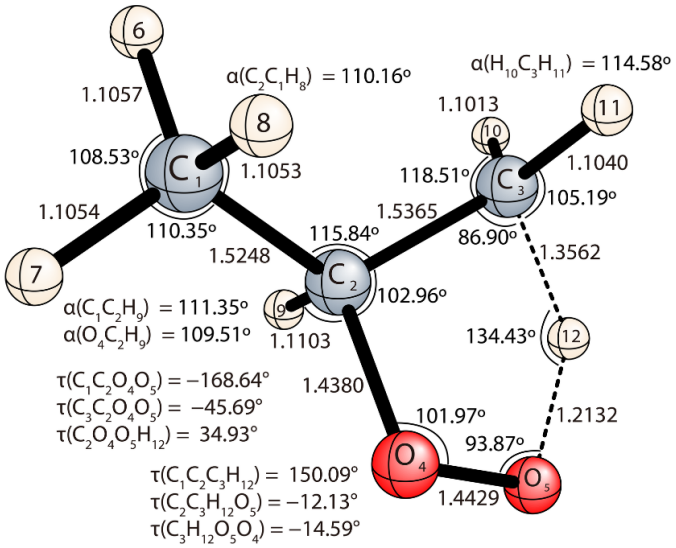

ROCCSD(T)/cc–pVDZ

TS3(C_1)

	X	*Y*	*Z*		*X*	*Y*	*Z*
C_1	1.706518	−0.901976	−0.002613	H_7	1.979778	−0.789763	−1.053374
C_2	0.761222	0.188774	0.418712	H_8	2.620256	−0.861049	0.595415
C_3	0.780776	1.431194	−0.179555	H_9	0.352371	0.113809	1.419898
O_4	−0.823946	−0.578883	−0.381380	H_{10}	0.197648	2.251640	0.218780
O_5	−1.954927	−0.022763	0.220790	H_{11}	1.291830	1.580373	−1.123325
H_6	1.247286	−1.880665	0.138434	H_{12}	−2.265960	0.585219	−0.463620

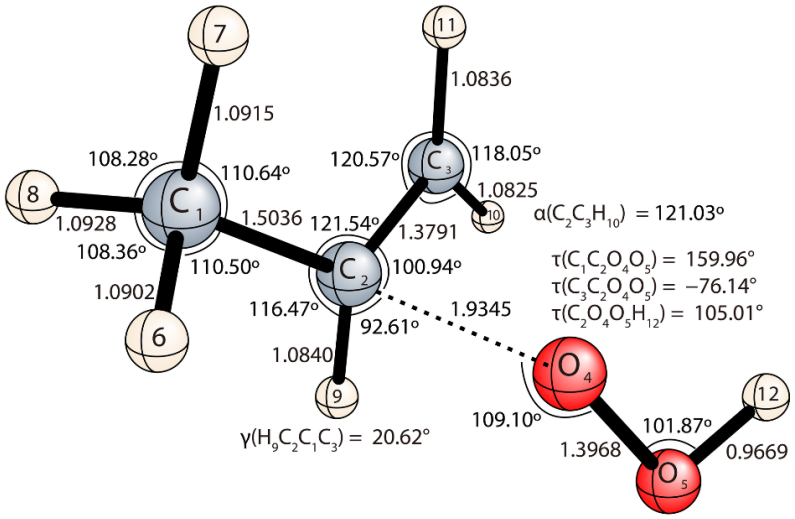

ROCCSD(T)/cc–pVTZ

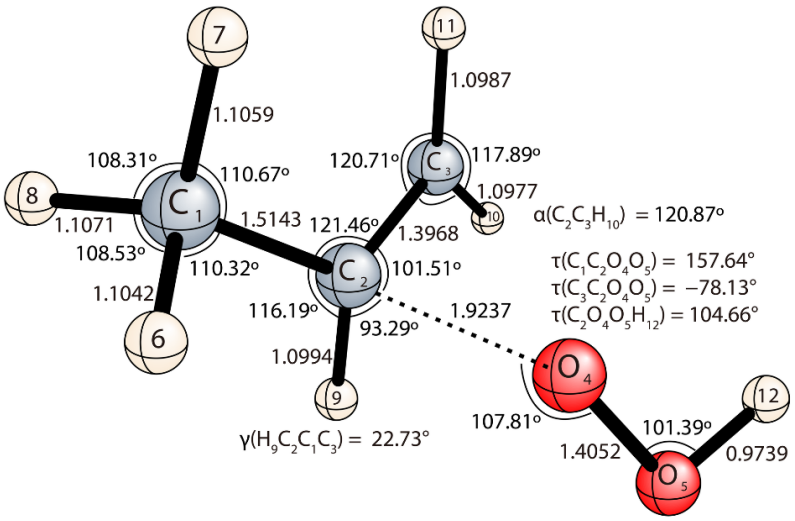

ROCCSD(T)/cc–pVDZ

TS4(C_1)

	X	*Y*	*Z*		*X*	*Y*	*Z*
C_1	−0.807774	−1.474683	0.136171	H_7	−1.652629	−1.945029	−0.372377
C_2	−0.558285	−0.093809	−0.422260	H_8	0.080412	−2.090580	−0.007264
C_3	−1.439250	1.008233	0.014302	H_9	−0.362412	−0.103679	−1.496935
O_4	0.412844	0.648381	0.279528	H_{10}	−1.511772	1.913290	−0.570513
O_5	1.945795	−0.105338	−0.037481	H_{11}	−1.897417	0.970149	0.992898
H_6	−1.021810	−1.412170	1.204792	H_{12}	2.334650	0.720436	−0.355939

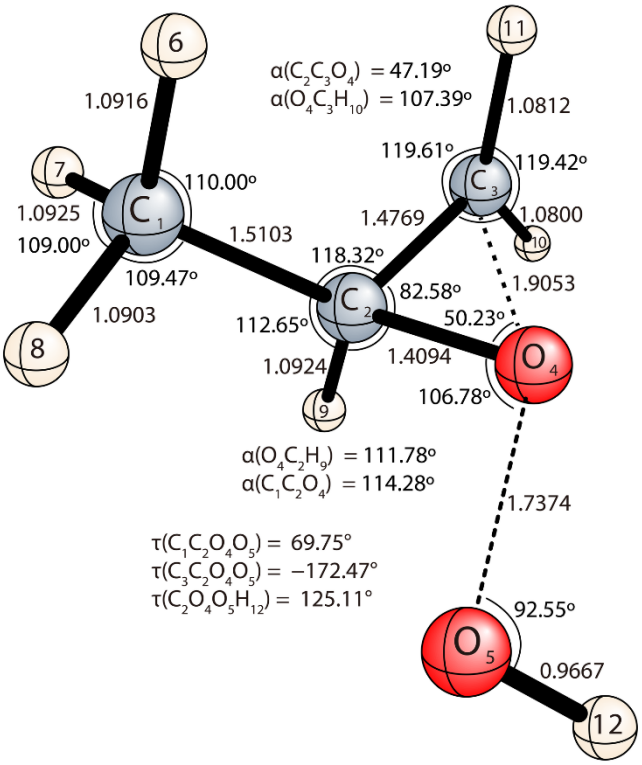

ROCCSD(T)/cc–pVTZ

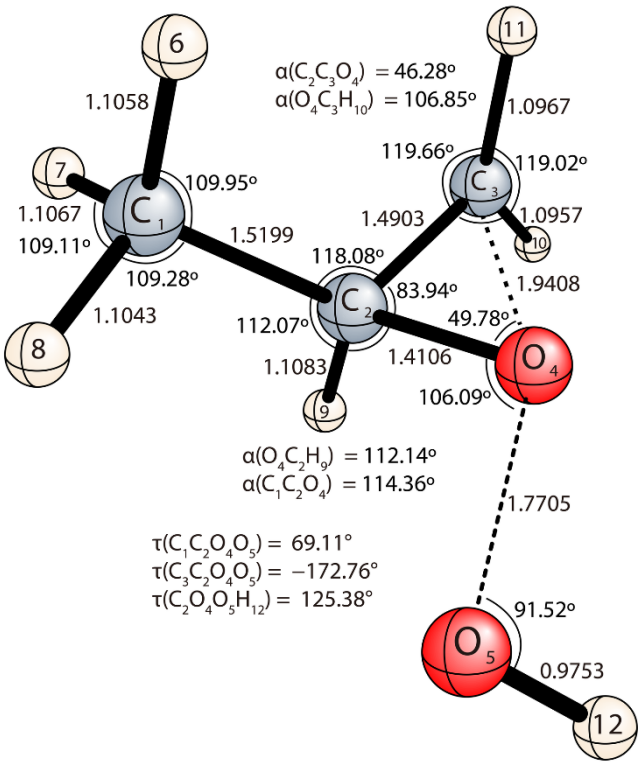

ROCCSD(T)/cc–pVDZ

Table A5. FC-ROCCSD(T)/cc-pVDZ harmonic vibrational frequencies (cm^{-1}).

i–propyl(C_s)	propene (C_s)	methyloxirane(C_1)	acetone (C_{2v})
111	197(a'')	208	59
148	416(a')	362	153
355	572(a'')	404	372
425	903(a'')	772	481
893	933(a')	857	527
928	936(a')	901	797
931	1000(a'')	976	877
1035	1055(a'')	1033	892
1154	1184(a')	1123	1073
1172	1307(a')	1147	1106
1356	1397(a')	1164	1242
1404	1444(a')	1180	1376
1414	1470(a'')	1285	1390
1463	1483(a')	1391	1452
1469	1699(a')	1447	1459
1474	3035(a')	1472	1459
1477	3107(a'')	1487	1479
3002	3129(a')	1537	1796
3005	3143(a')	3045	3044
3070	3156(a')	3101	3049
3071	3243(a')	3115	3122
3094		3129	3128
3094		3145	3172
3171		3195	3173

MIN1(C_1)	**MIN2**(C_1)
117	94
204	147
252	222
304	231
340	278
452	323
528	451
815	466
921	547
929	827
949	884
1125	914
1139	952
1180	1077
1198	1159
1340	1180
1358	1312
1404	1358
1413	1370
1471	1390
1476	1453
1481	1472
1500	1487
3051	3051
3054	3054
3079	3145
3138	3146
3145	3150
3149	3265
3159	3753

TS1(C_1)	**TS2**(C_1)	**TS3**(C_1)	**TS4**(C_1)
1359*i*	2548*i*	487*i*	970*i*
147	203	77	115
187	220	148	162
223	313	194	212
375	403	287	254
414	482	321	335
525	582	417	408
617	659	432	411
634	833	524	534
900	855	769	695
942	911	881	855
961	937	921	910
1005	977	936	923
1055	1116	1012	960
1190	1129	1059	1099
1275	1150	1186	1175
1297	1180	1264	1197
1308	1333	1381	1287
1393	1362	1384	1378
1438	1407	1433	1428
1468	1449	1469	1461
1477	1472	1484	1485
1585	1486	1558	1488
1620	1725	3048	3048
3038	3034	3128	3053
3117	3052	3147	3138
3120	3102	3149	3154
3145	3144	3176	3166
3179	3148	3252	3289
3216	3205	3723	3754

$OH(^2\Pi)$

Frequency	symmetry
3703	σ_g^+

$O_2(^3\Sigma_g^-)$

Frequency	symmetry
1587	σ_g^+

$HO_2(^2A'')$

Frequency	Symmetry
1097	a'
1428	a'
3644	a'

Table A6. FC-ROCCSD(T)/cc-pVTZ harmonic vibrational frequencies (cm^{-1}).

propene(C_s)	*i*–propyl(C_s)	methyloxirane(C_1)	acetone(C_{2v})
374(a'')	111	214	21
466(a')	141	365	141
673(a'')	347	406	372
916(a'')	405	777	481
979(a')	892	860	528
997(a')	935	908	795
1068(a'')	945	979	887
1109(a'')	1038	1046	895
1202(a')	1152	1132	1081
1319(a')	1183	1162	1116
1433(a')	1369	1171	1246
1466(a')	1413	1192	1387
1509(a'')	1419	1295	1395
1521(a')	1477	1402	1469
1629(a')	1486	1452	1474
2891(a')	1488	1490	1477
2961(a'')	1497	1504	1496
2982(a')	2967	1541	1786
2994(a')	2969	3039	3037
3008(a')	3045	3105	3042
3090(a')	3045	3112	3104
	3107	3117	3110
	3108	3134	3158
	3184	3197	3159

$OH(^2\Pi)$

Frequency	symmetry
3744	σ_g^+

$O_2(^3\Sigma_g^-)$

Frequency	symmetry
1577	σ_g^+

$HO_2(^2A'')$

Frequency	Symmetry
1132	a'
1436	a'
3675	a'

Table A7. FC-ROCCSD(T)/Mixed Hessian(TZ,DZ) harmonic vibrational frequencies (cm^{-1}).

MIN1(C_1)	**MIN2**(C_1)
111	80
197	147
244	224
302	230
340	282
450	337
526	465
819	480
920	570
935	845
953	908
1150	921
1157	954
1182	1067
1205	1176
1349	1180
1370	1326
1408	1371
1418	1382
1488	1400
1493	1469
1499	1491
1517	1503
3044	3049
3048	3061
3084	3129
3120	3134
3129	3147
3134	3264
3142	3780

TS1(C_1)	**TS2**(C_1)	**TS3**(C_1)	**TS4**(C_1)
1312*i*	2445*i*	376*i*	729*i*
149	205	79	116
192	213	145	166
231	314	189	211
391	405	291	254
417	485	317	352
534	585	421	418
626	658	434	423
638	861	537	545
908	874	814	743
950	918	918	858
975	948	929	926
1014	988	945	932
1069	1120	1018	973
1198	1136	1067	1096
1282	1153	1194	1179
1300	1186	1283	1203
1307	1342	1391	1295
1404	1376	1399	1391
1449	1413	1443	1432
1485	1461	1486	1476
1494	1490	1502	1496
1581	1503	1581	1504
1624	1724	3041	3046
3032	3041	3111	3064
3101	3045	3135	3121
3119	3101	3141	3137
3129	3126	3177	3168
3179	3131	3243	3287
3208	3199	3752	3798

Table A9. Single–point energies (in hartree) at FC-ROCCSD(T)/cc–pVTZ structures.

$OH(^2\Pi)$

	ROHF	ZAPT2	ROCCSD	ROCCSD(T)	ROCCSDT	UCCSDT(Q)
6–31G*	–75.376991	–75.517737	–75.533096	–75.534355	–75.534542	–75.534821
cc–pVDZ	–75.389974	–75.542292	–75.557497	–75.559258	–75.559457	
cc–pVTZ	–75.414411	–75.618400	–75.632521	–75.637677		
cc–pVQZ	–75.420840	–75.643127	–75.655333	–75.661584		
cc–pV5Z	–75.422634	–75.652458				

E(FC–ROCCSD(T)/cc–pCVTZ) = –75.641168

E(AE–ROCCSD(T)/cc–pCVTZ) = –75.694937

$O_2(^3\Sigma_g^-)$

	ROHF	ZAPT2	ROCCSD	ROCCSD(T)	ROCCSDT	UCCSDT(Q)
6–31G*	–149.591031	–149.953154	–149.944811	–149.955392	–149.955468	–149.957716
cc–pVDZ	–149.607151	–149.982573	–149.974762	–149.985688	–149.985803	
cc–pVTZ	–149.651627	–150.122095	–150.109564	–150.128985		
cc–pVQZ	–149.663019	–150.168314	–150.151998	–150.173814		
cc–pV5Z	–149.665971	–150.185733				

E(FC–ROCCSD(T)/cc–pCVTZ) = –150.136556

E(AE–ROCCSD(T)/cc–pCVTZ) = –150.244040

$HO_2(^2A'')$

	ROHF	ZAPT2	ROCCSD	ROCCSD(T)	ROCCSDT	UCCSDT(Q)
6–31G*	–150.161476	–150.490448	–150.511963	–150.520016	–150.520685	–150.522074
cc–pVDZ	–150.181572	–150.528493	–150.549802	–150.558619	–150.559351	
cc–pVTZ	–150.229598	–150.677943	–150.695352	–150.712707		
cc–pVQZ	–150.241373	–150.726296	–150.740007	–150.759863		
cc–pV5Z	–150.244530	–150.744680				

E(FC–ROCCSD(T)/cc–pCVTZ) = –150.720053

E(AE–ROCCSD(T)/cc–pCVTZ) = –150.827574

i–Propyl Radical (C_s)

	ROHF	ZAPT2	RCCSD	RCCSD(T)	RCCSDT	UCCSDT(Q)
6–31G*	–117.630459	–118.000689	–118.047027	–118.057264	–118.058207	–118.058677
cc–pVDZ	–117.640840	–118.055138	–118.105787	–118.117975	–118.118930	
cc–pVTZ	–117.674500	–118.183528	–118.226370	–118.246089		
cc–pVQZ	–117.682082	–118.222805	–118.259413	–118.281054		
cc–pV5Z	–117.683985	–118.236509				

E(FC–ROCCSD(T)/cc–pCVTZ) = –118.249313

E(AE–ROCCSD(T)/cc–pCVTZ) = –118.398627

Propene (C_s)

	ROHF	ZAPT2	RCCSD	RCCSD(T)	RCCSDT	UCCSDT(Q)
6–31G*	–117.070189	–117.451399	–117.490730	–117.503923	–117.504749	–117.505472
cc–pVDZ	–117.082113	–117.499795	–117.542181	–117.556898	–117.557708	
cc–pVTZ	–117.115994	–117.625793	–117.659856	–117.682468		
cc–pVQZ	–117.123685	–117.664774	–117.692491	–117.717089		
cc–pV5Z	–117.125605	–117.678425				

E(FC–ROCCSD(T)/cc–pCVTZ) = –117.685898

E(AE–ROCCSD(T)/cc–pCVTZ) = –117.835234

Methyloxirane(C_1)

	ROHF	ZAPT2	RCCSD	RCCSD(T)	RCCSDT	UCCSDT(Q)
6–31G*	–191.906900	–192.470594	–192.506220	–192.523774	–192.524516	–192.525943
cc–pVDZ	–191.921910	–192.527395	–192.567002	–192.586515	–192.587174	
cc–pVTZ	–191.980671	–192.730767	–192.758867	–192.790833		
cc–pVQZ	–191.994219	–192.794673	–192.814471	–192.849662		
cc–pV5Z	–191.997671	–192.817912				

E(FC–ROCCSD(T)/cc–pCVTZ) = –192.797738

E(AE–ROCCSD(T)/cc–pCVTZ) = –193.000945

Acetone (C_{2v})

	ROHF	ZAPT2	RCCSD	RCCSD(T)	RCCSDT	UCCSDT(Q)
6–31G*	–191.960018	–192.516724	–192.553461	–192.571178	–192.572161	–192.573526
cc–pVDZ	–191.976932	–192.576620	–192.617215	–192.637050	–192.637899	
cc–pVTZ	–192.033405	–192.774770	–192.804744	–192.836558		
cc–pVQZ	–192.047177	–192.838648	–192.860461	–192.895439		
cc–pV5Z	–192.050536	–192.861581				

E(FC–ROCCSD(T)/cc–pCVTZ) = –192.843721

E(AE–ROCCSD(T)/cc–pCVTZ) = –193.047020

MIN1 (C_1)

	ROHF	ZAPT2	RCCSD	RCCSD(T)	RCCSDT	UCCSDT(Q)
6–31G*	−267.272660	−267.991429	−268.049147	−268.071167	−268.072466	−268.07463
cc–pVDZ	−267.296544	-268.070494	−268.132282	−268.156525	−268.157872	
cc–pVTZ	−267.375917	−268.344999	−268.394620	−268.435457		
cc–pVQZ	−267.394436	−268.431887	−268.471624	−268.517007		
cc–pV5Z	−267.399204	−268.463755				

E(FC–ROCCSD(T)/cc–pCVTZ) = –268.445948

E(AE–ROCCSD(T)/cc–pCVTZ) = –268.702844

MIN2 (C_1)

	ROHF	ZAPT2	RCCSD	RCCSD(T)	RCCSDT	UCCSDT(Q)
6–31G*	−267.231957	−267.960398	−268.010040	−268.031090	−268.032037	−268.034291
cc–pVDZ	−267.260302	−268.043249	−268.097333	−268.121108	−268.122077	
cc–pVTZ	−267.341679	−268.323497	−268.363236	−268.403910		
cc–pVQZ	−267.360479	−268.411830	−268.441017	−268.486267		
cc–pV5Z	−267.365335	−268.444224				

E(FC–ROCCSD(T)/cc–pCVTZ) = –268.414376

E(AE–ROCCSD(T)/cc–pCVTZ) = –268.671146

TS1 (C_1)

	ROHF	ZAPT2	RCCSD	RCCSD(T)	RCCSDT	UCCSDT(Q)
6–31G*	−267.172420	−267.934844	−267.978937	−268.007212	−268.008579	−268.011976
cc–pVDZ	−267.203148	−268.021382	−268.070247	−268.101839	−268.103007	
cc–pVTZ	−267.280627	−268.296635	−268.330401	−268.379825		
cc–pVQZ	−267.299377	−268.384141	−268.407256	−268.461378		
cc–pV5Z	−267.304204	−268.416135				

E(FC–ROCCSD(T)/cc–pCVTZ) = –268.390330

E(AE–ROCCSD(T)/cc–pCVTZ) = –268.647127

TS2 (C_1)

	ROHF	ZAPT2	RCCSD	RCCSD(T)	RCCSDT	UCCSDT(Q)
6–31G*	−267.168286	−267.931337	−267.972882	−267.998107	−267.999222	−268.001991
cc–pVDZ	−267.196716	−268.014882	−268.061498	−268.089646	−268.090728	
cc–pVTZ	−267.276648	−268.293890	−268.325326	−268.371090		
cc–pVQZ	−267.295181	−268.381731	−268.402347	−268.452824		
cc–pV5Z	−267.300001	−268.414030				

E(FC–ROCCSD(T)/cc–pCVTZ) = –268.381551

E(AE–ROCCSD(T)/cc–pCVTZ) = –268.638226

TS3 (C_1)

	ROHF	ZAPT2	RCCSD	RCCSD(T)	RCCSDT	UCCSDT(Q)
6–31G*	–267.182588	–267.928304	–267.977811	–268.003507	–268.005053	–268.008002
cc–pVDZ	–267.202290	–268.005351	–268.065729	–268.094527	–268.096019	
cc–pVTZ	–267.283472	–268.284799	–268.330105	–268.376503		
cc–pVQZ	–267.301736	–268.387014	–268.407766	–268.458999		
cc–pV5Z	–267.307981	–268.406697				

E(FC–ROCCSD(T)/cc–pCVTZ) = –268.386808

E(AE–ROCCSD(T)/cc–pCVTZ) = –268.643475

TS4 (C_1)

	ROHF	ZAPT2	RCCSD	RCCSD(T)	RCCSDT	UCCSDT(Q)
6–31G*	−267.173149	−267.920943	−267.981165	−268.008384	−268.010898	−268.014216
cc–pVDZ	−267.203345	−268.002686	−268.066740	−268.096881	−268.099307	
cc–pVTZ	−267.282943	−268.284595	−268.331541	−268.379284		
cc–pVQZ	−267.302294	−268.374484	−268.409869	−268.462595		
cc–pV5Z	−267.307307	−268.407510				

E(FC–ROCCSD(T)/cc–pCVTZ) = –268.389729

E(AE–ROCCSD(T)/cc–pCVTZ) = –268.646269

(A) *i*–C_3H_7+O_2→MIN1 ($CH_3CHOOCH_3$, T)

	ΔE_e(ROHF)	+δ [ZAPT2]	+δ [ROCCSD]	+δ [ROCCSD(T)]	+δ [ROCCSDT]	+δ [UCCSDT(Q)]	NET
6–31G*	–32.110	+8.523	–12.376	–0.754	–0.176	+0.344	–36.548
cc–pVDZ	–30.468	+9.896	–11.891	–0.709	–0.174	[+0.344]	[–33.001]
cc–pVTZ	–31.244	+6.535	–12.117	–1.065	[–0.174]	[+0.344]	[–37.721]
cc–pVQZ	–30.958	+5.376	–12.202	–1.209	[–0.174]	[+0.344]	[–38.823]
cc–pV5Z	–30.904	[+4.964]	[–12.232]	[–1.260]	[–0.174]	[+0.344]	[–39.263]
CBS LIMIT	[–30.894]	[+4.531]	[–12.264]	[–1.314]	[–0.174]	[+0.344]	[–39.771]
FUNCTION	$a+be^{-cX}$	$a+bX^{-3}$	$a+bX^{-3}$	$a+bX^{-3}$	addition	addition	
X (Fit points) =	(3,4,5)	(3,4)	(3,4)	(3,4)			

FC–ROCCSD(T)/cc–pVTZ reference geometries

$\Delta E_{final} = \Delta E_e$(FPA) + ΔZPVE (harm) + Δ(rel) + Δ(core) = –39.77 + 4.91 + 0.13 –0.06 = **–34.79 kcal mol^{-1}**

(B) *i*–C_3H_7+O_2→MIN2 ($CH_3COOHCH_3$, TA^+)

	ΔE_e(ROHF)	+δ [ZAPT2]	+δ [ROCCSD]	+δ [ROCCSD(T)]	+δ [ROCCSDT]	+δ [UCCSDT(Q)]	NET
6–31G*	–6.568	+2.455	–7.309	–0.145	+0.045	+0.291	–11.231
cc–pVDZ	–7.725	+4.250	–7.057	–0.415	+0.063	[+0.291]	[–10.592]
cc–pVTZ	–9.759	–1.457	–5.916	–0.963	[+0.063]	[+0.291]	[–17.741]
cc–pVQZ	–9.650	–3.346	–5.581	–1.126	[+0.063]	[+0.291]	[–19.349]
cc–pV5Z	–9.651	[–4.019]	[–5.462]	[–1.184]	[+0.063]	[+0.291]	[–19.961]
CBS LIMIT	[–9.664]	[–4.725]	[–5.337]	[–1.244]	[+0.063]	[+0.291]	[–20.617]
FUNCTION	$a+be^{-cX}$	$a+bX^{-3}$	$a+bX^{-3}$	$a+bX^{-3}$	addition	addition	
X (Fit points) =	(3,4,5)	(3,4)	(3,4)	(3,4)			

FC–ROCCSD(T)/cc–pVTZ reference geometries

$\Delta E_{final} = \Delta E_e$(FPA) + ΔZPVE (harm) + Δ(rel) + Δ(core) = –20.62 + 2.96 + 0.20 + 0.02 = **–17.44 kcal mol^{-1}**

(C) *i*–C_3H_7+O_2→TS1

	ΔE_e(ROHF)	+δ [ZAPT2]	+δ [ROCCSD]	+δ [ROCCSD(T)]	+δ [ROCCSDT]	+δ [UCCSDT(Q)]	NET
6–31G*	30.792	–18.870	–3.827	–4.679	–0.218	–0.426	+2.772
cc–pVDZ	28.139	–17.893	–3.782	–5.320	–0.061	[–0.426]	[+0.657]
cc–pVTZ	28.552	–22.912	–2.168	–6.454	[–0.061]	[–0.426]	[–3.469]
cc–pVQZ	28.692	–24.313	–1.771	–6.693	[–0.061]	[–0.426]	[–4.573]
cc–pV5Z	28.710	[–24.813]	[–1.630]	[–6.778]	[–0.061]	[–0.426]	[–4.999]
CBS LIMIT	[28.707]	[–25.336]	[–1.482]	[–6.868]	[–0.061]	[–0.426]	[–5.466]
FUNCTION	$a+be^{-cX}$	$a+bX^{-3}$	$a+bX^{-3}$	$a+bX^{-3}$	addition	addition	
X (Fit points) =	(3,4,5)	(3,4)	(3,4)	(3,4)			

FC–ROCCSD(T)/cc–pVTZ reference geometries

$\Delta E_{final} = \Delta E_e$(FPA) + ΔZPVE (harm) + Δ(rel) + Δ(core) = –5.47 + 0.98 + 0.07 + 0.00 = **–4.42 kcal mol^{-1}**

(D) *i*–C_3H_7+O_2→TS2

	ΔE_e(ROHF)	+δ [ZAPT2]	+δ [ROCCSD]	+δ [ROCCSD(T)]	+δ [ROCCSDT]	+δ [UCCSDT(Q)]	NET
6–31G*	33.386	–19.263	–2.228	–2.765	–0.060	–0.032	9.037
cc–pVDZ	32.175	–17.850	–2.371	–3.159	–0.007	[–0.032]	[8.756]
cc–pVTZ	31.049	–23.686	–0.706	–4.157	[–0.007]	[–0.032]	[2.460]
cc–pVQZ	31.325	–25.434	–0.203	–4.406	[–0.007]	[–0.032]	[1.243]
cc–pV5Z	31.347	[–26.057]	[–0.024]	[–4.494]	[–0.007]	[–0.032]	[0.733]
CBS LIMIT	[31.331]	[–26.710]	[0.164]	[–4.587]	[–0.007]	[–0.032]	[0.159]
FUNCTION	$a+be^{-cX}$	$a+bX^{-3}$	$a+bX^{-3}$	$a+bX^{-3}$	addition	addition	
X (Fit points) =	(3,4,5)	(3,4)	(3,4)	(3,4)			

FC–ROCCSD(T)/cc–pVTZ reference geometries

$\Delta E_{final} = \Delta E_e$(FPA) + ΔZPVE (harm) + Δ(rel) + Δ(core) =0.16 +1.00 + 0.13 + 0.08 = **1.37 kcal mol^{-1}**

(F) *i*–C_3H_7+O_2→TS3

	ΔE_e(ROHF)	+δ [ZAPT2]	+δ [ROCCSD]	+δ [ROCCSD(T)]	+δ [ROCCSDT]	+δ [UCCSDT(Q)]	NET
6–31G*	24.411	–8.385	–7.224	–3.061	–0.331	–0.145	5.265
cc–pVDZ	28.678	–8.371	–11.007	–3.567	–0.265	[–0.145]	[5.323]
cc–pVTZ	26.766	–13.699	–9.409	–4.555	[–0.265]	[–0.145]	[–1.307]
cc–pVQZ	27.212	–24.636	–0.288	–4.880	[–0.265]	[–0.145]	[–3.002]
cc–pV5Z	26.340	[–28.531]	[2.960]	[–4.996]	[–0.265]	[–0.145]	[–4.637]
CBS LIMIT	[27.703]	[–32.617]	[6.368]	[–5.117]	[–0.265]	[–0.145]	[–4.073]
FUNCTION	$a+be^{-cX}$	$a+bX^{-3}$	$a+bX^{-3}$	$a+bX^{-3}$	addition	addition	
X (Fit points) =	(3,4,5)	(3,4)	(3,4)	(3,4)			

FC–ROCCSD(T)/cc–pVTZ reference geometries

$\Delta E_{final} = \Delta E_e$(FPA) + ΔZPVE (harm) + Δ(rel) + Δ(core) = –4.073+ 2.41 + 0.06 + 0.08 = **–1.52 kcal mol^{-1}**

(E) *i*–C_3H_7+O_2→TS4

	ΔE_e(ROHF)	+δ [ZAPT2]	+δ [ROCCSD]	+δ [ROCCSD(T)]	+δ [ROCCSDT]	+δ [UCCSDT(Q)]	NET
6–31G*	30.335	–9.689	–13.948	–4.016	–0.938	–0.377	1.366
cc–pVDZ	28.016	–6.037	–13.313	–4.410	–0.851	[–0.377]	[3.028]
cc–pVTZ	27.098	–13.903	–10.438	–5.399	[–0.851]	[–0.377]	[–3.869]
cc–pVQZ	26.862	–16.423	–9.471	–5.817	[–0.851]	[–0.377]	[–6.077]
cc–pV5Z	26.762	[–17.320]	[–9.126]	[–5.966]	[–0.851]	[–0.377]	[–6.877]
CBS LIMIT	[26.710]	[–18.262]	[–8.764]	[–6.122]	[–0.851]	[–0.377]	[–7.666]
FUNCTION	$a+be^{-cX}$	$a+bX^{-3}$	$a+bX^{-3}$	$a+bX^{-3}$	addition	addition	
X (Fit points) =	(3,4,5)	(3,4)	(3,4)	(3,4)			

FC–ROCCSD(T)/cc–pVTZ reference geometries

$\Delta E_{final} = \Delta E_e$(FPA) + ΔZPVE (harm) + Δ(rel) + Δ(core) = –7.67 + 1.87 + 0.05 + 0.16 = **–5.59 kcal mol^{-1}**

(F) *i*–C_3H_7+O_2→Propene+HO_2

	ΔE_e(ROHF)	+δ [ZAPT2]	+δ [ROCCSD]	+δ [ROCCSD(T)]	+δ [ROCCSDT]	+δ [UCCSDT(Q)]	NET
6–31G*	–6.385	+13.913	–14.340	–0.268	–0.299	+0.380	–6.999
cc–pVDZ	–9.848	+15.762	–13.088	–0.264	–0.296	[+0.380]	[–7.355]
cc–pVTZ	–12.215	+13.399	–13.278	–0.519	[–0.296]	[+0.380]	[–12.530]
cc–pVQZ	–12.524	+12.554	–13.263	–0.626	[–0.296]	[+0.380]	[–13.774]
cc–pV5Z	–12.663	[+12.253]	[–13.257]	[–0.664]	[–0.296]	[+0.380]	[–14.247]
CBS LIMIT	[–12.739]	[+11.938]	[–13.251]	[–0.704]	[–0.296]	[+0.380]	[–14.673]
FUNCTION	$a+be^{-cX}$	$a+bX^{-3}$	$a+bX^{-3}$	$a+bX^{-3}$	addition	addition	
X (Fit points) =	(3,4,5)	(3,4)	(3,4)	(3,4)			

FC–ROCCSD(T)/cc–pVTZ reference geometries

$\Delta E_{final} = \Delta E_e$(FPA) + ΔZPVE (harm) + Δ(rel) + Δ(core) = –14.67 + 0.76 + 0.06 + 0.10 = **–13.75 kcal mol^{-1}**

(G) *i*–C_3H_7+O_2→Methyloxirane +OH

	ΔE_e(ROHF)	+δ [ZAPT2]	+δ [ROCCSD]	+δ [ROCCSD(T)]	+δ [ROCCSDT]	+δ [UCCSDT(Q)]	NET
6–31G*	–39.158	+17.517	–8.152	+1.259	+0.056	+0.635	–27.844
cc–pVDZ	–40.093	+20.028	–7.513	+1.154	+0.133	[+0.635]	[–25.657]
cc–pVTZ	–43.270	+15.945	–7.474	+1.266	[+0.133]	[+0.635]	[–32.765]
cc–pVQZ	–43.899	+14.606	–7.349	+1.264	[+0.133]	[+0.635]	[–34.610]
cc–pV5Z	–44.145	[+14.129]	[–7.304]	[+1.263]	[+0.133]	[+0.635]	[–35.290]
CBS LIMIT	[–44.270]	[+13.628]	[–7.258]	[+1.263]	[+0.133]	[+0.635]	[–35.870]
FUNCTION	$a+be^{-cX}$	$a+bX^{-3}$	$a+bX^{-3}$	$a+bX^{-3}$	addition	addition	
X (Fit points) =	(3,4,5)	(3,4)	(3,4)	(3,4)			

FC–ROCCSD(T)/cc–pVTZ reference geometries

$\Delta E_{final} = \Delta E_e$(FPA) + ΔZPVE (harm) + Δ(rel) + Δ(core) = –35.87 + 1.49 + 0.15 –0.11 = **–33.34 kcal mol^{-1}**

(H) *i*–C_3H_7+O_2→Acetone+OH

	ΔE_e(ROHF)	+δ [ZAPT2]	+δ [ROCCSD]	+δ [ROCCSD(T)]	+δ [ROCCSDT]	+δ [UCCSDT(Q)]	NET
6–31G*	–72.489	+21.901	–8.849	+1.156	–0.095	+0.673	–57.702
cc–pVDZ	–74.620	+23.666	–8.134	+0.952	+0.014	[+0.673]	[–57.448]
cc–pVTZ	–76.361	+21.424	–8.650	+1.361	[+0.014]	[+0.673]	[–61.538]
cc–pVQZ	–77.131	+20.243	–8.614	+1.398	[+0.014]	[+0.673]	[–63.416]
cc–pV5Z	–77.318	[+19.823]	[–8.601]	[+1.411]	[+0.014]	[+0.673]	[–63.998]
CBS LIMIT	[–77.378]	[+19.382]	[–8.587]	[+1.424]	[+0.014]	[+0.673]	[–64.472]
FUNCTION	$a+be^{-cX}$	$a+bX^{-3}$	$a+bX^{-3}$	$a+bX^{-3}$	addition	addition	
X (Fit points) =	(3,4,5)	(3,4)	(3,4)	(3,4)			

FC–ROCCSD(T)/cc–pVTZ reference geometries

$\Delta E_{final} = \Delta E_e$(FPA) + ΔZPVE (harm) + Δ(rel) + Δ(core) = –64.47 + 0.15 + 0.11 –0.17 = **–64.38 kcal mol^{-1}**

APPENDIX B

SUPPORTING INFORMATION FOR CHAPTER 4

Table B1. Cartesian coordinates (Å) and depictions of FPA-Q2 optimized structures for *cis*-HO_3, *trans*-HO_3, **TSct**, and all species along the DRP

***cis*-$H_1O_2O_3O_4$ ($\tau = 0°$)**

	X	*Y*	*Z*
H_1	–0.914144	1.082572	0.000000
O_2	–1.228091	0.163179	0.000000
O_3	0.179793	–0.526975	0.000000
O_4	1.105892	0.295587	0.000000

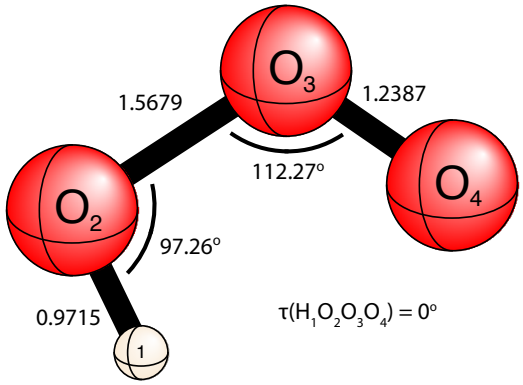

***trans*-$H_1O_2O_3O_4$ ($\tau = 180°$)**

	X	*Y*	*Z*
H_1	–1.788954	0.543348	0.000000
O_2	–1.243267	–0.257022	0.000000
O_3	0.226399	0.518247	0.000000
O_4	1.129579	–0.295463	0.000000

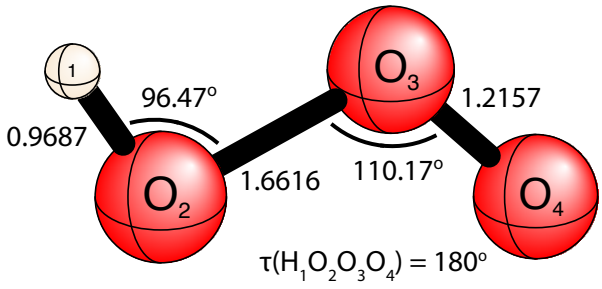

TSct ($\tau = 76.82°$)

	X	*Y*	*Z*
H_1	–0.914144	1.082572	0.000000
O_2	–1.228091	0.163179	0.000000
O_3	0.179793	–0.526975	0.000000
O_4	1.105892	0.295587	0.000000

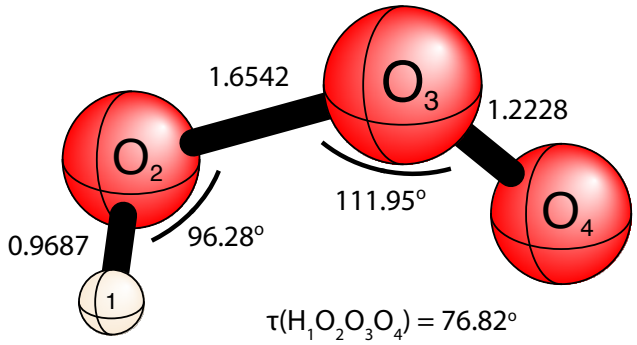

$\tau = 10°$

	X	*Y*	*Z*
H_1	–0.922313	1.070346	–0.164147
O_2	–1.229480	0.164132	0.003187
O_3	0.180858	–0.526788	0.003519
O_4	1.106738	0.295214	0.003637

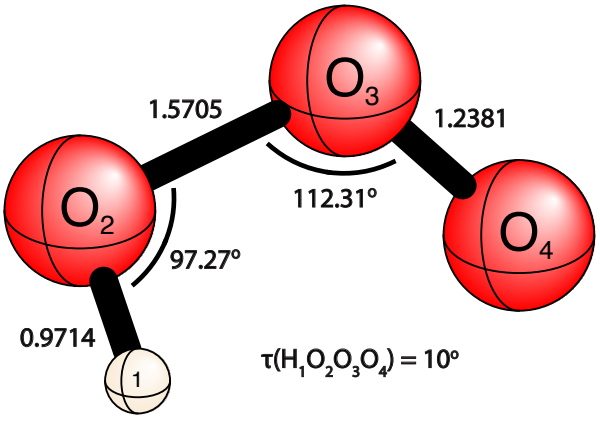

$\tau = 20°$

	X	*Y*	*Z*
H_1	–0.945494	1.033727	–0.323729
O_2	–1.233402	0.166768	0.005827
O_3	0.183968	–0.526278	0.007108
O_4	1.109046	0.294374	0.007464

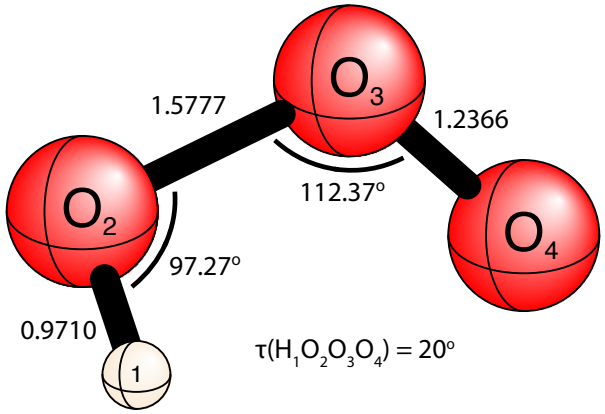

$\tau = 30°$

	X	*Y*	*Z*
H_1	–0.982774	0.975442	–0.469628
O_2	–1.238997	0.172515	0.011569
O_3	0.188122	–0.525902	0.009322
O_4	1.112760	0.291934	0.008694

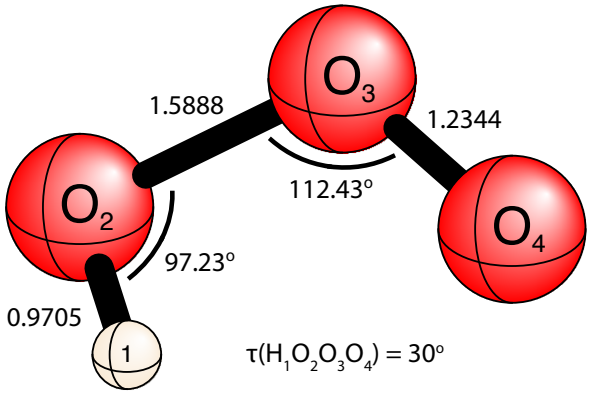

$\tau = 40°$

	X	*Y*	*Z*
H_1	–1.033371	0.892320	–0.601999
O_2	–1.246067	0.175856	0.016334
O_3	0.195065	–0.525050	0.011509
O_4	1.116104	0.292972	0.010087

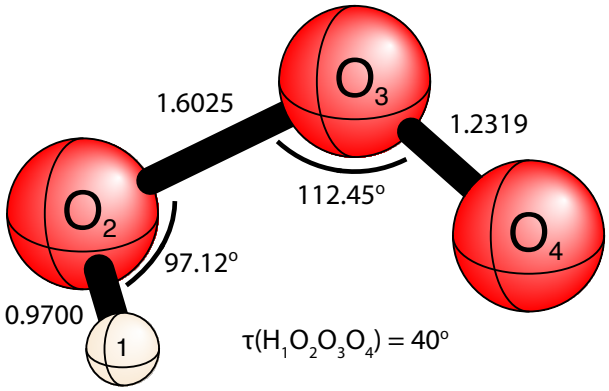

$\tau = 50°$

	X	*Y*	*Z*
H_1	–1.092591	0.789726	–0.715229
O_2	–1.253274	0.180242	0.021458
O_3	0.202651	–0.524382	0.013048
O_4	1.119436	0.294389	0.010555

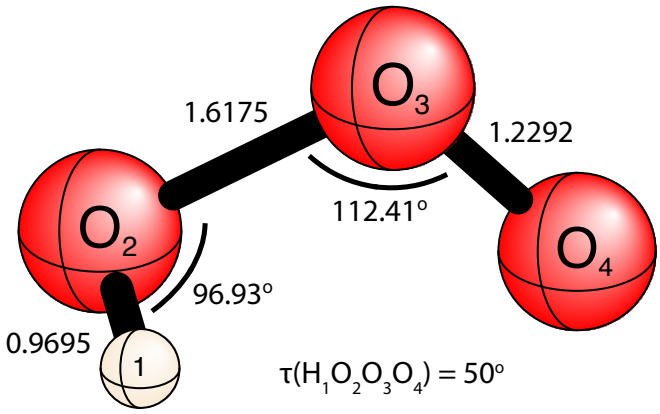

$\tau = 60°$

	X	*Y*	*Z*
H_1	–1.158470	0.670887	–0.805797
O_2	–1.259853	0.185548	0.026926
O_3	0.210333	–0.523926	0.013856
O_4	1.122500	0.296109	0.009986

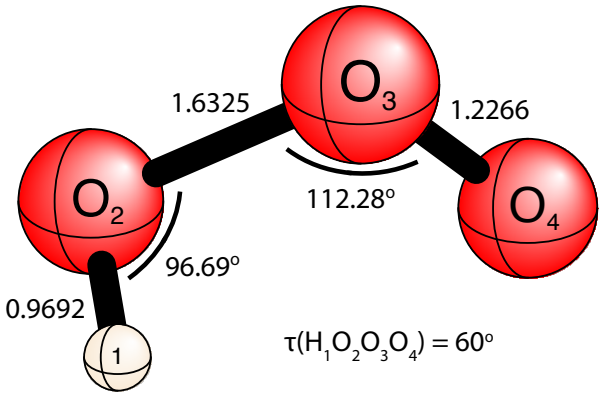

$\tau = 70°$

	X	*Y*	*Z*
H_1	–1.230021	0.537655	–0.871002
O_2	–1.265418	0.189565	0.032475
O_3	0.218310	–0.523224	0.013918
O_4	1.124610	0.299783	0.008488

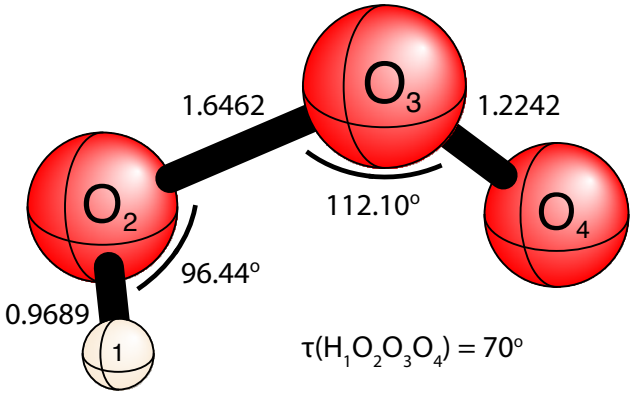

$\tau = 80°$

	X	*Y*	*Z*
H_1	–1.304316	0.396055	–0.908712
O_2	–1.269172	0.194181	0.038008
O_3	0.225174	–0.522483	0.013253
O_4	1.124615	0.303351	0.005987

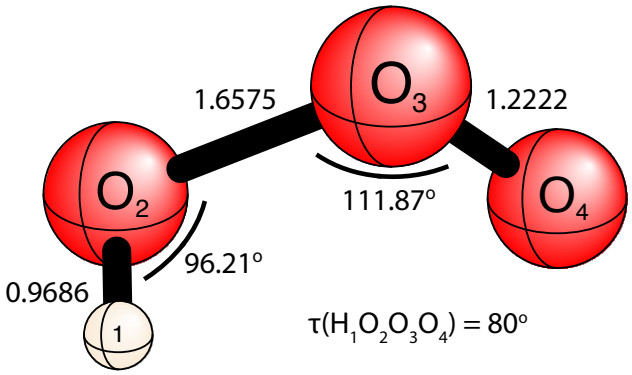

$\tau = 90°$

	X	*Y*	*Z*
H_1	–0.898504	–0.285454	–1.385419
O_2	0.059283	–0.199803	–1.270168
O_3	–0.008224	0.522115	0.229701
O_4	0.005555	–0.304324	1.127760

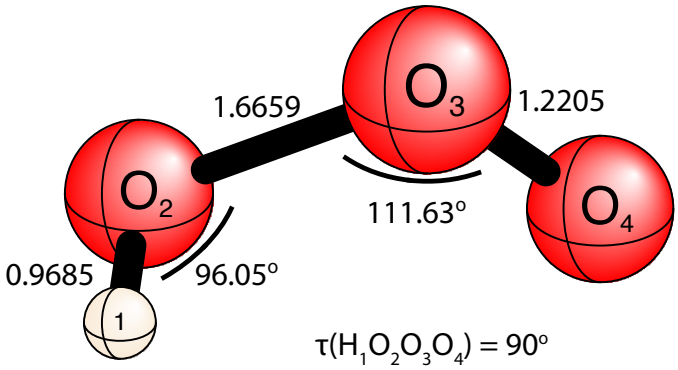

$\tau = 100°$

	X	*Y*	*Z*
H_1	–1.432869	–0.167832	0.921579
O_2	–1.260036	–0.264850	–0.026316
O_3	0.209405	0.531010	–0.017297
O_4	1.140916	–0.255585	–0.014455

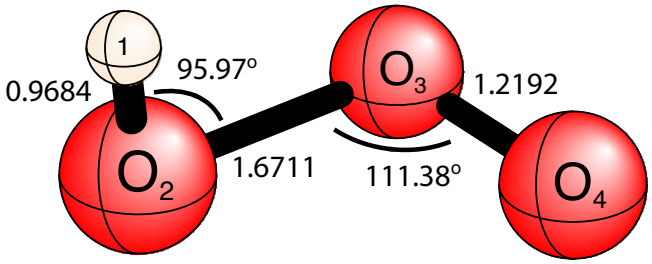

$\tau(H_1O_2O_3O_4) = 100°$

$\tau = 110°$

	X	*Y*	*Z*
H_1	–1.508187	–0.027652	0.878933
O_2	–1.258452	–0.267515	–0.025392
O_3	0.212993	0.529485	–0.016450
O_4	1.140501	–0.260230	–0.013543

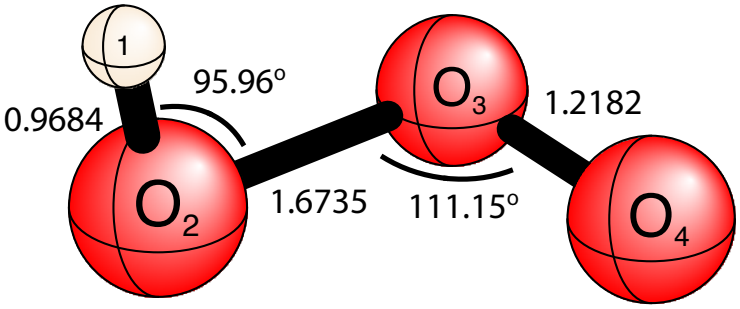

$\tau(H_1O_2O_3O_4) = 110°$

$\tau = 120°$

	X	*Y*	*Z*
H_1	–1.578275	0.103899	0.809213
O_2	–1.255605	–0.269521	–0.023941
O_3	0.215486	0.527767	–0.015043
O_4	1.139537	–0.264798	–0.012002

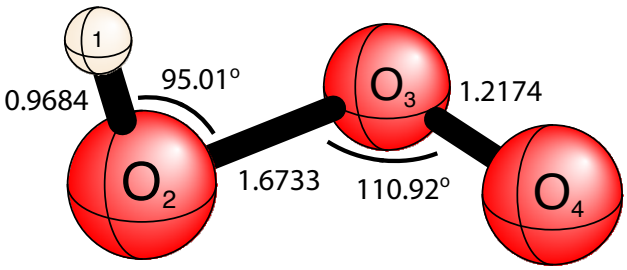

$\tau(H_1O_2O_3O_4) = 120°$

$\tau = 130°$

	X	*Y*	*Z*
H_1	–1.639567	0.226864	0.717477
O_2	–1.252769	–0.268193	–0.019475
O_3	0.218392	0.525533	–0.013894
O_4	1.137685	–0.271636	–0.011839

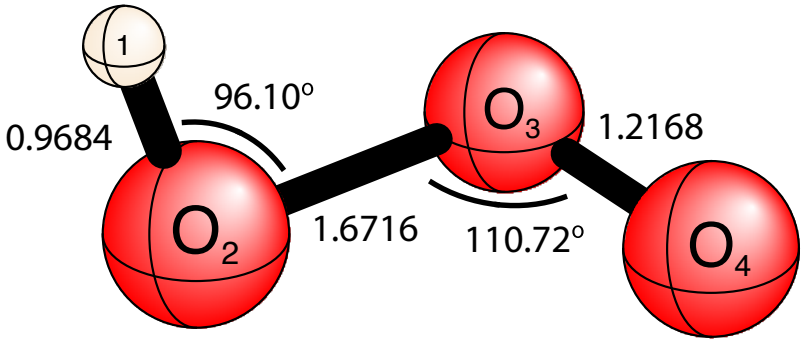

$\tau(H_1O_2O_3O_4) = 130°$

$\tau = 140°$

	X	*Y*	*Z*
H_1	–1.691844	0.334130	0.603369
O_2	–1.249789	–0.265948	–0.015032
O_3	0.220853	0.523337	–0.012091
O_4	1.135542	–0.278445	–0.010896

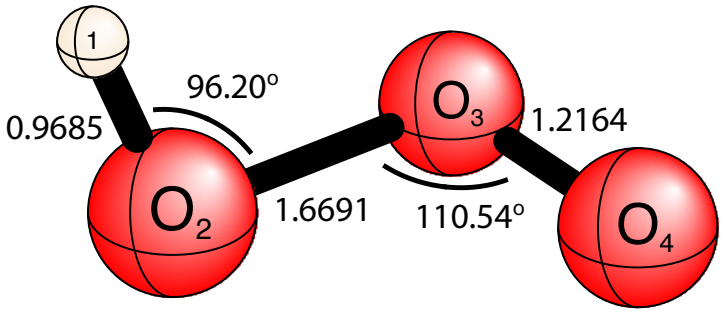

$\tau(H_1O_2O_3O_4) = 140°$

$\tau = 150°$

	X	*Y*	*Z*
H_1	–1.733433	0.423760	0.470232
O_2	–1.247306	–0.262011	–0.010893
O_3	0.223421	0.521147	–0.009622
O_4	1.133106	–0.285837	–0.009113

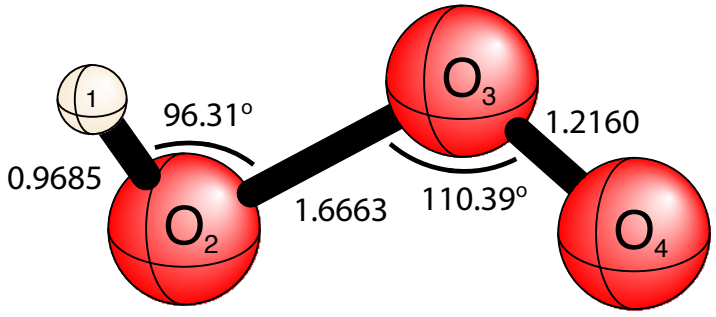

$\tau(H_1O_2O_3O_4) = 150°$

$\tau = 160°$

	X	*Y*	*Z*
H_1	–1.764809	0.486600	0.322065
O_2	–1.244746	–0.261388	–0.006985
O_3	0.224235	0.519935	–0.006784
O_4	1.131718	–0.289208	–0.006525

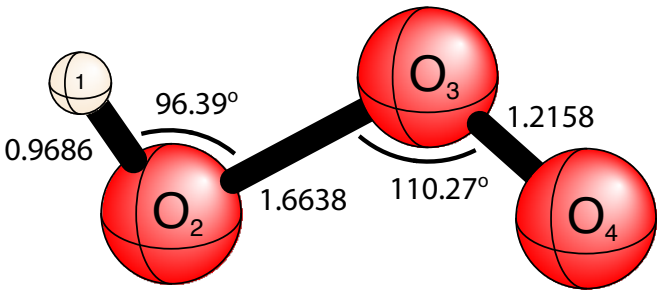

$\tau(H_1O_2O_3O_4) = 160°$

$\tau = 170°$

	X	*Y*	*Z*
H_1	–1.783425	0.527252	0.163681
O_2	–1.243392	–0.259373	–0.003397
O_3	0.225328	0.518903	–0.003489
O_4	1.130414	–0.292744	–0.003427

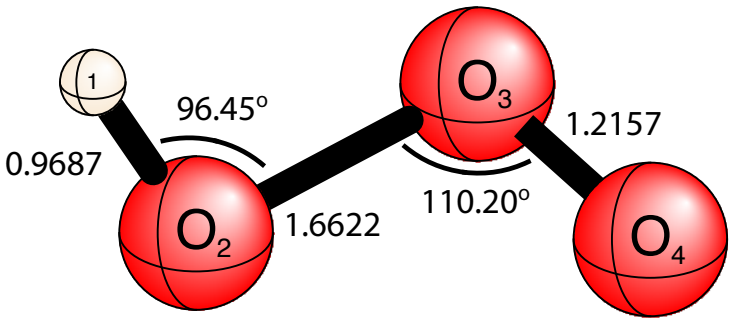

$\tau(H_1O_2O_3O_4) = 170°$

Table B2. Single-point energies (in hartree) for FPA-Q2 structures of *cis*-HO_3, *trans*-HO_3, and the **TSct.**

***cis*-HO_3 ($^2A''$)**

	ROHF	MP2	CCSD	CCSD(T)	CCSDT	CCSDT(Q)
cc-pVDZ	–224.936822	–225.497803	–225.520001	–225.540987	–225.542412	–225.546365
cc-pVTZ	–225.008302	–225.722013	–225.734790	–225.769730	–225.770603	
cc-pVQZ	–225.025666	–225.794512	–225.801049	–225.840026		
cc-pV5Z	–225.030219	–225.822099	–225.823424	–225.863984		
cc-pV6Z	–225.030797	–225.832869	–225.831086	–225.872201		

E(FC-ROCCSD(T)/cc-pCVTZ) = –225.844882

E(AE-ROCCSD(T)/cc-pCVTZ) = –226.022428

***trans*-HO_3 ($^2A''$)**

	ROHF	MP2	CCSD	CCSD(T)	CCSDT	CCSDT(Q)
cc-pVDZ	–224.925427	–225.495145	–225.517040	–225.540953	–225.542784	–225.547563
cc-pVTZ	–224.995881	–225.719234	–225.730430	–225.768540	–225.769699	
cc-pVQZ	–225.013524	–225.792426	–225.796958	–225.839237		
cc-pV5Z	–225.018165	–225.820265	–225.819397	–225.863322		
cc-pV6Z	–225.018783	–225.831119	–225.827090	–225.871594		

E(FC-ROCCSD(T)/cc-pCVTZ) = –225.844098

E(AE-ROCCSD(T)/cc-pCVTZ) = –226.021630

TSct

	ROHF	MP2	CCSD	CCSD(T)	CCSDT	CCSDT(Q)
cc-pVDZ	–224.925928	–225.495169	–225.516354	–225.539781	–225.541203	–225.545620
cc-pVTZ	–224.996743	–225.719284	–225.730056	–225.767624	–225.768407	
cc-pVQZ	–225.014326	–225.792253	–225.796451	–225.838150		
cc-pV5Z	–225.018953	–225.820018	–225.818855	–225.862180		
cc-pV6Z	–225.019548	–225.830818	–225.826507	–225.870402		

E(FC-ROCCSD(T)/cc-pCVTZ) = –225.843007

E(AE-ROCCSD(T)/cc-pCVTZ) = –226.020514

$\tau = 10°$

	ROHF	MP2	CCSD	CCSD(T)	CCSDT	CCSDT(Q)
cc-pVDZ	–224.936511	–225.497693	–225.519871	–225.540921	–225.542348	–225.546315
cc-pVTZ	–225.007973	–225.721899	–225.734632	–225.769642	–225.770514	
cc-pVQZ	–225.025343	–225.794408	–225.800892	–225.839942		
cc-pV5Z	–225.029898	–225.822001	–225.823269	–225.863902		
cc-pV6Z	–225.030477	–225.832772	–225.830930	–225.872119		

E(FC-ROCCSD(T)/cc-pCVTZ) = –225.843007

E(AE-ROCCSD(T)/cc-pCVTZ) = –226.020514

$\tau = 20°$

	ROHF	MP2	CCSD	CCSD(T)	CCSDT	CCSDT(Q)
cc-pVDZ	–224.935617	–225.497390	–225.519508	–225.540742	–225.542173	–225.546179
cc-pVTZ	–225.007029	–225.721589	–225.734187	–225.769398	–225.770268	
cc-pVQZ	–225.024415	–225.794127	–225.800451	–225.839709		
cc-pV5Z	–225.028977	–225.821736	–225.822832	–225.863677		
cc-pV6Z	–225.029558	–225.832509	–225.830492	–225.871894		

E(FC-ROCCSD(T)/cc-pCVTZ) = –225.844566

E(AE-ROCCSD(T)/cc-pCVTZ) = –226.022106

$\tau = 30°$

	ROHF	MP2	CCSD	CCSD(T)	CCSDT	CCSDT(Q)
cc-pVDZ	–224.934231	–225.496965	–225.518973	–225.540497	–225.541929	–225.545994
cc-pVTZ	–225.005564	–225.721152	–225.733523	–225.769050	–225.769912	
cc-pVQZ	–225.022975	–225.793740	–225.799797	–225.839383		
cc-pV5Z	–225.027549	–225.821373	–225.822183	–225.863361		
cc-pV6Z	–225.028133	–225.832148	–225.829841	–225.871578		

E(FC-ROCCSD(T)/cc-pCVTZ) = –225.844241

E(AE-ROCCSD(T)/cc-pCVTZ) = –226.021775

$\tau = 40°$

	ROHF	MP2	CCSD	CCSD(T)	CCSDT	CCSDT(Q)
cc-pVDZ	–224.932506	–225.496497	–225.518346	–225.540241	–225.541669	–225.545806
cc-pVTZ	–225.003740	–225.720670	–225.732733	–225.768662	–225.769508	
cc-pVQZ	–225.021183	–225.793325	–225.799025	–225.839028		
cc-pV5Z	–225.025770	–225.820986	–225.821416	–225.863017		
cc-pV6Z	–225.026356	–225.831766	–225.829072	–225.871234		

E(FC-ROCCSD(T)/cc-pCVTZ) = –225.843886

E(AE-ROCCSD(T)/cc-pCVTZ) = –226.021412

$\tau = 50°$

	ROHF	MP2	CCSD	CCSD(T)	CCSDT	CCSDT(Q)
cc-pVDZ	–224.930608	–225.496048	–225.517706	–225.540021	–225.541442	–225.545656
cc-pVTZ	–225.001729	–225.720205	–225.731907	–225.768289	–225.769113	
cc-pVQZ	–225.019210	–225.792943	–225.798225	–225.838698		
cc-pV5Z	–225.023809	–225.820634	–225.820620	–225.862699		
cc-pV6Z	–225.024399	–225.831418	–225.828275	–225.870916		

E(FC-ROCCSD(T)/cc-pCVTZ) = –225.843555

E(AE-ROCCSD(T)/cc-pCVTZ) = –226.021075

$\tau = 60°$

	ROHF	MP2	CCSD	CCSD(T)	CCSDT	CCSDT(Q)
cc-pVDZ	–224.928695	–225.495654	–225.517114	–225.539868	–225.541282	–225.545575
cc-pVTZ	–224.999699	–225.719795	–225.731119	–225.767971	–225.768773	
cc-pVQZ	–225.017218	–225.792623	–225.797466	–225.838426		
cc-pV5Z	–225.021830	–225.820343	–225.819865	–225.862439		
cc-pV6Z	–225.022421	–225.831132	–225.827518	–225.870657		

E(FC-ROCCSD(T)/cc-pCVTZ) = –225.843283

E(AE-ROCCSD(T)/cc-pCVTZ) = –226.020796

$\tau = 70°$

	ROHF	MP2	CCSD	CCSD(T)	CCSDT	CCSDT(Q)
cc-pVDZ	–224.926949	–225.495338	–225.516619	–225.539791	–225.541206	–225.545574
cc-pVTZ	–224.997837	–225.719462	–225.730436	–225.767733	–225.768520	
cc-pVQZ	–225.015395	–225.792378	–225.796813	–225.838233		
cc-pV5Z	–225.020017	–225.820125	–225.819215	–225.862257		
cc-pV6Z	–225.020611	–225.830921	–225.826867	–225.870477		

E(FC-ROCCSD(T)/cc-pCVTZ) = –225.843090

E(AE-ROCCSD(T)/cc-pCVTZ) = –226.020598

$\tau = 80°$

	ROHF	MP2	CCSD	CCSD(T)	CCSDT	CCSDT(Q)
cc-pVDZ	–224.925518	–225.495104	–225.516255	–225.516255	–225.541213	–225.545651
cc-pVTZ	–224.996302	–225.719216	–225.729909	–225.729909	–225.768372	
cc-pVQZ	–225.013896	–225.792208	–225.796311	–225.796311		
cc-pV5Z	–225.018526	–225.819979	–225.818716	–225.818716		
cc-pV6Z	–225.019121	–225.830781	–225.826369	–225.826369		

E(FC-ROCCSD(T)/cc-pCVTZ) = –225.842982

E(AE-ROCCSD(T)/cc-pCVTZ) = –226.020488

$\tau = 90°$

	ROHF	MP2	CCSD	CCSD(T)	CCSDT	CCSDT(Q)
cc-pVDZ	–224.924474	–225.494948	–225.516031	–225.539844	–225.541295	–225.545797
cc-pVTZ	–224.995169	–225.719052	–225.729558	–225.767538	–225.768332	
cc-pVQZ	–225.012792	–225.792104	–225.795979	–225.838101		
cc-pV5Z	–225.017428	–225.819895	–225.818384	–225.862140		
cc-pV6Z	–225.018026	–225.830705	–225.826040	–225.870368		

E(FC-ROCCSD(T)/cc-pCVTZ) = –225.842958

E(AE-ROCCSD(T)/cc-pCVTZ) = –226.020464

$\tau = 100°$

	ROHF	MP2	CCSD	CCSD(T)	CCSDT	CCSDT(Q)
cc-pVDZ	–224.923862	–225.494862	–225.515947	–225.539948	–225.541435	–225.545993
cc-pVTZ	–224.994487	–225.718965	–225.729389	–225.767571	–225.768392	
cc-pVQZ	–225.012131	–225.792059	–225.795822	–225.838152		
cc-pV5Z	–225.016772	–225.819865	–225.818229	–225.862195		
cc-pV6Z	–225.017372	–225.830684	–225.825890	–225.870429		

E(FC-ROCCSD(T)/cc-pCVTZ) = –225.843010

E(AE-ROCCSD(T)/cc-pCVTZ) = –226.020517

$\tau = 110°$

	ROHF	MP2	CCSD	CCSD(T)	CCSDT	CCSDT(Q)
cc-pVDZ	–224.923633	–225.494833	–225.515982	–225.540085	–225.541620	–225.546227
cc-pVTZ	–224.994206	–225.718940	–225.729377	–225.767672	–225.768535	
cc-pVQZ	–225.011862	–225.792060	–225.795820	–225.838265		
cc-pV5Z	–225.016506	–225.819877	–225.818228	–225.862312		
cc-pV6Z	–225.017110	–225.830705	–225.825894	–225.870553		

E(FC-ROCCSD(T)/cc-pCVTZ) = –225.843125

E(AE-ROCCSD(T)/cc-pCVTZ) = –226.020635

$\tau = 120°$

	ROHF	MP2	CCSD	CCSD(T)	CCSDT	CCSDT(Q)
cc-pVDZ	–224.923727	–225.494851	–225.516113	–225.540243	–225.541832	–225.546483
cc-pVTZ	–224.994263	–225.718963	–225.729492	–225.767821	–225.768735	
cc-pVQZ	–225.011924	–225.792098	–225.795943	–225.838425		
cc-pV5Z	–225.016569	–225.819923	–225.818355	–225.862476		
cc-pV6Z	–225.017177	–225.830759	–225.826027	–225.870724		

E(FC-ROCCSD(T)/cc-pCVTZ) = –225.843287

E(AE-ROCCSD(T)/cc-pCVTZ) = –226.020800

$\tau = 130°$

	ROHF	MP2	CCSD	CCSD(T)	CCSDT	CCSDT(Q)
cc-pVDZ	–224.923998	–225.494895	–225.516297	–225.540412	–225.542060	–225.546749
cc-pVTZ	–224.994507	–225.719010	–225.729674	–225.767992	–225.768963	
cc-pVQZ	–225.012168	–225.792156	–225.796137	–225.838609		
cc-pV5Z	–225.016814	–225.819987	–225.818554	–225.862667		
cc-pV6Z	–225.017425	–225.830830	–225.826232	–225.870921		

E(FC-ROCCSD(T)/cc-pCVTZ) = –225.843472

E(AE-ROCCSD(T)/cc-pCVTZ) = –226.020990

$\tau = 140°$

	ROHF	MP2	CCSD	CCSD(T)	CCSDT	CCSDT(Q)
cc-pVDZ	–224.924379	–225.494958	–225.516509	–225.540578	–225.542284	–225.547005
cc-pVTZ	–224.994867	–225.719071	–225.729891	–225.768164	–225.769194	
cc-pVQZ	–225.012525	–225.792228	–225.796368	–225.838800		
cc-pV5Z	–225.017170	–225.820063	–225.818791	–225.862864		
cc-pV6Z	–225.017784	–225.830911	–225.826474	–225.871124		

E(FC-ROCCSD(T)/cc-pCVTZ) = –225.843663

E(AE-ROCCSD(T)/cc-pCVTZ) = –226.021185

$\tau = 150°$

	ROHF	MP2	CCSD	CCSD(T)	CCSDT	CCSDT(Q)
cc-pVDZ	–224.924781	–225.495027	–225.516716	–225.540728	–225.542485	–225.547231
cc-pVTZ	–224.995255	–225.719134	–225.730104	–225.768318	–225.769400	
cc-pVQZ	–225.012907	–225.792303	–225.796598	–225.838975		
cc-pV5Z	–225.017551	–225.820140	–225.819027	–225.863047		
cc-pV6Z	–225.018167	–225.830991	–225.826715	–225.871312		

E(FC-ROCCSD(T)/cc-pCVTZ) = –225.843837

E(AE-ROCCSD(T)/cc-pCVTZ) = –226.021364

$\tau = 160°$

	ROHF	MP2	CCSD	CCSD(T)	CCSDT	CCSDT(Q)
cc-pVDZ	–224.925118	–225.495088	–225.516887	–225.540848	–225.542645	–225.547410
cc-pVTZ	–224.995580	–225.719186	–225.730277	–225.768438	–225.769561	
cc-pVQZ	–225.013228	–225.792366	–225.796788	–225.839115		
cc-pV5Z	–225.017871	–225.820205	–225.819222	–225.863194		
cc-pV6Z	–225.018487	–225.831058	–225.826912	–225.871463		

E(FC-ROCCSD(T)/cc-pCVTZ) = –225.843837

E(AE-ROCCSD(T)/cc-pCVTZ) = –226.021364

$\tau = 170°$

	ROHF	MP2	CCSD	CCSD(T)	CCSDT	CCSDT(Q)
cc-pVDZ	–224.925349	–225.495130	–225.517001	–225.540926	–225.542749	–225.547524
cc-pVTZ	–224.995805	–225.719222	–225.730391	–225.768514	–225.769664	
cc-pVQZ	–225.013449	–225.792410	–225.796915	–225.839205		
cc-pV5Z	–225.018090	–225.820249	–225.819353	–225.863290		
cc-pV6Z	–225.018708	–225.831103	–225.827045	–225.871560		

E(FC-ROCCSD(T)/cc-pCVTZ) = –225.8444067

E(AE-ROCCSD(T)/cc-pCVTZ) = –226.021599

Table B3. Vibration-rotation interaction constants (α_i, MHz) of *trans*-HO_3 isotopologoues obtained at the FPA-Q2 level of theory. Values in parenthesis are taken from Ref. 24.

HOOO

i	α_i^A	α_i^B	α_i^C
1	237.4 (265.3)	3.7 (2.1)	6.0 (5.2)
2	200.8 (224.4)	–166.6 (–177.3)	–126.4 (–134.2)
3	511.7 (563.7)	296.5 (304.8)	255.1 (262.0)
4	–219.7 (–161.0)	148.4 (157.1)	143.6 (151.0)
5	–78.7 (–9.8)	162.8 (173.8)	155.9 (165.8)
6	977.2 (1150.7)	75.7 (9.3)	2.3 (–48.7)

HO^{18}OO

i	α_i^A	α_i^B	α_i^C
1	247.0 (275.1)	2.3 (0.7)	4.9 (4.1)
2	230.5 (255.2)	–165.7(–176.0)	–126.7 (–134.4)
3	457.9 (506.8)	286.1 (294.1)	246.3 (253.0)
4	–230.2 (–174.8)	143.5 (151.9)	138.8 (145.9)
5	–87.7 (–26.0)	149.8 (160.2)	142.9 (152.3)
6	888.5 (1058.1)	73.2 (10.1)	5.6 (–43.3)

HOO^{18}O

i	α_i^A	α_i^B	α_i^C
1	208.9	3.6	5.9
2	222.9	–163.7	–121.2
3	486.1	301.0	254.8
4	–261.5	146.8	138.4
5	–57.5	159.0	152.5
6	848.3	76.3	2.7

$HOOO^{18}$

i	α_i^A	α_i^B	α_i^C
1	220.5	3.6	5.6
2	154.7	–139.0	–106.5
3	548.0	265.8	231.2
4	–126.5	131.9	130.4
5	–88.4	153.7	147.4
6	976.2	69.0	2.8

$HOO^{18}O^{18}$

i	α_i^A	α_i^B	α_i^C
1	192.8	3.5	5.5
2	178.4	–134.8	–100.7
3	521.8	268.6	230.0
4	–170.3	130.2	125.5
5	–66.7	150.3	144.4
6	847.3	69.5	3.2

$HO^{18}O^{18}O^{18}$

i	α_i^A	α_i^B	α_i^C
1	201.7 (226.5)	2.2 (0.7)	4.4 (3.7)
2	201.7 (226.8)	–135.8 (–143.7)	–102.3 (–108.0)
3	470.7 (512.9)	260.2 (226.2)	222.5 (227.9)
4	–182.4 (–134.3)	126.1 (133.6)	121.5 (127.9)
5	–75.6 (–17.3)	138.1 (147.4)	132.1 (140.5)
6	765.3 (921.4)	67.3 (8.0)	6.2 (–39.1)

DOOO

i	α_i^A	α_i^B	α_i^C
1	220.2 (237.9)	10.3 (9.7)	10.7 (10.5)
2	–2.4(2.3)	–157.5 (–68.1)	–123.0 (–131.1)
3	281.9 (331.8)	203.8 (211.8)	182.6 (189.3)
4	–284.7 (–215.5)	131.5 (138.1)	131.3 (137.0)
5	–0.6 (63.0)	146.2 (156.2)	141.5 (150.7)
6	1368.5 (1483.9)	50.7 (6.2)	–23.6 (–59.6)

DO^{18}OO

i	α_i^A	α_i^B	α_i^C
1	232.7	8.1	9.0
2	30.2	–157.3	–123.3
3	230.7	197.6	176.4
4	–276.9	128.5	127.7
5	–13.6	135.9	130.9
6	1247.5	50.6	–18.9

DOO^{18}O^{18}

i	α_i^A	α_i^B	α_i^C
1	175.2	9.8	9.7
2	–1.7	–134.2	–103.9
3	304.4	188.6	168.2
4	–226.0	115.5	115.1
5	–0.7	135.1	131.2
6	1201.6	45.8	–20.8

$DO^{18}O^{18}O^{18}$

i	α_i^A	α_i^B	α_i^C
1	187.0	7.7	8.2
2	28.0	–134.8	–104.7
3	255.3	183.1	162.7
4	–221.5	113.1	112.1
5	–13.1	125.3	121.0
6	1089.7	45.9	–16.5

Table B4. Inertial defects (Δ_e) obtained by semiexperimental equilibrium rotational constants (A_e^{semi}, B_e^{semi}, C_e^{semi}, MHz) for *trans*-HO_3. Experimental[b] Δ_0 values are shown in parentheses.

	Δ_e[a]	Δ_0[b]	Δ_e[c]
HOOO	−0.021	0.012	−0.018
$HO^{18}OO$	−0.023	0.011	−0.020
$HOO^{18}O$	−0.020	0.019	—
$HOOO^{18}$	−0.021	0.016	—
$HOO^{18}O^{18}$	−0.021	0.022	−0.018
$HO^{18}O^{18}O^{18}$	−0.020	0.024	−0.017
DOOO	−0.032	−0.042	−0.026
$DO^{18}OO$	−0.032	−0.042	—
$DOO^{18}O^{18}$	−0.031	−0.033	—
$DO^{18}O^{18}O^{18}$	−0.031	−0.042	—

[a] This Work [b] References 21-23 [c] Reference 24.

Table B5. Semiexperimental r_e structural parameters for *trans*-HO_3 from Schemes 1–4[a]

	$r_e(H_1O_2)$	$r_e(O_2O_3)$	$r_e(O_3O_4)$	$\theta_e(H_1O_2O_3)$	$\theta_e(O_2O_3O_4)$	fMAR (ppt)[b]
Scheme 1						
(*ABC*, 0, IM)	0.9589(52)	1.6617(37)	1.2201(35)	95.65(26)	110.28(10)	0.68
(*ABC*, 0, RC)	0.9604(23)	1.6665(8)	1.2160(9)	95.59(20)	110.14(3)	0.25
(*ABC*, 1, IM)	0.9608(17)	1.6646(33)	1.2179(32)	95.55(12)	110.19(9)	0.26
(*ABC*, 1, RC)	0.9604(13)	1.6662(11)	1.2164(11)	95.58(11)	110.15(3)	0.28
(*ABC*, 2, IM)	0.9606(17)	1.6658(20)	1.2167(19)	95.58(13)	110.16(6)	0.29
(*ABC*, 2, RC)	0.9606(17)	1.6658(20)	1.2167(20)	95.58(13)	110.16(6)	0.29
(*BC*, 0, IM)	0.9531(90)	1.6613(25)	1.2198(24)	95.99(46)	110.23(10)	1.66
(*BC*, 0, RC)	0.9528(87)	1.6617(25)	1.2195(25)	96.00(45)	110.32(10)	1.67
(*BC*, 1, IM)	0.9523(47)	1.6633(33)	1.2182(32)	96.02(26)	110.28(10)	1.63
(*BC*, 1, RC)	0.9521(47)	1.6635(33)	1.2187(32)	96.02(26)	110.23(10)	1.65
(*BC*, 2, IM)	0.9521(36)	1.6645(36)	1.2171(34)	96.01(20)	110.26(10)	1.74
(*BC*, 2, RC)	0.9521(36)	1.6645(36)	1.2171(34)	96.01(20)	110.26(10)	1.74
(*AC*, 0, IM)	0.9611(24)	1.6611(39)	1.2209(37)	95.43(16)	110.26(10)	0.34
(*AC*, 0, RC)	0.9598(38)	1.6663(10)	1.2159(11)	95.53(35)	110.13(4)	0.31
(*AC*, 1, IM)	0.9597(10)	1.6651(17)	1.2173(16)	95.46(10)	110.17(5)	0.26
(*AC*, 1, RC)	0.9594(16)	1.6660(11)	1.2164(10)	95.48(14)	110.15(3)	0.26
(*AC*, 2, IM)	0.9594(12)	1.6657(12)	1.2169(12)	95.46(10)	110.16(3)	0.26
(*AC*, 2, RC)	0.9594(12)	1.6657(12)	1.2169(12)	95.46(10)	110.16(3)	0.26
(*AB*, 0, IM)	0.9623(20)	1.6626(33)	1.2198(32)	95.56(15)	110.24(9)	0.30
(*AB*, 0, RC)	0.9610(31)	1.6666(9)	1.2159(11)	95.65(28)	110.14(4)	0.30
(*AB*, 1, IM)	0.9614(12)	1.6654(20)	1.2173(19)	95.62(9)	110.17(5)	0.36
(*AB*, 1, RC)	0.9610(17)	1.6664(11)	1.2163(11)	95.63(15)	110.15(3)	0.37
(*AB*, 2, IM)	0.9609(14)	1.6661(12)	1.2168(12)	95.61(12)	110.16(3)	0.42
(*AB*, 2, RC)	0.9609(14)	1.6661(12)	1.2168(12)	95.61(12)	110.16(3)	0.42

	$r_e(H_1O_2)$	$r_e(O_2O_3)$	$r_e(O_3O_4)$	$\theta_e(H_1O_2O_3)$	$\theta_e(O_2O_3O_4)$	fMAR (ppt)[b]
Scheme 2						
(*ABC*, 0, IM)	0.9607(51)	1.6605(58)	1.2212(55)	95.82(27)	110.30(16)	0.65
(*ABC*, 0, RC)	0.9617(17)	1.6678(11)	1.2146(10)	95.74(14)	110.09(3)	0.24
(*ABC*, 1, IM)	0.9615(37)	1.6640(78)	1.2185(71)	95.56(20)	110.21(20)	0.26
(*ABC*, 1, RC)	0.9603(14)	1.6677(19)	1.2150(18)	95.63(11)	110.11(5)	0.25
(*ABC*, 2, IM)	0.9601(30)	1.6675(46)	1.2152(43)	95.62(21)	110.11(12)	0.25
(*ABC*, 2, RC)	0.9601(30)	1.6675(46)	1.2152(43)	95.62(21)	110.11(12)	0.25
(*BC*, 0, IM)	0.9522(63)	1.6602(29)	1.2211(29)	96.30(34)	110.34(10)	1.62
(*BC*, 0, RC)	0.9524(63)	1.6605(29)	1.2208(29)	96.26(33)	110.33(10)	1.63
(*BC*, 1, IM)	0.9529(34)	1.6610(37)	1.2205(35)	96.05(19)	110.34(10)	1.57
(*BC*, 1, RC)	0.9529(34)	1.6611(36)	1.2203(35)	96.04(19)	110.34(10)	1.58
(*BC*, 2, IM)	0.9532(29)	1.6617(37)	1.2197(36)	95.96(16)	110.33(10)	1.64
(*BC*, 2, RC)	0.9533(29)	1.6617(37)	1.2197(36)	95.96(16)	110.34(10)	1.63
(*AC*, 0, IM)	0.9628(32)	1.6597(57)	1.2222(53)	95.61(23)	110.29(15)	0.34
(*AC*, 0, RC)	0.9607(22)	1.6677(9)	1.2144(10)	95.65(19)	110.09(3)	0.28
(*AC*, 1, IM)	0.9602(13)	1.6651(25)	1.2172(24)	95.47(7)	110.17(7)	0.25
(*AC*, 1, RC)	0.9592(10)	1.6676(12)	1.2149(11)	95.53(8)	110.11(3)	0.25
(*AC*, 2, IM)	0.9588(9)	1.6674(13)	1.2152(12)	95.50(7)	110.11(4)	0.24
(*AC*, 2, RC)	0.9588(9)	1.6674(13)	1.2152(12)	95.50(7)	110.11(4)	0.24
(*AB*, 0, IM)	0.9653(24)	1.6615(45)	1.2207(42)	95.67(14)	110.27(12)	0.28
(*AB*, 0, RC)	0.9623(19)	1.6680(10)	1.2145(10)	95.80(16)	110.10(3)	0.27
(*AB*, 1, IM)	0.9623(15)	1.6652(28)	1.2175(26)	95.64(9)	110.18(8)	0.30
(*AB*, 1, RC)	0.9610(12)	1.6680(12)	1.2149(12)	95.70(10)	110.11(3)	0.30
(*AB*, 2, IM)	0.9603(11)	1.6678(13)	1.2152(13)	95.65(9)	110.12(4)	0.32
(*AB*, 2, RC)	0.9604(11)	1.6677(13)	1.2152(13)	95.66(9)	110.11(4)	0.32

	$r_e(H_1O_2)$	$r_e(O_2O_3)$	$r_e(O_3O_4)$	$\theta_e(H_1O_2O_3)$	$\theta_e(O_2O_3O_4)$	fMAR (ppt)[b]
Scheme 3						
(*ABC*, 0, IM)	0.9562(72)	1.6629(93)	1.2195(91)	95.45(40)	110.27(24)	0.75
(*ABC*, 0, RC)	0.9577(22)	1.6649(16)	1.2182(16)	95.32(20)	110.20(5)	0.26
(*ABC*, 1, IM)	0.9599(34)	1.6645(73)	1.2181(69)	95.50(19)	110.20(20)	0.27
(*ABC*, 1, RC)	0.9598(15)	1.6651(23)	1.2177(22)	95.50(14)	110.18(6)	0.28
(*ABC*, 2, IM)	0.9608(28)	1.6651(42)	1.2174(41)	95.57(22)	110.17(12)	0.28
(*ABC*, 2, RC)	0.9608(28)	1.6651(42)	1.2174(41)	95.57(22)	110.17(12)	0.28
(*BC*, 0, IM)	0.9517(134)	1.6624(63)	1.2191(62)	95.72(62)	110.33(20)	1.82
(*BC*, 0, RC)	0.9518(126)	1.6625(67)	1.2191(63)	95.71(65)	110.33(21)	1.83
(*BC*, 1, IM)	0.9524(64)	1.6640(79)	1.2182(75)	95.87(35)	110.25(22)	1.83
(*BC*, 1, RC)	0.9524(64)	1.6641(80)	1.2181(76)	95.88(35)	110.25(22)	1.84
(*BC*, 2, IM)	0.9518(59)	1.6654(84)	1.2169(79)	96.00(32)	110.20(23)	1.89
(*BC*, 2, RC)	0.9518(59)	1.6654(84)	1.2169(79)	96.00(32)	110.20(23)	1.89
(*AC*, 0, IM)	0.9579(36)	1.6625(105)	1.2201(102)	95.26(21)	110.25(27)	0.33
(*AC*, 0, RC)	0.9561(37)	1.6646(18)	1.2184(19)	95.17(34)	110.20(6)	0.31
(*AC*, 1, IM)	0.9588(14)	1.6646(28)	1.2181(26)	95.39(8)	110.19(7)	0.28
(*AC*, 1, RC)	0.9585(18)	1.6649(21)	1.2179(20)	95.38(15)	110.19(6)	0.28
(*AC*, 2, IM)	0.9594(17)	1.6649(23)	1.2177(22)	95.44(14)	110.18(6)	0.27
(*AC*, 2, RC)	0.9594(17)	1.6649(22)	1.2177(21)	95.44(14)	110.18(6)	0.27
(*AB*, 0, IM)	0.9594(32)	1.6636(94)	1.2193(92)	95.38(26)	110.23(25)	0.29
(*AB*, 0, RC)	0.9579(31)	1.6650(18)	1.2182(18)	95.35(29)	110.20(6)	0.30
(*AB*, 1, IM)	0.9602(18)	1.6650(36)	1.2179(34)	95.53(12)	110.19(10)	0.37
(*AB*, 1, RC)	0.9599(21)	1.6653(21)	1.2177(20)	95.51(18)	110.19(6)	0.37
(*AB*, 2, IM)	0.9609(21)	1.6653(23)	1.2175(22)	95.58(17)	110.18(7)	0.41
(*AB*, 2, RC)	0.9609(20)	1.6653(23)	1.2175(22)	95.58(17)	110.18(7)	0.41

	$r_e(H_1O_2)$	$r_e(O_2O_3)$	$r_e(O_3O_4)$	$\theta_e(H_1O_2O_3)$	$\theta_e(O_2O_3O_4)$	fMAR (ppt)[b]
Scheme 4						
(*ABC*, 0, IM)	0.9631(54)	1.6608(69)	1.2205(66)	95.89(27)	110.29(19)	0.66
(*ABC*, 0, RC)	0.9641(22)	1.6668(15)	1.2151(15)	95.84(19)	110.11(4)	0.22
(*ABC*, 1, IM)	0.9621(39)	1.6640(83)	1.2183(79)	95.58(21)	110.20(21)	0.27
(*ABC*, 1, RC)	0.9613(17)	1.6666(25)	1.2158(24)	95.63(13)	110.13(7)	0.28
(*ABC*, 2, IM)	0.9607(34)	1.6663(57)	1.2162(54)	95.60(23)	110.14(16)	0.28
(*ABC*, 2, RC)	0.9607(34)	1.6663(57)	1.2162(54)	95.60(23)	110.14(16)	0.28
(*BC*, 0, IM)	0.9566(83)	1.6603(44)	1.2203(42)	96.26(43)	110.34(43)	0.16
(*BC*, 0, RC)	0.9561(89)	1.6606(48)	1.2201(45)	96.25(45)	110.33(16)	0.16
(*BC*, 1, IM)	0.9527(53)	1.6614(69)	1.2200(66)	96.11(29)	110.32(19)	0.16
(*BC*, 1, RC)	0.9527(53)	1.6616(71)	1.2199(67)	96.10(29)	110.32(19)	0.16
(*BC*, 2, IM)	0.9530(48)	1.6623(75)	1.2191(71)	95.98(26)	110.32(20)	0.17
(*BC*, 2, RC)	0.9530(48)	1.6623(75)	1.2191(71)	95.98(26)	110.32(20)	0.17
(*AC*, 0, IM)	0.9658(34)	1.6598(76)	1.2215(72)	95.61(18)	110.28(20)	0.32
(*AC*, 0, RC)	0.9634(37)	1.6667(16)	1.2150(17)	95.78(32)	110.10(5)	0.30
(*AC*, 1, IM)	0.9609(16)	1.6649(33)	1.2174(31)	95.49(9)	110.18(9)	0.25
(*AC*, 1, RC)	0.9601(17)	1.6665(22)	1.2158(21)	95.53(13)	110.13(6)	0.25
(*AC*, 2, IM)	0.9593(16)	1.6662(24)	1.2163(23)	95.47(11)	110.14(7)	0.25
(*AC*, 2, RC)	0.9593(16)	1.6662(24)	1.2163(23)	95.47(11)	110.14(7)	0.25
(*AB*, 0, IM)	0.9668(30)	1.6619(63)	1.2199(63)	95.80(18)	110.25(17)	0.28
(*AB*, 0, RC)	0.9649(30)	1.6670(16)	1.2150(16)	95.91(26)	110.11(5)	0.28
(*AB*, 1, IM)	0.9629(19)	1.6651(39)	1.2174(39)	95.67(12)	110.18(11)	0.36
(*AB*, 1, RC)	0.9621(19)	1.6669(22)	1.2158(21)	95.71(15)	110.14(6)	0.36
(*AB*, 2, IM)	0.9610(17)	1.6667(24)	1.2163(23)	95.63(13)	110.15(7)	0.41
(*AB*, 2, RC)	0.9610(17)	1.6667(24)	1.2163(23)	95.63(13)	110.15(7)	0.41

[a]Bond distances in Å; bond angles in degrees. Standard errors of the fit are given in parenthesis. Scheme 1 fits to all 10 HO_3 isotopologues (HO_3, $H^{18}OOO$, $HO^{18}OO$, $HOO^{18}O$, $HO^{18}O^{18}O$, $H^{18}O^{18}O^{18}O$, DO_3, $D^{18}OOO$, $DO^{18}O^{18}O$, $D^{18}O^{18}O^{18}O$), Scheme 2 fits to only singly-substituted isotopologues (HO_3, $H^{18}OOO$, $HO^{18}OO$, $HOO^{18}O$, DO_3), Scheme 3 fits to the HO_3 parent and all deuterated isotopologues (HO_3, DO_3, $D^{18}OOO$, $DO^{18}O^{18}O$, $D^{18}O^{18}O^{18}O$), and Scheme 4 fits to (HO_3, $H^{18}OOO$, $HO^{18}O^{18}O$, $H^{18}O^{18}O^{18}O$, DO_3). The fitting procedure is specified by (*x,y,z*), where *x* specifies which rotational constants are utilized [(*ABC*), (*BC*), (*AC*), (*AB*)], *y* gives the inverse power of uncertainty weights (n = 0, 1, 2), and *z* indicates fitting to inertial moments (IM) or directly to rotational constants (RC). [b]Fractional mean absolute residual in parts per thousand (ppt).

Table B6. Relative derivative quantities $R_{\lambda,ij} = \frac{100}{R_j}\frac{\partial R_j}{\partial \lambda_i}$ measuring the sensitivity of fitted internal coordinates (R_j) of *trans*-HO_3 to scaling factors (λ_i) for zero-point contributions from the vibrational normal modes (ν_i).[a]

R_λ	$r(H_1O_2)$	$r(O_2O_3)$	$r(O_3O_4)$	$\theta(H_1O_2O_3)$	$\theta(O_2O_3O_4)$
r_e fit					
λ_1	–0.98	0.30	–0.47	–0.39	–0.04
λ_2	1.21	1.60	–1.03	0.24	0.12
λ_3	8.69	–1.54	–1.57	4.96	–0.71
λ_4	1.93	–1.19	0.15	–0.11	–0.28
λ_5	0.44	–0.92	–0.31	0.75	–0.47
λ_6	–1.24	–1.60	1.57	3.11	0.62
r_0 fit					
λ_1	–0.93	0.31	–0.48	–0.52	–0.04
λ_2	1.20	1.66	–1.05	0.17	0.12
λ_3	8.58	–1.61	–1.62	6.51	–0.73
λ_4	2.06	–1.26	0.17	0.21	–0.27
λ_5	0.45	–0.95	–0.34	1.06	–0.48
λ_6	–1.69	–1.62	1.59	3.42	0.63

[a]All values obtained from (*ABC*, 2, IM) fits. See Table B5.

Table B7. Focal point analysis[a] for the vertical excitation energy [$T_v(^2A'' \rightarrow ^2A')$, kcal mol^{-1}][b] of *trans*-HO_3.

	ΔE_e(ROHF)	+δ [ROMP2]	+δ [ROCCSD]	+δ[ROCCSD(T)]	NET
cc-pVDZ	+47.98	+5.67	+1.81	+0.77	[+56.23]
cc-pVTZ	+47.67	+6.54	+0.49	+1.38	[+56.08]
cc-pVQZ	+47.37	+6.40	+0.32	+1.49	[+55.58]
cc-pV5Z	+47.24	+6.25	+0.29	+1.49	[+55.28]
cc-pV6Z	+47.21	+6.22	+0.27	+1.50	[+55.20]
CBS	[+47.20]	[+6.16]	[+0.26]	[+1.52]	[+55.14]
FPA-Q3 reference geometries					
T_v = **+55.14 kcal mol^{-1}**					

[a] For notation see footnote *a* of Table 4.6. [b] CASSCF and EOM-CCSD produce T_v values of 48.2 and 53.7 kcal mol^{-1}, respectively.

Table B8. Quadratic internal coordinate force constants F_{ij}, harmonic vibrational frequencies ω_i, and internal coordinates for HO_3.[a]

	trans-HO_3		*cis*-HO_3	
F_{ij}	CCSD(T) /cc-pVQZ[a]	FPA-Q2	CCSD(T) /cc-pVQZ[a]	FPA-Q2
11	7.8821	7.8494	7.6885	7.6449
21	–0.0294	–0.0213	0.0526	0.0628
22	0.6608	0.6564	1.0766	0.9525
31	–0.0802	–0.0797	–0.0502	–0.0524
32	1.2518	1.1056	1.5233	1.4759
33	9.9001	9.8056	8.5721	8.4183
41	–0.0107	–0.0118	0.0346	0.0299
42	0.1420	0.1441	0.2863	0.2786
43	0.1839	0.1702	0.0193	0.0285
44	0.6224	0.6060	0.7993	0.7961
51	0.0381	0.0337	–0.0374	–0.0302
52	0.0170	0.0353	–0.1666	–0.1746
53	0.3708	0.3290	0.5378	0.4973
54	0.2808	0.2689	–0.2513	–0.2396
55	1.2803	1.2556	1.4852	1.4668
66	0.0073	0.0138	0.0173	0.0195
$\omega_1(a')$	3756.9	3749.2	3709.5	3699.2
$\omega_2(a')$	1427.6	1423.9	1370.9	1365.4
$\omega_3(a')$	1130.9	1114.4	1231.5	1222.2
$\omega_4(a')$	532.3	526.6	612.4	605.7
$\omega_5(a')$	270.9	280.0	313.7	290.4
$\omega_6(a'')$	123.7	170.3	197.4	209.4

Internal coordinate set:

$S_1 = r(H_1O_2)$, $S_2 = r(O_2O_3)$, $S_3 = r(O_3O_4)$

$S_4 = \theta(H_1O_2O_3)$, $S_5 = \theta(O_2O_3O_4)$, $S_6 = \tau(H_1O_2O_3O_4)$

[a]The units of the force constants are consistent with energy in aJ, bond lengths in Å, and angles in radians; harmonic frequencies in cm^{-1}.

Table B9. Cubic force constants F_{ijk} of *trans*-HO_3 in internal coordinate space.[a,b]

ijk	CCSD(T) /cc-pVQZ[c]	FPA-Q2	*ijk*	CCSD(T) /cc-pVQZ[c]	FPA-Q2
111	–55.112	–54.923	511	(0.007)	(0.005)
211	0.089	0.118	521	–0.241	–0.219
221	–0.028	–0.032	522	–0.340	–0.200
222	–5.141	–4.258	531	(–0.104)	(–0.102)
311	0.156	0.111	532	–1.196	–1.234
321	(–0.108)	(–0.052)	533	(0.166)	(–0.079)
322	–4.751	–5.216	541	–0.061	–0.068
331	0.272	0.198	542	–0.225	–0.270
332	0.535	0.293	543	–0.383	–0.353
333	–79.256	–76.708	544	–0.043	–0.049
411	(0.099)	(0.106)	551	–0.205	–0.187
421	–0.169	–0.176	552	–2.517	–2.636
422	–0.734	–0.722	553	–1.828	–1.783
431	(–0.004)	(–0.016)	554	–0.270	–0.264
432	–0.258	–0.282	555	–2.368	–2.385
433	–0.226	–0.269	661	0.010	0.010
441	–0.076	–0.085	662	–0.028	–0.026
442	–1.339	–1.370	663	–0.083	–0.073
443	0.258	0.209	664	(0.002)	(0.0003)
444	–0.689	–0.711	665	–0.040	–0.033

[a]See footnote a of Table B8 for units of F_{ijk}. [b]Values in parenthesis denote F_{ijk} elements which contribute negligibly to the vibrational anharmonic constants x_{ij}. [c]Computed at the optimum FPA-Q2 geometry.

Table B10. Cubic force constants F_{ijk} of *cis*-HO_3 in internal coordinate space.[a]

ijk	CCSD(T) /cc-pVQZ	FPA-Q2	*ijk*	CCSD(T) /cc-pVQZ	FPA-Q2
111	–53.948	–53.790	511	0.126	0.137
211	0.304	0.314	521	0.202	0.183
221	–0.535	–0.497	522	–0.549	–0.328
222	–9.585	–8.606	531	0.121	0.131
311	0.221	0.203	532	–0.700	–0.931
321	–0.075	–0.034	533	–0.830	–0.730
322	–2.125	–2.824	541	0.024	0.032
331	0.225	0.142	542	0.046	0.085
332	–3.292	–2.589	543	0.170	0.137
333	–65.897	–65.327	544	–0.255	–0.283
411	0.331	0.342	551	0.140	0.124
421	–0.560	–0.569	552	–2.756	–2.787
422	–1.195	–1.234	553	–2.557	–2.519
431	0.222	0.225	554	0.012	0.015
432	0.101	0.070	555	–3.080	–3.093
433	–0.408	–0.315	661	0.060	0.060
441	–0.195	–0.180	662	–0.113	–0.105
442	–1.596	–1.640	663	0.027	0.037
443	0.001	–0.007	664	–0.058	–0.045
444	–1.069	–1.073	665	–0.005	0.001

[a]See footnote a of Table B8 for units of F_{ijk}.

Table B11. Quartic force constants F_{ijkl} of *trans*-HO_3 in internal coordinate space.[a,b]

ijkl	CCSD(T) /cc-pVQZ[c]	FPA-Q2	*ijkl*	CCSD(T) /cc-pVQZ[c]	FPA-Q2	*ijkl*	CCSD(T) /cc-pVQZ[c]	FPA-Q2
1111	341.03	335.28	4432	–0.80	–0.98	5531	(0.03)	(–0.18)
2111	(0.96)	(2.18)	4433	–0.90	–1.35	5532	5.35	4.95
2211	–2.34	–3.66	4441	(0.00)	(0.02)	5533	(–0.36)	(–0.05)
2221	(1.55)	(2.71)	4442	1.96	1.84	5541	(–0.25)	(–0.26)
2222	23.04	19.42	4443	0.50	0.62	5542	–0.41	–0.33
3111	(1.47)	(5.58)	4444	(1.06)	(0.64)	5543	(0.40)	(0.28)
3211	–1.00	–2.58	5111	0.73	0.11	5544	–0.48	–0.64
3221	(0.09)	(–1.57)	5211	–0.63	–0.67	5551	(0.85)	(0.70)
3222	–2.43	4.66	5221	(0.19)	(–0.12)	5552	4.42	5.07
3311	–2.29	–5.99	5222	2.72	2.40	5553	3.73	3.44
3321	(–1.04)	(–3.97)	5311	(–0.53)	(–0.33)	5554	0.50	0.70
3322	24.04	12.43	5321	(4.27)	(6.01)	5555	7.50	6.75
3331	(1.44)	5.34	5322	0.33	2.48	6611	–0.14	–0.05
3332	(–16.78)	(1.01)	5331	(–0.48)	(–0.83)	6621	(–0.12)	(–0.09)
3333	506.16	478.68	5332	(3.67)	0.50	6622	–0.09	–0.18
4111	(0.43)	(0.66)	5333	(–3.31)	(–0.28)	6631	(–0.02)	(–0.07)
4211	–0.78	–0.90	5411	(–0.28)	(–0.06)	6632	0.20	0.21
4221	(0.66)	(0.50)	5421	(1.95)	(2.45)	6633	–0.41	–0.48
4222	3.61	3.19	5422	–1.30	–1.46	6641	(–0.06)	(–0.05)
4311	–0.74	–1.33	5431	(1.90)	(2.72)	6642	0.05	0.09
4321	(3.46)	(7.12)	5432	2.37	2.57	6643	–0.15	–0.07
4322	–1.78	–1.03	5433	(–0.39)	(0.29)	6644	–0.09	–0.05
4331	(–0.11)	(–0.70)	5441	(0.07)	(–0.05)	6651	(–0.09)	(0.06
4332	(0.26)	(–0.65)	5442	(0.15)	(0.05)	6652	0.06	–0.27
4333	(0.98)	(1.57)	5443	–0.45	–0.40	6653	(–0.14)	(0.00)
4411	–1.34	–1.64	5444	–0.31	–0.14	6654	–0.31	–0.23
4421	(0.46)	(0.30)	5511	–0.69	–0.56	6655	–0.08	–0.05
4422	1.75	1.87	5521	(0.30)	(0.48)	6666	–0.03	–0.059[d]
4431	(–0.52)	(–1.07)	5522	1.84	1.58			

[a]See footnote a of Table B8 for units of F_{ijkl}. [b]Values in parentheses denote F_{ijkl} elements which contribute negligibly to the vibrational anharmonic constants. [c]Computed at the optimum FPA-Q2 geometry.[d]F_{6666} = –0.048 when τdisp = 0.06 rad.

Table B12. Quartic force constants F_{ijkl} of *cis*-HO_3 in internal coordinate space.[a]

ijkl	CCSD(T) /cc-pVQZ[b]	FPA-Q2	*ijkl*	CCSD(T) /cc-pVQZ[b]	FPA-Q2	*ijkl*	CCSD(T) /cc-pVQZ[b]	FPA-Q2
1111	340.31	333.75	4432	1.00	–0.14	5531	–0.14	0.06
2111	–1.95	0.20	4433	–0.12	–1.96	5532	6.65	7.43
2211	–0.47	–3.27	4441	–0.18	0.80	5533	2.27	2.35
2221	2.46	7.64	4442	2.33	3.22	5541	–0.08	–0.14
2222	68.74	60.94	4443	1.45	2.46	5542	1.10	0.83
3111	–1.44	1.51	4444	2.38	1.05	5543	0.11	0.09
3211	0.92	1.64	5111	–0.95	0.12	5544	0.31	0.27
3221	1.47	1.45	5211	–0.25	–0.22	5551	–1.11	–1.06
3222	–20.95	–22.61	5221	–0.06	0.29	5552	6.62	6.23
3311	0.80	–0.88	5222	9.07	10.67	5553	5.72	5.33
3321	–0.28	0.96	5311	0.43	0.96	5554	1.31	1.19
3322	32.80	28.72	5321	–3.16	–5.50	5555	12.31	12.58
3331	–0.12	2.80	5322	–1.88	–1.23	6611	0.13	0.39
3332	–15.24	–3.18	5331	0.01	0.76	6621	–0.23	–0.21
3333	444.64	425.62	5332	8.61	8.39	6622	0.43	0.42
4111	–0.81	3.21	5333	–7.45	–5.00	6631	0.19	0.07
4211	–1.13	–4.02	5411	–0.63	–0.88	6632	0.25	0.27
4221	3.75	1.29	5421	–0.61	3.39	6633	–0.63	–0.35
4222	2.17	6.79	5422	1.57	1.17	6641	–0.21	–0.22
4311	–0.05	–1.92	5431	–1.81	0.57	6642	0.25	0.13
4321	–2.88	10.05	5432	–1.43	1.26	6643	–0.02	–0.08
4322	–0.91	–3.41	5433	0.77	0.62	6644	0.03	–0.07
4331	–0.03	–1.50	5441	0.32	0.24	6651	–0.04	0.03
4332	0.96	–1.39	5442	0.45	0.21	6652	0.32	0.40
4333	0.76	3.77	5443	0.60	0.57	6653	–0.37	–0.22
4411	–1.73	–3.86	5444	0.88	1.13	6654	0.37	0.32
4421	2.01	0.45	5511	–0.27	–0.45	6655	–0.12	–0.04
4422	2.03	–0.09	5521	–0.31	0.09	6666	–0.11	–0.08
4431	–0.89	–1.34	5522	4.42	4.92			

[a]See footnote a of Table S8 for units of F_{ijkl}. [b]Computed at the optimum FPA-Q2 geometry.

Table B13. Anharmonicity constants x_{ij} (cm^{-1}) for *trans*-HO_3, *trans*-DO_3, *cis*-HO_3, and *cis*-DO_3 at the FPA-Q2 level of theory.

x_{ij}	*trans*-HO_3	*trans*-DO_3	*cis*-HO_3	*cis*-DO_3
11	–86.59	–45.93	–87.34	–46.47
21	–2.83	–1.79	–15.12	–4.11
22	–22.48	–23.96	–5.73	–19.73
31	–24.33	–10.88	–17.04	–11.42
32	43.67	24.22	–60.25	25.73
33	–25.86	–15.84	–8.45	–14.77
41	–2.55	–3.19	3.83	2.44
42	11.19	16.84	–7.35	15.39
43	–29.59	–27.30	–3.99	–25.52
44	–11.35	–10.00	–12.39	–11.59
51	–3.58	–2.37	4.88	3.15
52	29.10	7.72	–33.12	52.04
53	–50.10	–23.96	6.74	–60.37
54	–15.13	–12.99	–18.96	19.16
55	–4.43	–4.53	–18.46	–26.33
61	–2.24	–1.30	21.85	12.77
62	–7.92	–5.42	–19.82	5.87
63	–13.62	–12.81	0.60	–19.79
64	11.01	11.61	–14.38	–8.25
65	–18.64	–12.75	–31.64	–44.60
66	–12.02	–7.06	–14.84	–2.80

Table B14. Summary of final FPA-Q2 vibrational analysis for *cis*-HO_3 and *cis*-DO_3.[a]

	Description	TED[b]	ω	Δ_{anh}	Δ_{res}	Δ_{Cor}	ν
cis-HO_3							
ν_1	O–H str.	$S_1(100)$	3699.2	–192.5	0	17.0	3523.7
ν_2	term. O–O str.	$S_3(51)+S_4(44)–S_5(5)$	1365.4	–80.2	0	0.9	1286.1
ν_3	H–O–O bend	$S_4(50)–S_3(49)+S_5(1)$	1222.2	–55.2	0	1.3	1168.4
ν_4	O–O–O bend	$S_5(75)–S_2(15)+S_4(7)+ S_3(3)$	605.7	–46.2	0	1.0	560.5
ν_5	central O–O str.	$S_2(85)+S_5(19)–S_3(–3)–S_4(–1)$	290.4	–73.2	0	0.2	217.5
ν_6	H–O–O–O tors.	$S_6(100)$	209.4	–69.8	0	18.4	158.1
cis-DO_3.							
ν_1	O–D str.	$S_1(100)$	2694.2	–104.7	0	13.2	2602.7
ν_2	term. O–O str.	$S_3(94)+S_4(4)–S_5(2)$	1315.2	6.9	0	1.1	1323.2
ν_3	D–O–O bend	$S_4(78)–S_3(7)–S_5(14)+S_2(1)$	974.0	–76.2	0	0.9	898.8
ν_4	O–O–O bend	$S_5(63)–S_2(16)+S_4(19)+S_3(2)$	577.5	–22.9	0	1.4	555.9
ν_5	central O–O str.	$S_2(84)+S_5(21)–S_3(–3)–S_4(–1)$	283.4	–68.2	0	0.2	215.4
ν_6	D–O–O–O tors.	$S_6(100)$	161.9	–47.4	0	14.8	129.4

Internal coordinates: $S_1 = r(H_1O_2)$, $S_2 = r(O_2O_3)$, $S_3 = r(O_3O_4)$

$S_4 = \theta(H_1O_2O_3)$, $S_5 = \theta(O_2O_3O_4)$, $S_6 = \tau(H_1O_2O_3O_4)$

[a]All values in cm^{-1}. [b]The $S_i(k)$ entries specify the percentage proportions k of the total energy distribution (TED) of each normal vibration among the internal coordinates S_i. The phase of S_i in the normal-mode eigenvector precedes each $S_i(k)$ value. Contributions rounding to less than 1% in magnitude are not listed.

Table B15. Selected combination and overtone band differences of *cis*-HO_3 and *cis*-DO_3.

	FPA-Q2	Expt.[a]	MRCI+Q/AVQZ[b]
cis-HO_3			
ν_1	3523.7	3565.4	3538.1
$(\nu_1 + \nu_2) - \nu_1$	1271.0	—	—
$(\nu_1 + \nu_3) - \nu_1$	1151.3	1008.6	1160.4
$(\nu_1 + \nu_4) - \nu_1$	565.5	486.5	648.5
$(\nu_1 + \nu_5) - \nu_1$	222.3	243.6	218.6
$(\nu_1 + \nu_6) - \nu_1$	179.9	149.1	160.7
cis-DO_3			
ν_1	2602.7	2632.0	—
$(\nu_1 + \nu_2) - \nu_1$	1319.1	—	—
$(\nu_1 + \nu_3) - \nu_1$	887.4	791.0	—
$(\nu_1 + \nu_4) - \nu_1$	558.3	—	—
$(\nu_1 + \nu_5) - \nu_1$	218.6	389.0	—
$(\nu_1 + \nu_6) - \nu_1$	142.1	90.9/100.7	—

[a]Reference 15. [b]Reference 24.

Table B16. Force constants and spectroscopic data for O_2.[a]

	FPA-Q2	FPA-Q2[b]	FPA-Q2[c]	FPA-Q2[d]	FPA-P	FPA-P[b]	Expt.
f_{rr}	11.792	11.830	11.782	11.797	11.809	11.760	—
f_{rrr}	–87.537	–88.094	–87.600	–87.779	–88.216	–97.712	—
f_{rrrr}	558.062	563.046	559.905	549.256	571.102	558.850	—
ω_e	1581.95	1584.51	1581.28	1582.30	1583.10	1582.74	1580.19
$\omega_e x_e$	11.73	11.81	11.76	12.05	11.76	11.91	11.98
ν_0	1558.49	1560.89	1557.76	1558.21	1559.58	1556.01	1556.23
ν_0 (CN)	1558.2	1560.6	1557.5	1558.0	1559.3	1555.7	—
r_e	1.2074	1.2069	1.2072	1.2072	1.2070	1.2073	1.2075

[a]The units of the force constants are consistent with energy in aJ, harmonic and fundamental frequencies in cm^{-1}, bond lengths in Å. [b]Based off of a sextic force field. [c]Similar to b with the addition of a first-order relativistic correction computed from the one-electron mass-velocity and Darwin terms. [d]Similar to b with the addition of relativistic corrections based on the Douglas-Kroll transformation.

Table B17. Force constants and spectroscopic data for diatomic OH (OD).

	FPA-Q2	FPA-Q2[H]	FPA-P	Expt.
f_{rr}	7.8143	7.8149	7.8148	—
f_{rrr}	–54.59	–54.48	–54.48	—
f_{rrrr}	336.94	335.32	335.20	—
ω_e	3740.21 (2722.91)	3740.35 (2723.01)	3740.32 (2722.99)	3737.76 (2720.24)
$\omega_e x_e$	84.97 (45.03)	84.67 (44.88)	84.71 (44.90)	84.88 (44.06)
ν_0	3570.27 (2632.85)	3571.00 (2633.25)	3570.89 (2633.19)	3568.00 (2632.12)
ν_0 (CN)	3567.6 (2631.8)	3568.3 (2632.2)	3568.2 (2632.1)	—
r_e	0.9698	0.9696	0.9697	0.9697

Table B18. Optimized internal coordinates[a] along the DRP for the *cis–trans* isomerization of HO_3.

$\tau(H_1O_2O_3O_4)$	**0°**	**10°**	**20°**	**30°**	**40°**	**50°**	**60°**	**70°**
$r(H_1O_2)$	0.9715	0.9714	0.9710	0.9705	0.9700	0.9695	0.9692	0.9689
$r(O_2O_3)$	1.5679	1.5705	1.5777	1.5888	1.6025	1.6175	1.6325	1.6462
$r(O_3O_4)$	1.2387	1.2381	1.2366	1.2344	1.2319	1.2292	1.2266	1.2242
$\theta(H_1O_2O_3)$	97.26	97.27	97.27	97.23	97.12	96.93	96.69	96.44
$\theta(O_2O_3O_4)$	112.27	112.31	112.37	112.43	112.45	112.41	112.28	112.10

$\tau(H_1O_2O_3O_4)$	**76.8° (TSct)**	**80°**	**90°**	**100°**	**110°**	**120°**	**130°**	**140°**
$r(H_1O_2)$	0.9687	0.9686	0.9685	0.9684	0.9684	0.9684	0.9684	0.9685
$r(O_2O_3)$	1.6542	1.6575	1.6659	1.6711	1.6735	1.6733	1.6716	1.6691
$r(O_3O_4)$	1.2228	1.2222	1.2205	1.2192	1.2182	1.2174	1.2168	1.2164
$\theta(H_1O_2O_3)$	96.28	96.21	96.05	95.97	95.96	95.01	96.10	96.20
$\theta(O_2O_3O_4)$	111.95	111.87	111.63	111.38	111.15	110.92	110.72	110.54

$\tau(H_1O_2O_3O_4)$	**150°**	**160°**	**170°**	**180°**
$r(H_1O_2)$	0.9685	0.9686	0.9687	0.9687
$r(O_2O_3)$	1.6663	1.6638	1.6622	1.6616
$r(O_3O_4)$	1.2160	1.2158	1.2157	1.2157
$\theta(H_1O_2O_3)$	96.31	96.39	96.45	96.47
$\theta(O_2O_3O_4)$	110.39	110.27	110.20	110.17

[a]Bond distances in Å; bond angles in degrees.

Table B19. FPA-Q2 projected harmonic vibrational frequencies (cm^{-1}) along the DRP for the *cis–trans* isomerization of HO_3.

$\tau(H_1O_2O_3O_4)$	**0°**	**10°**	**20°**	**30°**	**40°**	**50°**	**60°**
ω_1(OH str.)	3699.8	3702.1	3708.3	3716.7	3725.0	3732.3	3738.6
ω_2(term. OO str.)	1365.5	1362.9	1356.1	1349.1	1345.9	1347.8	1354.2
ω_3(HOO bend)	1221.9	1221.9	1219.4	1212.1	1197.2	1175.0	1148.9
ω_4(OOO bend)	605.3	603.3	596.9	587.7	577.5	567.4	558.6
ω_5(central OO str.)	290.5	290.2	287.9	282.1	272.2	261.0	250.5

$\tau(H_1O_2O_3O_4)$	**70°**	**76.8° (TSct)**	**80°**	**90°**	**100°**	**110°**	**120°**
ω_1(OH str.)	3743.4	3745.9	3746.9	3749.5	3751.3	3752.3	3752.8
ω_2(term. OO str.)	1362.9	1369.7	1372.2	1381.3	1389.6	1394.7	1403.3
ω_3(HOO bend)	1122.4	1105.3	1099.0	1080.9	1069.8	1066.1	1069.1
ω_4(OOO bend)	551.4	547.3	546.0	542.1	539.3	538.3	535.1
ω_5(central OO str.)	242.4	238.9	237.7	236.8	239.3	244.0	251.8

$\tau(H_1O_2O_3O_4)$	**130°**	**140°**	**150°**	**160°**	**170°**	**180°**
ω_1(OH str.)	3752.6	3752.0	3751.3	3750.6	3750.0	3748.7
ω_2(term. OO str.)	1409.1	1414.0	1419.4	1421.4	1423.4	1424.1
ω_3(HOO bend)	1076.6	1086.8	1097.6	1106.3	1112.3	1113.6
ω_4(OOO bend)	533.0	530.9	528.0	527.8	526.9	526.3
ω_5(central OO str.)	259.5	266.5	272.7	276.7	279.2	279.9

Table B20. FPA-Q2 projected harmonic vibrational frequencies (cm^{-1}) along the DRP for the *cis–trans* isomerization of DO_3.

$\tau(H_1O_2O_3O_4)$	**0°**	**10°**	**20°**	**30°**	**40°**	**50°**	**60°**
ω_1(OD str.)	2694.7	2696.5	2701.0	2707.2	2713.2	2718.5	2723.0
ω_2(term. OO str.)	1315.4	1316.4	1319.3	1324.4	1331.6	1340.4	1350.7
ω_3(DOO bend)	973.6	970.3	959.0	941.0	917.4	890.0	861.5
ω_4(OOO bend)	577.0	575.5	570.3	563.3	556.1	549.8	545.4
ω_5(central OO str.)	283.5	283.0	280.3	274.4	265.1	254.9	245.7

$\tau(H_1O_2O_3O_4)$	70°	**76.8° (TSct)**	**80°**	**90°**	**100°**	**110°**	**120°**
ω_1(OD str.)	2726.4	2728.1	2728.9	2730.7	2731.9	2732.7	2733.1
ω_2(term. OO str.)	1361.4	1368.9	1371.7	1381.2	1389.5	1394.5	1402.9
ω_3(DOO bend)	834.1	817.1	810.7	793.6	784.7	784.5	791.9
ω_4(OOO bend)	542.8	541.7	541.5	540.5	538.3	535.4	528.2
ω_5(central OO str.)	238.9	236.2	235.3	235.3	238.2	243.0	250.7

$\tau(H_1O_2O_3O_4)$	**130°**	**140°**	**150°**	**160°**	**170°**	**180°**
ω_1(OD str.)	2733.1	2732.7	2732.3	2731.8	2731.4	2731.3
ω_2(term. OO str.)	1408.2	1412.7	1416.4	1419.2	1420.9	1421.4
ω_3(DOO bend)	804.2	818.6	832.7	844.1	851.6	853.7
ω_4(OOO bend)	521.0	513.8	507.7	502.9	500.0	498.7
ω_5(central OO str.)	258.1	265.1	271.1	275.5	278.1	278.9

Table B21. FPA-Q2 projected (P) vs. non-projected (NP) harmonic vibrational frequencies (cm^{-1}) for **TSct** of HO_3 and DO_3.

	P	NP
HO_3-TSct		
ω_1(OH str.)	3745.9	3745.9
ω_2(term. OO str.)	1369.7	1369.7
ω_3(HOO bend)	1106.0	1105.9
ω_4(OOO bend)	547.5	547.5
ω_5(central OO str.)	238.9	236.8
ω_6(HOOO tors.)	0	163.4i
DO_3-TSct		
ω_1(OD str.)	2728.1	2728.1
ω_2(term. OO str.)	1368.9	1368.9
ω_3(DOO bend)	817.6	817.5
ω_4(OOO bend)	541.8	541.8
ω_5(central OO str.)	236.2	235.0
ω_6(DOOO tors.)	0	124.5i

Table B22. Fourier coefficients (a_k) for the FPA-Q2 optimized internal coordinates along the DRP for *cis-trans* isomerization of HO_3.[a]

Functional form: $f(\tau) = a_0 + \sum_{k=1}^{9} a_k \cos(k\tau)$

Coefficient	$r(H_1O_2)$	$r(O_2O_3)$	$r(O_3O_4)$	$\theta(H_1O_2O_3)$	$\theta(O_2O_3O_4)$
a_0	0.485	0.820	0.612	48.263	55.740
a_1	1.17×10^{-3}	-4.48×10^{-2}	1.07×10^{-2}	0.512	1.167
a_2	7.96×10^{-4}	-2.55×10^{-2}	3.29×10^{-3}	0.411	–0.199
a_3	2.03×10^{-4}	-1.99×10^{-3}	7.61×10^{-4}	–0.097	–0.103
a_4	1.02×10^{-4}	9.29×10^{-5}	1.56×10^{-4}	–0.067	–0.055
a_5	3.32×10^{-5}	-5.35×10^{-5}	4.75×10^{-5}	–0.019	–0.012
a_6	1.08×10^{-5}	-7.76×10^{-5}	2.26×10^{-5}	–0.003	–0.003
a_7	3.99×10^{-6}	-1.38×10^{-5}	7.46×10^{-6}	–0.001	-5.45×10^{-4}
a_8	2.01×10^{-6}	-4.60×10^{-6}	3.19×10^{-6}	-1.61×10^{-4}	-2.07×10^{-4}
a_9	6.54×10^{-8}	-7.87×10^{-6}	1.56×10^{-6}	-4.86×10^{-4}	-3.80×10^{-5}

[a]Values of a_k for stretching coordinates are in Å; values of a_k for bond angles are in degrees.

Table B23. Fourier coefficients (a_k, in cm^{-1}) for the FPA-Q2 harmonic vibrational frequency and ZPVE functions along the DRP for *cis-trans* isomerization of HO_3.

Functional form: $F(\tau) = a_0 + \sum_{k=1}^{9} a_k \cos(k\tau)$

$F(\tau)$	ω_1	ω_2	ω_3	ω_4	ω_5	ZPVE
a_0	1869.46	691.73	564.68	276.54	131.54	–9.313
a_1	–20.720	–37.944	64.392	34.076	4.287	1.320
a_2	–12.131	6.366	44.219	11.641	24.943	25.497
a_3	–3.598	6.400	–8.623	5.461	2.188	–2.718
a_4	–1.721	4.452	–4.950	0.976	–1.979	–3.221
a_5	–0.598	2.174	–1.581	–0.093	–0.788	–1.018
a_6	–0.213	0.328	–0.805	0.248	–0.682	–0.691
a_7	–0.096	0.039	–0.144	0.030	–0.375	–0.417
a_8	–0.052	0.108	–0.113	–0.144	–0.123	–0.133
a_9	0.013	–0.069	0.057	0.025	–0.062	0.013

Table B24. Fourier coefficients (a_k, in cm^{-1}) for the FPA-Q2 harmonic vibrational frequency and ZPVE functions along the DRP for *cis-trans* isomerization of DO_3.

Functional form: $F(\tau) = a_0 + \sum_{k=1}^{9} a_k \cos(k\tau)$

$F(\tau)$	ω_1	ω_2	ω_3	ω_4	ω_5	ZPVE
a_0	1361.59	686.93	427.85	268.61	129.83	–23.64
a_1	–15.050	–52.841	62.850	31.940	0.894	13.898
a_2	–8.663	–6.238	60.158	–1.340	23.576	33.741
a_3	–2.718	–0.490	–3.206	7.429	2.415	1.712
a_4	–1.316	0.747	–2.041	2.096	–1.352	–0.933
a_5	–0.443	0.457	0.398	–0.397	–0.653	–0.319
a_6	–0.169	–0.158	–0.066	0.061	–0.569	–0.451
a_7	–0.090	–0.169	–0.088	0.186	–0.315	–0.238
a_8	–0.037	0.181	–0.108	–0.185	–0.106	–0.128
a_9	3.96×10^{-7}	0.044	–0.004	–0.009	–0.041	–0.006

Table B25. Fourier coefficients (a_k, in cm^{-1}) for the FPA-Q2 bare (V_e) and ZPVE-corrected (V_0) potential functions along the DRP for *cis-trans* isomerization of HO_3 and DO_3.

Functional form: $F(\tau) = a_0 + \sum_{k=1}^{16} a_k \cos(k\tau)$

$F(\tau)$	V_e	$V_0(HO_3)$	$V_0(DO_3)$
a_0	66.950	38.076	43.329
a_1	81.303	103.345	95.202
a_2	–183.181	–145.513	–149.385
a_3	–22.073	–21.172	–20.368
a_4	–7.594	–9.090	–8.453
a_5	–1.994	–2.432	–2.304
a_6	–0.483	–0.939	–0.870
a_7	–0.235	–0.526	–0.488
a_8	–0.032	–0.090	–0.097
a_9	0.007	–0.007	0.009
a_{10}	0.018	–0.078	–0.132
a_{11}	0.026	0.105	0.114
a_{12}	0.028	0.146	0.089
a_{13}	0.067	–0.081	–0.057
a_{14}	0.052	0.055	–0.013
a_{15}	0.105	0.149	0.149
a_{16}	0.085	–0.023	–0.054

Table B26. Fourier coefficients for the FPA-Q2 bare (G_0) and projected (G) kinetic energy matrix elements functions along the DRP for *cis-trans* isomerization of HO_3 and DO_3.[a]

Functional form: $F(\tau) = a_0 + \sum_{k=1}^{14} a_k \cos(k\tau)$

	HO_3		DO_3	
$F(\tau)$	G_0	G	G_0	G
a_0	0.639	0.617	0.372	0.359
a_1	0.048	–0.003	0.048	0.024
a_2	2.34×10^{-3}	0.014	0.002	0.013
a_3	-9.48×10^{-4}	0.037	–0.001	0.017
a_4	-1.04×10^{-4}	0.027	–0.001	0.011
a_5	-4.07×10^{-4}	0.008	-3.17×10^{-4}	0.004
a_6	-1.04×10^{-4}	0.004	-8.10×10^{-5}	0.002
a_7	-2.73×10^{-5}	0.003	-2.00×10^{-5}	0.001
a_8	-7.31×10^{-6}	0.002	-5.50×10^{-6}	0.001
a_9	-3.42×10^{-6}	6.52×10^{-4}	-2.38×10^{-6}	2.93×10^{-4}
a_{10}	-1.35×10^{-6}	1.67×10^{-4}	-8.25×10^{-7}	7.32×10^{-5}
a_{11}	-1.06×10^{-6}	-8.63×10^{-5}	-7.82×10^{-7}	-4.47×10^{-5}
a_{12}	-2.03×10^{-6}	-1.53×10^{-4}	-1.63×10^{-6}	-7.15×10^{-5}
a_{13}	4.31×10^{-7}	-5.86×10^{-5}	3.27×10^{-7}	-2.58×10^{-5}
a_{14}	8.62×10^{-7}	1.64×10^{-5}	4.81×10^{-7}	6.87×10^{-6}

[a]All quantities consistent with energy in cm^{-1}.

Table B27. Fourier coefficients (a_k, in cm^{-1}) for the FPA-Q2 $H(\tau)$ function.

Functional form: $F(\tau) = \sum_{k=1}^{9} a_k \sin(k\tau)$

	HO_3		DO_3
$F(\tau)$	$H(\tau)$	$F(\tau)$	$H(\tau)$
a_1	–0.008	a_1	0.020
a_2	0.022	a_2	0.035
a_3	–0.033	a_3	–0.025
a_4	–0.027	a_4	–0.024
a_5	–0.027	a_5	–0.011
a_6	–0.012	a_6	–0.006
a_7	–0.006	a_7	–0.004
a_8	–0.004	a_8	–0.002
a_9	-8.35×10^{-4}	a_9	-7.74×10^{-4}

[a]See Table B25.

Table B28. Parameters of WKB tunneling analysis for HO_3 isomerization.

Tunneling parameters	*cis*-HO_3 → *trans*-HO_3	*cis*-DO_3 → *trans*-DO_3
Collision energy (ε, kcal mol^{-1})	0.30	0.23
Collision frequency (ω_6, cm^{-1})	211	162
Effective barrier (kcal mol^{-1})	0.66	0.70
Turning points [(s_1, s_2), u$^{1/2}$ bohr]	(–1.39, 1.14)	(–1.99, 1.81)
Arc length interval (s_{cis}, s_{trans})	(–2.30, 3.10)	(–2.97, 4.13)
Effective barrier frequency (cm^{-1})	148i	114i
Barrier penetration integral (θ)	2.90	4.84
WKB Transmission probability (κ)	3.05×10^{-3}	6.26×10^{-5}
Half-life (τ)	1.79×10^{-11} s	1.14×10^{-9} s

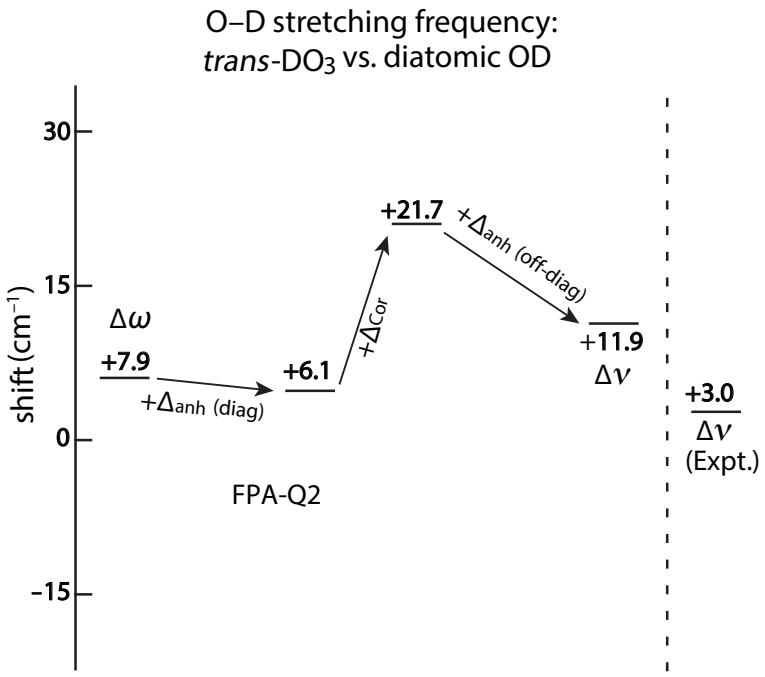

Figure B1. Components of the O–D frequency shift in going from diatomic OH to *trans*-HO_3.

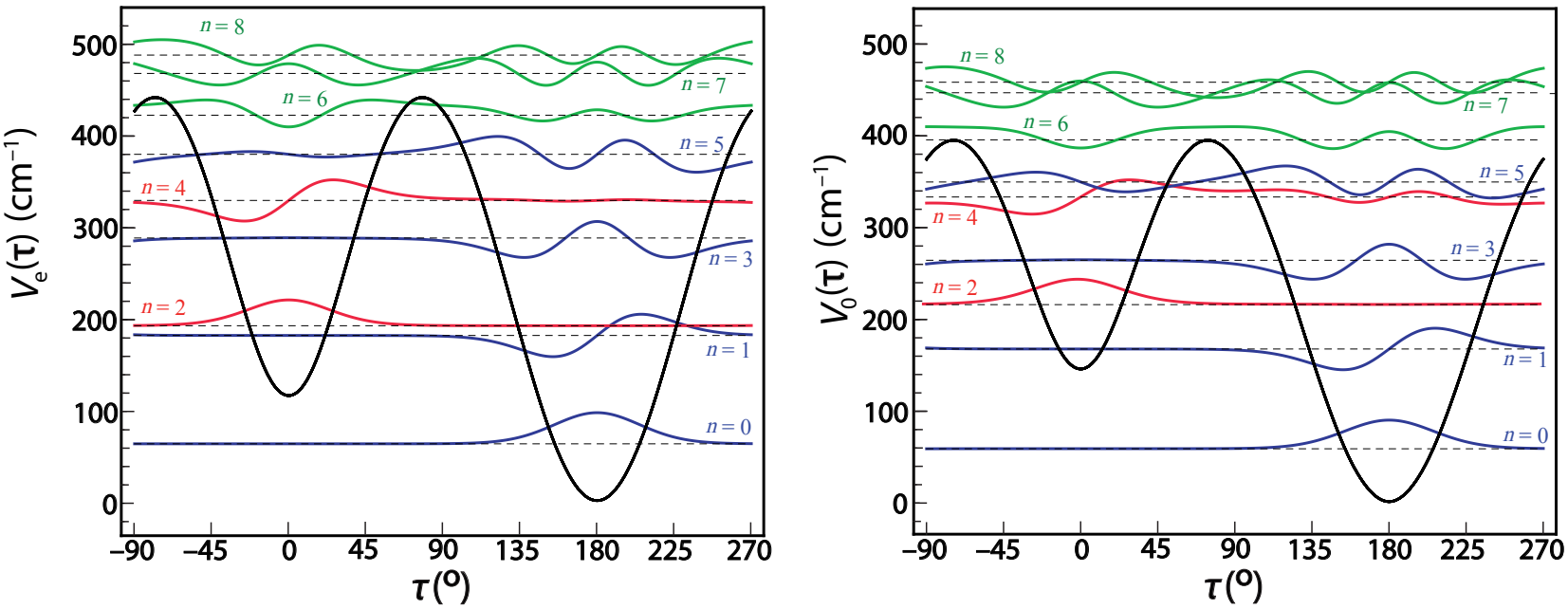

Figure B2 Wave functions for the torsional vibrations of the DO_3 radical, superimposed on the FPA-Q2 potential energy curve along the distinguished reaction coordinate τ. The left and right panels correspond to the bare (V_e) and ZPVE-corrected (V_0) potential energy functions, respectively. Blue, red, and green wave function curves correspond to predominantly *trans*-DO_3, *cis*-DO_3, and delocalized states, in order.

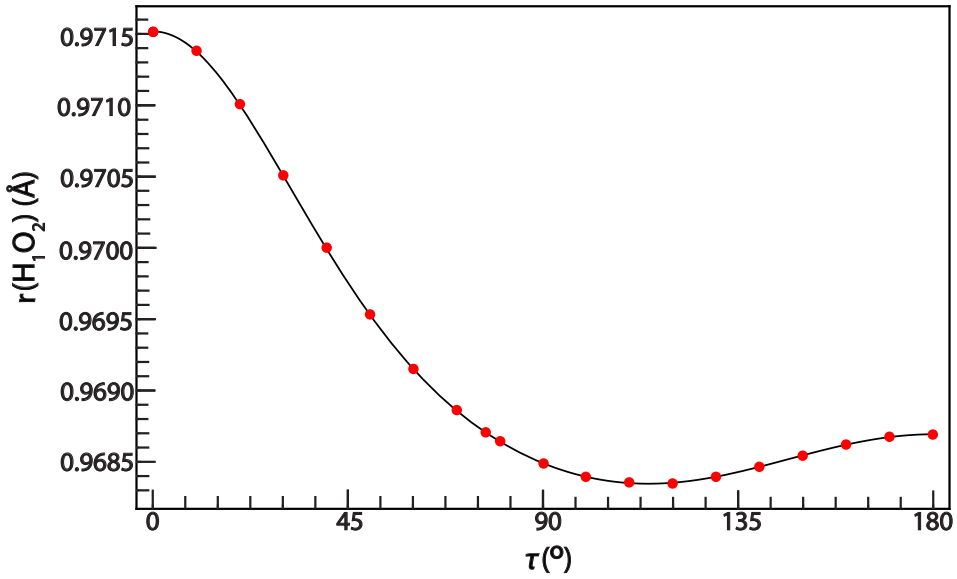

Figure B3. Variation of the FPA-Q2 H_1–O_2 distance with the torsional angle $\tau(H_1O_2O_3O_4)$ along the DRP for *cis-trans* isomerization of HO_3.

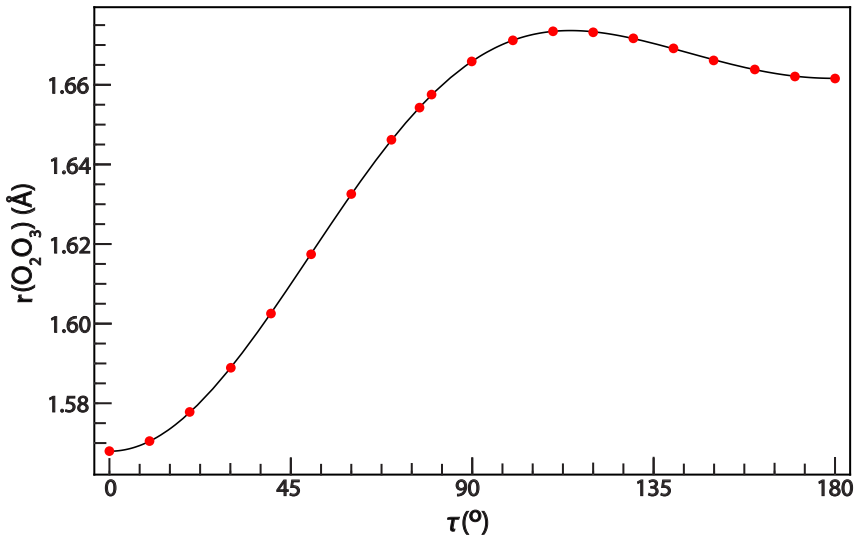

Figure B4. Variation of the FPA-Q2 central O_2–O_3 distance with the torsional angle $\tau(H_1O_2O_3O_4)$ along the DRP for *cis-trans* isomerization of HO_3.

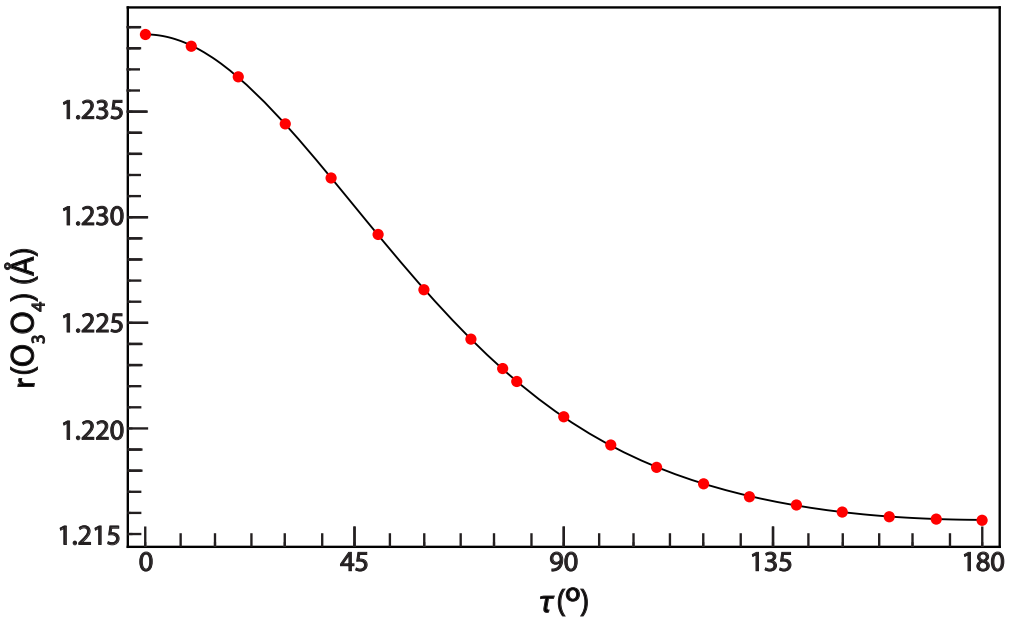

Figure B5. Variation of the FPA-Q2 terminal O_3–O_4 distance with the torsional angle $\tau(H_1O_2O_3O_4)$ along the DRP for *cis-trans* isomerization of HO_3.

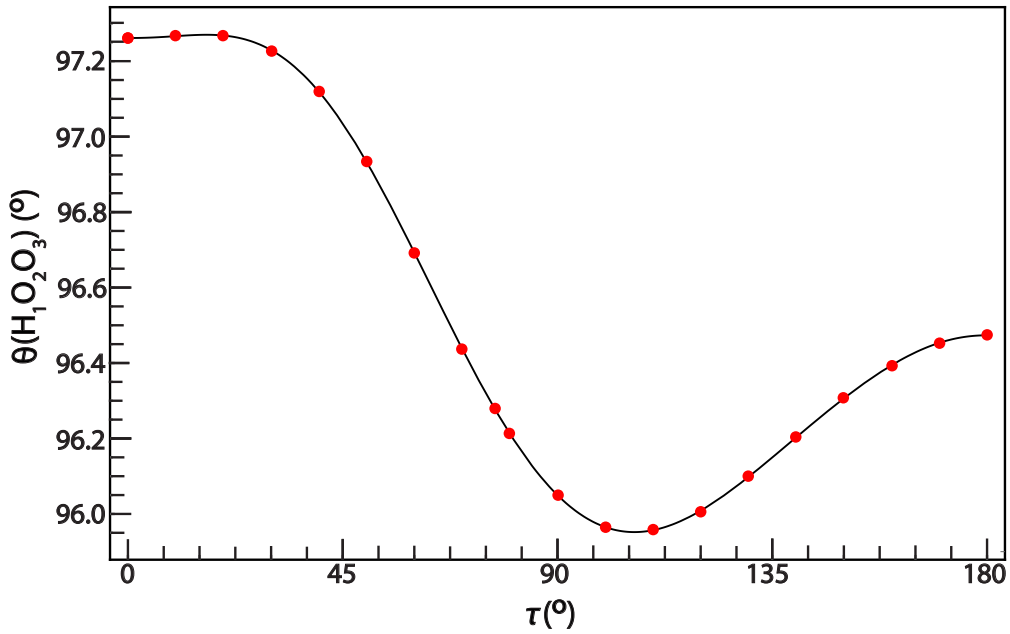

Figure B6. Variation of the FPA-Q2 H_1–O_2–O_3 bond angle with the torsional angle $\tau(H_1O_2O_3O_4)$ along the DRP for *cis-trans* isomerization of HO_3.

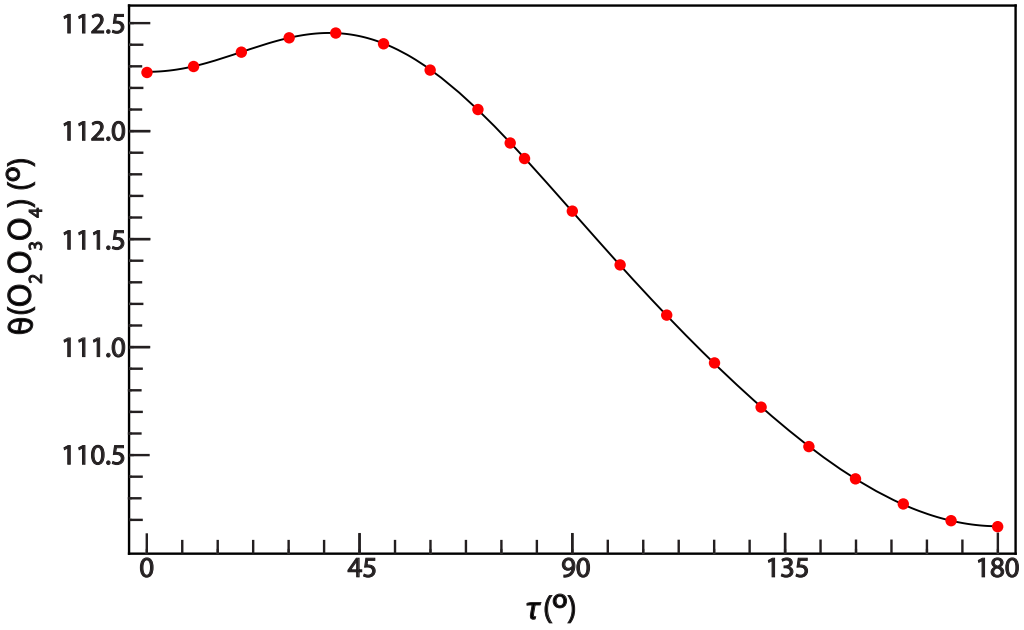

Figure B7. Variation of the FPA-Q2 O_2–O_3–O bond angle with the torsional angle $\tau(H_1O_2O_3O_4)$ along the DRP for *cis-trans* isomerization of HO_3.

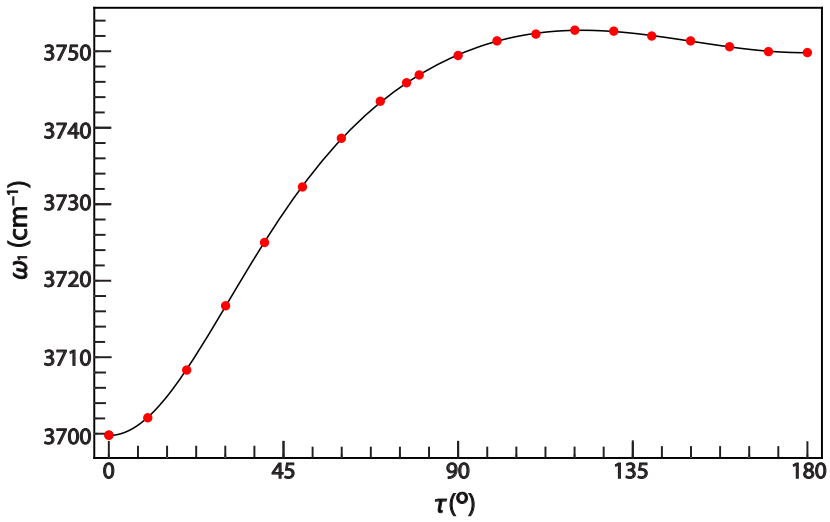

Figure B8. Variation of the FPA-Q2 harmonic vibrational frequency (ω_1, cm^{-1}) for the H_1–O_2 stretch with the torsional angle $\tau(H_1O_2O_3O_4)$ along the DRP for *cis-trans* isomerization of HO_3.

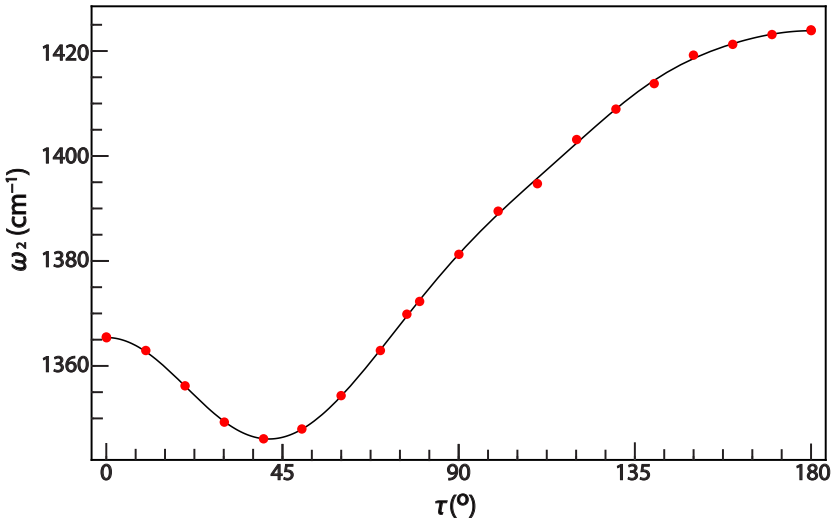

Figure B9. Variation of the FPA-Q2 harmonic vibrational frequency (ω_2, cm^{-1}) for the terminal O_3–O_4 stretch with the torsional angle $\tau(H_1O_2O_3O_4)$ along the DRP for *cis-trans* isomerization of HO_3.

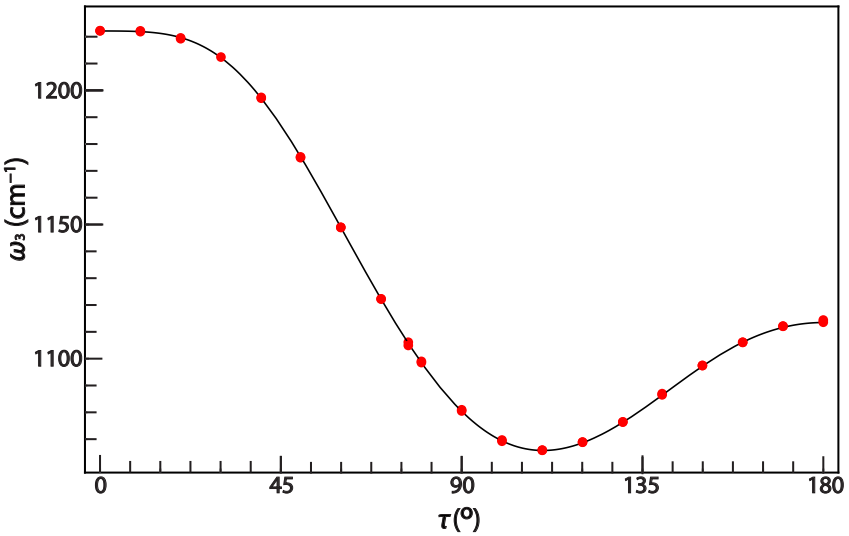

Figure B10. Variation of the FPA-Q2 harmonic vibrational frequency (ω_3, cm^{-1}) for the H_1–O_2–O_3 bend with the torsional angle $\tau(H_1O_2O_3O_4)$ along the DRP for *cis-trans* isomerization of HO_3.

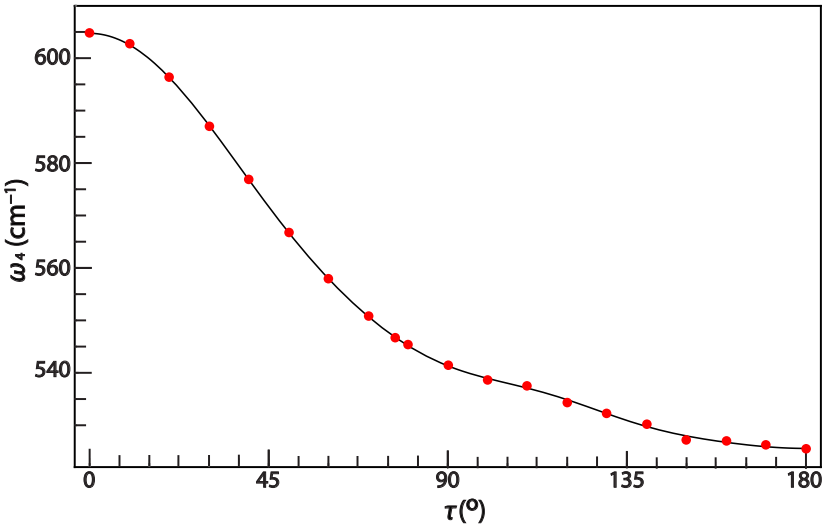

Figure B11. Variation of the FPA-Q2 harmonic vibrational frequency (ω_4, cm^{-1}) for the O_2–O_3–O_4 bend with the torsional angle $\tau(H_1O_2O_3O_4)$ along the DRP for *cis-trans* isomerization of HO_3.

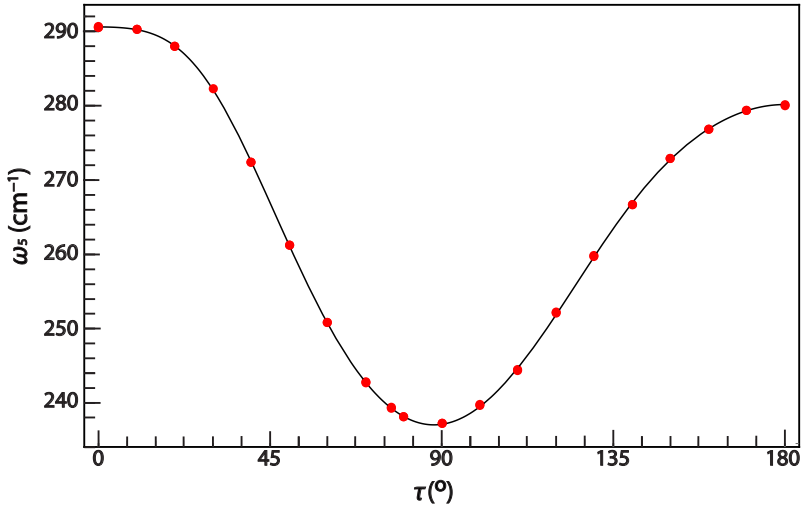

Figure B12. Variation of the FPA-Q2 harmonic vibrational frequency (ω_5, cm^{-1}) for the central O_2–O_3 stretch with the torsional angle $\tau(H_1O_2O_3O_4)$ along the DRP for *cis-trans* isomerization of HO_3.

Mathematical Derivation of Hermiticity Conditions

Under what conditions will the following general operator be Hermitian?

$$\hat{A} = -\frac{1}{2}G(s)\frac{d^2}{ds^2} + H(s)\frac{d}{ds} + L(s)$$

Take the adjoint of the operator:

$$\hat{A}^\dagger = -\frac{1}{2}\left(\frac{d^2}{ds^2}\right)^\dagger G(s)^* + \left(\frac{d}{ds}\right)^\dagger H(s)^* + L(s)^*$$

Employ the fact that d/ds is anti-Hermitian.

$$\hat{A}^\dagger = -\frac{1}{2}\left(\frac{d^2}{ds^2}\right)G(s)^* - \left(\frac{d}{ds}\right)H(s)^* + L(s)^* \;\Rightarrow$$

$$\hat{A}^\dagger = -\frac{1}{2}\left[G''(s)^* + 2G'(s)^*\frac{d}{ds} + G(s)^*\frac{d^2}{ds^2}\right] - H'(s)^* - H(s)^*\frac{d}{ds} + L(s)^*$$

Therefore,

$$\hat{A}^\dagger - \hat{A} = -\frac{1}{2}\left[G''(s)^* + 2G'(s)^*\frac{d}{ds} + G(s)^*\frac{d^2}{ds^2} - G(s)\frac{d^2}{ds^2}\right] - H'(s)^* - \left[H(s)^* + H(s)\right]\frac{d}{ds} + L(s)^* - L(s) \;\Rightarrow$$

$$\hat{A}^\dagger - \hat{A} = -\frac{1}{2}\left[G(s)^* - G(s)\right]\frac{d^2}{ds^2} - \left[G'(s)^* + H(s)^* + H(s)\right]\frac{d}{ds} - \frac{1}{2}G''(s)^* - H'(s)^* + L(s)^* - L(s)$$

In order for $\hat{A}^\dagger = \hat{A}$, the coefficients of the powers of the derivative operators must be zero.

Thus, there are 3 conditions for $\hat{A}$ to be Hermitian:

$$G(s)^* = G(s)$$

$$G'(s) + H(s)^* + H(s) = 0$$

$$-\frac{1}{2}G''(s) - H'(s)^* + L(s)^* - L(s) = 0$$

Taking the derivative of the second condition and placing the result into the third condition yields

$$H'(s) - H'(s)^* = 2\left[L(s) - L(s)^* \right] \quad .$$

In summary, $\hat{A}$ will be Hermitian if the following conditions are met:

$G(s)$ must be real.

$$\mathrm{Re}\left[H(s) \right] = -\frac{1}{2}G'(s)$$

$$\mathrm{Im}\left[H'(s) \right] = 2\,\mathrm{Im}\left[L(s) \right]$$

One application of these conditions is that for a real potential $V(s)$ and reduced inverse mass function $G(s)$, then

$$\hat{A} = -\frac{1}{2}G(s)\frac{d^2}{ds^2} - \frac{1}{2}G'(s)\frac{d}{ds} + V(s)$$

is a Hermitian operator whose eigenfunctions are orthonormal (or can be constructed to be so) over the complete coordinate space according to

$$\int_a^b \psi_m^*(s)\psi_n(s)\,ds = \delta_{mn} \quad .$$

The usual circumstance is that $(a,b) = (-\infty,+\infty)$; however, the orthonormality conclusion also holds if the coordinate s is an angle and $[a,b]$ is the interval of one period. The second case rests on proof that d/ds and d^2/ds^2 are anti-Hermitian and Hermitian, respectively, even if the coordinate space is finite but periodic. These proofs are straightforward and are given below.

Using integration by parts,

$$\int_a^b \phi^*(s)\psi'(s)\,ds = \phi^*(s)\psi(s)\Big|_a^b - \int_a^b \psi(s)[\phi'(s)]^*\,ds \quad \Rightarrow$$

$$\int_a^b \phi^*(s)\psi'(s)\,ds = -\left[\int_a^b \psi^*(s)\phi'(s)\,ds\right]^* + \phi^*(b)\psi(b) - \phi^*(a)\psi(a)$$

If the wave functions are periodic and [*a*,*b*] is the interval of one period, then

$\phi^*(b)\psi(b) = \phi^*(a)\psi(a)$. Hence, the operator $\frac{d}{ds}$ is anti-Hermitian.

In the case of $\frac{d^2}{ds^2}$, consecutive integration by parts is required.

$$\int_a^b \phi^*(s)\psi''(s)\,ds = \phi^*(s)\psi'(s)\Big|_a^b - \int_a^b \psi'(s)[\phi'(s)]^*\,ds \quad \Rightarrow$$

$$\int_a^b \phi^*(s)\psi''(s)\,ds = \phi^*(b)\psi'(b) - \phi^*(a)\psi'(a) - \int_a^b \psi'(s)[\phi'(s)]^*\,ds$$

However,

$$\int_a^b \psi'(s)[\phi'(s)]^*\,ds = \psi(b)[\phi'(b)]^* - \psi(a)[\phi'(a)]^* - \int_a^b \psi(s)[\phi''(s)]^*\,ds,$$

so that

$$\int_a^b \phi^*(s)\psi''(s)\,ds = \left[\int_a^b \psi^*(s)\phi''(s)\,ds\right]^* + \phi^*(b)\psi'(b) - \psi(b)[\phi'(b)]^* - \phi^*(a)\psi'(a) + \psi(a)[\phi'(a)]^*$$

Once again, if the wave functions are periodic and [*a*,*b*] is the interval of one period, then

$\phi^*(b)\psi'(b) - \psi(b)[\phi'(b)]^* = \phi^*(a)\psi'(a) - \psi(a)[\phi'(a)]^*$. Hence, the operator $\frac{d^2}{ds^2}$ is Hermitian.

Consider now the wave equation

$$-\tfrac{1}{2}G(s)\psi''(s)-\tfrac{1}{2}H(s)\psi'(s)+V(s)\psi(s)=E\psi(s)\quad . \tag{B1}$$

For a general choice of $H(s)$, the eigenfunctions are not orthogonal in the sense

$$\int_a^b \psi_m^*(s)\psi_n(s)\,ds \neq \delta_{mn}\ . \tag{B2}$$

However, if the model Hamiltonian is physically based, then we anticipate that a real-valued volume integration factor $J(s)$ exists such that

$$\int_a^b \psi_m^*(s)\psi_n(s)J(s)\,ds=\delta_{mn}. \tag{B3}$$

To find $J(s)$, let

$$\phi_n(s)=\psi_n(s)\sqrt{J(s)} \tag{B4}$$

so that

$$\int_a^b \phi_m^*(s)\phi_n(s)\,ds=\delta_{mn} \tag{B5}$$

by construction. Next, place into the wave equation $\psi(s)=\phi(s)J(s)^{-1/2}$, which yields

$$-\tfrac{1}{2}G\left(\phi''J^{-1/2}-\phi'J^{-3/2}J'+\tfrac{3}{4}\phi J^{-5/2}J'^2-\tfrac{1}{2}\phi J^{-3/2}J''\right)-\tfrac{1}{2}H\left(\phi'J^{-1/2}-\tfrac{1}{2}\phi J^{-3/2}J'\right)+VJ^{-1/2}\phi=EJ^{-1/2}\phi\ \Rightarrow$$

$$-\tfrac{1}{2}G\left(\phi''-\phi'J^{-1}J'+\tfrac{3}{4}\phi J^{-2}J'^2-\tfrac{1}{2}\phi J^{-1}J''\right)-\tfrac{1}{2}H\left(\phi'-\tfrac{1}{2}\phi J^{-1}J'\right)+V\phi=E\phi\quad\Rightarrow$$

$$-\tfrac{1}{2}G\phi''-\tfrac{1}{2}\left(H-GJ^{-1}J'\right)\phi'+\left(\tfrac{1}{4}HJ^{-1}J'-\tfrac{3}{8}GJ^{-2}J'^2+\tfrac{1}{4}GJ^{-1}J''+V\right)\phi=E\phi \tag{B6}$$

If we set

$$G'=H-GJ^{-1}J' \tag{B7}$$

and

$$U=\tfrac{1}{4}HJ^{-1}J'-\tfrac{3}{8}GJ^{-2}J'^2+\tfrac{1}{4}GJ^{-1}J''\,, \tag{B8}$$

then

$$-\tfrac{1}{2}G\phi'' - \tfrac{1}{2}G'\phi' + \left(U+V\right)\phi = E\phi \quad . \tag{B9}$$

From eq (B7),

$$J^{-1}J' = G^{-1}(H - G') \ , \tag{B10}$$

which may be integrated to obtain

$$\ln J = \int \frac{H(s)}{G(s)}\,ds - \ln G + \ln A \ , \tag{B11}$$

or

$$J(s) = \frac{A}{G(s)} \exp\left[\int \frac{H(s)}{G(s)}\,ds\right] \ , \tag{B12}$$

where A is an integration constant. It is not necessary to employ eq (B12), however. By differentiating eq (B10) we obtain

$$J^{-1}J'' - J^{-2}J'^{2} = -G^{-2}G'(H - G') + G^{-1}(H' - G'') \ . \tag{B13}$$

Substitution of eqs (B10) and (B13) into (B8) provides

$$U = \tfrac{1}{4}HG^{-1}(H - G') - \tfrac{1}{8}G^{-1}(H - G')^2 + \tfrac{1}{4}\left[H' - G'' - G^{-1}G'(H - G')\right] \ \Rightarrow$$

$$U = \tfrac{1}{4}\left(H' - G''\right) + \tfrac{1}{8}(H - G')\left[2HG^{-1} - G^{-1}(H - G') - 2G^{-1}G'\right] \ \Rightarrow$$

$$U = \tfrac{1}{4}\left(H' - G''\right) + \tfrac{1}{8}G^{-1}(H - G')^2 \tag{B14}$$

According to the conclusions above, the wave functions satisfying Eq. (B9) will obey the orthonormality condition (B5) and still yield the same energy levels as in Eq. (B1) if $U(s)$ is added to the potential energy function.